

Advanced control strategies to exploit the hydropower potential enhancing ancillary services provision to the power system

Présentée le 16 février 2024

Faculté des sciences et techniques de l'ingénieur
Groupe SCI STI RC
Programme doctoral en génie électrique

pour l'obtention du grade de Docteur ès Sciences

par

Francesco GERINI

Acceptée sur proposition du jury

Prof. A. Skrivervik, présidente du jury
Dr S.-R. Cherkaoui, Prof. M. Paolone, directeurs de thèse
Prof. F. Sossan, rapporteur
Prof. O. Bjarte Fosso, rapporteur
Prof. D. Dujic, rapporteur

*Everything should be made as simple as possible,
but not simpler.*
— Albert Einstein

To my parents...

Acknowledgements

This thesis has been made possible thanks to the support of many people, whom I hereby want to acknowledge and thank.

Firstly, I am thankful to my thesis director, Dr. Rachid Cherkaoui, for his unconditional support throughout the four years of my Ph.D. journey. Similarly, my deep appreciation goes to my co-supervisor, Prof. Mario Paolone, who is the reason for the amazing research environment in which I have had the pleasure to work. His dedication and energy towards teaching and research have been a great source of inspiration for me. I am also grateful to Elena Vagnoni for her unwavering support. My acknowledgment extends to Ms. Sophie Flynn for making my work life easier, at the expense of possibly making hers harder. Moreover, I want to express my gratitude to Prof. Carlo Alberto Nucci for sparking my scientific interest and getting me started on this journey. Along with Prof. Farhad Rachidi, their guidance was instrumental in leading me to EPFL at the perfect time.

A special thanks to Simone, for constantly helping me, you are one of the most altruistic people I have ever met. With you, I would like to acknowledge all my colleagues, Asja, Guglielmo, Tony, Yihui, Ji, Rahul, Sherif, Vladimir, Willem, Matthieu, Lucien, Pal, Lu, Dawn, Martin, Sinan, and many others, with whom I enjoyed spending time together in the lab. A special mention to my office mates, Johanna and Alex, who have shifted my work/life balance in both directions over these four years, and to Antonio, for consistently tipping the scales towards life. Finally, to Enea, for the soundtrack that accompanied my thesis journey.

A sincere thanks also to my friends, Cudi, Elena, Antonello, Chiara, Alice, Valentin, Tom, and Marija for the shared moments across these years.

My heartfelt gratitude goes to my parents, Grazia and Alberto, and my grandparents, who have always supported me unconditionally. I commemorate my grandpa, Riccardo, the first engineer in my life. I wish I could share all of this with you.

Last but not least, to Cloe, my constant source of support and love: thank you for being on my side, and making everything a little simpler.

Lausanne, February 4, 2024

Francesco Gerini

Abstract

The European Union's *Green Deal* aims for a 55% reduction in greenhouse gas emissions by 2030, to achieve the ambitious goal of climate neutrality by 2050. To reach this goal, a massive integration of *Renewable Energy Sources* (RES) into the power grid is necessary. As RES become a large part of the electricity generation mix, there is a growing need for grid services that ensure the grid remains within feasible operation limits in both steady-state and transient conditions. In this context, *Hydropower Plants* (HPPs), contributing to 16.8% of Europe's total electricity in 2022, emerge as vital assets for their controllability and flexibility and crucial for mitigating the intermittency of RES. In this Ph.D. thesis, we propose, discuss, and validate optimal control techniques for the enhanced provision of ancillary services by HPPs, specifically focusing on *Frequency Containment Reserve* (FCR) and *automatic Frequency Restoration Reserve* (aFRR). The thesis is divided into distinct parts, each addressing a specific aspect of optimizing HPP operations for aFRR or FCR provision, to answer the following main research question: "*How can the integration and control of HPPs with new technologies be optimized to enhance their role in ancillary service provision and ensure asset longevity?*"

The first part of the thesis focuses on aFRR provision. As known, aFRR is a fundamental grid service responsible for restoring the rated grid frequency by adjusting the power plant outputs in response to power imbalances. Activated within seconds, it operates up to 15 minutes, after which tertiary control intervenes. In this domain, *Pumped Storage Power Plants* (PSPs) play a fundamental role due to their ability to absorb, or produce, electricity. However, a challenge arises with PSPs equipped with fixed-speed pumps or reversible pump-turbines, as they are machines operated in "on-off" mode, offering limited power regulation capabilities. To address this challenge, we introduce a control framework methodology for PSPs to optimize the dispatch and aFRR reserve allocation among multiple units. The control considers the possibility of operating in *Hydraulic Short Circuit* (HSC) mode, enabling PSPs to actively participate in the aFRR market, even when their primary function is pumping. The objective of the optimal dispatching is to maximize efficiency and reduce the number of start and stop of the machines while the PSP is providing aFRR. To validate this methodology, we apply it to two distinct cases, one of which is a real-world study conducted at the PSP of Grand'Maison, France.

After addressing aFRR provision, the second part of the thesis focuses on the FCR service. The FCR plays a crucial role in maintaining the grid's frequency within a narrow and predefined

Abstract

range by responding to disturbances and restoring the power balance within seconds. We discuss the contribution of *Run-of-River* (RoR) power plants to the provision of FCR, presenting a multilevel control strategy for optimal discharge management. The proposed control strategy aims to operate the unit at the best efficiency, improve water flow management, and minimize component wear during FCR provision. Moreover, we explore the impact of FCR provision on RoR HPPs equipped with Kaplan turbines, introducing a modeling method for turbine performance, and combining operational data with existing characteristic curves for online efficiency estimation. The obtained models are leveraged to compute a new CAM relation for Kaplan units. The control strategy is validated by simulating a month of operation of the RoR HPPs plant located in Vogelgrun (France) and by comparing the results with operational statistics. Results show the effectiveness of the proposed control strategy in increasing the provision of FCR while decreasing the movements of the plant's turbine servomechanisms. However, despite advancements in aging monitoring and movement reduction in RoR HPPs, a large portion of servomechanism activity still comes from FCR provision. This is an inherent role of hydro, without additional support. For this reason, we proceed by focusing on the potential of *Battery Energy Storage Systems* (BESSs) as autonomous FCR providers, laying the basis for the last part of the thesis, where we explore the synergistic benefits achievable by integrating RoR power plants and BESS for enhanced FCR provision.

Indeed, while HPPs are fundamental assets for FCR provision, they suffer from FCR-related wear, increasing maintenance needs. Conversely, BESSs offer quick response-time but are limited by their energy and power capacity. In the last part of this thesis, we explore HPP and BESS integration, introducing an optimal control framework, based on a double layer *Model Predictive Control* (MPC), driving the hybrid system. The upper layer MPC acts as a state of energy manager for the BESS, employing a forecast of the required regulating energy for the next hour. The lower-layer MPC optimally allocates the power set-point between the turbine and the BESS. On top of BESS hybridization, we propose an alternative approach: re-purposing aging Kaplan turbines into variable-speed propellers by employing full-size frequency converters. The motivation behind the latter approach is to improve the provision of FCR without operating the blade servomechanism. In this configuration, the control strategy aims to maximize the efficiency of the overall system by controlling guide vanes and the rotational speed of the propeller turbine only.

On top of providing optimal control strategies, it becomes necessary to have experimental facilities able to test and validate the proposed solutions. Testing platforms are nowadays decoupling the hydraulic and the electric components, testing them separately. Therefore, they are not suitable for the validation of the control strategy under real grid conditions. For this reason, we present an experimental facility where different joint control techniques can be tested on reduced-scale models of hydraulic machines hybridized with a BESS. The presented test rig combines all the fundamental components, both on the hydraulic and the electrical side, within the same testing facility. On the updated platform, we validate the MPC-based control for BESS-hybridized RoR HPPs, considering a comparison with different control strategies

and different BESS sizes. The results demonstrate the superior performance of the proposed controller, compared to simpler techniques like dead-band control or the standalone RoR scenario, leading to improved FCR provision and reduced servomechanism stress. Moreover, the experiments reveal that Kaplan turbines repurposed as VARspeed propellers exhibit similar dynamic response characteristics compared to the standalone Kaplan operation, with the added benefit of effectively eliminating blade movements.

In conclusion, this thesis presents a set of strategies and control frameworks tailored for HPP operators, which are implementable at the plant level. These strategies demonstrate significant potential for enhancing grid stability and operational efficiency of HPPs. The successful validation of these approaches, with some controls experimentally verified and others validated through simulations on real-world case studies, proves their practicality and effectiveness. The research is supported by the XFLEX HYDRO Project under the European Union's Horizon 2020 program.

Key Words: Renewable Energy Sources, Hydropower Plants, Pumped Storage Power Plants, Run-of-River Power Plants, Kaplan Turbines, Battery Energy Storage Systems, Ancillary Services, Frequency Containment Reserve, Automatic Frequency Restoration Reserve, Convex Optimization, Model Predictive Control, Battery Hybrid Hydropower Plants, Variable-Speed Propellers, Hydraulic Short Circuit.

Résumé

Le *Green Deal* de l'Union européenne vise une réduction de 55% des émissions de gaz à effet de serre d'ici 2030, afin d'atteindre l'objectif ambitieux de la neutralité climatique d'ici 2050. Pour atteindre cet objectif, il est nécessaire d'intégrer massivement les *sources d'énergie renouvelables* (RES) dans le réseau électrique. Alors que les RES deviennent une part importante du mix de production d'électricité, il y a un besoin croissant de services système qui garantissent que le réseau reste dans des limites d'exploitation réalisables. Dans ce contexte, les centrales hydroélectriques, qui ont contribué à 16,8 % de la production totale d'électricité en Europe en 2022, apparaissent comme des actifs vitaux en raison de leur contrôlabilité et de leur flexibilité et sont essentielles pour atténuer l'intermittence des sources d'énergie renouvelables. C'est pour cela que ainsi, dans cette thèse de doctorat, nous proposons, discutons et validons des techniques de contrôle optimales pour l'amélioration de la fourniture de services système fréquence par les centrales hydroélectriques, en nous concentrant spécifiquement sur le *contrôle primaire de la fréquence* (FCR), et le *contrôle secondaire de la fréquence* (aFRR). La thèse est divisée en parties distinctes, chacune abordant un aspect spécifique de l'optimisation des opérations des centrales hydroélectriques pour la fourniture d'aFRR ou de FCR, afin de répondre à la question de recherche principale suivante : *Comment l'intégration et le contrôle des centrales hydroélectriques avec de nouvelles technologies peuvent-ils être optimisés pour renforcer leur rôle dans la fourniture de services système fréquence et assurer la longévité des actifs ?*

La première partie de la thèse se concentre sur la fourniture de l'aFRR. L'aFRR est un service fondamental du réseau chargé de rétablir la fréquence nominale du réseau en ajustant la production des centrales électriques en réponse aux déséquilibres des puissance échangées. Activé en quelques secondes, il fonctionne pendant 15 minutes au maximum, après quoi le contrôle tertiaire intervient. Dans ce domaine, les *centrales à pompage-turbinage* (PSP) jouent un rôle prépondérant en raison de leur capacité à absorber ou à produire de l'électricité. Cependant, un problème se pose avec les PSP équipées de pompes à vitesse fixe ou de pompes-turbines réversibles, car il s'agit de machines fonctionnant en mode "on-off", ce qui offre des capacités limitées de régulation de la puissance. Pour relever ce défi, nous introduisons une méthodologie de contrôle pour les PSP afin d'optimiser la répartition et l'allocation de la réserve aFRR entre plusieurs unités. Le contrôle prend en compte la possibilité de fonctionner en mode *court-circuit hydraulique* (HSC), ce qui permet aux PSP de participer activement au marché aFRR, même lorsque leur fonction principale est le pompage.

Résumé

L'objectif de la répartition optimale est de maximiser le rendement et de réduire le nombre de démarrages et d'arrêts des machines pendant que le PSP fournit de l'aFRR. Pour valider cette méthodologie, nous l'appliquons à deux cas distincts, dont l'un est une étude réelle menée au PSP de Grand'Maison, en France.

La deuxième partie de la thèse se concentre sur le service FCR. Le FCR joue un rôle crucial dans le maintien de la fréquence du réseau dans une plage étroite et prédéfinie en répondant aux perturbations et en rétablissant l'équilibre de la puissance (production/consommation) en quelques secondes. Nous examinons la contribution des centrales électriques *au fil de l'eau* (RoR) à la fourniture du FCR, en présentant une stratégie de contrôle à plusieurs niveaux pour une gestion optimale du débit. La stratégie de contrôle proposée vise à faire fonctionner l'unité au meilleur rendement, à améliorer la gestion du flux d'eau et à minimiser l'usure des composants pendant la fourniture de FCR. En outre, nous explorons l'impact de la fourniture de FCR sur les centrales hydroélectriques RoR équipées de turbines Kaplan, en introduisant une méthode d'évaluation de la performance des turbines, combinant les données opérationnelles avec les courbes caractéristiques existantes pour l'estimation du rendement en ligne. Les modèles obtenus sont utilisés pour calculer une nouvelle relation CAM pour les unités Kaplan. La stratégie de contrôle est validée en simulant un mois de fonctionnement de la centrale RoR HPP située à Vogelgrun (France) et en comparant les résultats avec les statistiques opérationnelles. Les résultats montrent l'efficacité de la stratégie de contrôle proposée pour augmenter la fourniture de FCR tout en diminuant les mouvements des servomécanismes des turbines de la centrale. Cependant, malgré les progrès réalisés dans le monitoring du vieillissement et la réduction des mouvements dans les centrales hydroélectriques RoR, une grande partie de l'activité des servomécanismes résulte toujours de la fourniture de FCR. Pour cette raison, nous nous concentrons sur le potentiel des systèmes de stockage d'énergie par batterie (BESS) en tant que fournisseurs autonomes de FCR, posant les bases de la dernière partie de la thèse, où nous explorons les avantages synergiques réalisables en intégrant les centrales électriques RoR et les BESS pour améliorer la fourniture de FCR.

En effet, alors que les centrales hydroélectriques sont des actifs fondamentaux pour la fourniture de FCR, elles subissent une usure significative en raison de leur utilisation intensive. Inversement, les BESS offrent une réponse rapide mais sont limités par leur capacité en termes d'énergie et de puissance. Dans la dernière partie de cette thèse, nous explorons l'intégration des HPP et des BESS, en introduisant un schéma de contrôle optimal, basé sur un *modèle de contrôle prédictif* (MPC) à deux niveaux, pilotant le système hybride. Le MPC du niveau supérieur agit comme un gestionnaire de l'état de l'énergie pour le BESS, en utilisant une prévision de l'énergie de régulation requise pour l'heure suivante. La distribution optimale du point de consigne de la puissance entre la turbine et le BESS est assurée par le MPC du niveau inférieur. En plus de l'hybridation du BESS, nous proposons une autre approche : la reconversion des vieilles turbines Kaplan en turbines à hélice à vitesse variable en utilisant des convertisseurs de fréquence. La motivation derrière cette dernière approche est d'améliorer la fourniture de FCR sans faire fonctionner le servomécanisme des aubes. Dans cette

configuration, la stratégie de contrôle vise à maximiser le rendement du système global en contrôlant uniquement les directrices et la vitesse de rotation de la turbine à hélice.

En plus de fournir des stratégies de contrôle optimales, il devient nécessaire de disposer d'installations expérimentales capables de tester et de valider les solutions proposées. Actuellement, les plateformes d'essai découplent les composants hydrauliques et électriques afin de les tester séparément. Ces mesures ne conviennent donc pas pour valider la stratégie de contrôle dans les conditions réelles du réseau. C'est pour cette raison que nous mettons en place une installation expérimentale dans laquelle différentes techniques de contrôle peuvent être testées sur des modèles à échelle réduite de machines hydrauliques combinées avec un BESS. Le banc d'essai présenté combine tous les composants fondamentaux, tant du côté hydraulique que du côté électrique, au sein d'une même installation d'essai. Sur la plateforme mise à jour, nous validons la commande basée sur le MPC pour les centrales électriques hybrides RoR avec BESS, en comparant différentes stratégies de commande et différentes tailles de BESS. Les résultats démontrent une performance supérieure du contrôleur proposé, par rapport à des techniques plus simples comme le contrôle de la bande morte, ce qui conduit à une meilleure fourniture de FCR et à une réduction de l'usure du servomécanisme. En outre, les expériences révèlent que les turbines Kaplan reconverties en turbines à hélice à vitesse variable présentent des caractéristiques de réponse dynamique similaires à celles du fonctionnement Kaplan autonome, avec l'avantage supplémentaire d'éliminer efficacement les mouvements des aubes.

En conclusion, cette thèse présente un ensemble de stratégies et de cadres de contrôle adaptés aux opérateurs de centrales hydroélectriques, qui peuvent être mis en œuvre au niveau de la centrale. Les stratégies présentées ont le potentiel de contribuer significativement à l'amélioration de la stabilité du réseau et du rendement opérationnel des centrales hydroélectriques. La validation réussie de ces approches, avec certaines vérifications expérimentales et d'autres validées par des simulations sur des études de cas réels, démontre leur efficacité. Cette recherche est soutenue par le projet XFLEX HYDRO dans le cadre du programme Horizon 2020 de l'Union européenne.

Contents

Acknowledgements	i
Abstract	iii
List of Figures	xv
List of Tables	xix
1 Introduction	1
I Automatic Frequency Restoration Reserve	9
2 Optimal Short-Term Dispatch of Pumped-Storage Hydropower Plants Including Hydraulic Short Circuit	13
2.1 Introduction	14
2.1.1 Context and Motivation	14
2.1.2 Chapter Contributions	15
2.2 Problem Statement	15
2.2.1 Context Regarding Power Plants Operation	15
2.2.2 Problem Formulation	16
2.2.3 Predictive Control	21
2.3 Results and Discussion	24
2.3.1 Case A: Simulation with 4 Reversible Variable Speed Units	24
2.3.2 Case B: Grand'Maison (FR) HPP with 12 Units	27
2.4 Discussion	32
II FCR Provision from HPP and BESS	35
3 Improving Frequency Containment Reserve Provision in Run-of-River Hydropower Plants	39
3.1 Introduction	40
3.2 Impact of Frequency Containment Reserve on Kaplan Turbines Wear and Tear	42
3.3 Optimal CAM Computation of Kaplan Turbines Accounting for FCR-Induced Wear and Tear	43

Contents

3.3.1	Problem Statement	43
3.3.2	Surrogate Model of a Kaplan Turbine	45
3.3.3	CAM Computation	46
3.3.4	Results	47
3.4	Improving Frequency Containment Reserve Provision in Run-of-River Hydropower Plants	51
3.4.1	Problem Statement	51
3.4.2	Multilevel Control Strategy	53
3.4.3	Results	61
3.5	Discussion	66
4	Optimal Frequency Containment Reserve Provision of Grid-Forming Converter-Interfaced BESSs	67
4.1	Introduction	68
4.1.1	Motivation	68
4.1.2	Chapter's Contribution	69
4.2	State-of-the-Art of BESSs Converters Controls	70
4.3	Problem Statement	71
4.3.1	Outline of the Control Framework for Grid-forming BESSs	71
4.3.2	Regulatory Framework	72
4.4	Framework	73
4.4.1	Day-Ahead	73
4.4.2	Intra-day	76
4.4.3	Real Time	79
4.5	Local Effects of Grid-Forming Converters Providing Frequency Regulation to Bulk Power Grids	82
4.5.1	State-of-the-Art Metrics	82
4.5.2	New Metric	83
4.6	Experimental Validation	83
4.6.1	Experimental Setup	83
4.6.2	Experimental Results	84
4.7	Discussion	86
III	Technology Integration in HPP for Enhanced FCR Provision	91
5	Control Strategies for Enhanced Frequency Containment Reserve Provision of Run-of-River Power Plants	95
5.1	Introduction	96
5.2	Enhanced Frequency Containment Reserve Provision from Battery Hybridized Hydropower Plants	97
5.2.1	Problem Statement	97
5.2.2	Control Framework	99

5.3	Experimental Investigation of Repurposed Kaplan Turbines as VARspeed Propellers for Maximizing FCR	105
5.3.1	Problem Statement	105
5.3.2	Control Framework	105
5.4	Discussion	106
6	Design of Experiments for a BESS-Hybridized Hydro Turbine Test Rig	107
6.1	Experimental Setup	108
6.1.1	Hydro-mechanical components	108
6.1.2	Electrical Components	109
6.1.3	Data-Flow and Software Infrastructure	111
6.2	Different configurations	113
6.2.1	Baseline ("Only Hydro") Setup	113
6.2.2	BESS Setup	113
6.2.3	VARspeed Setup	114
6.3	Experimental Test	115
6.3.1	Reduced-Scale Model	115
6.3.2	BESS Sizing	116
6.3.3	Grid Scenario	117
6.4	Key Performance Indicators (KPIs)	118
6.4.1	FCR Provision Quality	119
6.4.2	Wear and Tear Reduction	120
6.4.3	Hydraulic and Global Efficiencies	120
6.5	Discussion	121
7	Experimental Validation of Enhanced FCR Provision from RoR HPPs including a BESS-hybridized configuration	123
7.1	Overview	124
7.2	Optimal Control Strategy for BESS-Hybrid RoR HPPs	124
7.2.1	FCR Provision Quality	124
7.2.2	HPP Wear and Tear Reduction	125
7.2.3	Safe BESS Operation	127
7.2.4	Summary	128
7.3	Experimental Investigation of Repurposed Kaplan Turbines as Variable-Speed Propellers for Maximizing FCR	129
7.3.1	FCR Provision Quality	129
7.3.2	HPP Wear and Tear Reduction	129
7.3.3	Hydraulic and Global Efficiencies	130
7.3.4	Summary	131
7.4	Discussion	132
8	Conclusion	135

Contents

A	Convexification of Problem (3.6)	139
A.1	Methodology	139
A.2	Results	141
B	Forecasting the Grid's Frequency	143
B.1	Regulating Energy Forecasting	143
B.2	Short-Term Frequency Forecasting	145
C	Forecasting Load	147
	Curriculum Vitae	167

List of Figures

1.1	Graphical representation of the thesis structure.	8
2.1	Timeline of the control framework, showing the dispatch plan \hat{G} , the executed action $P_{0:t-1}^{co}$, and the future set points $P_{t:t+T}^{co}$	16
2.2	Normalised efficiency for the four machines in pumping (left side) and generating (right side) mode.	25
2.3	Solution of the algorithm for the 4 units case with (a) start-up cost of 25 without future-aware control (b) start-up cost of 25 with future-aware control (c) start-up cost of 50 without future-aware control.	26
2.4	Penstock and units distribution in the HPP of Grand'Maison (FR).	27
2.5	Normalized efficiency as a function of power produced by Pelton 1, for different combinations of active units.	29
2.6	Active power (P^{co}) and aFRR set-points (R^\dagger, R^\downarrow) for one month of operation. . .	29
2.7	Comparison between measurement and algorithm output, in terms of aggregated number of SUSL and average HPP efficiency.	31
2.8	Comparison between measurement and algorithm output, in terms of aggregated number of REND and average HPP efficiency.	31
3.1	Block-diagram of a Kaplan turbine control system.	42
3.2	Guide vanes opening α and blade opening β for a Kaplan turbine.	44
3.3	Active power error distribution for a one-month data set, with a time sampling of 1 second.	48
3.4	Comparison between the currently adopted CAM curve for the HPP of Vogelgrun and optimal CAM computed (dashed line) by Algorithm 3.	50
3.5	NoM J and distance z_j for a general trajectory of a moving organ (i.e., guide vane or blade) expressed in terms of percentage opening deviation.	52
3.6	Multilevel control strategy control diagram.	54
3.7	Set-point problem on a time scale.	55
3.8	Expected trajectories of the CDE due to FCR provision a period T (a) without and (b) with the action of the offset discharge \dot{V}_h^{OFF}	59
3.9	RMSE and R^2 of the linearization mapped over all the operation points.	62
3.10	PDF and CDF of the linearization R^2	63

List of Figures

3.11	Comparison of predicted value $\Delta \hat{V}_h^{\text{FCR}}$, the offset function $\Delta \hat{V}_h^{\text{OFF}}$ and the CDE in bold-red. In light-red the scenario with enhanced droop but without discharge management.	65
4.1	Main schemes of GFR and GFL controls.	70
4.2	Outline of the Control Framework for Grid-forming BESSs.	71
4.3	General feeder configuration used for the problem statement. The distribution feeder includes a group of buildings hosting stochastic and uncontrollable PV installations and a grid-connected BESS. The grid has a radial topology. The BESS is the sole controllable resource of the feeder. Dispatch and grid services are considered to be provided at the PCC.	74
4.4	Timeline of the control framework. The dispatch plan and the allocation of ancillary services are computed on the day ahead. The dispatch plan \hat{G} has a time resolution of 5 minutes (discrete time index n). During the day, the MPC problem is executed every 10 seconds (discrete time index k). Finally, the real time problem computes the final $f^{\text{set}}, \nu^{\text{set}}$ set-points every second s	77
4.5	Capability curves of the converter used for the experimental validation.	80
4.6	Input of the day-ahead problem. (a) shows 10 demand-generated scenarios, and their relative upper and lower bound. (b) shows the upper and lower bound for the PV production. (c) combines load and PV to show the prosumption scenario, input of the day ahead problem. Output of the day-ahead problem. (d) and (e) show the power and energy budget, respectively, allocated to perform the different services.	88
4.7	Experimental results for the 24-hour test. (a) compares the dispatch plan (in black) with the measured power at the PCC (shaded gray), the prosumption of the feeder (in dashed red), the BESS power flow (in shaded red), and the average power required for each 5-minute window for the provision of FCR service by the BESS. (b) shows the grid frequency and its 5-minute mean. The SOE of the battery during the test is visible in (c).	89
4.8	CDF of rRoCoF	90
5.1	DLMPC structure: inputs and outputs of the UL (in blue) and LL (in red).	98
5.2	Timeline of the problem: actuation of the UL in blue, i.e., each hour h , and of the LL in red, i.e., each second s	98
5.3	CAM Curves and expected efficiency for the Kaplan runner for a constant head $H = 10\text{ m}$ and a fixed speed of $n = 1500\text{ min}^{-1}$	104
5.4	Efficiency hill-chart and speed CAM of the VARspeed propeller with $\text{RBA} = 18^\circ$	106
6.1	Hydro-mechanical side of the PTMH-PF3 platform for reduced scale physical turbine model tests. The electrical connections are shown in Fig. 6.2. The blue arrows show the direction of the water flow.	108
6.2	Test-rig 3-phase schematics, with switches and PMU measuring.	109

6.3	Data-Flow of the PTMH PF3 testing platform. The different data flows (indicated by arrows in the figure) are detailed in Table 6.3.	111
6.4	Schematics of the PTMH PF3 power grid used in the " <i>Only Hydro</i> " setup.	114
6.5	Schematics of the PTMH PF3 power grid used in the " <i>BESS Hybrid</i> " mode.	114
6.6	Schematics of the PTMH PF3 power grid used in the " <i>VARspeed</i> " setup.	115
6.7	HBM strain gauge on the connecting rod of one blade of the Kaplan Turbine.	116
6.8	CDF of Frequency deviation in continental Europe, based on year-long time series collected between 2019 and 2020. The upper x-axis shows the FCR power associated with the frequency deviation, for a FCR droop of 125 kWhz^{-1}	117
6.9	Frequency Time Series for the test. Measurement from SwissGrid during the system split on the 8th of January 2021. Data available from [126].	118
6.10	Dead-band controller used as a benchmark.	119
7.1	Comparative analysis of blade torque oscillation across all test scenarios.	127
7.2	BESS SOE evolution during the different experiments.	128
7.3	Comparative analysis of blade torque oscillation across all test scenarios.	131
7.4	Hydraulic Efficiency η	132
7.5	Global Efficiency η^g	132
A.1	Surrogate model of the efficiency η^* , as a function of the guide vanes opening and the blade opening. The values for η , α , and β are normalized with respect to their maximum value.	141
A.2	Space of the solutions for Eq. (A.3) for $H = 12 \text{ m}$. The contour lines represent different discharge levels, normalized with respect to their maximum value.	142
B.1	In light gray, the CI of the expected evolution of $W_h(t)$ in 1-hour time intervals, EPFL data-set, (CI = 5-95%).	144
B.2	W_f Auto-Correlation Function (ACF) above and Partial Auto-Correlation Function (PACF) below.	146

List of Tables

2.1	Set-points for Case A (Simulation with 4 Reversible Variable Speed Units). . . .	24
2.2	Comparison of KPIs and Computational Time.	32
3.1	Performance of the Surrogate Models.	48
3.2	Statistical Characteristics of the Validation Tests.	49
3.3	Droop Coefficient Values kWhz^{-1}	63
3.4	v^F for Different Strategies.	64
4.1	Tracking Error Statistics (in kW).	85
6.1	Battery and Converter's Specifications.	110
6.2	Switches Configuration for the Different Testing Setups.	110
6.3	Data Flow Description for the PTMH PF3 Test Rig	112
6.4	Example of Electrical Measurements on the PTMH-PF3 Testing Platform During the Experiments.	113
6.5	List of Set-points Dispatched by the Central Controller.	113
6.6	Hydro-Mechanical Measurements on the PTMH-PF3 Testing Platform.	116
7.1	RMSE Values and Reduction (%) of the Tracking Error (TE) with respect to <i>Only Hydro</i>	125
7.2	Reduction in Mileage and Movements (%) of the GVO and RBA Servomechanisms.	126
7.3	RMSE Values and Reduction (%) of the Tracking Error (TE) with respect to <i>Only Hydro</i>	129
7.4	Reduction in Mileage and Movements (%) of the GVO and RBA servomechanisms.	130
7.5	KPIs Comparison with the 'Only Hydro' Scenario.	132
B.1	Comparison Between the Forecasting Models.	144

Nomenclature

Abbreviations

aFRR	Automatic Frequency Restoration Reserve
AR	Auto-Regressive
BESS	Battery Energy Storage Systems
CAM	Combinator Block in a Kaplan Governor, Linking GVA and RBO Values
CAPEX	Capital Expenditure
CC	Characteristic Curves
CDE	Cumulative Discharge Error
CDF	Cumulative Density Function
CI	Confidence Interval
DBF	Dead Band Filter
DESL	Distributed Electrical System Laboratory
DLMP	Double Layer Model Predictive Control
DSO	Distribution System Operator
EDF	Électricité de France
ENTSOE	European Network of Transmission System Operators for Electricity
EPFL	École Polytechnique Fédérale de Lausanne
FCR	Frequency Containment Reserve
FPGA	Field Programmable Gate Array
FSFC	Full-Size Frequency Converters
GCV	Generalized Cross Validation

Nomenclature

GFL	Grid-Following
GFR	Grid-Forming
GVO	Guide Vane Opening
HPP	Hydro Power Plant
HSC	Hydraulic Short Circuit
IEC	International Electrotechnical Commission
IFD	Integral Frequency Deviation
LL	Lower Layer
MAE	Maximum Absolute Error
MARS	Multivariate Adaptive Regression Spline
ME	Mean Error
MIP	Mixed Integer Programming
MPC	Model Predictive Control
MSE	Mean Square Error
NoM	Number of Movements
OEM	Original Equipment Manufacturer
OP	Optimization Problem
OR	Operating Range
PBC	Point of Battery Coupling
PCC	Point of Common Coupling
PDF	Probability Density Function
PID	Proportional–Integral–Derivative controller
PLL	Phase-Locked Loop
PMU	Phasor Measurement Units
PSP	Pumped-Storage Power Plants
PT	Pump Turbine
PTMH	Plateforme Technologique Machines Hydrauliques

PV	Photovoltaic
RBA	Runner Blade Angle
RBT	Runner Blade Torque
RES	Renewable Energy Sources
RMS	Root Mean Squared
RMSE	Root Mean Squared Error
RoCoF	Rate of Change of Frequency
RoR	Run-of-River
SOE	State of Energy
SUSD	Start-Up/Shut-Down
TE	Tracking Error
THD	Total Harmonic Distortion
TSO	Transmission System Operator
TTC	Three-Time-Constant
UDP	User Datagram Protocol
UL	Upper Layer
VARspeed	Variable-Speed
VR	Variation with Repetition
Functions	
$\phi(\mathbf{P}_t, H_t, \mathbf{X}_t)$	Power Losses of the HPP as function of power of the units and of the net head for each combination of operating machines \mathbf{X}_t .
$\psi(\mathbf{X}_t, \mathbf{X}_{t-1})$	Number of SUSD at time t with respect to the previous time-step.
$\eta^*(\alpha, \beta, n_{ED})$	Kaplan hydraulic efficiency as a function of GVO, RBA and IEC speed coefficient.
$\dot{V}^*(\alpha, \beta, n_{ED}), \bar{\dot{V}}_{\ell-1}$	Kaplan hydraulic discharge as a function of GVO, win RBA and IEC speed coefficient, linearization of the function around the point $\ell - 1$.
$\xi(v^{DC}, v^{AC}, P^{BESS}, Q^{BESS})$	Capability curve of the power converter as a function of the voltage on both the DC and AC side and of the BESS SOE.

Nomenclature

Indices

t	Time index (general).
s	Time index (s).
k	Time index (10 s).
m	Time index (min).
a	Time index (5 min).
h	Time index (h).
d	Time index (d).
i	Unit index $\in [1, I]$.
ℓ	CAM array index $\in [1, L]$.

Parameters

ρ, g	Water density and gravitational constant
D	Runner diameter
T	Number of steps in of the MPC horizon
K, A	Number of 10 s and 5 minutes periods in one day, i.e., 8640 and 288
$E_{\text{nom}}^{\text{BESS}}$	Rated BESS energy
$\omega_\phi, \omega_\psi, \omega_c$	Weight associated with the power losses and with the SUSL cost, non-negative parameter tuned to achieve the desired sparsity.
$\omega_\eta, \omega_{\dot{V}}$	Weight associated with the machine efficiency and with the discharge tracking, respectively
ω_P, ω_Q	Weight associated with the need to comply with active and reactive power set point.

Sets

Ω_X	Set of the all the combinations of operating machines.
$\Omega_{X,t}^{\text{co}}, \Omega_{X,t}^{\text{f}}$	Set of the possible combinations of operating machines, feasible for the power set-point only, and for power set-point and reserve at time t .
$\Omega_\alpha, \Omega_\beta$	Set of all the feasible values of guide vanes opening angle and blades opening angle.

Variables

Chapter 2:

$\hat{G}, \Delta G_t, P^{co}$	Scheduled dispatch plan, re-dispatch at time t and resulting active power request to the HPP.
$\hat{R}, \hat{R}^\uparrow, \hat{R}^\downarrow$	Scheduled secondary reserve (aFRR): Total, Upwards and Downwards.
$\mathbf{P}_t, \mathbf{P}_t^G, \mathbf{P}_t^P$	Arrays $\in \mathbb{R}^I$ containing the power output, generated and absorbed powers of all the units at time t .
$P_{i,t}, P_{i,t}^G, P_{i,t}^P$	Net, generated and absorbed active power of unit i at time t
$\mathbf{X}_t, \mathbf{X}_t^G, \mathbf{X}_t^P$	Array $\in \mathbb{R}^I$ containing the overall, generating and pumping states of all the units at time t .
$X_{i,t}, X_{i,t}^G, X_{i,t}^P$	Overall, Generation and Consumption state of unit i at time t
C, C^{co}, C^f	Number of total combinations, combinations feasible for P^{co} and combinations feasible for P^{co} and $R_t^\uparrow, R_t^\downarrow$, i.e., cardinality of the set Ω_X, Ω_X^{co} and Ω_X^f , respectively.
$\mathbf{P}_{t:t+T}^{co}$	Array $\in \mathbb{R}^T$ containing the HPP power set point array, containing element from time t to time $t + T$
O, \mathbf{O}	Objective function value and Array $\in \mathbb{R}^{C^f}$ containing the objective function value of each optimization problem run in each combination

Chapter 3:

α, β	Guide vanes and runner blades opening angle.
n, H, n_{ED}	Rotational speed, net head, IEC speed coefficient of the hydraulic machine.
η, \dot{V}	Hydraulic efficiency and discharge.
f, σ_f	Grid frequency and frequency droop for FCR provision.
τ_W	Water starting time
$\mathbf{CAM}_\alpha, \mathbf{CAM}_\beta, \mathbf{CAM}_{\dot{V}}$	Arrays $\in \mathbb{R}^L$ containing the GVO, the RBA and the discharge of the CAM lookup table.
y, y^*, γ, γ_l	MARS approximation function representing efficiency or discharge in the study and its surrogate model, set of coefficients for the basis functions and unknown coefficient for the l^{th} basis function.

Nomenclature

$\mathbf{x}, x_{v(l,b)}, x_0, t_{l,b}$	MARS vector of independent variables which includes α , β , and n_{ED} , input variable corresponding to the l^{th} truncated linear function, uni-variate knot and not value corresponding to $x_{v(l,mb)}$.
$B_m(\mathbf{x}), b_m^+(x, t), b_m^-(x, t)$	MARS Basis function combining uni-variate basis functions, truncated linear function for positive values, and truncated linear function for negative values.
NoS, NoIV, NoB, NoLF	MARS Number of samples, number of MARS independent variables, number of basis functions, and number of truncated linear functions, respectively.
P^{HPP}, P^m, η^e	Electrical and mechanical power of the hydroelectric unit, electrical efficiency.
z_j, J, Z	Distance of a single movement, number of movements, cumulated distance and j for a servomechanism.
$\dot{V}^{DISP}, \dot{V}^{FCR}, \dot{V}^{OFF}$	Hydraulic discharge set point related to dispatch, FCR and offset.
$\dot{V}^{SET}, \Delta V_h, \Delta V_h^{FCR}$	Hydraulic discharge set point, CDE for the hour h and CDE due to FCR provision.
κ, v^F	Conversion factor between produced energy and amount of water that flows through the HPP, duration of the period in which the discharge error is within the limit.
E_h^{FCR}	Energy to be provided in hour h due to FCR provision.
$W_h, \hat{W}_h, \hat{W}_h^\uparrow, \hat{W}_h^\downarrow$	Realization and prediction of the integral of frequency deviation over the hour h , with its 5% CI and its 95% CI.
σ_f^D, σ_f^P	Maximum frequency droop for FCR provision, according to the maximum admissible CDE and the maximum unit power.
$v_{\alpha_o}, v_{\alpha_c}, v_{\beta_o}, v_{\beta_c}$	Normalized maximum speeds in opening and closing of the servomotor acting on the guide vanes and blades.
v_{β_o}, v_{β_c}	Normalized maximum speeds in opening and closing of the servomotor acting on the runner blades.

Chapter 4:

$\tilde{\theta}_g$	Grid voltage angle.
σ_f, σ_v	Frequency and voltage droop for FCR provision and voltage support.
SOE	BESS state of charge.

G, S, F	Composite active power flow at the PCC, Feeder Prosumption and BESS active power offset.
\hat{S}, F^o	Forecast profile of feeder prosumption and computed BESS power offset profile.
$f_s^{\text{set}}, v_s^{\text{set}}$	Frequency and voltage set-points at time s for the GFR converter.
$P_s^{\text{BESS, set}}, Q_s^{\text{BESS, set}}$	Active and reactive power set-points at time s for the GFL converter.
f, v	Grid frequency and voltage.
$v^{\text{AC}}, v^{\text{DC}}$	AC voltage and DC voltage
$\eta_{\text{ch}}, \eta_{\text{dch}}$	Charging and discharging efficiencies of the BESS.
rRoCoF	Relative rate-of-change-of-frequency.
\underline{k}, \bar{k}	Lower and upper bounds of the time window.
$G_k^*, G_k^+, \Delta G_k^F$	Dispatch for the 5 minute, expected average composite flow at the PCC at the end of a 5-minute window and deviation caused by the FCR response of the GFR converter.
$\underline{i}_{k:k}^o$	Computed control action trajectory of the BESS current.
$\underline{v}_{k:k}$	Battery DC voltage.
x_k	State vector of the voltage model.
$\phi^v, \psi_i^v, \psi_1^v$	Transition matrices for the TTC electrical equivalent circuit model of the BESS voltage on the DC bus.
$\phi^{\text{SOE}}, \psi_i^{\text{SOE}}$	Transition matrices for the SOE model of the BESS.
Chapters 5 to 7:	
$P^{\text{BESS}}, Q^{\text{BESS}}$	BESS active and reactive power.
$P^{\text{HPP}}, Q^{\text{HPP}}$	HPP active and reactive power.
$P^{\text{HPP, set}}, P^{\text{BESS, set}}$	Set-point for the Hydropower Plant and BESS power output.
$P_h^0, \text{SOE}, E_h^{\text{FCR}}$	Constant hourly offset for BESS and HPP, BESS state of charge, energy to be provided in hour h due to FCR provision.
σ_f, f, \hat{f}	Frequency droop, grid frequency and predicted grid frequency.
$W_h, \hat{W}_h, \hat{W}_h^\uparrow, \hat{W}_h^\downarrow$	Realization and prediction of the integral of frequency deviation over the hour h , with its 5% CI and its 95% CI.

Nomenclature

$\eta_{\text{ch}}, \eta_{\text{dch}}$	Charging and discharging efficiencies of the BESS.
TE	Tracking Error.
$v^{\text{AC}}, v^{\text{DC}}$	AC voltage and DC voltage
α, β	Guide vanes and runner blades opening angle.
n, H, n_{ED}	Rotational speed, net head, IEC speed coefficient of the hydraulic machine.
$T, P^{\text{m}}, P^{\text{h}}$	Torque and mechanical power on the shaft of the hydroelectric unit at time s , hydraulic power.
$\eta, \eta^{\text{e}}, \eta^{\text{g}}$	Hydraulic, electrical and global efficiency of the Hydroelectric unit at time.

Appendix A:

α, β	Guide vanes and runner blades opening angle.
λ, ζ_{η}	Eigenvalues and respective Spectral abscissa for the efficiency meta-model of a Kaplan turbine
n, H, n_{ED}	Rotational speed, net head, IEC speed coefficient of the hydraulic machine.
η, \dot{V}	Hydraulic efficiency and discharge.

Appendix B:

E_h^{FCR}	Energy to be provided in hour h due to FCR provision
σ_f, f, \hat{f}	Frequency droop, grid frequency and predicted grid frequency.
$W_h, \hat{W}_h, \hat{W}_h^{\uparrow}, \hat{W}_h^{\downarrow}$	Realization and prediction of the integral of frequency deviation over the hour h , with its 5% CI and its 95% CI
v^{F}	Duration of the period in which the discharge error is within the limit.

Appendix C:

$\Omega_{A,B,C,D1,D2}$	Subsets of consumption data corresponding to different days of the week and holidays.
\mathcal{G}, \mathcal{C}	Set of historical observations at the PCC point and historical load consumption dataset.
$\mathcal{P}_{n,d}$	Historical measure of the BESS power at time n and day d .
$S_a^{\uparrow}, S_a^{\downarrow}$	Maximum and minimum expected realizations of prosumption.

1 Introduction

Context and Motivation

The European Union has committed to a significant reduction in greenhouse gas emissions, aiming for at least a 55% decrease by 2030 compared to 1990 levels, as part of the "*European Green Deal*", to achieve climate neutrality by 2050 [1]. To achieve these goals, the integration of *Renewable Energy Sources* (RES) into the European power grid is essential. However, this shift introduces several challenges, especially when dealing with energy sources that cannot be controlled directly, like wind and solar. As RES become a large part of the electricity generation mix, there is a growing need for grid services that ensure the grid remains within feasible operation limits in both steady-state and transient conditions. Two critical ancillary services in this context are the *Frequency Containment Reserve* (FCR) and the *automatic Frequency Restoration Reserve* (aFRR). FCR quickly responds to sudden changes in energy supply or demand, while aFRR restores the nominal grid frequency over longer periods [2].

Hydropower plants emerge as vital assets in the European interconnected power transmission grid, contributing to a substantial 16.8% of the total electricity generated in 2022 [3]. Furthermore, hydropower is known for its controllable nature, with the potential to provide the flexibility needed to mitigate the intermittency of RES [4]. Several studies in the literature, including [4], [5], and [6], highlight the pivotal role of hydropower in achieving ambitious high RES scenarios by supporting power grid balancing and enhancing the flexibility of the European power system. While hydropower plants have played a significant role in frequency regulation [7, 8], the impact of continuous regulation on the lifetime of these assets remains an important limitation [9].

In this Ph.D. thesis, we explore the hydropower potential to provide fundamental grid services with the primary objective of optimizing the operation of *Hydropower Plants* (HPPs) while simultaneously enhancing the provision of aFRR or FCR and extending the lifetime of hydroelectric assets. Each section of this thesis contributes to this purpose, from understanding the technical intricacies to proposing control strategies and validating their real-world effectiveness. In synthesis, we aim to respond to the following main research question:

How can we optimize the integration and control of hydropower plants with new technologies to boost their role in ancillary service provision and ensure asset longevity?

Given the broad scope of the main research question, this section introduces a series of research sub-challenges as a structured approach to addressing the central question, starting with the role of *Pumped Storage Power Plants* (PSPs) in providing aFRR and the associated operational concerns. More specifically, PSPs are highly effective in providing aFRR due to their unique ability to switch between pumping and generating modes. However, due to aFRR provision, HPPs may frequently undergo multiple start-ups and shutdowns, potentially accelerating the aging and wear of the units. This arises a first research sub-challenge:

- (a) *How can we maximize aFRR provision of PSPs while reducing the number of start-ups and stops of its units?*

In addition to offering aFRR service to the power system, HPPs contribute significantly to FCR provision [4]. A portion of this reserve can be supplied by *Run-of-River* (RoR) power plants, accounting for 5.93% of the total electricity generated in the ENTSOE area [10] in 2021. For example, in Germany, where RoR accounts for only 3% of the national energy mix, different studies [10, 11] estimate the RoR potential FCR support to be almost 95% of the total FCR national needs. However, the commitment to continuous power regulation imposes wear and tear on hydraulic and mechanical components [12, 9]. According to [13], enhancing FCR actions of HPPs has a considerable effect on the wear and tear of the hydraulic and mechanical systems. Acknowledging the importance of FCR-induced wear on RoR HPPs, we aim to answer the following research sub-questions:

- (b) *How does FCR provision affect RoR HPPs equipped with Kaplan turbines?*
- (c) *Which control strategy can improve FCR provision of RoR HPPs, while slowing down the aging of its units?*

Recognizing the challenges and limitations posed by FCR-induced wear and tear in HPP, our attention turns to *Battery Energy Storage Systems* (BESS). BESSs offer an attractive solution characterized by high ramping capability, efficiency, and commercial availability [14]. BESSs have found their place in the power grid landscape, participating in ancillary services such as frequency and voltage regulation [15]. BESSs have been investigated for providing frequency and voltage regulation services in various studies, such as [15], [16], [17], [18], [19], and [20]. For instance, [15] presents a method for the optimal sizing and operation of a BESS used for FCR in a small isolated power system. [16] and [17] explore the potential of BESSs participating in frequency regulation markets. These studies demonstrate the versatility of BESSs in providing a range of grid services. However, the finite capacity of BESSs, constrained by power and energy limitations, often restricts its ability to provide grid services reliably [18]. For this reason, the following research sub-questions are treated in this thesis:

- (d) What are the main limitations of BESSs when providing FCR?*
- (e) How can we maximize the ancillary service provision of BESS assets?*

As a matter of fact, both BESSs and HPPs exhibit attributes that make them integral players in the domain of FCR provision. Hydropower offers a powerful solution but faces challenges related to wear and tear when providing flexibility. Concurrently, BESS are recognized for their quick response capabilities¹, though they are limited by their energy and power constraints. Interestingly, an integration of these two systems showcases notable synergistic potential, combining the flexibility of hydropower with the rapid-response capabilities of BESS to enhance grid service provision. This combination not only maximizes the strengths of both technologies but also effectively addresses their inherent limitations. This approach has garnered increasing interest in the literature [22, 23, 24, 25]. However, many existing contributions primarily propose simple control techniques based on dead-band control or fuzzy logic [24, 22]. Others discuss HPP-BESS hybridization for specific applications such as penstock fatigue reduction in medium-head HPPs [25]. Moreover, most of the above-mentioned contributions rely on simulations or have limited experimental validation [23]. For this reason, the following questions remain unanswered:

- (f) What are the optimal strategies for RoR HPPs hybridized with BESS to improve FCR provision and extend the HPP asset lifetime?*
- (g) What alternative approaches, besides BESS hybridization, could effectively enhance FCR provision of RoR HPPs?*
- (h) How can the benefits of RoR HPPs and BESSs integration for FCR provision be effectively evaluated through experiments?*

In this thesis, we address the main research question by answering each of the enumerated sub-challenges.

The presented work is fully supported by the XFLEX HYDRO Project, funded primarily by the European Union's Horizon 2020 research and innovation programme [26].

¹Especially when their interfacing power converters are operated as grid-forming units [21].

Thesis Outline

The thesis is organized as follows: The first part delves into aFRR provision from PSPs, therefore answering to research sub-question (a), while the second part focuses on FCR provision by RoR HPPs and BESS as single operating technologies. This part discusses the main contributions of the two technologies to the FCR market and their limitation, addressing research sub-questions (b)-(d). Finally, Part III delves into the integration of these technologies to enhance their FCR capabilities (sub-questions (f)-(h)). The need to separate these parts arises due to the distinct functionalities, requirements, and time horizons of each service, ensuring a comprehensive understanding of their respective roles and challenges.

Part I

Chapter 2 focuses on research sub-question (a), presenting a methodology to optimize the dispatch and aFRR provision between multiple units in a PSP that makes use of the *Hydraulic Short Circuit* (HSC) operating mode. HSC allows for the simultaneous generation and pumping from different units of the same plant. The objective of the optimal dispatching is to maximize efficiency and reduce the number of start and stop of the machines while providing fundamental grid ancillary services as the aFRR. The methodology is applied and validated in two different cases, including a real study case on the power plant of Grand'Maison² (France).

Part II

Chapter 3 addresses the research sub-question (c) by developing a model-based control strategy for optimal asset management of hydroelectric units in RoR HPPs. The proposed control strategy aims to operate the unit at the best efficiency, to improve the water flow management and to minimize components wear during FCR provision. This approach is designed for a double-regulated turbine (Kaplan) with adjustable guide vanes angle and runner blades angle and can be extended to other turbines adopted in RoR HPPs. Moreover, the chapter proposes a data-driven method to estimate the performance decrease of Kaplan turbines due to FCR provision, therefore answering to research sub-question (b). The control strategy is validated by simulating a month of operation for the full-scale RoR HPP located in Vogelgrun² (France) and by comparing the results with operational statistics.

In Chapter 4, we introduce and validate a control and scheduling mechanism for grid-forming converter-linked BESSs that offer multiple services to the electrical grid, with particular focus on FCR provision. The framework operates in three stages: day-ahead scheduling, intra-day adjustments, and real-time tracking. The scheduling framework ties the available BESS capacity directly to the amount of FCR provision. The efficacy of this approach is experimentally confirmed using a 720 kVA/560 kWh BESS available at the *École Polytechnique Fédérale de*

²The power plant is operated by *Électricité de France* (EDF). Operational statistics, as well as other relevant information have been made available within the context of the EU-H2020 XFLEX HYDRO project

Lausanne (EPFL) campus and connected to the local 20 kV medium-voltage power grid. The results of this chapter are exhaustive answers to research sub-questions (e) and (d).

Part III

Chapter 5 compares two possible solutions to enhance FCR provision in HPP. The integration of a BESS with RoR HPPs is firstly analyzed, and a suited control, relying on a double-layer *Model Predictive Control* (MPC), is proposed to tackle research question (f). The upper layer MPC acts as a BESS *State of Energy* (SOE) manager, employing a forecast of the required regulating energy for the next hour. The lower-layer MPC optimally allocates the power set-point between the turbine and the BESS. To explore research sub-question (g), we consider the re-purposing of aging Kaplan turbines into variable-speed propellers by employing full-size frequency converters. This constitutes an alternative approach, besides BESS hybridization, that can enhance FCR capability while reducing fatigue on Kaplan units.

Chapter 6 discusses the design of experiments for the validation of the framework proposed in Chapter 5. The need for defining a precise way to assess the benefits of different solutions and control strategies has been expressed in research sub-question (h). This chapter not only discusses the design of the experimental platform developed but also defines suited *Key Performance Indicators* (KPIs) to compare the different approaches.

Chapter 7 presents the results of the experimental campaign of the optimal control strategy for BESS-hybridized HPP developed in Chapter 5. Reduced-scale experiments are performed on a one-of-a-kind testing platform to validate the proposed MPC-based control considering a comparison with different control strategies and different BESS sizes. Moreover, the chapter compares the latter results with those obtained by controlling the Kaplan turbine as a variable-speed propeller.

Finally, Chapter 8 summarizes the main findings of the thesis and future perspectives.

Overview

A graphical outline of the thesis is proposed in Fig. 1.1. It is worth noting that, given the large number of subjects treated in this thesis, the literature surveys are integrated at the beginning of each chapter, when necessary.

Contribution

The original contributions of each chapter of this thesis are listed below.

Chapter 2

- (i) Integrating the established HSC mode into a control scheme to enhance the regulation capabilities of PSPs.
- (ii) Presenting an optimization framework to enhance aFRR provision by PSPs.
- (iii) Reformulating a complex *Mixed Integer Programming* (MIP) problem into a series of tractable convex optimization sub-problems, introducing a computationally efficient approach to solve the optimization problem of point (ii).

Chapter 3

- (iv) Integrating knowledge from characteristic curves and operational statistics of a Kaplan turbine to build an accurate efficiency surrogate model, which represents the unit performance evolution while aging.
- (v) Presenting a methodology that leverages Kaplan surrogate models to compute optimal CAM curves, ensuring that the control system is continuously optimized throughout the unit's lifetime.
- (vi) Enhancing the RoR HPPs FCR provision and developing a discharge management framework. This strategy ensures adherence to discharge set points, reduces discharge control-induced unit wear and tear, and maximizes hydraulic efficiency.

Chapter 4

- (vii) Development of a control framework for *Grid-Forming* (GFR) converter-interfaced BESS. This framework, grounded on existing *Grid-Following* (GFL) control strategies [27, 28, 29], optimize multiple services including feeder dispatchability, FCR, and voltage regulation in the face of uncertainties from demand, distributed generation, and grid frequency.
- (viii) Experimental validation of the framework of point (vii) using a 560 kWh BESS linked to a 720 kVA GFR-controlled converter, overseeing the operation of a 20 kV distribution feeder with both traditional consumption and distributed *Photo-Voltaic* (PV) generation.
- (ix) Assessment of the enhanced FCR response provided by the GFR-controlled BESS.

Chapter 5

- (x) Development of a model-based control framework for the hydro-BESS hybrid system, aiming to enhance FCR provision.
- (xi) Introduction of a two-layer MPC: The faster layer leverages the flexibility of the BESS for rapid response, while the slower layer utilizes the hydro component to ensure sustainable BESS operation and overall system stability.

Chapter 6

- (xii) Design of the experimental platform developed explicitly for the experimental validation of the control framework proposed in Chapter 5 for BESS-hybridized HPPs, and comparison with alternative solutions.
- (xiii) Definition of suited KPIs to evaluate the FCR response of the HPPs + BESS system and the wear on the HPP servomechanisms.

Chapter 7

- (xiv) Experimental validation of the methodology developed in Chapter 5, integrating BESS with RoR HPPs using a double-layer MPC to improve FCR and reduce wear.
- (xv) In-depth comparison between BESS hybridization of a Kaplan turbine and the variable-speed control when the same unit operates as a propeller with fixed blades.

Introduction

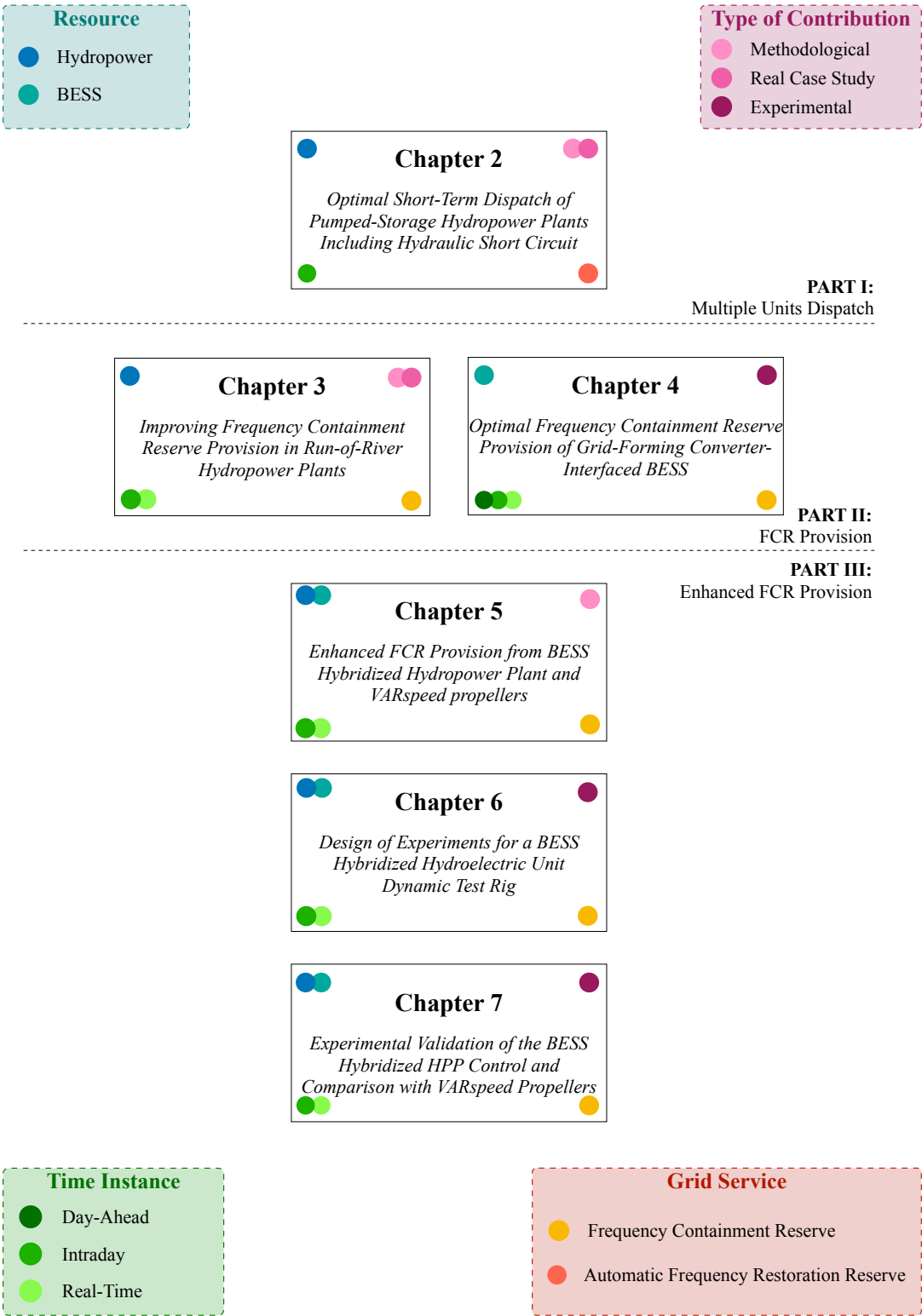


Figure 1.1: Graphical representation of the thesis structure.

Automatic Frequency Restoration Reserve

Part I

Preface

aFRR is a fundamental grid service responsible for restoring the rated grid frequency by adjusting the power plant outputs in response to power imbalances. Activated within seconds, it operates up to 15 minutes, after which tertiary control intervenes [30]. In this domain, PSPs play an instrumental role in delivering this service due to their ability to absorb, or produce, power. However, a challenge arises with PSPs equipped with fixed-speed pumps or reversible pump-turbines, as they function as "on-off" machines thus offering limited regulation capabilities.

The introduction of HSC operations offers a solution to this challenge. The HSC technology allows for precise control over power absorption during the pumping phases, reshaping the role of PSPs within HPPs. This advancement not only enhances the capabilities of PSPs but also enables them to actively participate in the aFRR market, even when their primary function is pumping.

In Part I, we introduce a comprehensive methodology crafted to optimize the dispatch and aFRR reserve allocation among multiple units within an HPP, harnessing the full potential of HSC technology. To exemplify the practicality and effectiveness of this methodology, we apply it to two distinct cases, one of which is a real-world study conducted at the PSP of Grand'Maison, France.

2 Optimal Short-Term Dispatch of Pumped-Storage Hydropower Plants Including Hydraulic Short Circuit

This chapter proposes a methodology to optimize the dispatch and frequency restoration reserve between multiple units in a HPP that makes use of the HSC operating mode. HSC allows for the simultaneous generation and pumping from different units of the same plant. The objective of the optimal dispatching is to maximize efficiency and reduce the number of start and stop of the machines while the HPP is providing aFRR. We first introduce an original MIP problem and discuss its computational complexity. Then, we propose an optimal dispatching algorithm obtained by efficiently solving a set of convex optimization sub-problems, as opposed to the original MIP. The methodology is applied, and validated, in two different cases, including a real study case in France given by the Grand'Maison PSP. The study cases demonstrate the ability to include HSC in short-term dispatch, consider future set-points for optimizing power trajectory, and find the optimal solution to the HPP dispatching problem while guaranteeing a computationally tractable approach.

The chapter includes results from [P1].

Research sub-questions:

- (a) *How can we maximize aFRR provision of PSPs while reducing the number of start-ups and stops of its units?*

2.1 Introduction

2.1.1 Context and Motivation

As already discussed in Chapter 1, in Europe, the market share of RES is expected to grow from 37% in 2021 to 69 % in 2030 [31], for the majority by increasing variable sources in the form of wind and PV. At the same time, the significant decommissioning of dispatchable thermal power plants contributes to the decrease of assets providing regulation services to the power grid. The dramatic increase in intermittent renewable generation, and the declining proportion of thermal power plants, calls for more balancing power from existing controllable power plants.

New markets exist, and others are being advanced, to encourage the provision of ancillary services ranging from long-term storage to near real-time frequency regulation. Therefore, plant owners are increasingly encouraged to improve the flexibility of their assets to increase participation in these markets [9]. Hydropower plays a key role in this context, and in previous years several technologies have been implemented to extend the flexibility of hydroelectric units [32]. These modernization efforts involve *Capital Expenditure* (CAPEX) investments for new equipment and also upgrades of the existing infrastructure with particular attention to digital solutions for advanced monitoring and optimal control of the units.

The so-called HSC operating mode is a recent development for PSPs, which allows simultaneous generation and pumping from different units of the same plant without the need for new equipment. As a consequence, the use of HSC results in a continuous power regulation range from positive to negative values. Fixed speed pumps, or reversible *Pump Turbines* (PT), are "on-off" machines that cannot be regulated [33, 34]. The HSC operation provides the ability to control the power absorption during pumping and, therefore, raises the opportunity for PSPs to extend their participation to regulation markets [35]. In particular, HSC allows for participating in the aFRR market, even when the HPP is mainly pumping. In the literature, evidence of the benefits of HSC operation has been presented by numerical simulations to improve frequency regulation of isolated power systems [36, 37]. Furthermore, many studies have been performed to assess the performance and safety of HSC operation by highlighting increasing head losses, risks related to the efficiency and stability of the hydraulic machine, flow re-circulations in the waterways, and interactions between different groups [38, 33, 34].

From a control point of view, the definition of the best configuration for power dispatch within the groups of a hydroelectric plant, including the HSC operating mode, is not straightforward, especially when the PSP is equipped with many units or with an added degree of freedom such as variable rotational speed. Optimization models have been developed for the participation of a PSP equipped with reversible units in the day-to-day energy and ancillary services markets considering HSC operation [39] or variable speed technology [40, 41]. While several efforts have been made to propose optimization strategies to participate in the energy markets, how to optimize power and reserve dispatch between multiple groups in a PSP is still not

understood and has drawn increasing attention of plant owners and stakeholders in the field.

2.1.2 Chapter Contributions

In light of the aforementioned research interests and industrial needs, this chapter proposes a methodology to dispatch PSP while:

- (i) Including the possibility of HSC operation;
- (ii) Considering both dispatch (i.e. the result of an external optimization considering the day-ahead energy market) and regulating market set-points (i.e. participation in the aFRR market);
- (iii) Considering information about future set-points to optimize the PSP power trajectory over the day.

In the literature, similar problems are formulated as MIP problems [42, 39]. Typical solvers for MIP problems are hardly suitable to be used in short-term applications due to their computational complexity, and cannot ensure the global optimality of the solution, due to their heuristic nature. Furthermore, the studies by [42, 39] consider the scenario where the HPP acts as the sole unit participating in the electricity market. However, it is important to note that this is frequently not the actual operational context, as elaborated in Section 2.2.1. For this reason, this chapter proposes the original, non approximated, MIP scheduling problem and, then, a way to efficiently solve a set of convex *Optimization Problems* (OPs) that ensure the global optimality of the original problem while guaranteeing a computationally treatable approach.

This chapter is organized as follows: Section 2.2 provides an introduction to the control problem and presents the problem statement within its relevant context. Section 2.3 evaluates the performance of the proposed algorithm through the analysis of two specific case studies. Finally, Section 2.4 summarizes the conclusions drawn from the study and explores potential future research studies.

2.2 Problem Statement

2.2.1 Context Regarding Power Plants Operation

In many European countries, the electricity market has long been dominated by a handful of large players [43]. To date, market regimes tend to embed energy storage and power generation within the central management of these major energy utility companies [44]. The entire generation assets of these companies are controlled by a centralized dispatch center [45], while the different power plants are merely responsible for applying the received production orders. Centralized dispatching allows energy utility companies to perform internal re-dispatch during

Chapter 2. Optimal Short-Term Dispatch of Pumped-Storage Hydropower Plants Including Hydraulic Short Circuit

the day of operation. This means that, often, the set-points received by each HPP are not the result of market dynamics, but of internal intra-day optimizations triggered by contingencies or erroneous forecasts. In this case, the HPP is only supposed to split the received power set-point into the different units, and not to solve a dispatch problem accounting for market prices in the optimization.

For this reason, while many contributions propose to solve a hydro unit commitment problem considering the HPP as a single player in the market, this study proposes a method to define the optimal set-point splitting policy for an HPP that receives power set points from a centralized dispatch center. The latter is considered the entity controlling a fleet of different power plants, including the targeted HPP. More precisely, the central optimizer communicates the dispatch plan \hat{G} to the HPP on the day ahead and, then, updates it every time step t with intra-day re-dispatch ΔG_t for the future time step(s). As Fig. 2.1 shows, at any time $t-1$, the HPP receives information regarding the total power to be produced P^{co} and the secondary reserve \hat{R} to be allocated from time t to time $t+T$. The reserve \hat{R} is composed of separate upward \hat{R}^\uparrow and downward \hat{R}^\downarrow reserve components. For each time t , the total set points $\mathbf{P}_{t:t+T}^{co}$ feed the

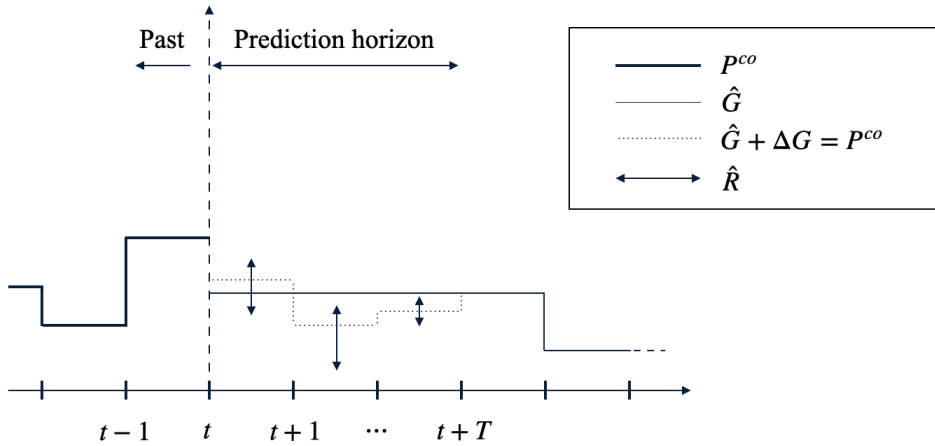


Figure 2.1: Timeline of the control framework, showing the dispatch plan \hat{G} , the executed action $P_{0:t-1}^{co}$, and the future set points $P_{t:t+T}^{co}$.

optimizer, responsible for optimally splitting the future set points for the different units. In particular, the presented control must steer the operation of multiple reversible units in a PSP, minimizing the total power losses and the number of unit start-ups and stops.

2.2.2 Problem Formulation

Let us consider an HPP composed of I reversible PTs, the active power delivered (or absorbed) by each machine at time t is defined by \mathbf{P}_t :

$$\mathbf{P}_t = [P_1, P_2, \dots, P_I]_t. \quad (2.1)$$

where for each element of the array $P_{i,t}$ ($i = 1, \dots, I$) we may define $P_{i,t}^G$ as the generated power by unit i (in generating mode):

$$P_{i,t}^G = \begin{cases} P_{i,t}, & \text{if } P_{i,t} > 0. \\ 0, & \text{otherwise.} \end{cases} \quad \forall i \in [1, I] \quad (2.2)$$

and $P_{i,t}^P$ as the absorbed power of unit i (in pumping mode):

$$P_{i,t}^P = \begin{cases} -P_{i,t}, & \text{if } P_{i,t} < 0. \\ 0, & \text{otherwise,} \end{cases} \quad \forall i \in [1, I]. \quad (2.3)$$

For each time t , the two arrays containing the components of P_t are, respectively:

$$\mathbf{P}_t^G = [P_1^G, P_2^G, \dots, P_I^G]_t. \quad (2.4)$$

$$\mathbf{P}_t^P = [P_1^P, P_2^P, \dots, P_I^P]_t. \quad (2.5)$$

By construction, all the elements in \mathbf{P}_t^G and \mathbf{P}_t^P are greater or equal than zero and:

$$\mathbf{P}_t = \mathbf{P}_t^G - \mathbf{P}_t^P. \quad (2.6)$$

To represent the generating/pumping *state* of each machine, we introduce two additional integers arrays \mathbf{X}_t^G and \mathbf{X}_t^P :

$$X_{i,t}^G = \begin{cases} 1, & \text{if } P_{i,t}^G > 0. \\ 0, & \text{otherwise.} \end{cases} \quad \forall i \in [1, I] \quad (2.7)$$

and

$$X_{i,t}^P = \begin{cases} 1, & \text{if } P_{i,t}^P > 0. \\ 0, & \text{otherwise.} \end{cases} \quad \forall i \in [1, I] \quad (2.8)$$

Similarly to Eq. (2.6), the overall state array is defined as the difference between the generating state \mathbf{X}_t^G and the pumping state \mathbf{X}_t^P .

$$\mathbf{X}_t = \mathbf{X}_t^G - \mathbf{X}_t^P, \quad (2.9)$$

where each element of the array can assume the following values:

$$X_{i,t} = \begin{cases} +1, & \text{generating mode.} \\ 0, & \text{machine is off.} \\ -1, & \text{pumping mode.} \end{cases} \quad (2.10)$$

Chapter 2. Optimal Short-Term Dispatch of Pumped-Storage Hydropower Plants Including Hydraulic Short Circuit

For the whole HPP, given a set point P_t^{co} , the secondary reserve $\hat{R}_t^\downarrow, \hat{R}_t^\uparrow$ to be allocated¹ and the head H_t between the HPP higher and lower reservoir², the control problem at time t can be formulated as:

$$[\mathbf{P}_t, \mathbf{X}_t] = \arg \min \omega_\phi \phi(\mathbf{P}_t, H_t) + \omega_\psi \psi(\mathbf{X}_t, \mathbf{X}_{t-1}) \quad (2.11a)$$

$$\text{s.t.} \quad \sum_{i=1}^I [P_i^G - P_i^P]_t = P_t^{\text{co}} \quad (2.11b)$$

$$\sum_i P_{i,t}^G - \hat{R}_t^\downarrow \geq \sum_i X_{i,t}^G \cdot P_{i,\min}^G \quad (2.11c)$$

$$\sum_i P_{i,t}^G + \hat{R}_t^\uparrow \leq \sum_i X_{i,t}^G \cdot P_{i,\max}^G \quad (2.11d)$$

$$X_{i,t}^G \cdot P_{i,\min}^G \leq P_{i,t}^G \leq X_{i,t}^G \cdot P_{i,\max}^G \quad (2.11e)$$

$$X_{i,t}^P \cdot P_{i,\min}^P \leq P_{i,t}^P \leq X_{i,t}^P \cdot P_{i,\max}^P \quad (2.11f)$$

$$\forall i \in [1, I]$$

$$(2.2) - (2.9)$$

where $\phi(\mathbf{P}_t, H_t)$ indicates the losses (in %), as a function of the operating points of the active machines and $\psi(\mathbf{X}_t, \mathbf{X}_{t-1})$ models the total Start-Up/Shut-Down (SUSD) cost of the different units, meaning the cumulative cost of all units being start-up or shut down at time t . The weight $\omega_\psi / \omega_\phi$ represents the number of percent losses that the power plant operator is willing to accept to avoid the SUSD of a unit. The operational limits of each unit i are indicated as $P_{i,\min}^G, P_{i,\max}^G, P_{i,\min}^P$ and $P_{i,\max}^P$. The tracking of the given set point is satisfied thanks to Eq. (2.11b). The amount of secondary reserve, downward \hat{R}_t^\downarrow and upward \hat{R}_t^\uparrow , is ensured by constraints (2.11c) and (2.11d), respectively. Each unit is kept within its physical operational limits by constraints (2.11e) and (2.11f). Due to the presence of \mathbf{X}_t , (2.11) is a mixed-integer programming problem. Similarly to unit commitment problems, this class of OPs can be solved through different methods including: Lagrangian Relaxation, Branch and Bound, Genetic algorithm-based approach, etc. [46]. Unfortunately, these methods cannot guarantee the global optimality of the solution. To modify Problem (2.11), and ensure the global optimality of the identified solution, the following hypotheses are introduced:

Hypothesis 1. Being Ω_X the set of all the possible combinations of operating machines, for each combination $\mathbf{X}_t^* \in \Omega_X$, the losses function $\phi(P_{i,t}, H_t)$ is a convex function for the variables $P_{i,t}, \forall i \in [1, I]$.

Hypothesis 2. H_t is an independent input of the problem or, at most, depends only on the combination of operating machines \mathbf{X}_t^* .

In Section 2.3.2, it is discussed why these hypotheses apply to the real HPP. If Hp. (1) and (2)

¹We assume the secondary reserve aFRR to be provided by the generating assets of the power plant and not by regulating pumps. A generalization of the problem is possible, but not considered in this thesis.

²We assume the I units composing the HPP to share the same reservoirs.

are fulfilled, for each fixed $\mathbf{X}_t^* \in \Omega_X$, (2.11) is a convex optimization problem since the term $\psi(\mathbf{X}_t^*, \mathbf{X}_{t-1})$ becomes a constant. We ensure the global optimum for Problem (2.11) by solving a convex problem for each $\mathbf{X}_t^* \in \Omega_X$ and then selecting the combination whose OP returns the lower objective function value. For every combination $\mathbf{X}_t^* \in \Omega_X$, the problem (2.11) becomes:

$$[\mathbf{P}_t] = \arg \min \phi(\mathbf{P}_t, H_t) + \frac{\omega_\psi}{\omega_\phi} \psi(\mathbf{X}_t^*, \mathbf{X}_{t-1}) \quad (2.12a)$$

$$\text{s.t.} \quad \sum_{i=1}^I [P_i^G - P_i^P]_t = P_t^{\text{co}} \quad (2.12b)$$

$$\sum_i P_{i,t}^G - \hat{R}_t^\dagger \geq \sum_i X_{i,t}^G \cdot P_{i,\min}^G \quad (2.12c)$$

$$\sum_i P_{i,t}^G + \hat{R}_t^\dagger \leq \sum_i X_{i,t}^G \cdot P_{i,\max}^G \quad (2.12d)$$

$$X_{i,t}^{G*} \cdot P_{i,\min}^G \leq P_{i,t}^G \leq X_{i,t}^{G*} \cdot P_{i,\max}^G \quad (2.12e)$$

$$X_{i,t}^{P*} \cdot P_{i,\min}^P \leq P_{i,t}^P \leq X_{i,t}^{P*} \cdot P_{i,\max}^P \quad (2.12f)$$

$$\forall i \in [1, I]$$

$$(2.2) - (2.9)$$

where $(\psi(\mathbf{X}_t^*, \mathbf{X}_{t-1}))$ is a constant term and the cost ω_ψ/ω_ϕ indicates the additional losses that the HPP operator is willing to accept to avoid the start-up/shutdown of a unit in percent. The set of all the possible combinations of operating machines as pumps, turbines, or being shut down, corresponds to the *Variations with Repetition* (VR) set, i.e. the different ordered arrangements, of a 3-element subset $(-1, 0 \text{ and } 1)$ of an I -set, that allows for repetitions. The number of possible combinations C is the cardinality of the latter set:

$$C = \text{card}(\text{VR}_{3,I}) = 3^I \quad (2.13)$$

As an example, in the case of two units:

$$C = \text{card}(\text{VR}_{3,2}) = 3^2 = 9, \quad (2.14)$$

and:

$$\text{VR}_{\{-1,0,1\},2} = \begin{bmatrix} [-1 & -1] \\ [0 & -1] \\ [1 & -1] \\ [-1 & 0] \\ [0 & 0] \\ [1 & 0] \\ [-1 & 1] \\ [0 & 1] \\ [1 & 1] \end{bmatrix}. \quad (2.15)$$

To ensure the global optimality of the solution for the OP (2.11), (2.12) has to be solved C

Chapter 2. Optimal Short-Term Dispatch of Pumped-Storage Hydropower Plants Including Hydraulic Short Circuit

times. However, with a high number of turbines I in the PSP³, the problem can become computationally intractable. To decrease computational complexity, it is possible to reduce the size of Ω_X without losing optimality. In fact, for a given set point P_t^{co} , not all combinations $\text{VR}_{3,I}$ are feasible. Constraints (2.12e-2.12f) can be converted into a filter for the combinations X_t to test. The set of the filtered combinations, according to the feasibility of P_t^{co} is defined as:

$$\Omega_{X,t}^{\text{co}} = \{X_t \in \text{VR}_{3,I} \mid X_t \text{ is feasible for } P_t^{\text{co}}\}, \quad (2.16)$$

where the feasibility condition is respected if:

$$\mathbf{X}_t^G \cdot \mathbf{P}_{\min}^G + \mathbf{X}_t^P \cdot \mathbf{P}_{\min}^P \leq P_t^{\text{co}}, \quad (2.17a)$$

&

$$\mathbf{X}_t^G \cdot \mathbf{P}_{\max}^G + \mathbf{X}_t^P \cdot \mathbf{P}_{\max}^P \geq P_t^{\text{co}}. \quad (2.17b)$$

The cardinality of the set $\Omega_{X,t}^{\text{co}}$ is expressed as:

$$C_t^{\text{co}} = \text{card}(\Omega_{X,t}^{\text{co}}) \quad (2.18)$$

In particular, Eq. (2.17a) guarantees that the set point P_t^{co} is greater than the minimum power that can be generated/consumed, while (2.17b) ensures that the set point P_t^{co} is lower than the maximum power that can be generated/consumed. Similarly, also (2.12c-2.12d) can be converted into a filter to reduce the number of combinations to test for ensuring optimality.

$$\Omega_{X,t}^f = \{X_t \in \Omega_{X,t}^{\text{co}} \mid X_t \text{ is feasible for } R_t^\uparrow, R_t^\downarrow\}, \quad (2.19)$$

with cardinality $C_t^f = \text{card}(\Omega_{X,t}^f)$. It can be proven that the amount of reserve provided by a set of units operating inside their operational limits only depends on the number of active units if the total production P^{co} is fixed. Indeed, for a certain secondary reserve request, the feasibility for Eq. (2.19) is satisfied if:

$$\begin{aligned} P_t^{\text{co}} - \hat{R}_t^\downarrow &\geq \mathbf{X}_t^G \cdot \mathbf{P}_{\min}^G \\ &\& \\ P_t^{\text{co}} + \hat{R}_t^\uparrow &\leq \mathbf{X}_t^G \cdot \mathbf{P}_{\max}^G \end{aligned} \quad (2.20)$$

For any set-point P_t^{co} and secondary reserve request $R_t^\uparrow, R_t^\downarrow$, the number of feasible combinations $\text{card}(\Omega_{X,t}^f) = C_t^f$ is lower or equal to the number of VR:

$$C_t^f \leq C_t^{\text{co}} \leq C. \quad (2.21)$$

Additional constraints can be added to reduce the number of combinations in $\Omega_{X,t}$ (e.g.

³A consistent number of PSP currently operating in Europe are characterized by a large number of units, i.e. Cortes La Muela Power Station, Spain, 9 units or Grand'Maison Power Plant, France, 12 units. In the latter, equipped with 4 Pelton units and 8 reversible pump turbines, the number of possible combinations is $C = 8^3 \cdot 4^2 = 104976$.

unavailability of certain units). However, they are treated in the result sections, since they are case-specific. Once C_t^f OPs are solved, their objectives functions values $F([\mathbf{P}, \mathbf{X}]_t)$ are compared, and the best solution is selected. The full procedure is defined in Algorithm 1.

Algorithm 1

```

1: procedure SOLVE PROBLEM (2.11) FOR:  $(P_t^{\text{co}}, R_t^\uparrow, R_t^\downarrow)$ 
2:   Compute  $VR_{3,I}$  possible combinations of active units
3:   Filter the feasible combination for  $P_t^{\text{co}}$  with Eq. (2.16)
4:   Obtain  $\Omega_{X,t}^{\text{co}}$ 
5:   Filter the feasible combination for  $R_t^{\uparrow\downarrow}$  with Eq. (2.19)
6:   Obtain  $\Omega_{X,t}$ 
7:    $i = 1$ 
8:   for each  $X_t^* \in \Omega_{X,t}$  do
9:     Solve Problem (2.12)
10:    if (2.12) is feasible then
11:      Save the solution  $[\mathbf{P}, \mathbf{X}]_t^*$ 
12:      Save objective function  $O(i) = F([\mathbf{P}, \mathbf{X}]_t^*)$ 
13:       $i = i + 1$ 
14:    else
15:      Ignore  $X_t^*$ 
16:    end if
17:  end for
18:  Select  $[\mathbf{P}, \mathbf{X}]_t^*$  for which  $F([\mathbf{P}, \mathbf{X}]_t^*)$  is min  $[\mathbf{O}]$ 
19: end procedure

```

2.2.3 Predictive Control

Problem (2.11) only considers information about the next set-point P_t^{co} and reserve request $R_t^\uparrow, R_t^\downarrow$ and the state of the HPP up to the last time instance $t - 1$. A generalized version of the OP, computing the optimal trajectory from time t_0 to time $t_0 + T$ for each unit i , is here below:

$$\begin{aligned}
[\mathbf{P}, \mathbf{X}]_{t_0:t_0+T} = \arg \min & \sum_{t=t_0}^{t_0+T} \phi(\mathbf{P}_t, H_t) + \frac{\omega_\psi}{\omega_\phi} \psi(\mathbf{X}_t, \mathbf{X}_{t-1}) \\
\text{s.t. } & \sum_{i=1}^N [P_i^G - P_i^P]_t = P_t^{\text{co}} \\
& \sum_i P_{i,t}^G - \hat{R}_t^\downarrow \geq \sum_i X_{i,t}^G \cdot P_{i,\min}^G \\
& \sum_i P_{i,t}^G + \hat{R}_t^\uparrow \leq \sum_i X_{i,t}^G \cdot P_{i,\max}^G \\
& X_{i,t}^G \cdot P_{i,\min}^G \leq P_{i,t}^G \leq X_{i,t}^G \cdot P_{i,\max}^G \\
& X_{i,t}^P \cdot P_{i,\min}^P \leq P_{i,t}^P \leq X_{i,t}^P \cdot P_{i,\max}^P \\
& \forall i \in [1, I], \quad \forall t \in [t_0, t_0 + T]
\end{aligned} \tag{2.22}$$

(2.2) – (2.9)

Chapter 2. Optimal Short-Term Dispatch of Pumped-Storage Hydropower Plants Including Hydraulic Short Circuit

where the subscript $t_0:t_0+T$ indicates all the discrete indices between t and $t+T$. If Hps. (1) and (2) are fulfilled, problem (2.22) can be solved as a set of convex optimization problems for each possible trajectory $\mathbf{X}_{t_0:t_0+T}^*$. In this case, the number of combinations to be tested $C_{t_0:t_0+T}^f$ grows even considering the reduction through Eq. (2.16) and (2.19), as it consists in all the possible combinations of multiple time instances. In particular, $C_{t_0:t_0+T}^f$ is equal to the product of the number of combinations for each time instance C_t^f , as the choice of time t affects the SUSD costs at time $t+1$.

$$C_{t_0:t_0+T}^f = \prod_{t=t_0}^{t_0+T} \text{card}(\Omega_{X,t}) = \prod_{t=t_0}^{t_0+T} C_t^f \quad (2.23)$$

However, it can be proven that the global optimality of the solution can be ensured by solving the optimization problem only a reduced number of times. A rationale for the latter statement is hereby presented.

Let us consider Problem (2.22) for $T = 1$, i.e. one future step ($t+1$) to compute the next operating point \mathbf{P}_t :

- At step t , for P_t^{co} and $R_t^\uparrow, R_t^\downarrow$, only C_t^f combinations are feasible.
- At step $t+1$, for P_{t+1}^{co} and $R_{t+1}^\uparrow, R_{t+1}^\downarrow$, only C_{t+1}^f combinations are feasible.

As in Equation (2.23), the number of possible trajectories to be tested corresponds to the product of the number of combinations per time step:

$$C_{t:t+1}^f = C_t^f \cdot C_{t+1}^f \quad (2.24)$$

For each combination $\mathbf{X}_t^* \in \Omega_{X,t}, \Omega_{X,t+1}$ the SUSD objective of Problem (2.22) becomes a constant value ($\psi(\mathbf{X}_t^*, \mathbf{X}_{t-1})$) and, therefore, it does not affect the solution of the optimization problem. For each combination \mathbf{X}_t^* Problem (2.12) can be simplified as:

$$\begin{aligned} [\mathbf{P}_t] &= \arg \min \phi(\mathbf{P}_t, H_t) \\ \text{s.t. } & \sum_{i=1}^N [P_i^G - P_i^P]_t = P_t^{\text{co}} \\ & \sum_i P_{i,t}^G - \hat{R}_t^\downarrow \geq \sum_i X_{i,t}^G \cdot P_{i,\min}^G \\ & \sum_i P_{i,t}^G + \hat{R}_t^\uparrow \leq \sum_i X_{i,t}^G \cdot P_{i,\max}^G \\ & X_{i,t}^{G*} \cdot P_{i,\min}^G \leq P_{i,t}^G \leq X_{i,t}^{G*} \cdot P_{i,\max}^G \\ & X_{i,t}^{P*} \cdot P_{i,\min}^P \leq P_{i,t}^P \leq X_{i,t}^{P*} \cdot P_{i,\max}^P \\ & \forall i \in [1, I] \\ & (2.2) - (2.9) \end{aligned} \quad (2.25)$$

and the constant SUSD cost can be added to the objective in a second step. Finally, Problem

(2.25) only depends on time step t , and not on past and/or future instances. Indeed, this problem has to be solved only C_t^f for time t plus C_{t+1}^f for time $t + 1$. On the other side, the SUSD constants have to be computed for all the possible $C_t^f \cdot C_{t+1}^f$ and, then, combined with the $C_t^f + C_{t+1}^f$ objectives. Generalizing to any number of future steps, Eq. (2.25) has to be solved $\sum_{t=t_0}^{t_0+T} C_t^f$ times, while the SUSD cost has to be computed $\prod_{t=t_0}^{t_0+T} C_t^f$ times and combined to the value of the objective function (see Line 19 in Algorithm 2). Nevertheless, the computation of the $\psi(\mathbf{X}_t^*, \mathbf{X}_{t-1})$ is extremely fast, as it does not require any optimization. An updated version of Algorithm 1, including predictive control, is illustrated in Algorithm 2. In the latter algorithm it is visible how problem (2.25) is solved at Line 9 only for each t and each X_t^* , i.e. only $\sum_{t=t_0}^{t_0+T} C_t^f$ times. Concurrently, the SUSD costs are evaluated at Line 17 for every X_t^* and X_{t-1}^* pairing, amounting to $\prod_{t=t_0}^{t_0+T} C_t^f$ occurrences.

Algorithm 2

```

1: procedure SOLVE (2.22) FOR:  $(\mathbf{P}_{t:t+T}^{\text{co}}, \mathbf{R}_{t:t+T}^{\uparrow}, \mathbf{R}_{t:t+T}^{\downarrow})$ 
2:   Compute  $VR_{3,I}$  possible combinations of active units
3:   for each  $t \in [t_0, t_0 + T]$  do:
4:     Filter  $VR_{3,I}$  for  $P_t^{\text{co}}$  with Eq. (2.16)
5:     Obtain  $\Omega_{X,t}^{\text{co}}$ 
6:     Filter  $\Omega_{X,t}^{\text{co}}$  for  $R_t^{\uparrow\downarrow}$  with Eq. (2.19)
7:     Obtain  $\Omega_{X,t}$ 
8:     for each  $X_t^* \in \Omega_{X,t}$  do:
9:       Solve Problem (2.25):
10:      if (2.25) is feasible then
11:        Save the solution  $[\mathbf{P}, \mathbf{X}]_t^*$ 
12:        Save  $O(\mathbf{X}_t^*) = F([\mathbf{P}, \mathbf{X}]_t^*)$ 
13:      else
14:        Ignore  $X_t^*$ 
15:      end if
16:      for each  $X_{t-1}^* \in \Omega_{X,t-1}$  do:
17:        Compute the SUSD cost  $\psi(\mathbf{X}_t^*, \mathbf{X}_{t-1}^*)$ 
18:        Sum SUSD cost with losses:
19:         $H_t = \sum_{t_0}^t \frac{\omega_\psi}{\omega_\phi} \psi(\mathbf{X}_t^*, \mathbf{X}_{t-1}^*) + O(\mathbf{X}_t^*)$ 
20:      end for
21:    end for
22:  end for
23:  Select  $[\mathbf{P}, \mathbf{X}]_{t_0:t_0+T}^*$  for which:
24:   $H_{t_0+T}([\mathbf{P}, \mathbf{X}]_{t:t+T}^*)$  is min  $[\mathbf{H}]$ 
25: end procedure

```

This simplification significantly reduces the computational complexity, especially when applied within the context of predictive control. To illustrate, let us consider a HPP equipped with 6 units operating under predictive control, with $T = 1$. In this scenario, the total number of optimization problems to be solved experiences a substantial reduction. In its original form,

Chapter 2. Optimal Short-Term Dispatch of Pumped-Storage Hydropower Plants Including Hydraulic Short Circuit

the computational complexity is:

$$3^6 \cdot 3^6 = 531,441$$

With the proposed simplification, the computational complexity becomes:

$$3^6 + 3^6 = 1,458$$

This translates to a remarkable acceleration of the algorithm, resulting in a speedup factor of around 350.

2.3 Results and Discussion

2.3.1 Case A: Simulation with 4 Reversible Variable Speed Units

Let us consider a HPP equipped with 4 units, with the following operational constraints:

- minimum power in generating mode: 190 MW
- maximum power in generating mode: 380 MW
- minimum power in pumping mode: −300 MW
- minimum power in pumping mode: −390 MW

For the sake of simplicity, we model the efficiencies $\eta_{1,2,3,4}$ of the four machines as represented in Fig. 2.2, such that for a given head and power set-point: $\eta_1 > \eta_2 > \eta_3 > \eta_4$.

Time t	Set-point P_t^{co}	C_t^{co}
00 : 00	200	4
00 : 30	375	4
01 : 00	400	6
01 : 30	380	10
02 : 00	400	6
02 : 00	−400	18
03 : 00	−400	18
03 : 30	350	4
04 : 00	350	4
04 : 30	400	6
05 : 00	400	6
05 : 30	800	5

Table 2.1: Set-points for Case A (Simulation with 4 Reversible Variable Speed Units).

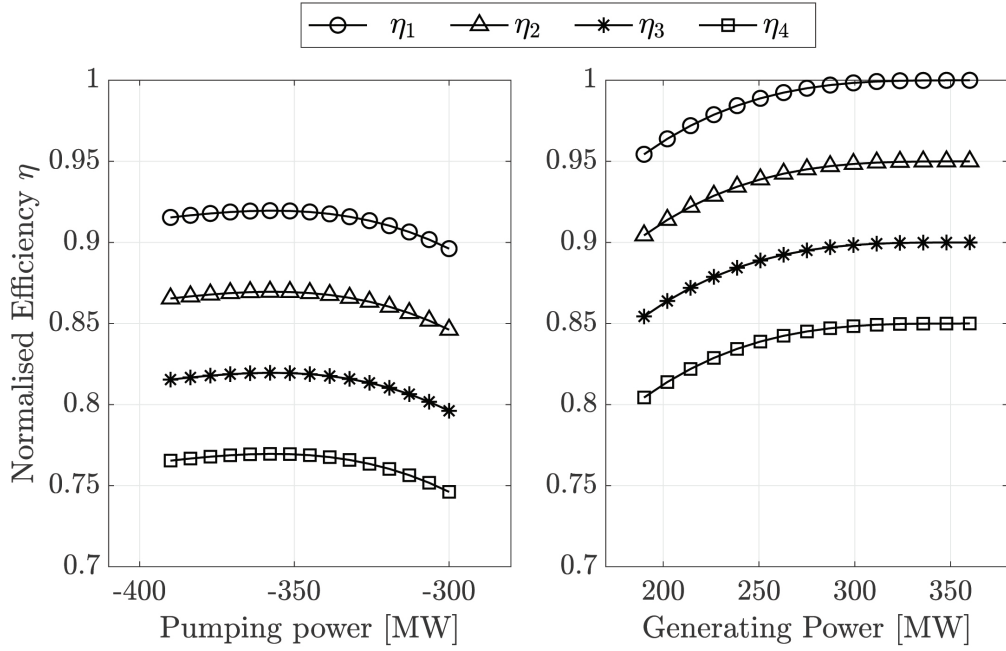


Figure 2.2: Normalised efficiency for the four machines in pumping (left side) and generating (right side) mode.

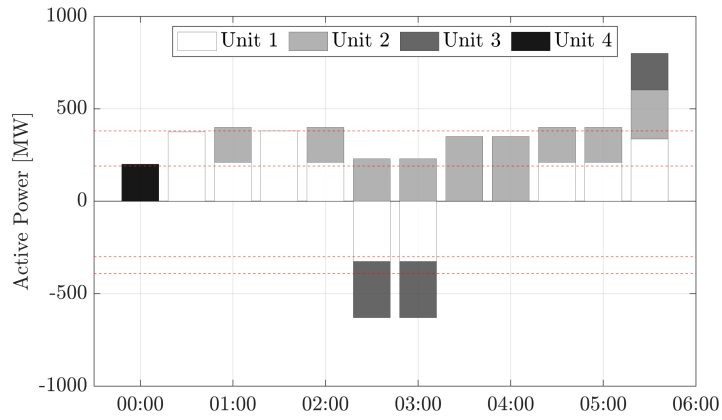
It is worth mentioning that the characteristic curves of Fig. 2.2 are not representative of any existing turbine, but rather examples to better understand the behavior of the control algorithm. In this respect, the optimization problem is run for a set of subsequent set-points, considering different start-up costs and comparing past-aware to future-aware techniques. The following cases are studied:

- (a) start-up cost ω_ψ/ω_ϕ of 12.5 % without predictive control ($T = 0$) ;
- (b) start-up cost ω_ψ/ω_ϕ of 12.5 % with predictive control ($T = 1$) ;
- (c) start-up cost ω_ψ/ω_ϕ of 25 % without predictive control ($T = 0$).

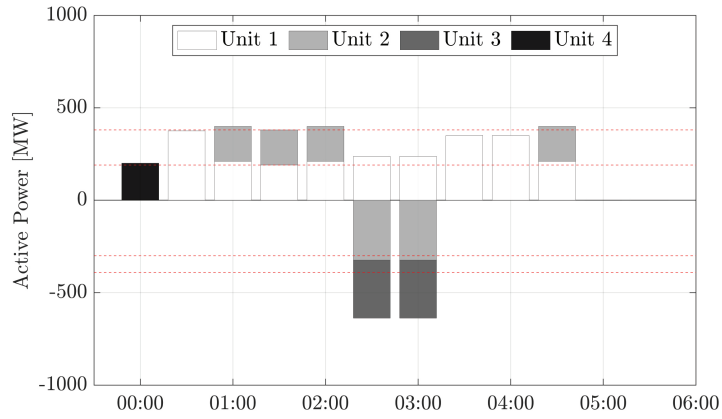
The set-points sequence, together with time instances and number of combinations per time step, is displayed in Table 2.1. In this study case, the amount of aFRR is fixed to zero, not to reduce the number of possible combinations.

For all the tests, the initial condition (operation at 00:00) is Unit 4 (i.e. the least efficient) providing the 200 MW requested. The first decision is taken for time 00:30. In this case, the effect of the start-up cost is visible by comparing case (a) with case (c), where the cost is twice as high. In case (a) the algorithm proposes to shut down Unit 4 and start Unit 1 (i.e., the most efficient), while in case (c) the greater start-up cost forces Unit 4 to maintain its operation until 02:00. The impact of future-aware control can be seen by observing cases (a) and (b), characterised by the same start-up cost, at time 01:30. The past-aware control recognizes that

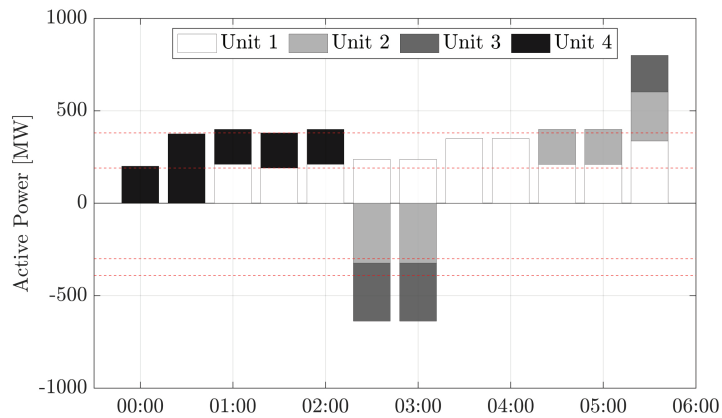
Chapter 2. Optimal Short-Term Dispatch of Pumped-Storage Hydropower Plants Including Hydraulic Short Circuit



(a)



(b)



(c)

Figure 2.3: Solution of the algorithm for the 4 units case with (a) start-up cost of 25 without future-aware control (b) start-up cost of 25 with future-aware control (c) start-up cost of 50 without future-aware control.

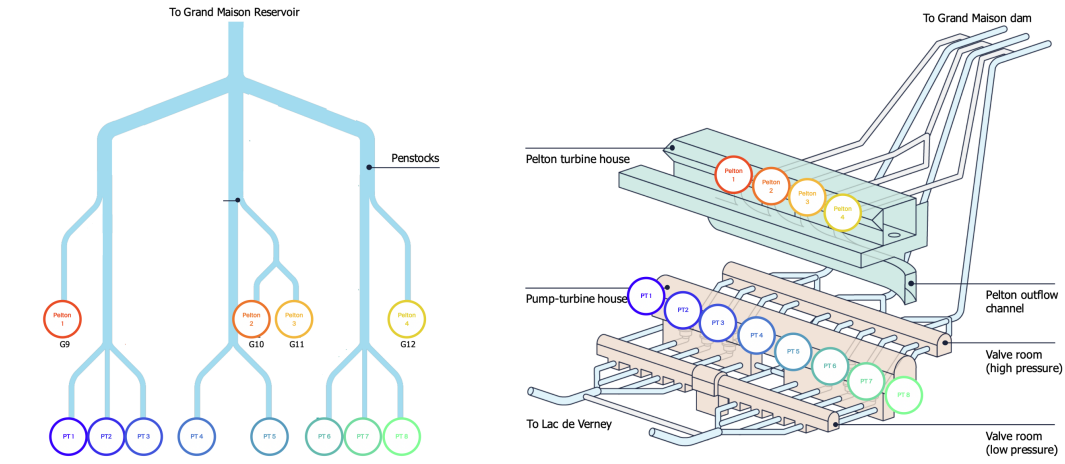


Figure 2.4: Penstock and units distribution in the HPP of Grand'Maison (FR).

the sole Unit 1 operating at maximum power (380 MW) is more efficient than the operation of two machines at their minimum ($2 \times 190 \text{ MW}$), as visible from Fig. 2.2. On the other hand, future-aware control takes into consideration that Unit 2 will have to be turned on in the next iteration and proposes not to turn it off at 01:30, as visible in case (b). Quantitatively, the different behavior of cases (a) and (b) implies that the gain in efficiency obtained at 01:30 by operating only Unit 1 is greater than the loss for one start-up cost but not greater than two. Similarly, at time step 02:30, when the hydropower plant switches to HSC mode, case (a) and (b) differ in the choice of the operating turbines. Given that $\eta_1 \geq \eta_2$, in case (a) Unit 1 takes most of the pumping power, while Unit 2 is left turbinizing to avoid an excessive start cost. In case (b), knowledge of the set point for 03:30-04:00 drives the decision to operate Unit 1 as a turbine in the hydraulic short circuit, so that the best unit can continue operating at future times. Overall, case (a) and (b) differ in the number of starts and stops (11 for case (a) and 10 for case (b)) and in the total losses (10 MWh versus 8 MWh, respectively). At the end of the considered period, the future aware control outperforms the past aware strategy, being able to reduce the cumulated objective function value.

2.3.2 Case B: Grand'Maison (FR) HPP with 12 Units

The Grand'Maison HPP is situated in the Isère department of southeastern France. The power plant was built between 1978 and 1988 and is currently operated by EDF. The power plant has a total installed capacity of 1800 MW, making it one of the largest hydroelectric power plants in Europe. As visible from Fig. 2.4, the plant's generating capacity is provided by 4 Pelton turbines, each with a capacity of 170 MW and 8 reversible PT units. While the operating range of the Pelton turbines is relatively broad (60 to 190 MW), the PT units can only operate at the fixed power of 125 MW in turbine mode and -155 MW in pump mode. The direct consequence is that each time the power plant pumps or operates only PT machines, it is unable to provide aFRR regulation. For this reason, the possibility of HSC operation, driven by the presented

control framework, is hereby presented.

2.3.2.A HSC Feasibility and Power Plant Modeling

Multiple preliminary studies on HSC implementation have been conducted [34, 47] to analyze the change in flow paths in the penstocks compared to the normal turbine or pump modes. These studies underline the feasibility of HSC operation. Indeed, for all the penstock junctions, even if the head losses increase in HSC mode compared to the turbine and pump modes, they never exceed 1% of the gross head, which is lower than the head losses in the penstocks. The losses model $\phi(\mathbf{P}_t, H_t)$ is obtained from the 1D SIMSEN [48] model described and validated in [33]. The latter is used to simulate 18000+ operating points across 3500+ combinations. For each combination \mathbf{X}_t , an analytical model is fitted. For this purpose, the *Multivariate Adaptive Regression Spline* (MARS) technique [49] is employed, as done in [P2] for obtaining the hill chart of a Kaplan turbine. The MARS model is used to produce a set of fittings using quadratic polynomials, one for each combination of operating machines, with coefficients of determination $R^2 \geq 96\%$ for all fittings. Indeed, due to the complexity of the power plant, the loss model must consider the combination of operating machines. In fact, if a Pelton machine (i.e., Pelton 2 in Fig. 2.4) is operating, its efficiency is affected by the PT operating on the same penstock (i.e., PT4 and PT5). As a consequence, the losses model ϕ for this study case becomes a set of losses models, for each combination of operating machines:

$$\phi = \phi(\mathbf{P}_t, H_t, \mathbf{X}_t) = \phi_{\mathbf{X}_t}(\mathbf{P}_t, H_t) \quad \forall \mathbf{X}_t \quad (2.26)$$

This set of models is suited to be used in the proposed methodology since an optimization problem is solved for each combination. Fig. 2.5 shows an example of the models defined by Eq. (2.26). The figure displays the overall normalized efficiency as a function of the power of Pelton 1, for different combinations of operating units. It is worth noting that the most efficient combination is the one where Pelton 1 operates as a single unit. The second most efficient combination is "Pelton 1 + PT4", as PT4 is not on the same penstock as Pelton 1 (see Fig. 2.4). If PT1 is in operation the efficiency drops, as two machines are operating on the same penstock.

2.3.2.B Hypotheses Verification

This section examines the validity of Hypotheses 1 and 2 in the context of the Grand'Maison case study, prior to the application of the framework. Hypothesis 1 requires the convexity of the loss function for each machine combination. This condition is equivalent to verifying that the efficiency hill chart of the machines is concave. In the existing literature, it is a customary approach to represent the machine hill chart using quadratic polynomials [50, 51], or to directly assume the concavity of the machine hill chart [52, 53]. In the specific scenario of the Grand'Maison project, the efficiency model is established by fitting concave quadratic curves, as outlined in the latter subsection. As a consequence, Hp. 1 is satisfied. Regarding

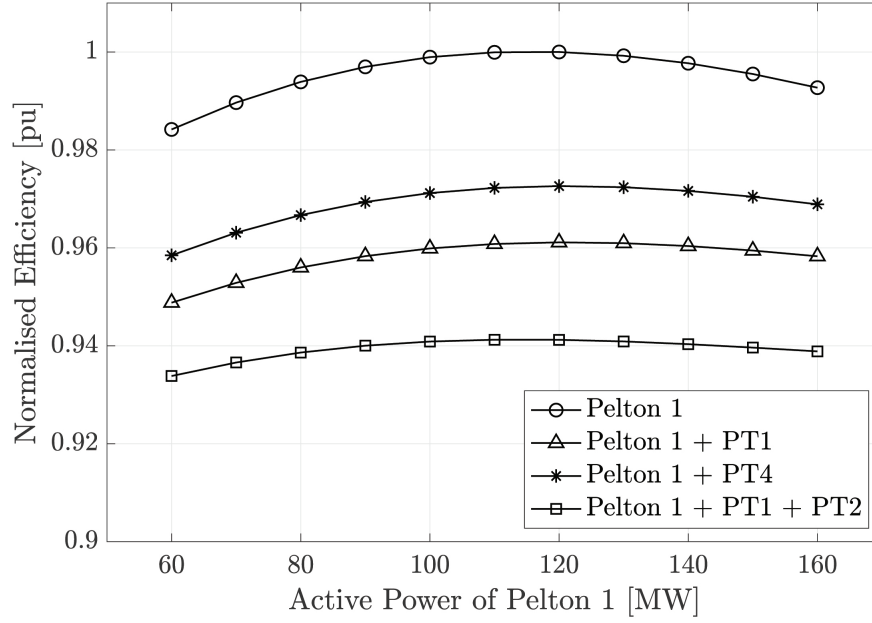


Figure 2.5: Normalized efficiency as a function of power produced by Pelton 1, for different combinations of active units.

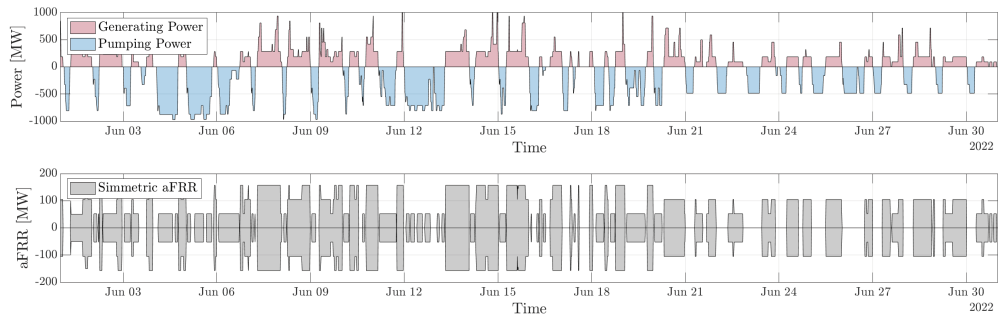


Figure 2.6: Active power (P^{co}) and aFRR set-points ($R^{\uparrow}, R^{\downarrow}$) for one month of operation.

Chapter 2. Optimal Short-Term Dispatch of Pumped-Storage Hydropower Plants Including Hydraulic Short Circuit

the verification of Hp. 2, the upper reservoir at Grand'Maison can store up to 140 million cubic meters of water, while its lower reservoir at Verney has a storage capacity of 15 million cubic meters of water. The flow rate of the penstocks can handle up to 216.3 cubic meters per second, which is distributed as follows:

- 75.9 cubic meters per second for the four Pelton units.
- 140.4 cubic meters per second for the underground power plant, i.e. the 8 PT units.

As a direct result, even when considering the maximum discharge through the penstock within the 15-minute time frame of the problem, the upper reservoir's water volume experiences a variation of less than 0.15%, while the lower reservoir's volume changes by less than 1.5%. As further proof, historical data on the net head for one year of operation is taken into consideration. This data set contains measurements of the water head in both the higher and lower reservoirs, sampled every minute, spanning from January 1, 2022, at 00:00:00 to December 31, 2022. During this year-long period, 99% of the variations in the water head occurring within 15 minutes are less than 40 cm, representing a mere 0.043% of the total net head variation. Additionally, 99% of the variations in the water head over 1 hour are less than 1.45 meters, accounting for only 0.16% of the total net head variation. These findings offer substantial evidence to affirm that Hp. 2 is fully satisfied.

2.3.2.C Results

To evaluate the performance and computational complexity of Algorithm 1, the framework is applied to optimize one year of operation of the Grand'Maison HPP, and the results are compared with the implementation. In particular, the algorithm is executed every 15 minutes, without predictive control, taking as input historical data from the 1st of January 2022 to the 31 of December 2022. The results, in terms of the aggregated number of movements and the average HPP efficiency, are displayed in Fig. 2.7 and Fig. 2.8.

These figures show the performance evaluation of the proposed algorithm, considering SUSD cost and efficiency as KPIs. The results indicate that the proposed algorithm outperforms the current control logic in both cost and SUSD efficiency.

When the algorithm is operated with $\omega_\phi / \omega_\psi = 0\%$, it exhibits larger efficiency performance while accepting a higher SUSD cost. This suggests that the algorithm can optimize the set-point of the power plant, resulting in higher overall efficiency. However, it is important to note that this optimization comes at the expense of increased start-up and shut-down costs.

Alternatively, when the algorithm is operated with $\omega_\phi / \omega_\psi = 100\%$, the number of start-ups and stops is reduced. Despite this reduction, the algorithm still outperforms the measurements in terms of efficiency. This implies that, even if the algorithm targets the minimization of start-up and shutdown costs, it manages to achieve a higher overall efficiency compared to the

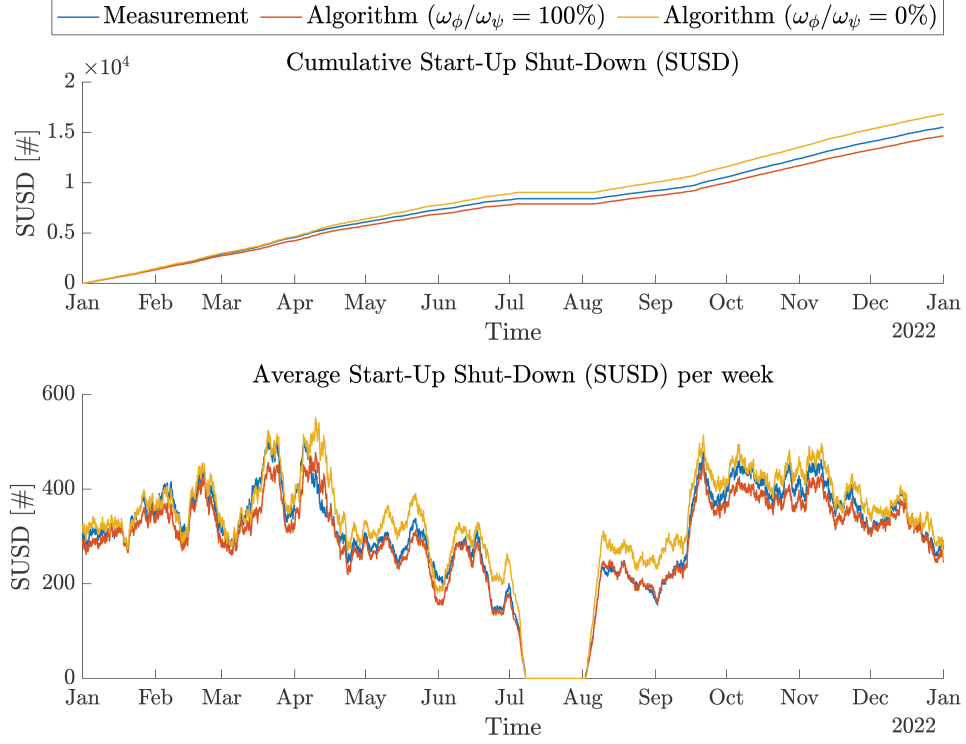


Figure 2.7: Comparison between measurement and algorithm output, in terms of aggregated number of SUSD and average HPP efficiency.

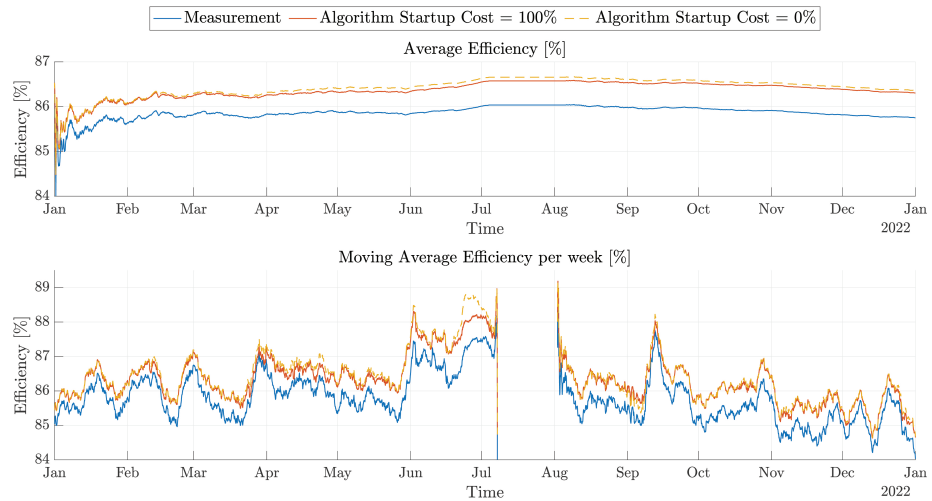


Figure 2.8: Comparison between measurement and algorithm output, in terms of aggregated number of REND and average HPP efficiency.

Chapter 2. Optimal Short-Term Dispatch of Pumped-Storage Hydropower Plants Including Hydraulic Short Circuit

other algorithms. In conclusion, Fig. 2.7 and Fig. 2.8 demonstrate the ability of the proposed algorithm to optimize the power dispatch in terms of efficiency and reduction of start-up and stops.

In addition to evaluating the performance in terms of SUSD cost and efficiency, it is essential to consider the computational time and complexity of the proposed algorithm. These factors are crucial, particularly in real-time applications where the set point for aFRR needs to be adjusted frequently (i.e. every 15 minutes). The computational time for each set-point computation using the proposed algorithm was measured, yielding an average time of 1 second and a maximum time of 7 seconds. This indicates that the algorithm is capable of generating optimized set points within a reasonable time frame. The relatively low standard deviation suggests consistent and predictable computational performance.

A quantitative analysis of KPIs and computational time, over the year of operation is proposed in Table 2.2

Algorithm	Color	Efficiency (%)	SUSD	Computational Time (s)		
				Mean	Std	Max
Measurement	Blue	85.75	15508	-	-	-
Algorithm (No Cost)	Red	86.36 (+0.61%)	16809 (+8.3%)	0.93	0.88	6.00
Algorithm (Cost)	Yellow	86.30 (+0.55%)	14651 (-5.5%)	1.02	0.86	7.02

Table 2.2: Comparison of KPIs and Computational Time.

2.4 Discussion

This chapter presents a comprehensive methodology for optimizing the power dispatch and reserve allocation in hydropower plants, leveraging the HSC operating mode to answer to the research sub-question: *How can we maximize aFRR provision of PSPs while reducing the number of start-up and stops of its units?*

The proposed approach solves a series of convex optimization problems efficiently, rather than relying on a single MIP problem. The methodology is successfully applied to two distinct full-size pumped storage hydropower plants as test cases to demonstrate the performance and versatility of the algorithm developed. The first study case showcases the framework capability to consider future set points and optimize the operational trajectory of a power plant by optimizing the overall efficiency and start-ups and stops. By incorporating HSC operation, the methodology enables the generating and pumping modes from different units within the same plant, leading to more flexible and efficient dispatch strategies. The second study case further validates the applicability of the framework, particularly for power plants with a large number of units, resulting in increased computational complexity and a larger number of operational combinations to consider. Despite the size of the problem (12 units, for a total of 100k + different operational combinations), the proposed methodology efficiently solves the short-

term dispatch problem and provides optimal solutions while ensuring a computationally feasible approach (sub-minute) to provide grid regulation. On top of reducing the number of start-ups and stops, the algorithm allows the HPP to provide more aFRR regulation bandwidth, if needed by the power plant operator.

Overall, the presented methodology offers a tool for hydropower plant operators to optimize power dispatch and reserve allocation, taking into account the potential of HSC operation. By adopting this framework, hydropower plants can enhance their operational efficiency, maximize participation in energy markets, and minimize the number of unit starts-up and stops. The successful application of the methodology in real study cases emphasizes its practicality and potential for broader implementation in the hydropower industry. Future studies could focus on estimating start-up and stop costs for each unit, allowing for a more accurate cost function in the objective of the optimization problems. By incorporating a refined cost estimate, the optimization framework can further enhance its ability to provide optimal dispatch strategies and improve the overall economic performance of hydroelectric plants.

FCR Provision from HPP and BESS Part II

Preface

The FCR is a vital component of the electricity grid management system in Europe. It plays a crucial role in maintaining the grid's frequency within a narrow and predefined range (49.8 ↔ 50.2 Hz) by responding to disturbances and restoring the power balance within seconds. Using turbine regulators in power stations, FCR serves as a rapid and automatic correction mechanism to counteract abrupt changes in supply or demand that could deviate the grid's rated frequency. Within the European interconnected power grid, all *Transmission System Operators* (TSO) must adhere to ENTSO-E rules, adjusting their FCR reserve annually based on ENTSO-E requirements [30].

Since its establishment in Germany back in 2007, the collaborative FCR market has expanded its reach to include Austria, Belgium, Denmark, the Netherlands, France, Germany, Slovenia, and Switzerland. This market now encompasses over 50% of the FCR demand within the ENTSO-E area, boasting a total capacity of more than 1500 MW.

Part II centers on the contribution of RoR power plants to the provision of FCR, offering a comprehensive assessment of the advantages and disadvantages associated with their participation in this role. Additionally, it delves into the potential of BESS as autonomous FCR providers and lays the bases for Part III, where we explore the synergistic benefits achievable by integrating RoR power plants and BESS for enhanced FCR supply across the grid.

3 Improving Frequency Containment Reserve Provision in Run-of-River Hydropower Plants

This chapter explores the impact of FCR provision on RoR HPPs equipped with Kaplan turbines. Initially, it introduces a modeling method for Kaplan turbine performance, combining operational data with existing characteristic curves for online efficiency estimation. The obtained models are leveraged to compute a new CAM relation for the Kaplan unit, by means of a suitably defined convex optimization problem. The second part of the chapter presents a multilevel control strategy for optimal discharge management in RoR HPPs. The proposed control strategy aims to operate the unit at the best efficiency, to improve water flow management, and to minimize components wear during FCR provision. The optimal discharge set-point is computed for maximizing the FCR provision while controlling the head of the river. The discharge set-point combines three terms: the dispatch plan set-point, the regulating discharge, proportional to the grid frequency deviation, and an offset term computed to control the average flow through the machine. Furthermore, a method to forecast the energy required in the following hour for the provision of grid frequency regulation is exploited to enhance the unit's FCR action. The control strategy is validated by simulating a month of operation of the RoR HPPs plant located in Vogelgrun (France) and by comparing the results with operational statistics. Results show the effectiveness of the proposed control strategy able to increase the provision of FCR while decreasing the movements of the plant's turbine servomechanisms.

The chapter includes results from [P2, P3].

Research sub-questions:

- (b) How does FCR provision affect RoR HPPs equipped with Kaplan turbines?
- (c) Which control strategy can improve FCR provision of RoR HPPs, while slowing down the aging of its units?

3.1 Introduction

RoR HPPs contributed to 217.1 TWh of the 3659.1 TWh produced in the ENTSOE region in 2018, 16.7% of total renewable generation [54] and 5.93 % of the total generated electricity in the ENTSOE area [10]. These power plants are often equipped with double-regulated machines (i.e. machines able to control guide vanes and blade opening angles), namely Kaplan turbines. Kaplan turbines are used thanks to their ability to guarantee high-efficiency values through a wide range of water discharge conditions. RoR HPPs do not encounter the big disadvantage of having to deal with the water hammer phenomenon when providing fast regulation, a critical issue that affects long-penstock HPPs [55]. In Germany, where RoR accounts for only 3% of the national energy mix, different studies [10, 11] estimate the RoR potential FCR support to be almost 95% of the total FCR national needs. Nevertheless, some difficulties are encountered when providing flexibility with RoR HPPs. According to [13], enhancing frequency control actions of HPPs has a considerable effect on the wear and tear of the hydraulic and mechanic system. For Kaplan turbines, the continuous movement of guide vanes and blades, due to both FCR provision and set-point compliance, increases the wear and tear of the mechanic and hydraulic components and, therefore, affects the turbine's lifetime and performance [13]. [9] shows that the governor setting directly influences the efficiency loss: the higher the frequency droop, the greater the efficiency loss. Finally, [56] assesses a relation between wear and blade vibration, which causes a decrease in performance that can eventually lead to outages. As a direct consequence, the machine behavior can deviate from the one described by the original *Characteristic Curves* (CC) [57]. Performance loss might increase even more as the control system relies strongly on the CC knowledge.

Kaplan turbines can be considered as nonlinear systems with four independent, operational, and control variables: (i) guide vanes opening angle α , (ii) rotor blades opening angle β , (iii) net head H and (iv) rotational speed n . For a given head and with rotational speed fixed by the grid frequency, the actual control system relates the two control variables α , β with a block known as combinator or CAM, to maximize the turbine efficiency. This relation is computed by leveraging the knowledge of the CC and might be affected by imprecision and machine aging (e.g. cavitation), causing an even larger efficiency loss. Due to the increasing FCR provision demand, it is important to monitor possible deviations in turbine behavior to update the control of the unit. In particular, it becomes necessary to occasionally update the CAM curve. The generation of new CAM curves is generally a very expensive process that requires the power plant to stop producing for several days to carry out specific tests. To address this problem, new methodologies to evaluate and update the machine's performance are required. Recent studies [58, 59, 60] have shown interest in applying data-driven methods to perform online estimation of Kaplan performance. Nevertheless, the strategy proposed in [58] has the disadvantage of altering the system operation to collect information about the turbine characteristics, and [59] does not present any control-related application. Despite these efforts, there is still a lack of knowledge on how to leverage data from online monitoring for control purposes. For this reason, in the first part of this chapter, we propose: (i) a methodology

to model the performances of Kaplan units with analytical functions, leveraging both the available CC and the normal operational statistics; (ii) a time-efficient computation of the CAM curve based on convex optimization. The results of this work are the answer to research sub-question (b):

How does FCR provision affect RoR HPPs equipped with Kaplan turbines?

After estimating the performance of aging Kaplan turbines, we leverage the obtained information to develop an optimal discharge tracking framework. Tracking the discharge set-point with good accuracy assumes great importance in RoR HPPs [61, 62]. This results from the necessity of complying with the day-ahead dispatch, and of controlling the river head for safety reasons. The increase in frequency control actions can enlarge the discrepancy between the discharge set-point established by day-ahead markets and the real value of the discharge. Therefore, a flow management action is required to verify that the discharge deviation originated by FCR provision is limited over time. As previously discussed, continuous movements of the guide vanes and blades, due to both FCR provision and set-point compliance, increase the wear and tear of the mechanic and hydraulic components and, therefore, affect the turbine lifetime and performance [13]. In this direction, [12] proposes a dedicated setting of the *Proportional-Integral-Derivative* (PID) parameters and the introduction of controller filters to partially reduce the reaction of hydropower units to frequency deviations. Similarly to [12], many studies focus on the design and tuning of PID parameters to reduce FCR-induced wear and tear in hydropower units [63, 64, 65, 66, 67]. Nevertheless, to the best of the author's knowledge, while the literature focuses on the governor settings, the formulation of control problems for the optimal discharge management of RoR HPPs providing FCR and, at the same time, minimizing the unit wear to increase lifetime and minimize maintenance, is not thoroughly addressed. Therefore, novel control strategies are required to optimize the asset management of RoR HPPs while increasing the provision of FCR to enhance the flexibility of modern power systems. By targeting the fulfillment of this gap, the second part of this chapter proposes a multilevel control strategy that embeds a discharge control framework capable of: (i) selecting the maximum frequency droop that allows the HPP to operate while respecting the discharge set-point, (ii) containing the discharge error during operation, and (iii) reducing the *Number of Movements* (NoM) due to its discharge management action. At the same time, the proposed framework targets efficiency maximization for the HPP. The real-time control, formulated as a convex optimization problem, ensures time-efficient computation, as well as optimality and uniqueness of the determined control set-point. The developed framework addresses the research needs outlined in research sub-question (c):

Which control strategy can improve FCR provision of RoR HPPs, while slowing down the aging of its units?

The chapter is organized as follows. Section 3.2 discusses the relation between FCR provision and the decrease in the machine lifetime and performance. Section 3.3 describes the learning

algorithm method to obtain the analytical functions modeling machine efficiency and discharge by integrating operational statistics and CAM computation for the HPP. In Section 3.4 the control framework is proposed. In particular, Section 3.4.1 presents the control problem, while Section 3.4.2 presents the whole multilevel control strategy. The simulation results are discussed in Section 3.5.

3.2 Impact of Frequency Containment Reserve on Kaplan Turbines Wear and Tear

To implement the FCR provision in HPP equipped with Kaplan turbines, PI controllers have been widely used [68]. Fig. 3.1 shows a block diagram of a Kaplan turbine control system from [69], where P^m indicates the output power of the turbine and H the head measurements.

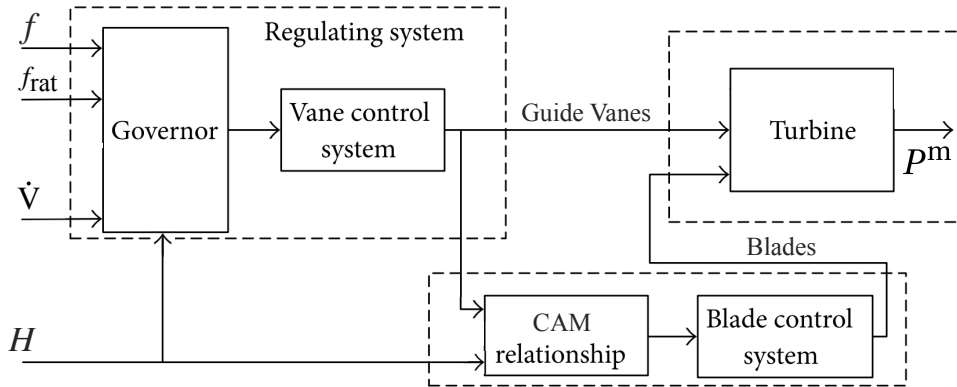


Figure 3.1: Block-diagram of a Kaplan turbine control system.

The CAM relation block is responsible for maximizing efficiency by linking β with α and H , therefore influencing the turbine performance. The governor system is responsible for deciding the opening of the guide vanes, according to the discharge set-point, \dot{V}^{SET} , and the deviation of the grid frequency f from its nominal value f_{nom} . Inside the governor, the droop control σ_f establishes a linear relationship between the change in power output (ΔP) and frequency deviation (Δf). In essence, if the frequency decreases below its nominal value, the governor increases power output to compensate, and conversely, it reduces power output if the frequency exceeds the nominal value. A higher droop value corresponds to a larger provision on FCR and causes the governor system to increase the NoM of guide vanes and blades. The existing literature [9, 13, 70, 71] has analyzed how continuous movement of the guide vanes and blades regulating mechanisms, mainly due to FCR provision, affect the wear and tear. Hydraulic turbines are also known for suffering load variations and fast

3.3 Optimal CAM Computation of Kaplan Turbines Accounting for FCR-Induced Wear and Tear

regulation since they are not designed for such operating conditions [70]. In particular, the provision of FCR is responsible for: (i) an increase of wear and fatigue [13, 67] and (ii) a decrease of the machine performance, especially in terms of efficiency [9]. As the request for FCR continuously increases, more alarming operational data are collected. [71] reports an investigation on RoR power plants where FCR has been recently implemented causing an increment of the measured pressure signals of the runner servomotor by a factor of 60. Moreover, [9] shows that the governor setting directly influences the efficiency loss: the higher the frequency droop, the greater the efficiency loss. Consequently, HPP owners are interested in reducing the FCR provision, to minimize the effect of wear and tear on their assets. In this direction, [12] proposes a dedicated setting of the PID parameters and the introduction of controller filters to partially reduce the reaction of hydropower units to frequency deviations. Nevertheless, from the power system point of view, the provision of FCR from HPPs is of fundamental importance. For this reason, the decline of turbine performance can be reduced, but not avoided. The following section proposes a way to quantify the deviation in the turbine behavior and an adaptation of the control system leveraging the acquired information during the turbine operation.

3.3 Optimal CAM Computation of Kaplan Turbines Accounting for FCR-Induced Wear and Tear

3.3.1 Problem Statement

The scope of Section 3.3 is to propose a tool to track changes in Kaplan units' performance, and to update the CAM relation to better fit the machine characteristics to correctly predict the power production. In this direction, the study can be divided into two sub-problems: (i) integration the knowledge of the CC with operational statistics to build an accurate surrogate model of the turbine performance; (ii) proposing an effective way to compute the optimal CAM curves based on surrogate models and update the control of the unit.

3.3.1.A Modeling Kaplan Turbines

The purpose of the surrogate models is to predict the machine characteristics such as the turbine efficiency η and discharge \dot{V} , for every operating point. In particular, since the final goal is the deployment of these models for control purposes, efficiency and discharge should be modeled as a function of the controllable variables of the system. For this reason, according to [72], η and \dot{V} are modeled as nonlinear functions of: (i) guide vanes opening angle α , (ii) blades opening angle β , (iii) net head H and (iv) rotational speed n . Fig. 3.2 graphically illustrates the variables α and β .

$$\eta = \eta(\alpha, \beta, H, n) \quad (3.1)$$

$$\dot{V} = \dot{V}(\alpha, \beta, H, n) \quad (3.2)$$

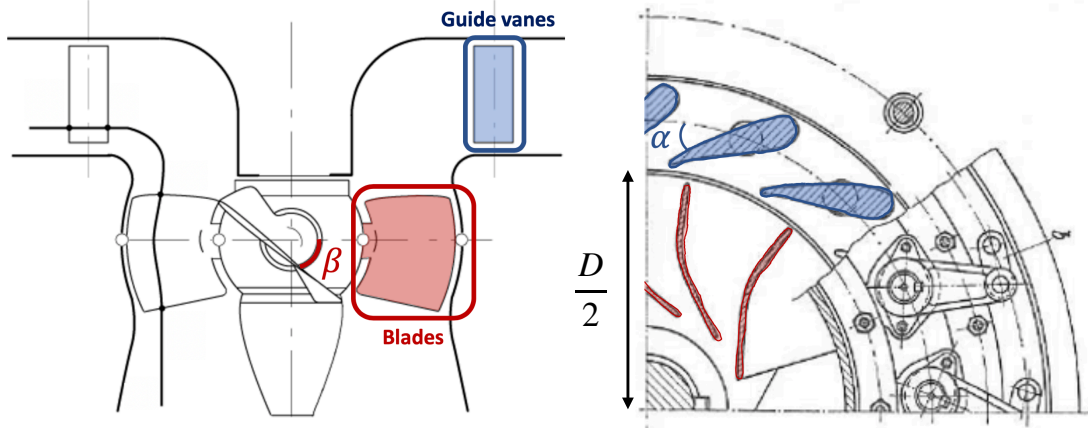


Figure 3.2: Guide vanes opening α and blade opening β for a Kaplan turbine.

Functions (3.1) and (3.2), in general unknown in an explicit/analytical form, represent the stationary behavior of the turbine, fundamental for the computation of the CAM relation. Nevertheless, in RoR power plants, the dynamic effects related to pressure waves in the penstock are very small, due to the very limited length of the penstock itself. A common value used to quantify the importance of dynamic effects in HPPs is the *water starting time* τ_W , defined in [68] as the time required for a certain head H_0 to accelerate the water in the penstock from standstill to a certain velocity. RoR power plants are usually characterized by low values of τ_W , representing fast dynamics. Therefore, it is possible to neglect the dynamic behavior and consider Eqs. (3.1) and (3.2) as representative of the whole hydraulic system.

3.3.1.B CAM Curve for Kaplan Turbines

The CAM control block indicates the relation between α and β that maximizes the efficiency for a given head value and a fixed rotational speed. For each head, the CAM is usually built as a two-column lookup table containing different values of α and the corresponding β , where each line corresponds to a certain discharge set-point (for a fixed speed). A process for the CAM computation is hereby proposed. By considering a given value of head H , the rotational speed equal to its rated value n_{nom} , and a set of L discharge set-points for which the CAM is fitted:

$$\text{CAM}_{\dot{V}} = \left[\dot{V}_1, \dot{V}_2, \dots, \dot{V}_\ell, \dots, \dot{V}_L \right] \quad (3.3)$$

3.3 Optimal CAM Computation of Kaplan Turbines Accounting for FCR-Induced Wear and Tear

The CAM computation objective is to determine two arrays:

$$\begin{aligned}\mathbf{CAM}_\alpha(H) &= [\alpha_1, \alpha_2, \dots, \alpha_\ell, \dots, \alpha_L] \\ \mathbf{CAM}_\beta(H) &= [\beta_1, \beta_2, \dots, \beta_\ell, \dots, \beta_L]\end{aligned}\tag{3.4}$$

so that:

$$\dot{V}(\alpha_\ell, \beta_\ell, H, n_{\text{nom}}) = \dot{V}_\ell \quad \forall \ell = 1, \dots, L\tag{3.5}$$

where the couple $(\alpha_\ell, \beta_\ell)$ maximizes the turbine efficiency. For each head H and for each value of discharge \dot{V}_ℓ , we propose to compute the values of α_ℓ and β_ℓ by solving Problem (3.6):

$$\begin{aligned}[\alpha_\ell, \beta_\ell] &= \arg \max \quad \eta(\alpha_\ell, \beta_\ell, H, n_{\text{nom}}) \\ \text{s.t.} \quad &\dot{V}(\alpha_\ell, \beta_\ell, H, n_{\text{nom}}) = \dot{V}_\ell \\ &\alpha_\ell, \beta_\ell \in \Omega_{\alpha, \beta}\end{aligned}\tag{3.6}$$

where $\Omega_{\alpha, \beta}$ represents the set of feasible values of α and β . To solve Problem (3.6) it is necessary to provide a parametric approximated representation of Eqs. (3.1) and (3.2).

3.3.2 Surrogate Model of a Kaplan Turbine

This subsection describes a methodology for building the analytical functions modeling the efficiency η and the discharge \dot{V} to solve the optimization problem expressed in Problem (3.6). Starting from Eqs. (3.1) and (3.2) and constraining $n = n_{\text{nom}}$, the *International Electrotechnical Commission* (IEC) speed coefficient n_{ED} is introduced to reduce the number of variables and generalize the problem:

$$n_{\text{ED}} = \frac{n_{\text{nom}} \cdot D}{\sqrt{gH}}\tag{3.7}$$

where D is the diameter of the runner, visible in Fig. 3.2. Therefore, the surrogate models of the efficiency η^* and of the discharge \dot{V}^* are built as a function of α , β and n_{ED} .

$$\eta^* = \eta^*(\alpha, \beta, n_{\text{ED}})\tag{3.8}$$

$$\dot{V}^* = \dot{V}^*(\alpha, \beta, n_{\text{ED}})\tag{3.9}$$

For this purpose, the MARS technique [49] is employed. This technique is selected for its ability to fit Eqs. (3.8) and (3.9) with analytical functions, continuous in their first derivative, which are particularly suitable to be used by optimization frameworks. Furthermore, the MARS modeling allows for evaluating the influence of each independent variable by using only an initial exploration data set which is well suited to validate the independent variables selected in this study. A similar approach can be found in [73, 74]. In the following, a brief summary of the MARS formulation is recalled. By considering a dependent variable y^* (η^* and \dot{V}^* in this study) as a function of the independent variables \mathbf{x} (α , β and n_{ED}), the MARS

Chapter 3. Improving Frequency Containment Reserve Provision in Run-of-River Hydropower Plants

approximation is built as a linear statistical model:

$$y^* = y^*(\mathbf{x}, \gamma) = \gamma_0 + \sum_{l=1}^{\text{NoB}} \gamma_l \cdot B_l(\mathbf{x}) \quad (3.10)$$

where NoB is the number of independent basis functions and γ_l the unknown coefficient for the l^{th} basis function. $B_l(\mathbf{x})$ denotes the basis function which is built as a combination of univariate basis functions b_l^\pm in the form of a truncated linear function:

$$\begin{aligned} b_l^+(x, x_0) &= |x - x_0|_+ = \max(0, x - x_0) \\ b_l^-(x, x_0) &= |x_0 - x|_+ = \max(0, x_0 - x) \end{aligned} \quad (3.11)$$

where x_0 is an univariate knot. From (3.11), each $B_l(\mathbf{x})$ is created by multiplying an existing basis function by a truncated linear function involving a new variable, as follows:

$$B_l(\mathbf{x}) = \prod_{b=1}^{\text{NoLF}} \max(0, \pm(x_{v(b,l)} - t_{b,l})) \quad (3.12)$$

where NoLF indicates the number of truncated linear functions multiplied in the b^{th} basis function, $x_{v(b,l)}$ is the input variable corresponding to the l^{th} truncated linear function, and $t_{b,l}$ is the knot value corresponding to $x_{v(b,l)}$. A forward step-wise algorithm, based on linear regression, selects the model basis functions, the corresponding coefficients, and the appropriate knots. It is followed by a backward procedure to prune the model terms to eliminate over-fitting [49]. To train the algorithm, a data set is collected using the original CC of the machine and one-year operational statistics, as it will be further detailed in Section 3.3.4. The model fitting performances are evaluated by the *Mean Square Error* (MSE), by the *Coefficient of Determination* R^2 , and by the *Generalized Cross Validation* error (GCV) computed as:

$$\text{GCV} = \frac{1}{\text{NoS}} \frac{\sum_{j=1}^{\text{NoS}} (y(\mathbf{x}) - y^*(\mathbf{x}))^2}{\left(1 - \frac{\text{NoIV}}{\text{NoS}}\right)} \quad (3.13)$$

where NoIV is the number of MARS independent variables and NoS the number of samples y in the data-set. It is worth noting that the MARS technique does not imply the convexity (nor the concavity) of the obtained η^* and \dot{V}^* . This is an important observation that has consequences on the CAM curve computation discussed next.

3.3.3 CAM Computation

Problem (3.6) is non-convex due to the analytical forms of Eqs. (3.8) and (3.9). However, a way to convexify the problem, to target the global optimal solution and to ensure time-efficient computation, is proposed in Appendix A. In particular, the appendix proposes a way to assess the concavity/convexity of the efficiency meta-model and a linearization of the discharge meta-model. The solutions of the convexified problem (A.5) are couples of values

3.3 Optimal CAM Computation of Kaplan Turbines Accounting for FCR-Induced Wear and Tear

$[\alpha_\ell, \beta_\ell]$ for each head and discharge, to populate the CAM lookup table. The procedure for the computation of the CAM lookup table for a fixed value of head is described by Algorithm 3. This procedure has to be repeated for different head values.

Algorithm 3 CAM Computation.

```

1: procedure CAM COMPUTATION( $\eta^*, \dot{V}^*, n_{\text{nom}}, \text{CAM}_{\dot{V}}$ )
2:   Fix a single value of head  $H$ 
3:   Initialization:  $\ell = 1$ 
4:   Concavity Check:  $\zeta_\eta(\alpha, \beta) \leq 0$  (see Appendix A)
5:   while  $\ell \leq L$  do:
6:     Solve Problem (A.5) for  $\alpha_\ell, \beta_\ell$ 
7:      $\ell = \ell + 1$ 
8:   end while
9:    $\text{CAM}_\alpha(H) = [\alpha_1, \alpha_2, \dots, \alpha_\ell, \dots, \alpha_L]$ 
10:   $\text{CAM}_\beta(H) = [\beta_1, \beta_2, \dots, \beta_\ell, \dots, \beta_L]$ 
11:  Output:  $\text{CAM}_\alpha(H), \text{CAM}_\beta(H)$ 
12: end procedure

```

3.3.4 Results

To showcase its applicability, the proposed method is applied to the case study given by the HPP of Vogelgrun: an HPP in service since 1959 that features 4 units, rating 39 MW each. After more than 60 years of operation, it can be expected that the turbine's performance has deviated from its original behavior. In addition to difficulties in predicting with acceptable accuracy (< 5%) the unit output power, it becomes necessary to check whether the control strategy is still able to maximize the unit efficiency. Therefore, CAM checks are performed regularly. To avoid stopping production, the tool presented in the previous subsections, able to perform an online estimation, is applied.

3.3.4.A Surrogate Model Construction and Validation

The operational statistics of one-year operation of a Kaplan unit at the Vogelgrun RoR hydropower plant are used. In particular, the data set contains the average value over 1 minute¹ of the active power output of the synchronous generator P^{HPP} , net head H , discharge \dot{V} , guide vanes opening angle α and blades opening angle β . The steady-state operating conditions, with a head variation rate lower than 2% per minute, are selected and all transients of the machine are excluded. Starting from the acquired data, the efficiency of the hydraulic machine is computed as follows:

$$\eta = \frac{P^{\text{m}}}{\rho \cdot g \cdot H \cdot \dot{V}} = \frac{P^{\text{HPP}}}{\rho \cdot g \cdot H \cdot \dot{V} \cdot \eta^e} \quad (3.14)$$

¹This sampling is acceptable for the RoR of Vogelgrun, because the head of the Rhine river is extremely constant, given the size of the river. For other RoR HPPs the sampling averaging has to be re-assessed to have constant head over the sampling time.

Parameter	Efficiency Model	Discharge Model
R^2	0.9884	0.9992
GCV	0.0006	5.2865
MSE	0.0006	5.1799

Table 3.1: Performance of the Surrogate Models.

where ρ is the water density, equal to 1000 kg m^{-3} , $g = 9.81 \text{ m s}^{-2}$ is the gravitational acceleration and η^e is the efficiency of the synchronous generator. To update the CC and determine the analytical functions of the discharge and efficiency, a new training data set is built by considering: (i) the totality of the existing data of the CC (19,400 samples) and (ii) 50% of the operational statistics, randomly selected, counting for 101,000 examples. The MARS technique is used to build the surrogate models. Both models are then validated on the remaining 50% of the aforementioned operational statistics and verified on a testing data set made by 1-month operational statistics of the successive year. The fitting performances, as defined in section 3.3.2, are listed in Tab. 3.1. To test the accuracy of the surrogate models η^* and \dot{V}^* , their ability to model the power output of the unit is taken into consideration, by computing $P^{\text{HPP}*}$ as follows:

$$P^{\text{HPP}*} = \rho \cdot g \cdot H \cdot \eta^*(\alpha, \beta, n_{\text{ED}}) \cdot \dot{V}^*(\alpha, \beta, n_{\text{ED}}) \cdot \eta^e \quad (3.15)$$

The error $P^{\text{HPP}*} - P^{\text{HPP}}$, visible in Fig. 3.3, has zero mean (i.e. has no bias) and is contained between $\pm 2.4\%$ in 95% of the cases and between $\pm 4\%$ in 99.5% of the cases. Therefore, a satisfactory accuracy of the surrogate model is achieved. In Appendix A.2, a further step is made, in order to assess the concavity of η^* .

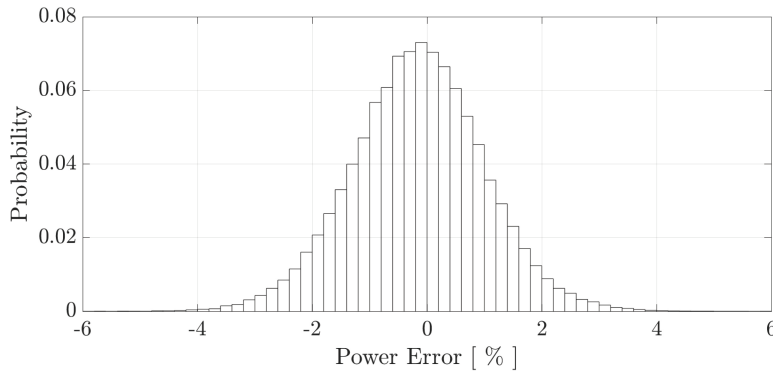


Figure 3.3: Active power error distribution for a one-month data set, with a time sampling of 1 second.

3.3.4.B CAM computation Validation

To be able to perform an unbiased performance assessment of the methodology, this subsection illustrates the difference in the power output between the currently adopted CAM operation and the new proposed CAM operation, by inputting the same time series of \dot{V} and

3.3 Optimal CAM Computation of Kaplan Turbines Accounting for FCR-Induced Wear and Tear

Table 3.2: Statistical Characteristics of the Validation Tests.

Test	Data-set length	Data-set sampling	mean(H) [m]	std(H) [m]	mean(\dot{V}) [m ³ s ⁻¹]	std(\dot{V}) [m ³ s ⁻¹]
Test 1	1 month	1 sec	11.78	0.19	244	52
Test 2	1 year	1 min	12.01	0.22	203	65

H in both simulations. Moreover, the power output for the two operations is computed using (3.15) and the same model for η^* and \dot{V}^* . Since the currently adopted CAM curves in the HPP of Vogelgrun are computed for four different head values: 9, 11, 12.5, and 14 meters, while all the other values are interpolated, the same technique is used for the new CAM computation. With $L = 400$ (i.e. to guarantee Eq. (A.5) to hold), the entire computation requires less than 45 minutes on a standard laptop equipped with a 2.8 GHz Quad-Core Intel Core i7 processor. Fig. 3.4 shows a comparison between the currently adopted CAM curve and the updated CAM. The CAM curves produced by the optimization problem have a close similarity with the currently adopted CAMs. Nevertheless, the new curves can track in a more accurate way the best efficiency point, over the full range of discharge and head. The performance of the new CAMs is assessed on two data sets, with different distributions of the input variables head and discharge. Some information about the statistical characteristics of the tests is contained in Table 3.2. The table indicates the mean value of head and discharge with the symbols $\text{mean}(H)$, $\text{mean}(\dot{V})$ respectively, and at the standard deviation of the same quantities with the symbol $\text{std}(H)$ and $\text{std}(\dot{V})$. The head range is limited between 11 and 13 m in both tests, while the discharge values vary over a wide range of values, i.e. between 50 and 250 m³s⁻¹.

Both tests show an increase in the performances of the HPP with the new CAM curve. In particular, the simulations underline an improvement of 1.5% in the total production for Test 1 and of 2.6% for Test 2, due to better tracking of the best efficiency point.

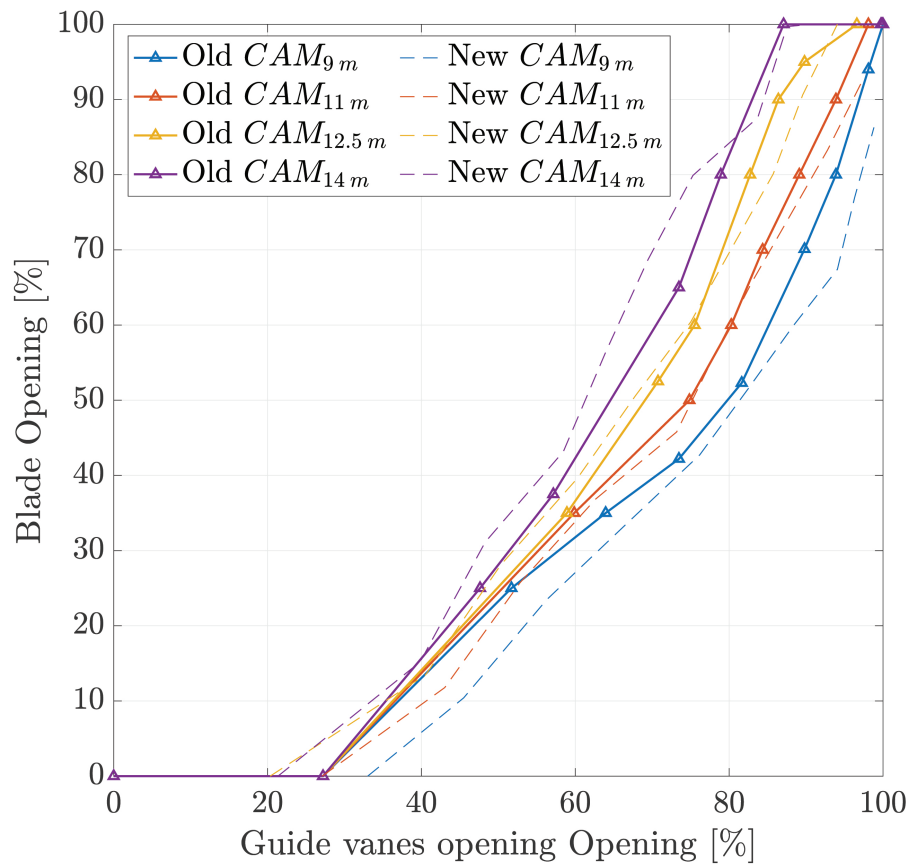


Figure 3.4: Comparison between the currently adopted CAM curve for the HPP of Vogelgrun and optimal CAM computed (dashed line) by Algorithm 3.

3.4 Improving Frequency Containment Reserve Provision in Run-of-River Hydropower Plants

3.4.1 Problem Statement

In the previous section, we discussed the machine's wear patterns and the modifications required in the internal governor CAM curves due to efficiency variations. Moving forward, Section 3.4 introduces a control strategy to enhance FCR provision while minimizing wear. However, movements due to direct FCR provision remain unaltered, primarily when hydro operates as the sole FCR provider. Altering this would inadvertently diminish the FCR action. However, there is room to optimize certain movements triggered by the FCR action but not intrinsically tied to it, like the discharge management control. This distinction is further clarified in Section 3.4.1.B. Concerning RoR HPPs, the primary objectives of the control technique presented in this section are:

- (A) Enhance FCR provision.
- (B) Construct a discharge management framework that meets the discharge set-point and minimizes HPP unit wear.
- (C) Fully utilize the hydro machine's operational range, treating guide vanes and blades as decoupled variables to maximize efficiency across all head conditions.

3.4.1.A Improving FCR Provision

In droop-based frequency control systems, increasing the FCR provision means increasing the droop of the unit's frequency containment reserve. A way to calculate the highest value of frequency droop that can be achieved compatibly with the operating condition of the HPP is proposed in Section 3.4.2.A. In particular, special attention is applied to the modeling of the relation between frequency-droop value and deviation of the realized discharge from its set point.

3.4.1.B Discharge Management Framework

The increase of the frequency droop coefficient, i.e. the increase of FCR provision, leads to two main problems: (i) increase of the wear and tear of the hydraulic and mechanic system of the HPP unit; (ii) difficulties in complying with the HPP discharge set-point. The proposed discharge management framework targets the mitigation of both problems. According to [13], in double regulated turbines, for both guide vanes and blades, the wear and tear phenomenon is mainly influenced by:

- the cumulative distance of movements Z ;

Chapter 3. Improving Frequency Containment Reserve Provision in Run-of-River Hydropower Plants

- the total amount of movement direction changes J .

Over a time period that includes J movements, the so-called *cumulative distance* Z is defined by [13] as:

$$Z = \sum_{j=1}^J z_j \quad (3.16)$$

where z_j is the distance of one single movement. A way to compute the NoM J and the distance of each single movement z_j , proposed by [13], is shown in Fig. 3.5, where J is considered as the number of direction changes of the actuators controlling the opening of either guide vanes or blades. In RoR power plants, the two main factors contributing to the increase of guide vanes and blades movements are:

- FCR provision;
- discharge management.

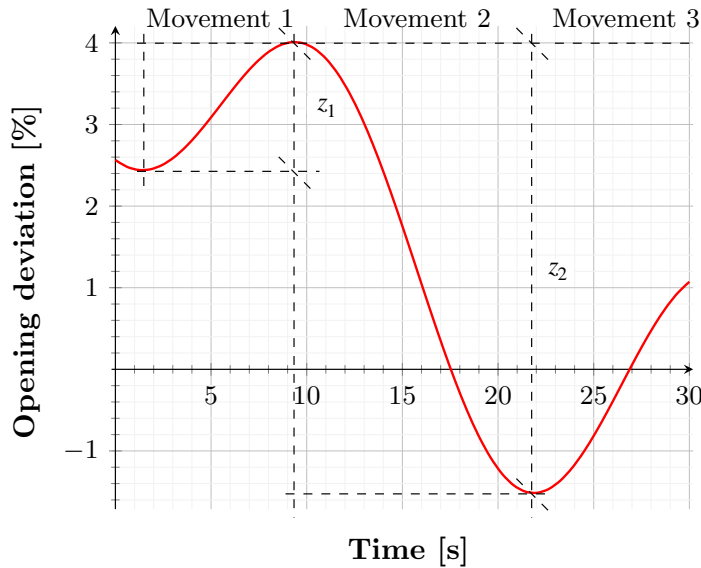


Figure 3.5: NoM J and distance z_j for a general trajectory of a moving organ (i.e., guide vane or blade) expressed in terms of percentage opening deviation.

Indeed, by enhancing the FCR provision, the cumulative distance Z increases. Working with a higher droop inevitably results in having longer movements z_j of guide vanes and blades, and, therefore, more wear and tear.² Furthermore, the provision of FCR indirectly increases the NoM of guide vanes and blades because it requires a discharge management system to compensate for the discharge deviations originated by FCR. This latter effect can be

²This is true if hydropower is the sole provider of FCR services. Chapter 5 discusses how to increase FCR provision while minimizing hydropower action if a BESS is connected in parallel with the HPP.

reduced by developing a control targeting the minimization of the NoM J originated by the discharge management while enhancing the FCR provision of the HPP. The development of this framework is shown in detail in Section 3.4.2.B.

3.4.1.C Exploiting the Full HPP Operating Range

The optimal control is performed by decoupling the action of guide vanes and blades as an alternative to the general gate-based control, which has been proven to be a successful strategy in [60]. The standard operation of the Kaplan unit is considered, while start-up and stop procedures are not the objects of this study. Equations (3.1) and (3.2) represent the stationary behavior of the turbine. Since RoR power plants are characterized either by the absence of a penstock or by the presence of a very short one, it is possible to neglect the turbine dynamic behavior and consider (3.1) and (3.2) as representative of the hydraulic system. Given the analytic expressions for η and \dot{V} , knowing the head H and the rotational speed \hat{n} , the control problem can be written as in (3.6). The set-point given to the HPP is considered to be a set-point in discharge \dot{V}^{SET} , which is often the case for RoR power plants. In fact, the river head is usually monitored and controlled by dispatchers, who communicate the discharge set-point to the different HPPs.

3.4.2 Multilevel Control Strategy

The control framework is composed of multiple layers, executing the computations on different time horizons:

- (A) Daily computation of the droop coefficient σ_f (DROOP in Fig. 3.6), accordingly with the usual market practice in most of the European countries³
- (B) Hourly computation of the discharge offset term based on a forecast of the discharge required in the following period to perform FCR with the computed droop (OFF in Fig. 3.6).
- (C) Real-time control, by solving a convex optimization problem taking into account the provision of FCR and having as input the sum of discharge set points and hourly offset (OPT in Fig. 3.6).

The discharge set-point \dot{V}^{SET} fed into the optimization problem is calculated by summing three contributions:

- (i) the original set-point given by the day-ahead dispatch plan \dot{V}^{DISP} ;

³The transmission system operators of Germany, France, Belgium, the Netherlands, Austria and Switzerland share frequency containment reserve on a common platform [75] daily. The market for FCR-N is also based on day-ahead bidding in the Nordic countries [76].

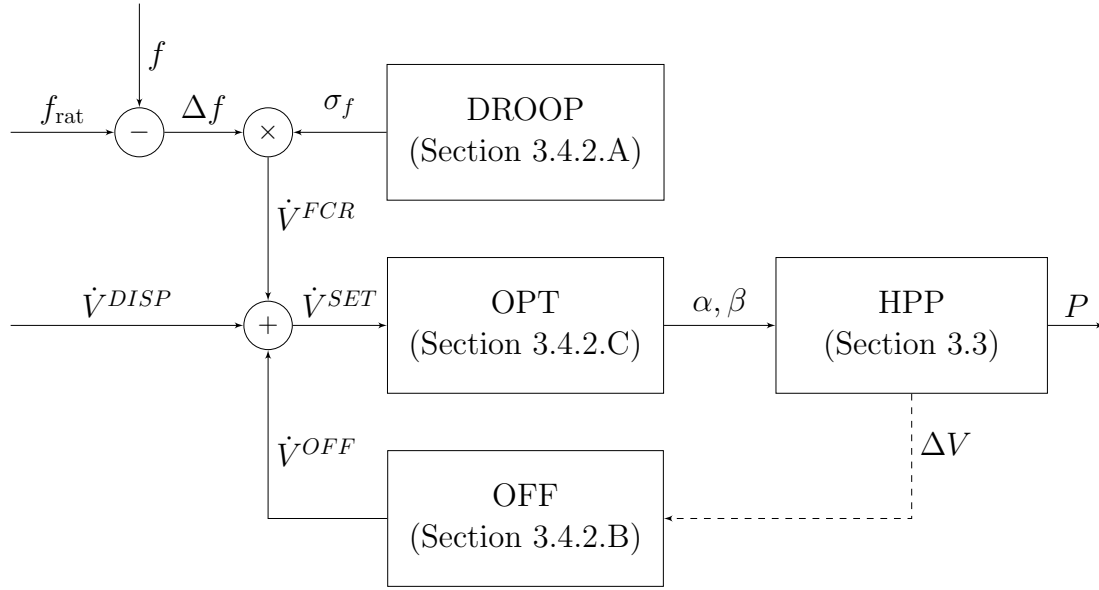


Figure 3.6: Multilevel control strategy control diagram.

- (ii) a droop-based frequency regulation originating a deviation from the main set-point \dot{V}^{FCR} ;
- (iii) an offset discharge term, computed periodically, to ensure that the discharge deviation is contained within certain limits, chosen a priori to ensure the correct management of the river \dot{V}^{OFF} .

The HPP block refers to the power plant model and is considered as described by Eqs. (3.8) and (3.9). The strategy is to be applied to RoR hydropower plants equipped with Kaplan turbines. Nevertheless, by removing the latter level of the computation (OPT), the control can be extended to any kind of RoR hydropower plant equipped with other types of turbines. In this case, the obtained set point \dot{V}^{SET} is simply considered as the sole input of the governing system. The division of the control problem in different time horizons allows relaxing the constraints on the HPP set-points, therefore, adding a degree of freedom to the control problem. For instance let us consider a certain discharge set-point \dot{V}_h^{DISP} for hour h , coming from the dispatch plan. The consequence, in an ordinary control system, is a control action that at every time step m , (i.e. each minute) imposes a discharge set-point \dot{V}_m equal to \dot{V}_h^{DISP} , for the entire hour, as follows:

$$\dot{V}_m \approx \dot{V}_h^{DISP} \quad \forall m \in [1, \dots, 60] \quad (3.17)$$

Nevertheless, except for the case of extremely small rivers, the head is not a function of a single power plant discharge and it changes, generally very slowly, as a consequence of many external parameters. Therefore, there is no need for strictly applying (3.17) for the calculation

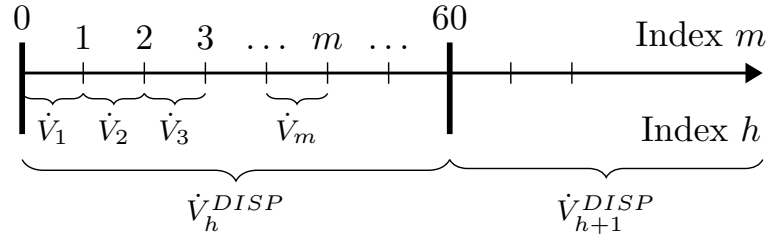


Figure 3.7: Set-point problem on a time scale.

of \dot{V}_m , and the problem can be relaxed and expressed in its integral form:

$$\Delta V_h = \sum_{m=1}^{60} \dot{V}_m - 60 \cdot \dot{V}_h^{\text{DISP}} \approx 0 \quad (3.18)$$

where ΔV_h indicates the *Cumulative Discharge Error* (CDE), expressed in m^3 for the hour h . By imposing this latter to be equal to zero, Eq. (3.18) ensures the set-point request to be fulfilled at the end of every period (i.e. every hour). A further element of complexity is given by the discharge set-point which is modified due to FCR provision. Even if at every minute m the set-point $\dot{V}_m = \dot{V}_h^{\text{DISP}}$ is fed into the control system, a deviation from the given set-point is always introduced by the FCR provision modifying the discharge through the hydraulic machine. At every hour h , the error accumulated ΔV_h is:

$$\Delta V_h = \Delta V_{h-1} + \Delta V_h^{\text{FCR}} \quad (3.19)$$

where: ΔV_{h-1} is the CDE of the previous hour and ΔV_h^{FCR} is the cumulative deviation due to FCR provision, in the hour h . The term ΔV_h^{FCR} is related to the energy E_h^{FCR} , required over the hour h to provide frequency control, as follows:

$$\Delta V_h^{\text{FCR}} = \frac{E_h^{\text{FCR}}}{\kappa_h} \quad (3.20)$$

where κ is a conversion factor between produced energy and the amount of water flowing through the hydropower unit.

$$\kappa = \rho g H \eta \quad (3.21)$$

In Eq. (3.20) the terms κ_h indicates the average value of κ over the hour h . For a droop based FCR provision, the energy E_h^{FCR} can be computed as [77]:

$$E_h^{\text{FCR}} = \sigma_f \int_h \Delta f dt = \sigma_f W_h \quad (3.22)$$

where W_h is defined as the integral of the frequency deviation over hour h and Δf indicates the deviation of the frequency from its nominal value. Eqs. (3.20) and (3.22) express the link between W_h and the amount of additional water (positive or negative) that has to flow through the turbine to provide FCR in a certain period. The quantity W_h is supposed to be zero over a

Chapter 3. Improving Frequency Containment Reserve Provision in Run-of-River Hydropower Plants

long period, if the aFRR is well planned in the synchronous area (i.e. the Synchronous grid of Continental Europe in the case of the HPP of Vogelgrun). However, this is not verified for a shorter time window (e.g., 1 h). If no action is taken, the discharge could deviate considerably from its expected value because of the FCR provision, causing the alteration of the river head as well. In order to optimize discharge management, this study proposes to deploy a forecasting tool to obtain a prediction \hat{W}_h of the quantity W_h . The tool is presented in Appendix B.

3.4.2.A Optimal Daily Droop Coefficient

As mentioned in Section 3.4.1, one of the objectives of the framework is the improvement of the hydropower regulation action. In droop-based frequency control, this can be done by augmenting the droop value. For this reason, this first block of the framework determines, daily, the optimal value of the droop coefficient as the one with the highest value and capable of satisfying the operating condition of the HPP. The choice is limited by two factors. The first limitation comes from the inevitable increase in the deviation of the HPP discharge from the discharge set-point due to the droop enhancement. Hence, it is necessary to accept a certain CDE ΔV_{\max} and compute the maximum droop that allows respecting this condition. The second constraint is due to the power limitation of the hydraulic machine. If the turbine is already operating close to its maximum (or minimum) power, it could be impossible to perform FCR provision as requested. It is possible to map these two limitations in two constraints.

1. Maximum admissible CDE.
2. Maximum power of the machine.

Therefore, the problem of the droop computation can be divided into two sub-problems, each one giving a possible value of droop as output. Every day, the droop is calculated to be the minimum of these two values: σ_f^D and σ_f^P , respectively.

Maximum Admissible CDE

Every hour h of the day d , considering a droop-based FCR action with droop equal to σ_f^D , the term ΔV_h^{FCR} can be predicted starting from the prediction \hat{W}_h and considering Eq. (3.20) and Eq. (3.22) as follows:

$$\Delta V_h^{\text{FCR}} \in \left[\frac{\sigma_f^D}{\kappa_h} \left(\hat{W}_h - \hat{W}_h^{\uparrow\downarrow} \right), \frac{\sigma_f^D}{\kappa_h} \left(\hat{W}_h + \hat{W}_h^{\uparrow\downarrow} \right) \right] \quad (3.23)$$

where $\hat{W}_h^{\uparrow\downarrow}$ corresponds to the 5-95% *Confidence Interval* (CI) of the \hat{W}_h prediction of W_h for the hour h , with a CI equal to 95% and κ_h indicates the average value of κ over the hour h . The target of the discharge management is to introduce a water volume ΔV_h^{OFF} able to compensate

3.4 Improving Frequency Containment Reserve Provision in Run-of-River Hydropower Plants

for the effect of ΔV_h^{FCR} and for the CDE of the previous hour ΔV_{h-1} , as visible from (3.24):

$$\Delta V_{h-1} + \Delta V_h^{\text{OFF}} + \frac{\sigma_f^D}{\kappa_h} \hat{W}_h = 0 \quad (3.24)$$

If Eq. (3.24) is satisfied for every hour h of a day d , the maximum possible CDE depends only on the forecasting accuracy. In particular, once the maximum permitted cumulative discharge error ΔV_{max} is decided by the river authorities, or by the HPP owner, the maximum acceptable droop for the day d can be computed similarly to [78] by solving (3.25):

$$\Delta V_{\text{max}} = \frac{\hat{W}_f^{\uparrow\downarrow} \cdot \sigma_f^D}{\kappa_d} \quad (3.25)$$

$$\sigma_f^D = \frac{\kappa_d \cdot \Delta V_{\text{max}}}{\hat{W}_f^{\uparrow\downarrow}} \quad (3.26)$$

where κ_d indicates the average value of κ over the day d . The latter equation shows that having a lower uncertainty on the forecast allows increasing the acceptable droop and the provision of FCR⁴. Similarly, by allowing a bigger ΔV_{max} , an increase in FCR provision can be achieved. On the other side, ΔV_{max} is limited by river controlling authorities.

Maximum Power of the Machine Limitation

A second limitation on the droop is given by the maximum power of the machine. To ensure continuous operation, the droop has to be selected to comply with the maximum power capacity of the machine. This means that the power deviation caused by FCR provision plus the dispatch production \hat{G}_h for every hour h of the day d must not be greater than the maximum power capacity of the machine. This limitation is expressed for a day d by considering the maximum values of both the components in (3.27).

$$d_p^P = \frac{P_n - (\hat{G}_{\text{max}} + \kappa_d \Delta V_{\text{max}} / 2 \Delta T)}{\Delta f_{\text{max}}} \quad (3.27)$$

where P_{nom} is the nominal power of the machine and \hat{G}_{max} maximum value of the dispatched power over the day d , namely:

$$\hat{G}_{\text{max}} = \max_{h=1}^{24} (\hat{G}_h) \quad (3.28)$$

$$\sigma_f = \min(\sigma_f^D, \sigma_f^P) \quad (3.29)$$

⁴This statement is true if the turbine is not operating close to the maximum power (See next paragraph).

3.4.2.B Hourly Offset Discharge

The second objective of the framework is to ensure the discharge set-point to be satisfied while minimizing the wear and tear of the HPP unit. Ideally, the target is to implement a single action (offset discharge) able to bring the CDE to 0. To achieve this objective, the error of the previous period and the forecast of the discharge needed to perform FCR in the following interval are computed. To this end, we can rearrange (3.24) as follows:

$$\Delta V_h^{\text{OFF}} = -\left(\Delta V_{h-1} + \frac{\sigma_f}{\kappa_h} \hat{W}_h\right) \quad (3.30)$$

To minimize the NoM of guide vanes and blades, the ΔV_h^{OFF} is given by a discharge offset that is constant over the duration T of the hour so that the offset function causes only one movement of the governing system at the beginning of the interval and not a continuous action characterized by multiple movements over the period. As a consequence:

$$\dot{V}_h^{\text{OFF}} = \frac{\Delta V_h^{\text{OFF}}}{T} \quad (3.31)$$

A graphical representation of the offset function impact on the discharge error can be seen in Fig. 3.8.

By considering the initial value of ΔV_h as contained within the limits $(\pm \Delta V_{\text{max}})$, the forecasting tool predicts the value of \hat{W}_h which is converted into the predicted cumulative discharge deviation for FCR provision $\Delta \hat{V}_h^{\text{FCR}}$ according to (3.20). In Fig. 3.8, the light gray area represents the CI of the prediction. As it is visible, without any action in terms of offset function, there is a consistent portion of the CI that exceeds the limit ΔV_{max} (dark grey area in Fig. 3.8a). As defined in (3.24) the offset function equates ΔV_{h-1} plus the prediction $\Delta \hat{V}_h^{\text{FCR}}$ to centre the CI in 0. By operating this control action at every period, the error is limited within $\pm \Delta V_{\text{max}}$, chosen a priori by the power plant owner, in agreement with the river management authority.

3.4.2.C Real-Time Optimal Control

Fig. 3.6 shows the lowest level of control, interacting directly with the HPP, and taking as input the droop calculated in Section 3.4.2.A and the offset computed in Section 3.4.2.B. This subsection is specifically addressing the control problem for double-regulated units. It can be neglected in case of applications to any RoR HPPs controlled in power and equipped with single regulated turbines.

The discharge set-point \dot{V}_h^{DISP} from the dispatch plan is summed with \dot{V}_h^{OFF} and with the discharge deviation given by the droop-controlled FCR action \dot{V}_s^{FCR} .

$$\dot{V}_s^{\text{SET}} = \dot{V}_h^{\text{DISP}} + \dot{V}_h^{\text{OFF}} + \dot{V}_s^{\text{FCR}} \quad (3.32)$$

3.4 Improving Frequency Containment Reserve Provision in Run-of-River Hydropower Plants

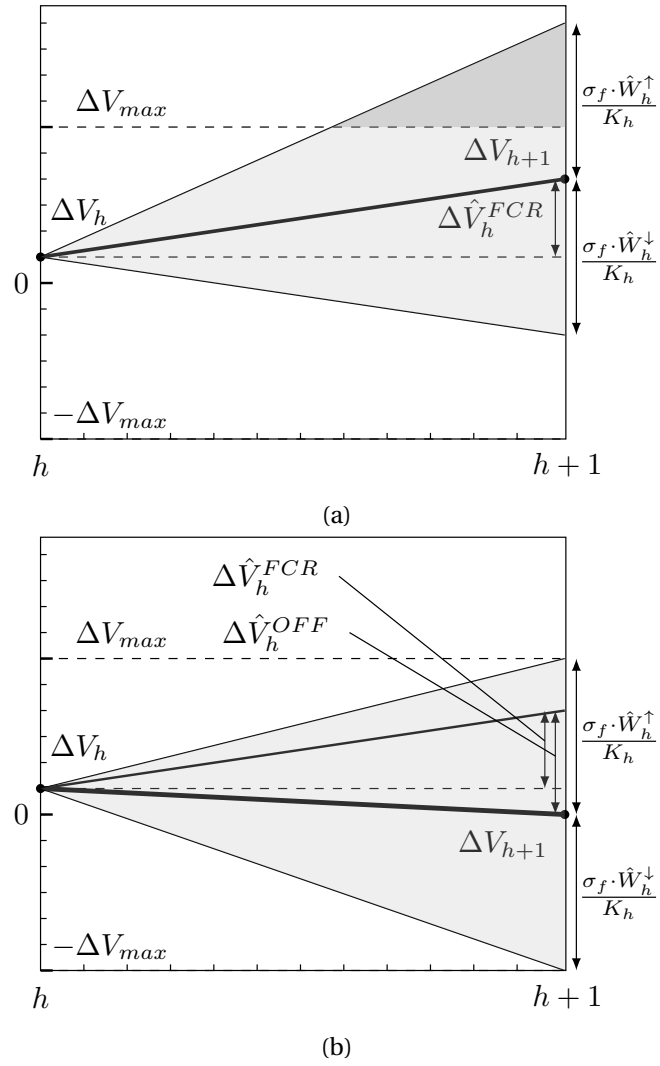


Figure 3.8: Expected trajectories of the CDE due to FCR provision a period T (a) without and (b) with the action of the offset discharge \hat{V}_h^{OFF} .

Chapter 3. Improving Frequency Containment Reserve Provision in Run-of-River Hydropower Plants

with:

$$\dot{V}_s^{\text{FCR}} = \frac{\Delta f_s \cdot \sigma_f}{\rho g H_s \eta_s} \quad (3.33)$$

where the values of η_s and H_s are approximated with η_{s-1} and H_{s-1} . The term Δf_s is the frequency deviation $50 - f_s$.

Similarly to Problem (3.6), the control problem can be stated as: *For a given discharge set-point \dot{V}^{SET} and external condition n_{ED} (i.e. head H and rotational speed n) find the combination of guide vanes and blades opening angles that maximizes the efficiency.*

Every time instance, e.g. every second s , given the measurements of head H_s , rotational speed n_s and guide vanes and blades position in the previous second $\alpha_{s-1}, \beta_{s-1}$, the mathematical formulation of the problem uses as objective function a weighted sum of two contributions, ensuring the best efficiency operation and the discharge tracking as in (3.34):

$$\begin{aligned} \min_{\alpha, \beta} \quad & \omega_\eta \cdot \left[1 - \eta^*(\alpha, \beta, n_{\text{ED},s}) \right] + \\ & \omega_{\dot{V}} \cdot \left[\dot{V}_s^{\text{SET}} - \dot{V}^*(\alpha, \beta, n_{\text{ED},s}) \right]^2 \\ \text{s.t.} \quad & \alpha, \beta \in \Omega_{\alpha, \beta} \\ & \alpha_{s-1} + v_{\alpha_c} \Delta s \leq \alpha \leq \alpha_{s-1} + v_{\alpha_o} \Delta s \\ & \beta_{s-1} + v_{\beta_c} \Delta s \leq \beta \leq \beta_{s-1} + v_{\beta_o} \Delta s \end{aligned} \quad (3.34)$$

where Δs is the amount of time between consecutive set-points, and $v_{\alpha_o}, v_{\alpha_c}$ are respectively the normalized maximum speeds in opening and closing of the servomotor acting on the guide vanes. The quantities v_{β_o}, v_{β_c} are the corresponding quantities for the blades servomotor. Constraints $\Omega_{\alpha, \beta}$ ensure that the operation is within feasible positions of guide vanes and blades. Finally, the last two constraints consider the maximum speed of the servomotors, to avoid changes in the moving organs which are physically impossible, because of a finite servomotor speed. Similarly to Problem (3.34), Problem (3.34) is convex if:

1. $\eta^*(\alpha, \beta, n_{\text{ED},s})$ is concave;
2. $\dot{V}^*(\alpha, \beta, n_{\text{ED},s})$ is linear.

While concavity of η^* , has been discussed and proved in Appendix A, the linearization of \dot{V}^* considering the servomechanism constraints of Eq. (3.34) is discussed here below.

Linearity of \dot{V}^* : The function \dot{V}^* is built as indicated in Section 3.3.2, as a sum of piece-wise polynomials of different orders. To reach good accuracy of the discharge model, it is probable for the polynomials composing \dot{V}^* to be non-linear, as indicated in [72]. Nevertheless, when applying (3.34), the constraints related to the servomotors speed are forcing the solution α, β to be close to $\alpha_{s-1}, \beta_{s-1}$. Therefore, at every second s , \dot{V}^* can be seen as a relatively

small deviation from $\dot{V}^*(\alpha_{s-1}, \beta_{s-1}, n_{ED,s})$. Since the turbine discharge is a smooth function of H, α and β , usually represented with low-order polynomials [72, 79, 80], it is possible to linearize \dot{V}^* around $\alpha_{s-1}, \beta_{s-1}$, indicated in this chapter with the term $\overline{V}^*(\alpha, \beta, n_{ED,s})|_{\alpha_{s-1}, \beta_{s-1}}$. The linearized form can be substituted in the second term of the objective function of (3.34), obtaining Problem (A.5). If (A.5) is inserted in (3.34) as visible in (3.35), and (A.3) is satisfied, then (3.35) is a convex optimization problem.

$$\begin{aligned}
 \min_{\alpha, \beta} \quad & \omega_\eta \cdot \left[1 - \eta^*(\alpha, \beta, n_{ED,s}) \right] + \\
 & \omega_{\dot{V}} \cdot \left[\dot{V}_s^{\text{SET}} - \overline{V}^*(\alpha, \beta, n_{ED,s})|_{\alpha_{s-1}, \beta_{s-1}} \right]^2 \\
 \text{s.t.} \quad & \alpha, \beta \in \Omega_{\alpha, \beta} \\
 & \alpha_{s-1} + v_{\alpha_c} \Delta t \leq \alpha \leq \alpha_{s-1} + v_{\alpha_o} \Delta t \\
 & \beta_{s-1} + v_{\beta_c} \Delta t \leq \beta \leq \beta_{s-1} + v_{\beta_o} \Delta t
 \end{aligned} \tag{3.35}$$

This formulation allows the control problem to output the global optima by applying any kind of gradient-based or interior point solver.

3.4.3 Results

In this section, a validation of the method is presented and the performances of the framework are evaluated by numerical simulations in the Matlab environment. The simulation results are compared with measured data of the full-size RoR HPP Vogelgrun, owned by EDF, on the Rhine River (France). Unit 1 is selected to be part of this study, and, therefore, the efficiency and discharge of this unit have to be modeled as a function of the measurable variables. The simulation is built with the following characteristics:

- (i) The simulation time is one month, starting from April 15, 2020, with a time sampling rate of 1 minute.⁵
- (ii) Every day, the computation of the droop for the following day is performed, based on the information of the day-ahead dispatch.
- (iii) Every hour, the discharge set-point offset is computed based on the frequency information of the previous 8 hours, as required by the *Auto-Regressive* (AR) model for the forecast of W_h .
- (iv) Every minute, a new operating point is chosen for the turbine by the optimization problem.⁶

⁵Length and sampling rate of the simulation are chosen based on the richest data-set available for the considered power plant.

⁶The sampling for the operation point is chosen based on the state-of-the-art controller in the considered power plant, a faster control could be implemented, as the problem formulation allows for a fast resolution.

3.4.3.A Linearization of the Discharge Model

The fitting performance and the concavity of the surrogate models have been previously discussed in Section 3.3.4. In this subsection, the error introduced by the linearization of \dot{V} is estimated. As previously mentioned in Section 3.4.2.C, the linearization of \dot{V} should not introduce a considerable error for two reasons:

- the turbine discharge is a smooth function of H, α and β , usually represented with low-order polynomials[79, 72, 80];
- the servomotors controlling α and β are subject to hard limitations in the movements, in terms of maneuvering speed.

The numerical proof of the above statement is given here below for the turbine object of the study. A mapping of the *Root-Mean-Square Error* (RMSE) and the *Coefficient of Determination* (R^2) over the entire domain is visible in Fig. 3.9. Moreover, Fig. 3.10 shows the statistical quantities *Cumulative Density Function* (CDF) and *Probability Density Function* (PDF) for R^2 . All the indicators have been computed by considering 10000 points equally distributed in the feasible region $\Omega_{\alpha, \beta}$. Both the indicators (RMSE ≤ 0.2 and $R^2 \geq 0.99$) demonstrate that the linearization can be considered as feasible for control purposes. A further step is made to

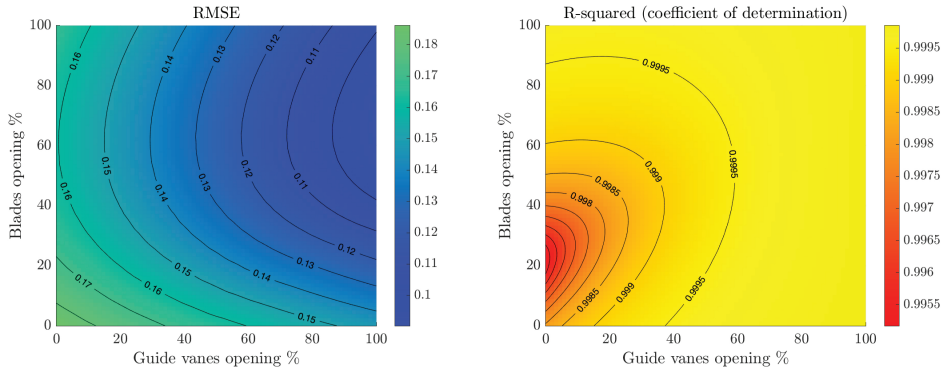


Figure 3.9: RMSE and R^2 of the linearization mapped over all the operation points.

assess the concavity of η^* . Since the non-convex area represents only a small portion of the domain, this does not drastically affect the result.

3.4.3.B Control Strategy Validation

Droop Computation:

The method presented in Section 3.4.2.A proposes that the daily droop should correspond to the minimum value between:

- The droop σ_f^D , based on the maximum admissible CDE.

3.4 Improving Frequency Containment Reserve Provision in Run-of-River Hydropower Plants

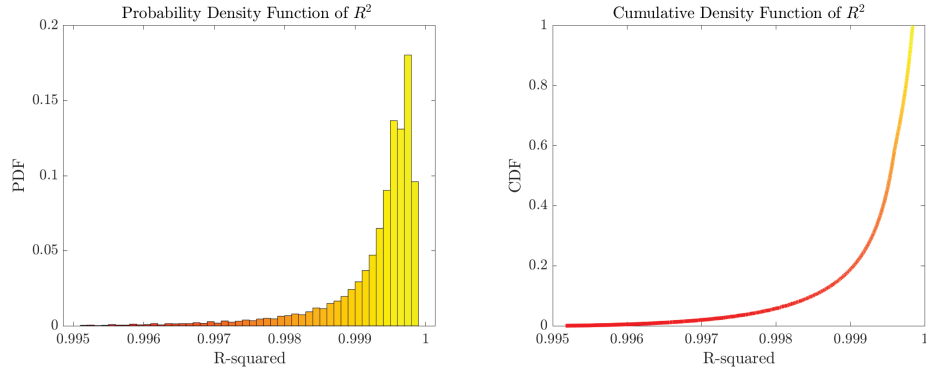


Figure 3.10: PDF and CDF of the linearization R^2 .

	CI	κ_d with H_{\min}	κ_d with H_{avg}
σ_f^D	95%	20415	21275
	99%	15553	16162
σ_f^P	95%	56746	79246
	99%	56746	79246

Table 3.3: Droop Coefficient Values kWhz^{-1} .

- The droop σ_f^P , compatible with the turbine power rating.

According to (3.26), it is necessary to estimate the conversion factor κ_d to compute the maximum droop coefficient σ_f^D . Since the choice has to be made every day for the following one, the estimation of κ_d has to be made based on the day-ahead dispatch. The value of κ_d depends on the quantities H_d and η_d , according to (3.21). To compute these quantities, the following approach is considered: a probability density function of the head values over one year is computed and, by considering a CI of 95%, the minimum head H_{\min} is considered to compute κ_d . The estimation of η_d is made by knowing the discharge set-point from the day-ahead dispatch and by considering H_{\min} as the head for the day after. This approach allows making the optimization more robust since the choice of H_{\min} as reference head for the calculation leads to the computation of a lower value of maximum droop. The achieved results are compared with the estimation of η_d where the average value of head H_{avg} is considered. The results, for two different CI for the frequency forecaster and two different approaches in the computation of the conversion factor κ_d are compared in Table 3.3. The current frequency droop in the HPP of Vogelgrun is $\sigma_f = 17.5 \text{ MWhz}^{-1}$. For the computation of these droops, the chosen value for the maximum admissible error ΔV_{\max} is 9000 m^3 , corresponding to 1% of the total amount of water flowing through one unit, in one hour, when the unit operates with a constant discharge value of $250 \text{ m}^3 \text{ s}^{-1}$.

During the analyzed month, the discharge set-points are not close to the maximum value of discharge of the HPP. As a consequence, by looking at Table 3.3, it is possible to observe that

Chapter 3. Improving Frequency Containment Reserve Provision in Run-of-River Hydropower Plants

the droop σ_f^P , computed according to (3.27), is always greater than σ_f^D and, therefore, this latter is adopted. In all cases, the optimally determined droop is higher than the corresponding value given by state-of-the-art approaches.

Discharge Management Validation: Four scenarios (two different CIs in the forecasting tools and two different approaches in the computation of κ_d) are simulated and compared in terms of reliability, to test the algorithm's robustness. A graphical representation of the results for the less robust case (CI= 95% and κ_d computed with H_{avg}), is given in Fig. 3.11. The CDE is shown in bold red for 12 of the 720 simulated hours. It is possible to observe the predicted discharge error due to FCR action $\Delta \hat{V}_h^{FCR}$ and the relative action $\Delta \hat{V}_h^{OFF}$ of the control. Every hour, the estimation $\Delta \hat{V}_h^{FCR}$ is computed. The offset function $\Delta \hat{V}_h^{OFF}$ is calculated according to (3.24). It is noticed that, without the offset function calculated in the discharge management framework, the error ΔV would increase and get greater than the limits, as highlighted in Fig. 3.11 by the red thin curve. The direct consequence would be that, over time, the head of the river would deviate from the expected one, since the power plant is operating with a different discharge value. By applying the framework, the error is contained within the limits ($\pm 1\%$). Furthermore, the discharge is controlled just by acting on guide vanes and blade opening angle once per hour, i.e. limiting the NoM due to discharge management. This represents a noticeable improvement compared to state-of-the-art controls adopted for the operation of RoR HPPs, where the discharge is re-adjusted every minute to minimize the error due to frequency control.

To assess the performances of the proposed framework, the term v^F can be defined as the duration of the period in which the discharge error is within the limit ΔV_{max} , expressed in percentage of the simulation duration. Table 3.4 shows the values of v_T for the different approaches, while the droop computation is shown in Table 3.3. For the case considering κ_d with H_{avg} , the proposed framework is able to enhance the droop, obtaining an average value over 30 days that corresponds to 121% of the value obtained by the state-of-the-art operational practices in the HPP of Vogelgrun. Despite the increase of FCR provision, the discharge of the RoR HPP is managed by operating just one movement per hour and by containing the discharge error within $\pm 1\%$ for 97.70% of the time, within $\pm 1.5\%$ in 99.85% of the time and between $\pm 2.2\%$ during the whole simulation.

	CI	κ_d with H_{min}	κ_d with H_{avg}
v^F	95%	98.18%	97.70%
	99%	99.74%	99.67%

Table 3.4: v^F for Different Strategies.

Validation of the Real-Time Optimal Control: The latter layer of the framework, to be applied in case of double-regulated turbines, consists in the computation of α and β by Eq. (3.35), given

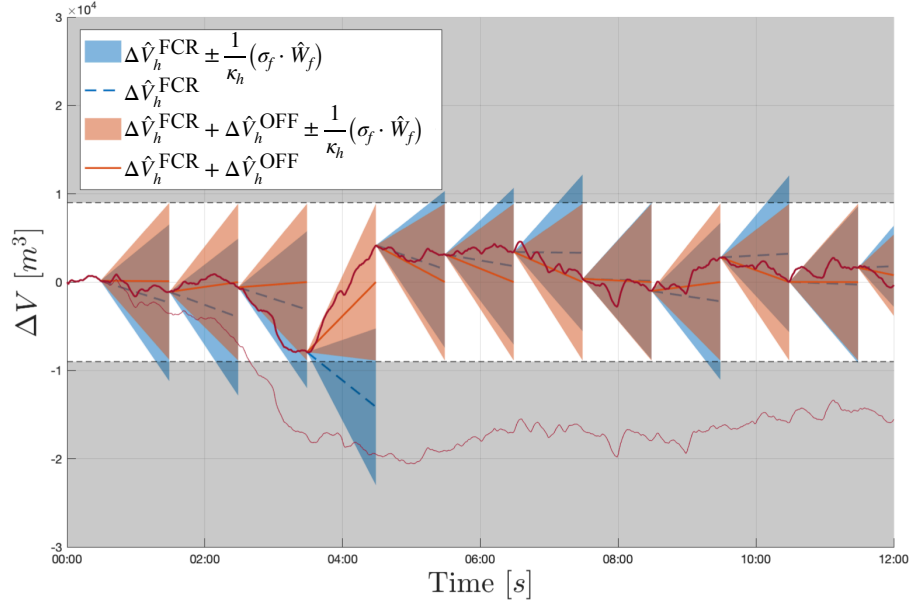


Figure 3.11: Comparison of predicted value $\Delta \hat{V}_h^{\text{FCR}}$, the offset function $\Delta \hat{V}_h^{\text{OFF}}$ and the CDE in bold-red. In light-red the scenario with enhanced droop but without discharge management.

a certain discharge set-point, defined in Eq. (3.32). The solution is found by taking advantage of the Yalmip toolbox coupled with `fmincon` solver, in the Matlab environment. Without considering the effect of the last two constraints, it can be proved that the choice of α and β given by Eq. (3.35) coincides with the output of the general gate-dominant control, where the relation between α and β is defined by the CAM block look-up table. This result is supported by [81], where the decoupling of guide vanes and blades control is proved to outperform the gate-dominant control just in high transient conditions, such as load rejections, which are not treated in this study. Furthermore, based on the existing literature, it can be expected the wear and tear to be reduced. As indicated in [82], when performing FCR provision Kaplan units may be operating slightly off-CAM since the blades regulating mechanism is slower and lags behind the guide vanes regulating mechanism. Since Eq. (3.35) takes as input already the discharge set-point that includes FCR, it is able to propose a solution for α and β that respects the servomotors speeds and maximizes the efficiency. As stated in [9], the efficiency loss due to off-cam operation due to FCR provision is almost negligible, but its effect on the wear reduction strategies is not. Therefore, it is not possible to state that the optimization problem represents an improvement in terms of efficiency, with respect to the gate-dominant approach, but still it leads to a reduction in the wear and tear originated by the FCR provision. Moreover, the proposed optimal control is formulated in order to be integrated with additional information, such as wear and tear estimation, that steer the optimization towards the maximization of multiple objectives.

3.5 Discussion

As turbine performance decreases with time, and the increasing provision of FCR accelerates this process, a method to update the characteristic curves of a Kaplan turbine has been presented. The proposed tool allows for performing a fast online check of the CAM relation, without altering the HPP production. It has been proven that, by leveraging operational statistics, it is possible to better predict power production and perform a more accurate control of the hydroelectric unit. In particular, the method updates the CAM relation based on the online monitored performance of the machine and by solving a convex optimization problem targeting the optimum efficiency. This algorithm results in non-negligible performance improvements with respect to a turbine control system where the machine aging is not taken into consideration. The proposed method is validated via numerical simulations, and its performance is assessed. The case study results show that thanks to the updated CAM, the unit can operate at a better efficiency by achieving a generation increase of 2.6% over one year of operation.

Moreover, a droop-based control framework to enhance FCR provision with a RoR HPP has been presented. The computation of the droop coefficient and the discharge management rely on the forecast of the energy required for FCR provision over a time horizon of one hour, performed by AR models. It has been shown that, by considering the information provided by such forecasts, the HPP control can provide more regulating power while ensuring the system's reliability in terms of discharge control. The discharge deviation from the set point, caused by the provision of flexibility, is controlled by computing an offset discharge once per hour which, therefore, reduces the number of movements of the regulating components of the hydroelectric unit. This constitutes an improvement for the standard control system that imposes continuous movements of guide vanes and blades to respect the discharge set-point.

Both the "CAM online estimation" and "discharge management" frameworks are solutions that can be effectively integrated into existing hydropower plant control systems developed by *Original Equipment Manufacturers* (OEMs), without necessitating significant alterations. For this reason, these tools offer benefits mainly to power plant operators. However, despite advancements in aging monitoring and movement reduction in RoR HPPs, a large portion of servomechanism activity still comes from FCR provision. This is an inherent role of hydro, without additional support. The next chapter will explore how BESS could significantly support hydropower in enhancing FCR provision while reducing the wear on its components.

4 Optimal Frequency Containment Reserve Provision of Grid-Forming Converter-Interfaced BESSs

This Chapter proposes and experimentally validates a joint control and scheduling framework conceived for grid-forming converter-interfaced BESSs providing multiple services to the electrical grid. Particular attention is given to FCR provision, along with dispatching the operation of a distribution feeder hosting heterogeneous and uncontrollable prosumers. The provision of voltage control to the local distribution grid is also considered as additional service. The framework consists of three phases. In the day-ahead scheduling phase, a robust optimization problem is solved to compute the optimal dispatch plan and frequency droop coefficient, accounting for the uncertainty of the aggregated prosumption. In the intra-day phase, a model predictive control algorithm is used to compute the power set-point for the BESS to achieve the tracking of the dispatch plan. Finally, in a real-time stage, the power set-point originated by the dispatch tracking is converted into a feasible frequency set-point for the grid-forming converter by means of a convex optimization problem accounting for the capability curve of the power converter. The proposed framework is experimentally validated by using a grid-scale 720 kVA / 560 kWh BESS connected to a 20 kV distribution feeder in the EPFL campus hosting stochastic and uncontrollable prosumption.

The chapter includes results from [P4] and [P5].

Research sub-questions:

- (d) What are the main limitations of BESSs when providing FCR?
- (e) How can we maximize the ancillary service provision of BESS assets?

4.1 Introduction

4.1.1 Motivation

In recent years, converter-interfaced BESSs are considered a mature technology for grid frequency regulation because of their large ramping rates, high round-trip efficiency, and commercial availability [14, 28, 15, 83]. BESSs interface with the grid through four-quadrant power converters [84], typically controlled to provide grid ancillary services ranging from frequency regulation up to energy management [27]. Indeed, the usage of BESSs has been investigated to provide frequency and voltage regulation services [15, 16, 17, 18, 19, 20]. In [15], a method for optimal sizing and operation of a BESS used for FCR provision in a small isolated power system is presented. [16] and [17] explore the potential use of BESSs participating in frequency regulation markets. [16] proposes an approach that allows LiFePO₄ BESSs to achieve the lowest tender price in the "Firm Frequency Regulation" market of the UK National Grid. In addition, [18] proposes to deploy BESSs to control the voltage of a radial grid characterized by high penetration of distributed generation, and [19] utilizes BESSs to track voltage set-point requested by TSOs in an optimal and coordinated manner. Finally, the work in [20] proposes a method to control a BESS, together with other flexible resources, to achieve the dispatch of a microgrid. Nevertheless, the control strategies proposed in the above studies focus on the provision of a single ancillary service, which may not fully exploit the potential of the BESS from both technical and economic standpoints.

In this respect, the development of control frameworks for BESSs providing multiple ancillary services to the power system is of high interest to fully take advantage of BESSs investments [85, 86]. The state-of-the-art has presented optimal solutions for ancillary services provision [27, 28, 29]. In particular, [27] proposes to solve an optimization problem that allocates the battery power and energy budgets to different services in order to maximize battery exploitation. Nevertheless, to the author's best knowledge, the dispatch tracking problem proposed in [27] is oversimplified and does not ensure the BESS operation is within the physical limits. On the other hand, [28] tackles the problem of dispatching the operation of a cluster of stochastic prosumers through a two-stage process. This consists of a day-ahead dispatch plan (determined by data-driven forecasting) and real-time tracking of the dispatch plan realized by adjusting the real power injections of the BESS with a suitably proposed MPC. Finally, [29] proposes a control method for BESSs to provide concurrent FCR and voltage regulation services to the local grid.

Despite the efforts, all the proposed solutions rely on the hypothesis to send active/reactive set-points to the BESS power converter, which is implicitly assumed to operate as a GFL unit, therefore ignoring the possibility of controlling it in GFR mode ¹.

Even if the majority of converter-interfaced resources are currently controlled as GFL units [87, 88, 89], future low-inertia grids are advocated to host a substantiate amount of GFR units

¹We recall the definitions of GFR and GFL converters in Section 4.2.

providing support to both frequency/voltage regulation and system stability [90, 91, 91]. Recent studies have proved GFR control strategies to outperform GFL in terms of frequency regulation performance in low-inertia power grids [92]. Furthermore, the impact of GFR converters on the dynamics of low-inertia grids has been investigated in [21]. The study quantitatively proved the positive impact of GFR units in limiting grid frequency deviations and in damping frequency oscillations in case of contingencies. Nevertheless, the existing scientific literature lacks studies assessing the performance of GFR units in supporting the frequency containment of large interconnected power grids. Moreover, to the best of the author's knowledge, GFR units have never been proven able to provide services such as feeder dispatchability. Studies on the GFR units synchronizing with AC grids are mostly limited to ancillary services provision, and their validations are based on either simulation [92, 93] or experiments where the external grid is represented by an ideal slack bus with emulated voltage [94, 95].

4.1.2 Chapter's Contribution

With respect to the existing literature discussed above, the contributions of this chapter are the following.

- Development of a control framework for GFR converter-interfaced BESS, tackling the optimal provision of multiple services, which relies on GFL control strategies [27, 28, 29]. The control framework is specifically applied for the simultaneous provision of feeder dispatchability, FCR, and voltage regulation. The aim is to maximize battery exploitation in the presence of uncertainties due to stochastic demand, distributed generation, and grid frequency.
- Experimental validation of the proposed framework by using a 560 kWh BESS interfaced with a 720 kVA GFR-controlled converter to dispatch the operation of a 20 kV distribution feeder hosting both conventional consumption and distributed PV generation.
- Performance assessment of the GFR-controlled BESS providing simultaneously dispatching tracking and FCR provision. In particular, the frequency regulation performance of the GFR-controlled BESS is evaluated and compared with respect to where the BESS converter is controlled as a GFL unit.

The section is organized as follows. Section 4.2, provides an introduction to power converter control, with particular attention to the differences between GFR and GFL. Section 4.3 proposes the general formulation of the control problem for the BESS providing multiple services simultaneously, while a description of the three-stage control framework is given in Section 4.4. Section 4.5 proposes appropriate metrics evaluating the impact of the frequency regulation provided by BESSs to bulk power grids and Section 4.6 provides the validation of the proposed framework through real-scale experiments. Finally, Section 4.7 summarizes the original con-

tributions and main outcomes of the Chapter and proposes perspectives for further research activities.

4.2 State-of-the-Art of BESSs Converters Controls

As mentioned in Section 4.1, GFR and GFL controls are the two approaches currently used to control converter-interfaced BESSs [96, 97]. This section reports the description of GFR and GFL controllers proposed by [96].

GFR units are based on a power converter that controls the magnitude and angle of the voltage at the *Point of Battery Coupling* (PBC). As a consequence, the knowledge of the fundamental frequency phasor of the grid voltage at the PBC is not strictly necessary. Fig. 4.1a presents a general structure of the GFR control [96], where the modulated voltage angle is linked with the converter active power, while the voltage magnitude is regulated by taking into account of voltage or/and reactive power reference.

GFL units are based on a power converter that controls the current injection to adjust the active and reactive power injection at the PCB. To this end, the injected current is controlled with a specific phase displacement with respect to the grid voltage at the PBC. Consequently, the fundamental frequency phasor of the grid voltage at the PBC is needed at any time to correctly calculate the converter reference currents. Fig. 4.1b shows the classical structure of the GFL control [96], where the grid voltage angle $\tilde{\theta}_g$ is estimated thanks to a *Phase Locked-Loop* (PLL) control [96], and used by the Park's transformation. The outer control loops can adjust the amplitude and angle of the current reference currents to inject the required amount of active and reactive power. Grid-supporting GFL converters can be applied to adjust active and reactive power set points under frequency or voltage deviations.

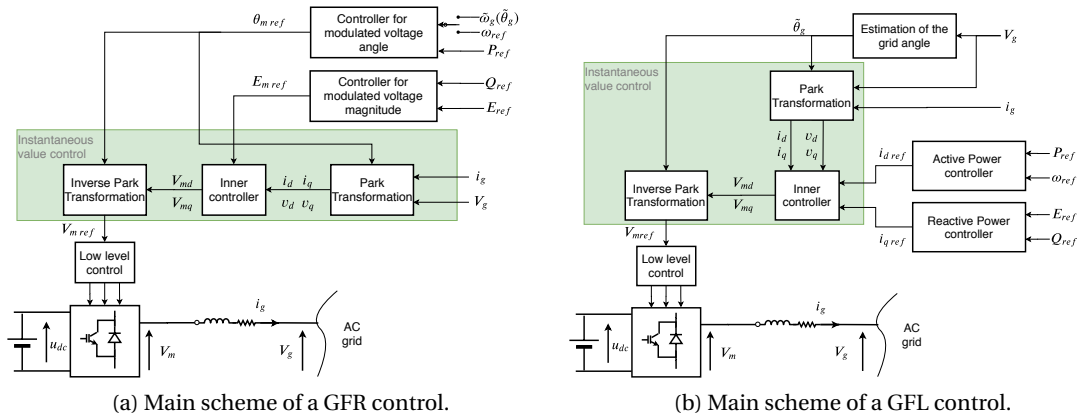


Figure 4.1: Main schemes of GFR and GFL controls.

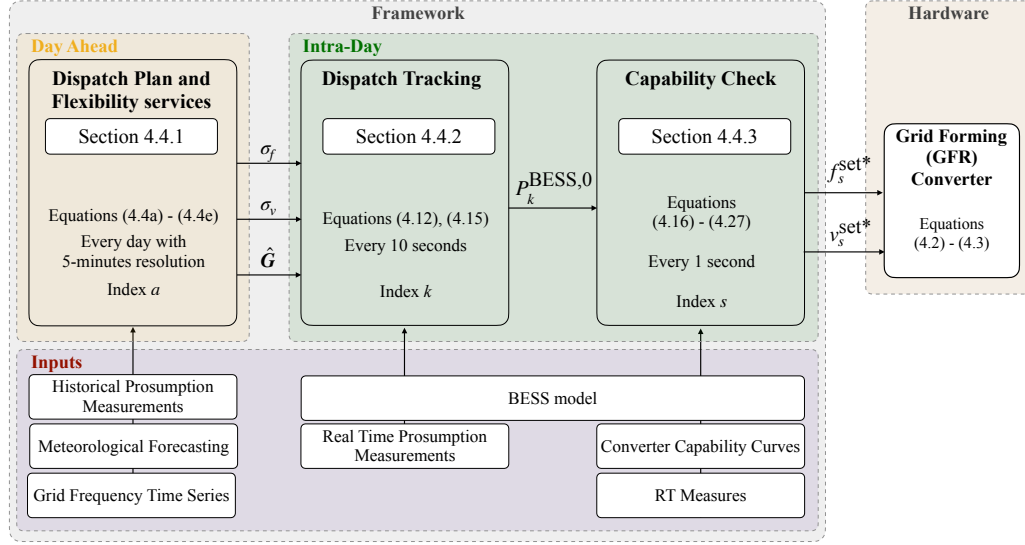


Figure 4.2: Outline of the Control Framework for Grid-forming BESSs.

4.3 Problem Statement

4.3.1 Outline of the Control Framework for Grid-forming BESSs

In this section, the dispatchability of distribution feeders and the simultaneous provision of FCR and voltage regulation are tackled by controlling a GFR converter-interfaced BESS. Specifically, the framework ensures the control of the operation of a group of prosumers (characterized by both conventional demand and PV generation that are assumed to be uncontrollable). The aim is to ensure a scheduled power trajectory at 5 minutes resolution, named dispatch plan, determined the day before operation. The day-ahead scheduler relies on a forecast of the local prosumption. The multiple-service-oriented framework consists of three stages as summarized by Fig. 4.2 where each stage is characterized by a different time horizon:

- (i) The dispatch plan is computed on the day-ahead (i.e., in agreement with most common practices), where the feeder operator (e.g. the *Distribution System Operator* (DSO)) determines a dispatch plan based on the forecast of the prosumption while accounting also for the regulation capacity of BESSs [98]. Specifically, an optimization problem is solved to allocate the battery power and energy budgets to the different services. This is done by determining a dispatch plan at a 5-minute resolution based on the forecast of the prosumption and computing the droop for the FCR provision.
- (ii) In the intermediate level stage, with a 5-minute horizon, the active power injections of the BESS are adjusted by means of a MPC, targeting both the correction of the mismatch

between presumption and dispatch plan (as proposed by [28]) and the FCR provision. The MPC is actuated every 10 seconds to both ensure correct tracking over the 5-minute window and avoid overlapping the dispatch tracking with the FCR action.

- (iii) In the final stage, computed each second, the MPC active power command is converted into a feasible frequency set-point for the GFR converter. As a matter of fact, the feasible PQ region of the BESS power converter is a function of the battery DC-link and AC-grid status [29]. To comply with the converter power capability, the feasibility of the grid-forming frequency reference set-point is ensured by solving every second an efficient optimization problem that takes into account the dynamic capability curve of the DC-AC converter and adjusts the set point accordingly. Eventually, the feasible frequency set-point is implemented in the GFR controller which intrinsically superposes the frequency control action on the active power dispatch.

4.3.2 Regulatory Framework

Since the framework is developed to enhance the provision of different ancillary services, it is necessary to consider the corresponding regulatory framework. As the experimental activities are performed at the EPFL campus, in Lausanne (Switzerland), the Chapter refers to the grid code of the Swiss TSO, SwissGrid [30, 99, 100, 101, 102]. Nevertheless, the rules for other European TSOs are mostly similar. The most important aspects are the tender periods for the ancillary services market and the technical requirements to be considered eligible to provide a specific service.

4.3.2.A Tender Period

The choice of the timing for the droop computation is related to the market regulating the provision of ancillary services. Different balancing and ancillary services markets in EU member states have different market closing times for the procurement of the ancillary services, as well as different sets of participants and activation time [103]. Therefore, the choice of the time horizon for the droop computation is market/country-dependent. By referring to [99], the calls for the tender of FCR provision of SwissGrid are every day, one day ahead with respect to the delivery date. Moreover, a platform operated daily has been established in Germany for sharing the reserves among the TSOs from Germany, France, Belgium, the Netherlands, Austria, and Switzerland [75]. These are the reasons that justify the author's choice of computing the droop with intervals of one day.

4.3.2.B Technical Requirement

The technical requirements fixed by TSOs on the insensitivity range² and activation speed [100] can be easily fulfilled by BESSs, as the requests are rather mild when compared with the BESSs' large ramping capability [14, 83]. The most constraining requirement for BESS is the necessity of ensuring continuous activation [101] for at least 15 min for a deviation of 200 mHz in the grid frequency. As formalized later, this constraint is implemented in the day-ahead section of the proposed framework in terms of limits on the values of SOE of the BESS, i.e., SOE_{\min} and SOE_{\max} .

4.3.2.C Provision of Multiple Service

According to [102], when a dispatch plan is defined with the TSO, any additional service provided must consider the dispatch plan as a basis for the evaluation of the service. That is, if dispatchability and FCR are simultaneously provided, the dispatch plan represents the basis for the evaluation of the FCR service. To comply with this request, the term ΔG_k^F , defined in Eq. (4.11) is added to Eq. (4.10).

4.4 Framework

4.4.1 Day-Ahead

The objective of the day ahead is to compute a dispatch plan \hat{G} for a distribution feeder and to simultaneously contract with the TSO a certain frequency droop for the BESS FCR provision. A representation of the feeder and the corresponding power flows is shown in Fig. 4.3. The BESS bidirectional real power flow is denoted by P^{BESS} , while G is the composite power flow as seen at the feeder's *Point of Common Coupling* (PCC). The aggregated building demand is denoted by S and, if grid losses are neglected, it is estimated as:

$$S = G - P^{\text{BESS}} \quad (4.1)$$

On top of achieving feeder dispatchability, the proposed framework allows the GFR-controlled BESS to react to the grid-frequency variation in real time, i.e., providing FCR. The latter action is automatically performed by the converter operated in GFR mode, where the power flowing through the BESS can be computed as:

$$P^{\text{BESS}} = \sigma_f \cdot (f - f^{\text{set}}) \quad (4.2)$$

$$Q^{\text{BESS}} = \sigma_v \cdot (v - v^{\text{set}}) \quad (4.3)$$

²We use the term "insensitivity range" to mean the frequency dead-band under which no FCR action is required, typically around 10 mHz in the ENTSO continental Europe synchronous area [104].

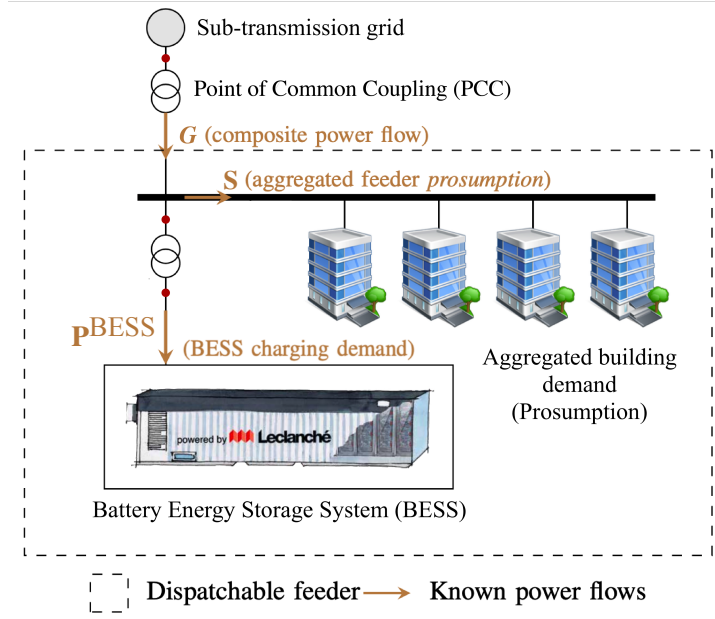


Figure 4.3: General feeder configuration used for the problem statement. The distribution feeder includes a group of buildings hosting stochastic and uncontrollable PV installations and a grid-connected BESS. The grid has a radial topology. The BESS is the sole controllable resource of the feeder. Dispatch and grid services are considered to be provided at the PCC.

In Eq. (4.2) and Eq. (4.3) σ_f and σ_v are respectively the frequency and voltage droop³ fixed at the day-ahead stage, while f^{set} and v^{set} are the frequency and voltage reference set-point (i.e., real-time command) of the GFR converter. The target of the control problem is to regulate the composite power flow G to respect the dispatch plan fixed on the day-ahead planning and the FCR action accorded with the TSO.

The formulation of the day-ahead problem considering the provision of both FCR and dispatchability proposed by [27] can be adapted to the grid-forming case. The mathematical

³While the σ_f is computed in the day-ahead problem for the FCR service, the σ_v is considered to allow for adjusting reactive power in the real-time stage (see Section 4.4.3) and is determined according to the voltage control practice recommend in [104].

formulation is hereby proposed:

$$[\sigma_f^0, \mathbf{F}^0] = \underset{\sigma_f \in \mathbb{R}^+, \mathbf{F} \in \mathbb{R}^N}{\operatorname{argmax}} (\sigma_f) \quad (4.4a)$$

subject to:

$$SOE_0 + \frac{1}{E_{\text{nom}}^{\text{BESS}}} \left[\frac{T}{N} \sum_{a=0}^A (F_a + S_a^\uparrow) + \sigma_f W_a^\uparrow \right] \leq SOE_{\text{max}}, \quad (4.4b)$$

$$SOE_0 + \frac{1}{E_{\text{nom}}^{\text{BESS}}} \left[\frac{T}{N} \sum_{a=0}^A (F_a + S_a^\downarrow) + \sigma_f W_a^\downarrow \right] \geq SOE_{\text{min}}, \quad (4.4c)$$

$$F_a + S_a^\uparrow + 0.2\sigma_f \geq P_{\text{max}}^{\text{BESS}}, \quad (4.4d)$$

$$F_a + S_a^\downarrow + 0.2\sigma_f \leq P_{\text{max}}^{\text{BESS}}, \quad (4.4e)$$

where:

- T is the total scheduling time window (i.e., $T = 86400$ seconds) discretized in A time steps ($A = 288$, i.e., the dispatch plan is divided into 5 minutes windows) and each step is denoted by the subscript a with $a = 0, \dots, A - 1$.
- $\hat{\mathbf{S}} = \hat{S}_1, \dots, \hat{S}_A$ is the forecast profile of feeder prosumption and $\mathbf{F}^0 = F_1, \dots, F_A$ is the BESS power offset profile which is computed to keep the BESS stored energy at a value capable of compensating for the difference between prosumers' forecasted and realized power [28]. The day-ahead dispatch plan $\hat{\mathbf{G}} = \hat{G}_1, \dots, \hat{G}_A$ is the sum of the above two terms, as in Eq. (4.1).
- σ_f is the FCR droop expressed in kWhHz^{-1} .
- W_a denotes the integral of frequency deviations over a period of time, and it represents the energy content of the signal given by the frequency deviation from its nominal value. The term W_a , multiplied by σ_f , gives the BESS energy throughput associated with the FCR action within the period a .
- The BESS limits in terms of SOE and power are expressed respectively with SOE_{min} , SOE_{max} , $P_{\text{min}}^{\text{BESS}}$ and $P_{\text{max}}^{\text{BESS}}$, while $E_{\text{nom}}^{\text{BESS}}$ is the nominal BESS energy.

It is worth mentioning that the optimization problem described by Eqs. (4.4a) to (4.4e) prioritizes the dispatchability of the feeder over the FCR provision on the day-ahead planning. This choice is nevertheless user-dependent, based on the economical convenience of the provided service or grid core requirements. For example, if the user stipulates a contract with the TSO for FCR provision, this service can be prioritized, and the remaining energy can be allocated for the dispatch service. Inevitably, this will not always be achieved if the prosumption stochasticity is too high⁴.

⁴Further discussion can be found in Section 4.6

Chapter 4. Optimal Frequency Containment Reserve Provision of Grid-Forming Converter-Interfaced BESSs

Interestingly, Problem (4.4) establishes a relation between the amount of available BESS capacity and the provision of the FCR service, i.e. a value of $\sigma_f \cdot W_a$. The straightforward outcome of this section is that the main limit to FCR provision for BESS is related to the limited energy capacity.

4.4.2 Intra-day

In the intra-day stage a MPC algorithm is used to target the fulfillment of the mismatch between average presumption for every 5 minutes and the combined dispatch plan and FCR action agreed upon with the TSO for the same time window. Since the MPC action is assumed to give a time-sampling of 10 seconds, the index $k = 0, 1, 2, \dots, K - 1$ is introduced to denote the rolling 10 seconds time interval, where $K = 8640$ is the number of 10-second-periods in 24 hours. The value of the presumption set-point retrieved from the dispatch plan for the current 5-minute slot is indicated by the k -index as:

$$G_k^* = \hat{G}_{\lfloor \frac{k}{30} \rfloor} \quad (4.5)$$

where $\lfloor \cdot \rfloor$ denotes the nearest lower integer of the argument, and 30 is the number of 10-second intervals in a 5-minute slot. The first and the last 10-second interval for the current 5 minutes are denoted as \underline{k} and \bar{k} , respectively:

$$\underline{k} = \lfloor \frac{k}{30} \rfloor \cdot 30 \quad (4.6)$$

$$\bar{k} = \underline{k} + 30 - 1 \quad (4.7)$$

A graphical representation of the execution timeline for the MPC problem is given in Fig. 4.4 displaying the first thirty-one 10-second intervals of the day of operation. The figure shows the BESS power set-point P_2^o , which has been computed by knowing the presumption realizations S_0 and S_1 , and the average presumption set-point to be achieved in the 5-minute interval (i.e., the first value of the dispatch plan \hat{G}_0). A similar control problem, not including the simultaneous provision of FCR by the BESS, is described in [28]. For this reason, the MPC problem proposed in [28] is modified as follows, to account for the provision of multiple services by means of a GFR converter. Considering Eq. (4.1), the average composite power flow at the PCC (presumption + BESS injection) is given by averaging the available information until k as:

$$G_k = \frac{1}{k - \underline{k}} \cdot \sum_{j=\underline{k}}^{k-1} (S_j + P_j^{\text{BESS}}) \quad (4.8)$$

Then, it is possible to compute the expected average composite flow at the PCC at the end of the 5 minutes window as:

$$G_k^+ = \frac{1}{30} \left((k - \underline{k}) \cdot G_k + \sum_{j=\underline{k}}^{\bar{k}} \hat{S}_{j|k} \right) \quad (4.9)$$

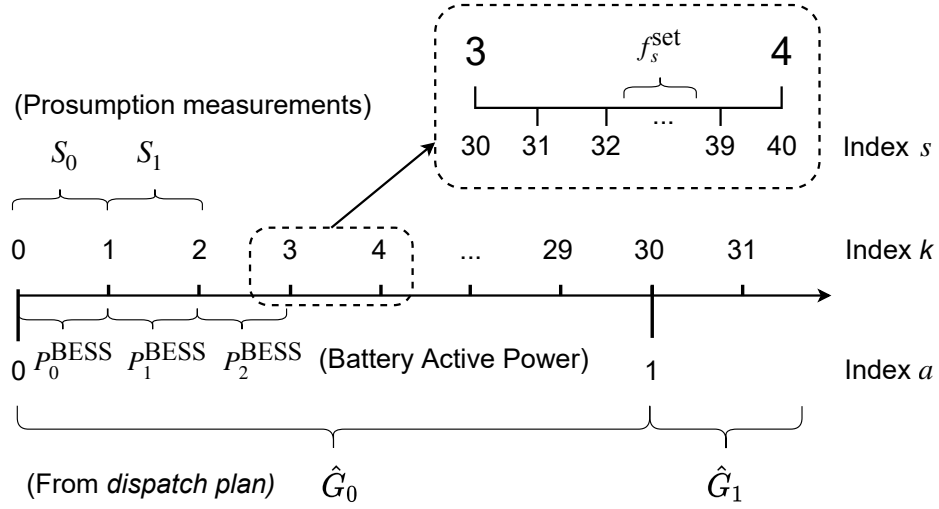


Figure 4.4: Timeline of the control framework. The dispatch plan and the allocation of ancillary services are computed on the day ahead. The dispatch plan \hat{G} has a time resolution of 5 minutes (discrete time index n). During the day, the MPC problem is executed every 10 seconds (discrete time index k). Finally, the real time problem computes the final $f^{\text{set}}, v^{\text{set}}$ set-points every second s .

where a persistent⁵ forecast is used to model future realizations, namely $\hat{S}_{j|k} = S_{k-1}, j = k, \dots, \bar{k}$. The energy error between the realization and the target (i.e. dispatch plan plus FCR energy) in the 5-minute slot is expressed (in kWh) as:

$$e_k = \frac{300}{3600} \cdot (G_k^* - G_k^+ + \Delta G_k^F) \quad (4.10)$$

where 300 s and 3600 s are the number of seconds in a 5 min and 1 h intervals, respectively. The additional term ΔG_k^F considers the deviation caused by the FCR response of the GFR converter:

$$\Delta G_k^F = \frac{1}{30} \sum_{j=k}^{k-1} (50 - f_j) \cdot \sigma_f \quad (4.11)$$

where f_j is the frequency measurement at time j . Finally, the MPC can be formulated to minimize the error e_k over the 5-minute window, subject to a set of physical constraints such as BESS SOE, DC voltage and current operational limit. It should be noted that including the term ΔG_k^F in the energy error function fed to the MPC allows for decoupling the dispatch plan tracking with the FCR response provided by the BESS in each 5-minute slot. In particular, the omission of this term while operating the BESS in GFR mode can create conflicts between dispatch plan tracking and FCR provision. As in [28], in order to achieve a convex formulation of the optimization problem, the proposed MPC problem targets the maximization of the sum of the equally weighted BESS DC-side current values over the shrinking horizon from k to \bar{k} in

⁵As shown in [105], the persistent predictor performs well, given the short MPC horizon time.

Chapter 4. Optimal Frequency Containment Reserve Provision of Grid-Forming Converter-Interfaced BESSs

its objective (4.12a) while constraining the total energy throughput to be smaller or equal to the target energy e_k . The optimization problem is formulated as:

$$\mathbf{i}_{\bar{k}|k}^o = \arg \max_{\mathbf{i} \in \mathbb{R}^{(k-\bar{k}+1)}} (\mathbf{1}^T \mathbf{i}_{\bar{k}|k}) \quad (4.12a)$$

subject to:

$$\alpha \mathbf{v}_{\bar{k}|k}^T \mathbf{i}_{\bar{k}|k} \leq e_k \quad (4.12b)$$

$$\mathbf{1} \cdot \mathbf{i}_{\min} \leq \mathbf{i}_{\bar{k}|k} \leq \mathbf{1} \cdot \mathbf{i}_{\max} \quad (4.12c)$$

$$\mathbf{1} \cdot \Delta \mathbf{i}_{\min} \leq \mathcal{H} \mathbf{i}_{\bar{k}|k} \leq \mathbf{1} \cdot \Delta \mathbf{i}_{\max} \quad (4.12d)$$

$$\mathbf{v}_{\bar{k}|k} = \phi_v x_k + \psi_i^v \mathbf{i}_{\bar{k}|k} + \psi_1^v \mathbf{1} \quad (4.12e)$$

$$\mathbf{1} \cdot \mathbf{v}_{\min} \leq \mathbf{v}_{\bar{k}|k} \leq \mathbf{1} \cdot \mathbf{v}_{\max} \quad (4.12f)$$

$$\mathbf{SOE}_{\bar{k}|k} = \phi^{\text{SOE}} \mathbf{SOE}_k + \psi_i^{\text{SOE}} \mathbf{i}_{\bar{k}|k} \quad (4.12g)$$

$$\mathbf{1} \cdot \mathbf{SOE}_{\min} \leq \mathbf{SOE}_{\bar{k}|k} \leq \mathbf{1} \cdot \mathbf{SOE}_{\max} \quad (4.12h)$$

where:

- $\mathbf{i}_{\bar{k}|k}^o$ is the computed control action trajectory, $\mathbf{1}$ denotes the all-ones column vector, the symbol \leq is the component-wise inequality, and the bold notation denotes the sequences obtained by stacking in column vectors the realizations in time of the referenced variables, e.g. $\mathbf{v}_{\bar{k}|k} = [v_k, \dots, v_{\bar{k}}]^T$.
- In (4.12b), the BESS energy throughput (in kWh) on the AC bus is modeled as $E_{\bar{k}|k}(\cdot) = \alpha \mathbf{v}_{\bar{k}|k}^T \mathbf{i}_{\bar{k}|k}$, where $\mathbf{v}_{\bar{k}|k}$ and $\mathbf{i}_{\bar{k}|k}$ are the battery DC voltage and current, respectively, and $\alpha = 10/3600$ is a converting factor from average power over 10 seconds to energy expressed in kWh.
- The inequality (4.12c) and (4.12d) are the constraints on the magnitude and rate of change for the BESS current, respectively. The matrix $\mathcal{H} \in \mathbb{R}^{(k-\bar{k}+1) \times (k-\bar{k}+1)}$ is

$$\mathcal{H} = \begin{bmatrix} 1 & -1 & 0 & 0 & \dots & 0 \\ 0 & 1 & -1 & 0 & \dots & 0 \\ \vdots & \vdots & \vdots & \vdots & \vdots & \vdots \\ 0 & 0 & 0 & \dots & 1 & -1 \end{bmatrix} \quad (4.13)$$

- The equality (4.12e) is the *Three-Time-Constant (TTC)* electrical equivalent circuit model of the voltage on DC bus, whose dynamic evolution can be expressed as a linear function of battery current by applying the transition matrices $\phi^v, \psi_i^v, \psi_1^v$. x_k is the state vector

of the voltage model ⁶. The inequality (4.12f) defines the BESS voltage limits. The TTC model for computing the DC voltage and the estimation of x_k are described in [28].

- The equality (4.12g) is the evolution of the BESS SOE as linear function of the variable $i_{k|k}^o$, where ϕ^{SOE} and ψ_i^{SOE} are transient matrices obtained from the BESS SOE model:

$$SOE_{k+1} = SOE_k + \frac{10}{3600} \frac{i_k}{C_{\text{nom}}} \quad (4.14)$$

where C_{nom} is BESS capacity in Ah. The discretized state-space matrix for the SOE model can be easily obtained from (4.14) with $A_s = 1$, $B_s = 10/3600/C_{\text{nom}}$, $C_s = 1$, $D_s = 0$. Finally, (4.12h) enforces the limits on BESS SOE.

The optimization problem is solved at each time step k obtaining the control trajectory for the whole residual horizon from the index k to \bar{k} , i.e., $i_{\bar{k}|k}$. However, only the first component of the current control trajectory is considered for actuation, i.e., $i_{k|k}^o$. Finally, $i_{k|k}^o$ is transformed into a power set-point P_k^0 , computed as:

$$P_k^{\text{BESS},0} = v_k \cdot i_k^o \quad (4.15)$$

Since the control decision is re-evaluated every 10 seconds, errors in the voltage predictions and short-term consumption forecast that arise in the current actuation period are absorbed in the next cycle, where updated measurements are used.

4.4.3 Real Time

The real-time control stage is the final stage of the framework, whose output f_{set} , v_{set} is the input for the GFR BESS converter. Thanks to the day-ahead problem, sufficient BESS energy capacity is guaranteed in the MPC tracking problem. To ensure the BESS operation to be within the power limits, a static physical constraint of control actions is considered in the day-ahead stage in (4.4d) and (4.4e) and during the dispatch tracking in (4.12c) and (4.12d). Nevertheless, these constraints do not account for the dependency of the converter feasible PQ region on DC voltage and AC grid voltage conditions since they are only known in real time. In this respect, the real-time controller is implemented to both keep the converter operating in the PQ feasible region identified by the capability curve and to convert the power set-point from the MPC problem into a frequency reference set-point to feed the GFR converter. An example is provided in Fig. 4.5, where the capability curves of the converter used for the experimental validation of the framework are displayed.

⁶This modeling choice is taken according to [28], where a more accurate model, compared with the commonly adopted two-time constant model in the literature [106], is implemented. The TTC model allows for better capturing dynamics of BESSs, in case the future development of the framework will require the MPC problem to be solved with smaller time steps. Nevertheless, to compute the BESS predictions with a 10-second time horizon, lower-order models could be used.

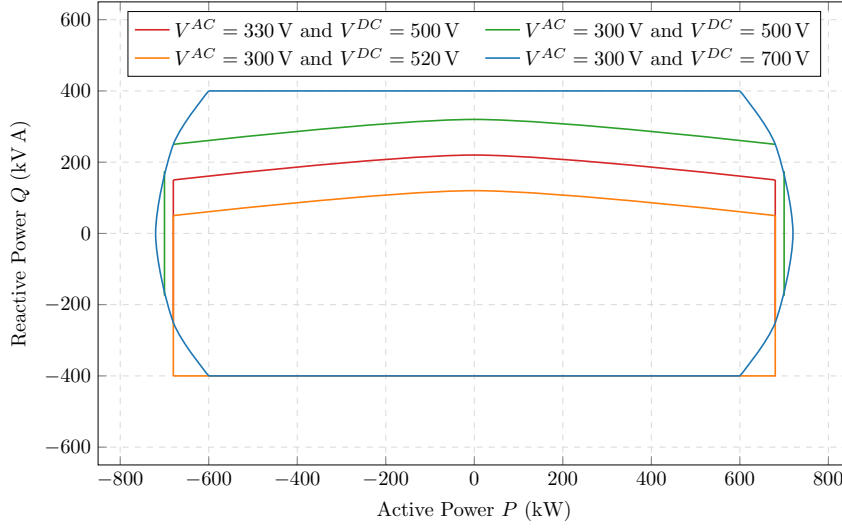


Figure 4.5: Capability curves of the converter used for the experimental validation.

4.4.3.A Capability Curve

As proved in [29], the converter PQ capability curve h can be modeled as a function of the BESS DC voltage v_s^{DC} and the module of the direct sequence component of the phase-to-phase BESS AC side voltages v_s^{AC} at time s :

$$\xi(P_s^{\text{BESS}}, Q_s^{\text{BESS}}, v_s^{DC}, v_s^{AC}, SOE_s) \leq 0 \quad (4.16)$$

where the BESS SOE is considered for the selection of the capability curve because the estimation of v_s^{DC} relies on the battery TTC model whose parameters are SOE-dependent [29]. In particular, the v_s^{DC} is estimated using the TTC model of DC voltage, thus, the same formula as (4.12e):

$$v_s^{DC} = \phi_v x_s + \psi_i^v i_s^{DC} + \psi_1^v \mathbf{1} \quad (4.17)$$

Equation (4.17) is solved together with the charging or discharging DC-current equation as follows:

$$i_s^{DC} \approx \frac{P_s^{DC}}{v_s^{DC}} \quad (4.18)$$

where the active power at the DC bus is related to the active power set-point AC side of the converter as shown by Eq. (4.19).

$$P_s^{DC} = \begin{cases} P_s^{\text{BESS, set}} \cdot \eta_{\text{ch}}, & \forall P_s^{\text{BESS, set}} \geq 0 \\ P_s^{\text{BESS, set}} / \eta_{\text{dch}}, & \forall P_s^{\text{BESS, set}} < 0 \end{cases} \quad (4.19)$$

$P_s^{\text{BESS, set}}$ is the set-point from the MPC, computed in (4.15) and expressed as:

$$P_s^{\text{BESS, set}} = P_s^{\text{BESS,0}} \quad (4.20)$$

Once the DC voltage v_s^{DC} is known, the magnitude of the direct sequence component v_s^{AC} of the phase-to-phase voltage at the AC side of the converter is estimated via the Thévenin equivalent circuit of the AC grid, expressed as

$$v_s^{AC} \approx \sqrt{(v_s^{AC,m})^2 + X_T^2 \frac{(P_s^{\text{BESS, set}})^2 + (Q_s^{\text{BESS, set}})^2}{3(v_s^{AC,m})^2}} \quad (4.21)$$

where the secondary side voltage $v_s^{AC,m}$ is obtained by dividing the primary side voltage by the transformer ratio, and X_T is the reactance of the step-up transformer, as shown in Fig. 4.3. Equations (4.16) to (4.21) represent the relation between active and reactive power set-points with the converter capability curve.

4.4.3.B Set-Point Conversion for GFR Converters

Together with a feasibility check for the power set-point $P_s^{\text{BESS, set}}$, the real-time controller is responsible for converting the power set-point into a frequency reference set-point to feed the GFR converter. In particular, the power output of a GFR converter can be expressed, starting from Eq. (4.22), as:

$$P^{\text{BESS}} = \sigma_f \cdot (f - f_{\text{nom}}) + \sigma_f \cdot (f_{\text{nom}} - f_s^{\text{set}}) = P^{\text{BESS, fcr}} + P_s^{\text{BESS, set}} \quad (4.22)$$

where f_{nom} is the nominal frequency, the term $P_s^{\text{BESS, fcr}}$ corresponds to the power delivered with respect to the FCR action, f is the grid frequency⁷. As visible from Equation (4.22), the relation between the power set-point P_{set} of the GFR converter and the input f_{set} is linear:

$$P_s^{\text{BESS, set}} = \sigma_f \cdot (f_{\text{nom}} - f_s^{\text{set}}) \quad (4.23)$$

Similarly, for the reactive power:

$$Q_s^{\text{BESS, set}} = \sigma_v \cdot (v_{\text{nom}} - v_s^{\text{set}}) \quad (4.24)$$

where v_{nom} is the nominal voltage. Equations (4.23) to (4.24) represent the relation between active/reactive power and frequency/voltage set-point fed to a GFR converter.

⁷It should be noted that the frequency control action $P_s^{\text{BESS, fcr}}$ and the grid frequency f are not denoted with subscript s because they are not controlled variables in the optimization problem. Instead, f depends on the interconnected power grid, and $P_s^{\text{BESS, fcr}}$ is the automatic response of GFR control with response time in the order of tens of milliseconds.

4.4.3.C Real-Time Problem Formulation

Finally, given a set-point in power $P_s^{\text{BESS, set}}, Q_s^{\text{BESS, set}}$ ⁸ coming from the MPC problem, the GFR converter optimal references are computed by solving the following optimization problem:

$$\begin{aligned} [f_s^{\text{set*}}, v_s^{\text{set*}}] = \\ = \arg \min \omega_P (P_s^{\text{BESS, set*}} - P_s^{\text{BESS, set}})^2 + \omega_Q (Q_s^{\text{BESS, set*}} - Q_s^{\text{BESS, set}})^2 \end{aligned} \quad (4.25)$$

subject to (4.16) - (4.24). Equations (4.16) - (4.21) represent the relation between active/reactive power with the converter capability curve and (4.23), (4.24) represent the relation between active/reactive power with frequency/voltage set-point fed to the GFR controller. To convexify the problem in (4.25) subject to (4.16) - (4.21) we proceed as proposed in [29]. This is possible because constraints (4.23) - (4.24) are linear, since σ_f and σ_v are fixed. The optimization problem is defined to find the optimal active and reactive power set-point compatible with the capability curve of the converter. In particular, if the original set-points are feasible, the optimization problem returns the obvious solution $P_s^{\text{BESS, set*}} = P_s^{\text{BESS, set}}$ and the converter reference points are:

$$f_s^{\text{set*}} = f_{\text{nom}} - \frac{P_s^{\text{BESS, set*}}}{\sigma_f} = f_{\text{nom}} - \frac{P_s^{\text{BESS, set}}}{\sigma_f} \quad (4.26)$$

$$v_s^{\text{set*}} = v_{\text{nom}} - \frac{Q_s^{\text{BESS, set*}}}{\sigma_v} = v_{\text{nom}} - \frac{Q_s^{\text{BESS, set}}}{\sigma_v} \quad (4.27)$$

4.5 Local Effects of Grid-Forming Converters Providing Frequency Regulation to Bulk Power Grids

4.5.1 State-of-the-Art Metrics

To evaluate the impact of the frequency regulation provided by BESSs to low-inertia grids, [92] proposes the hereby listed metrics:

- PDF of the frequency, where the standard deviation of the grid-frequency statistical distribution is observed to assess the capability of the control strategy in limiting the frequency deviations from the nominal value.
- *Integral Frequency Deviation* (IFD):

$$\text{IFD} = \sum_{\text{mu}=1}^{\text{NoM}} \sum_s^{\text{NoS}} |f_{\text{mu},s} - f_{\text{nom}}| \quad (4.28)$$

where NoM is the number of measurement units, NoS is the total sampling number of frequency measurements available in the area where the FCR is delivered, and $f_{\text{mu},s}$ is

⁸In order to prioritize the active power, the reactive power set-point $Q_s^{\text{BESS, set}}$ can be set as zero.

the frequency measured by the measurement unit "mu" at sample s .

Both frequency PDF and IFD establish a relation between grid-frequency measurements and control actions of the converter-interfaced BESS. Nevertheless, it is not possible to measure the influence of a small frequency control provider on the bulk power grid, as the frequency can be considered independent from the single action of a small power converter. Therefore, the frequency PDF and IFD cannot be considered as reliable metrics.

4.5.2 New Metric

To characterize the local effect of a converter-interfaced BESS providing frequency regulation and to identify the difference between the GFR and GRL controls, we proposed a new metric based on *Phasor Measurement Units* (PMUs) measurements performed locally, i.e., on the distribution feeder where the BESS is installed. The frequency measurements at the PCC of the distribution feeder, as well as the phase angle differences between the voltage controlled by the converter unit and the PCC voltage are taken into consideration to derive the following metric:

- *Relative Rate-of-Change-of-Frequency* (rRoCoF):

$$\text{rRoCoF} = \left| \frac{\Delta f^{\text{PCC}} / \Delta t}{\Delta P^{\text{BESS}}} \right| \quad (4.29)$$

where Δf^{PCC} is the difference between one grid frequency sample and the next (once-differentiated value) at the bus where the BESS is connected to, ΔP is the once-differentiated BESS active power, and Δt is the sampling interval.

The rRoCoF metric measures the RoCoF regulation at PCC. Since the RoCoF is weighted by the delivered active power of the BESS, it can be used to compare the local performance of GFR versus GFL converter in large interconnected electrical systems.

4.6 Experimental Validation

4.6.1 Experimental Setup

For the experimental campaign, a 20 kV distribution feeder in the EPFL campus equipped with a BESS is considered, as shown in Fig. 4.3. The distribution feeder includes a group of buildings characterized by a 140 kW base load, hosting a 105 kW rooftop PV installation and a grid-connected 720 kVA/560 kWh Lithium-Titanate BESS. The BESS is interfaced with the grid through a three-phase, two-level converter with IGBT/Diodes pairs and characterized by:

- (i) a rated Power of 720 kVA.

Chapter 4. Optimal Frequency Containment Reserve Provision of Grid-Forming Converter-Interfaced BESSs

- (ii) a nominal AC voltage of 300 V.
- (iii) *Total Harmonic Distortion* (THD) max, 3%.
- (iv) a DC voltage ranging from 500 V to 980 V.
- (v) a rated DC Current of 1360 A.
- (vi) and a round-trip efficiency $\geq 97\%$.

The targeted grid has a radial topology and is characterized by co-axial cable lines with a cross-section of 95 mm^2 and a length of a few hundred meters, therefore, the grid losses are negligible [107]. The measuring system is composed of a PMU-based distributed sensing infrastructure. The measuring infrastructure allows for acquiring in real-time accurate information of the power flows G , S and P^{BESS} , thanks to the PMUs' fast reporting rate (i.e., 50 frames per second) and high accuracy which in terms of 1 standard deviation is equal to 0.001 degrees (i.e. $18 \mu\text{rad}$) [108].

4.6.2 Experimental Results

This subsection reports the results of a day-long experiment, taking place on the EPFL campus on a working day (Friday, i.e., day-category C according to Appendix C).

4.6.2.A Day Ahead

The input and output information of the day-ahead dispatch process for the experimental day is shown in Fig. 4.6. The generated scenarios \mathbf{S} for the prosumption are shown in Fig. 4.6a, where \mathbf{S}^{\downarrow} and \mathbf{S}^{\uparrow} are the lower and upper bounds shown in thick black lines, while all the scenarios are represented by thin colored lines. The upper and lower bound of the PV forecast, expressed in terms of PV production in kW, are shown in Fig. 4.6b, while the net demand scenarios at the PCC, obtained according to Eqs. (C.2) and (C.3), are shown in Fig. 4.6c. The upper and lower bound of the prosumption, namely S_n^{\uparrow} and S_n^{\downarrow} , are input to the dispatch plan. Finally, Fig. (4.6d) and (4.6e) show respectively the power and energy budget allocated for the forecasting uncertainty of the stochastic PV production (in dark gray) and demand (in light gray). The remaining energy budget is allocated for the FCR service, resulting in a droop $\sigma_f = 116 \text{ kWhz}^{-1}$.

4.6.2.B Dispatch Tracking

The results of the dispatch tracking are visible in Fig. 4.7. In particular, Fig. 4.7a shows the power at the PCC (in shaded gray), the prosumption (in dashed red), and the dispatch plan (in black). It is observed that the dispatch plan is tracked by the GFR-converter-interfaced BESS when the grid frequency (visible in Fig. 4.7b) is close to 50 Hz. Nonetheless, when the grid

frequency has a significant deviation from 50 Hz, the GFR converter provides a non-negligible amount of power ΔG^F to the feeder. This contribution is visible in shaded blue in Fig. 4.7a, and causes a deviation of the average PCC power from the dispatch plan, as targeted by Eq. (4.9). Moreover, as visible in Fig. 4.7c the BESS SOE is contained within its physical limits over the day. To evaluate the dispatch plan-tracking performance, RMSE, *Mean Error* (ME), and

	ME	MAE	RMSE
No Dispatch Tracking	-3.49	47.00	18.26
Dispatch Tracking	0.11	16.93	3.00
Dispatch + FCR Tracking	-0.45	0.79	1.43

Table 4.1: Tracking Error Statistics (in kW).

Maximum Absolute Error (MAE) are considered. In particular, these indicators are visible in Section 4.6.2.B for three different cases: (i) no dispatch tracking case, where the error is computed as the difference between prosumption and dispatch plan; (ii) dispatch tracking case, where the error is computed as the difference between flow at the PCC and dispatch plan; (iii) dispatch tracking + FCR case, where the error is computed as the difference between flow at the PCC and dispatch plan + FCR contribution, as targeted by the MPC problem (4.12a). The obtained results demonstrate the good performance of the dispatch + FCR tracking framework. The overall results are comparable with the one presented in [28], even though the tracking problem in this study is complicated by the fact that the BESS is operated with a grid-forming converter providing frequency regulation.

4.6.2.C Frequency Regulation

To assess the performance of the GFR converter in regulating the frequency at the PCC, we adopt the metric rRoCoF proposed in Section 4.5.

The rRoCoF is computed from different frequency time series, corresponding to the following four cases.

- *Case 1:* rRoCoF computed considering the 24 hour-long experiment where GFR-controlled BESS is providing multiple services.
- *Case 2:* rRoCoF computed considering a 15-minute window around a significant frequency transient (i.e., around 00:00 CET) during the same day-long experiment.
- *Case 3:* rRoCoF computed with a dedicated 15-minute experiment where GFR-controlled BESS is only providing FCR with its highest possible frequency-droop (1440 kWhz^{-1}) during a significant grid-frequency transient.
- *Case 4:* rRoCoF computed with a dedicated 15-minute experiment where GFL-controlled

Chapter 4. Optimal Frequency Containment Reserve Provision of Grid-Forming Converter-Interfaced BESSs

BESS is only providing FCR with its highest possible frequency-droop (1440 kWhz^{-1}) during a significant grid-frequency transient.

While *Case 1* and *Case 2* rely on the measurements obtained from the experiment carried out in this study, *Case 3* and *Case 4* leverage an historical frequency data set, also used in the experimental validation proposed in [P5]. It should be noted that the same experimental setup described in Section 4.6.1 is utilized in [P5]. The measurements at hour transition are considered in order to evaluate GFR/GFL units' frequency regulation performance under relatively large frequency variations.

Fig. 4.8 shows the CDF of the rRoCoF values for the four cases. First, it is observed that the CDF results of *Case 1* and *Case 2* are very close. This illustrates the robustness of the metric rRoCoF. In particular, since rRoCoF is normalized by the BESS power injection, the frequency dynamics and the frequency droop of the BESS controller have little effect on the result of CDF. Moreover, the comparison between *Case 2* and *Case 3* shows negligible differences in the rRoCoF CDF, proving that the provision of dispatchability service by the GFR converter does not drastically affect its frequency regulation performance. Finally, the comparison between GFR and GFL-controlled BESS (i.e., *Case 2* vs *Case 4*) is reported from [P5], to show that the GFR unit achieves significantly lower rRoCoF for per watt of regulating power injected by the BESS.

4.7 Discussion

A comprehensive framework for the simultaneous provision of multiple services (i.e., feeder dispatchability, frequency, and voltage regulation) to the grid by means of a GFR-converter-interfaced BESS has been proposed. The framework consists of three stages. The day-ahead stage determines an optimal dispatch plan and a maximum frequency droop coefficient by solving a robust optimization problem that accounts for the uncertainty of the prosumption forecast. In the intra-day stage, a MPC method is used in the operation process to achieve the tracking of the dispatch plan while allowing for FCR properly delivered by the BESS. Finally, the real-time controller is implemented to convert the power set-points from MPC into frequency references accounting for the capability curve of the converter.

An experimental campaign was conducted on a 20 kV distribution feeder at the EPFL campus. This feeder services a cluster of buildings with a 140 kW base load and features a 105 kW peak rooftop PV installation, along with a grid-connected 720 kVA / 500 kWh Lithium Titanate BESS. Over a 24-hour experiment, the BESS showcased efficient dispatch tracking, mirroring the findings in [28] related to GFL converter-interfaced BESS dispatchability. Moreover, the rRoCoF metric has been used to show that the provision of dispatchability service by the GFR converter does not affect its frequency regulation performance. Experimental results resonated with the simulations from the IEEE 39-bus emulated grid discussed in [92] and confirmed the positive effects of GFR converters with respect to the GFL one, resulting in a

"stillier" grid frequency.

Overall, BESSs demonstrate their ability to supply FCR support, especially if interfaced with GFR converters, while concurrently providing various grid services. Nevertheless, a notable operative constraint is given by the BESS power and energy budgets, which limit the extent of FCR provision. The next chapters discuss how in a hybrid (BESS + HPP) system hydropower can mitigate the capacity limit and allow BESSs to continuously provide ancillary services.

Chapter 4. Optimal Frequency Containment Reserve Provision of Grid-Forming Converter-Interfaced BESSs

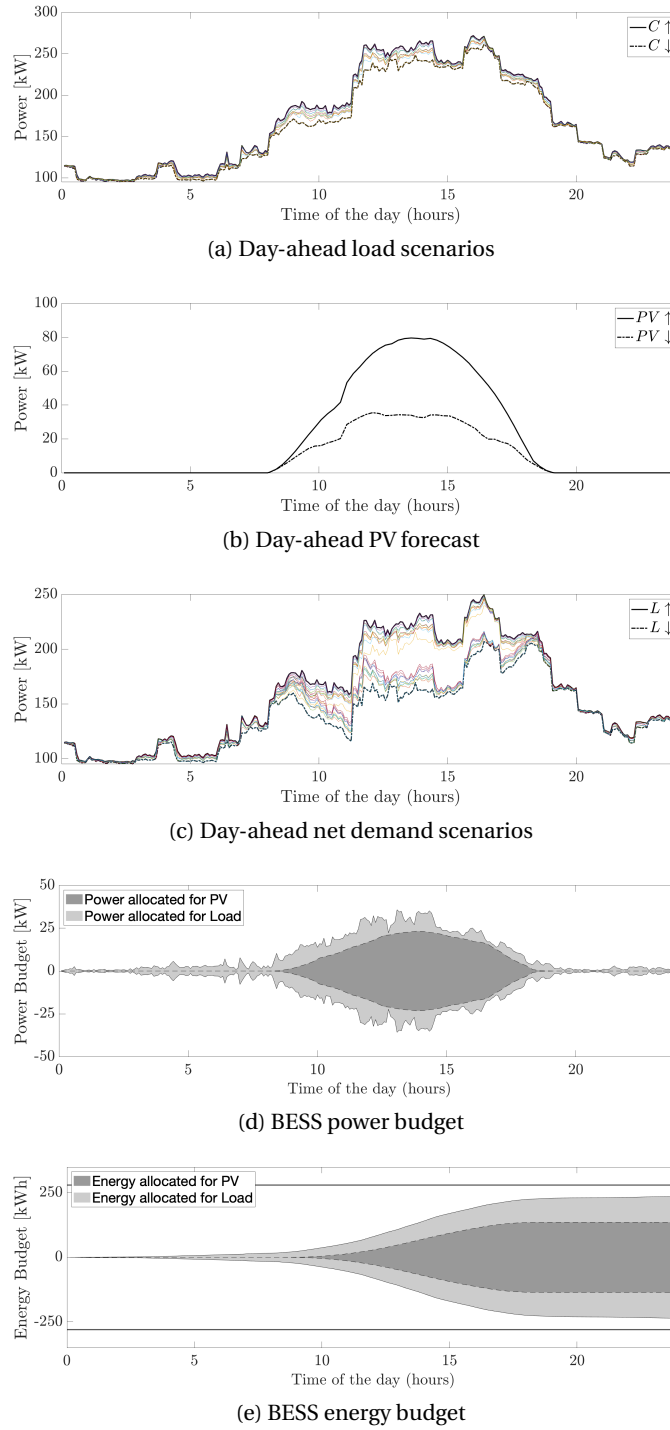
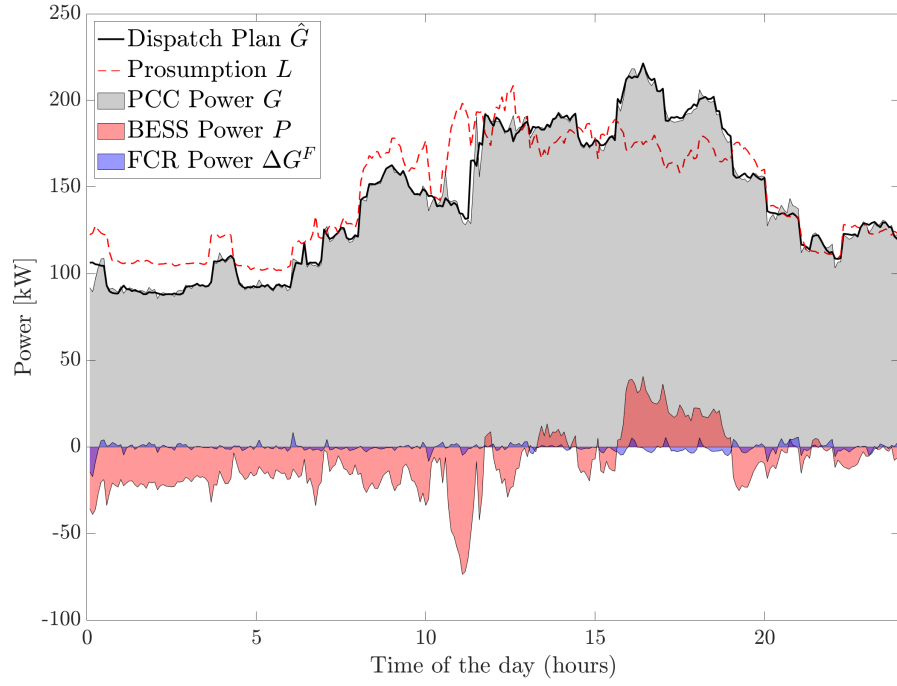
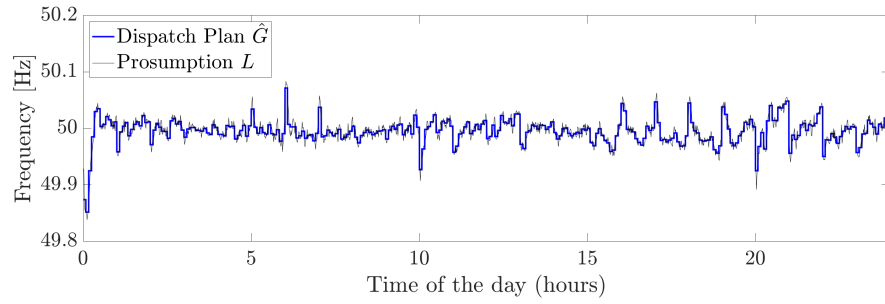


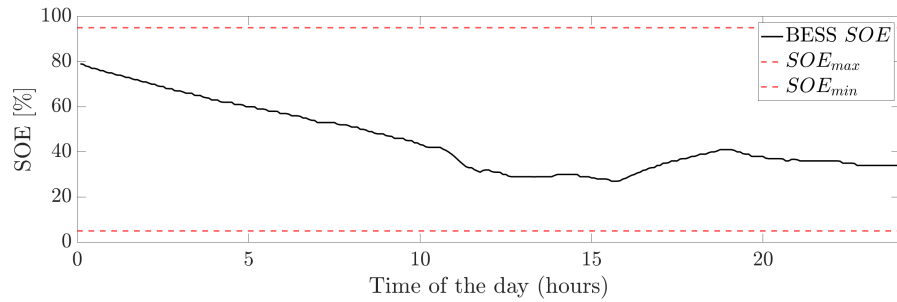
Figure 4.6: Input of the day-ahead problem. (a) shows 10 demand-generated scenarios, and their relative upper and lower bound. (b) shows the upper and lower bound for the PV production. (c) combines load and PV to show the prosumption scenario, input of the day ahead problem. Output of the day-ahead problem. (d) and (e) show the power and energy budget, respectively, allocated to perform the different services.



(a) Day-ahead load scenarios



(b) Day-ahead PV forecast



(c) Day-ahead net demand scenarios

Figure 4.7: Experimental results for the 24-hour test. (a) compares the dispatch plan (in black) with the measured power at the PCC (shaded gray), the prosumption of the feeder (in dashed red), the BESS power flow (in shaded red), and the average power required for each 5-minute window for the provision of FCR service by the BESS. (b) shows the grid frequency and its 5-minute mean. The SOE of the battery during the test is visible in (c).

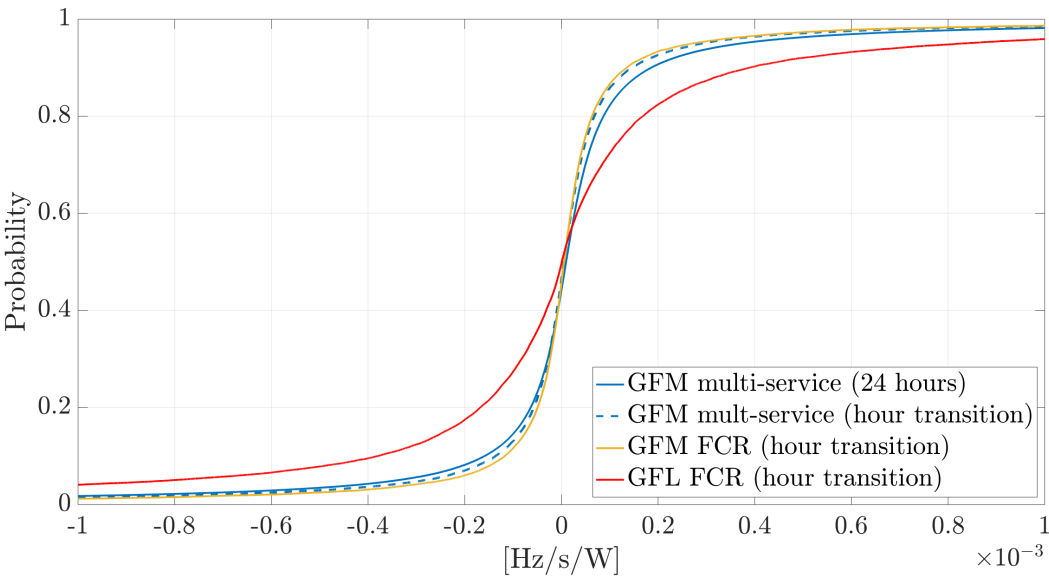


Figure 4.8: CDF of rRoCoF.

Technology Integration in HPP for

Enhanced FCR Provision

Part III

Preface

The significance of FCR in Europe's electricity grid cannot be overstated. As discussed in Part II, while HPPs are fundamental assets for FCR provision, they suffer from FCR-related wear, increasing maintenance needs. Conversely, BESSs offer quick response-time but are limited by their energy and power capacity.

In Part III, we explore HPP and BESS integration, introducing an optimal control framework for hybrid systems integrating both technologies. Additionally, we compare this approach with the integration of full-size frequency converters enabling the variable speed operation of Kaplan turbines retrofitted as propellers.

Chapter 5 details the control strategies for both technologies. To validate both control strategies, we adapt a reduced-scale turbine testing platform to allow for dynamic testing. To validate both control strategies, Chapter 6 outlines the design of experiments, i.e., the adaptation of an existing reduced-scale turbine testing platform to allow for dynamic testing. The experimental validation and framework performance are discussed in Chapter 7.

5 Control Strategies for Enhanced Frequency Containment Reserve Provision of Run-of-River Power Plants

This chapter presents the control strategies developed to address the wear and tear of RoR HPPs providing enhanced FCR. Firstly, the study proposes the integration of a BESS with RoR HPPs controlled by a double-layer MPC. The upper layer MPC acts as a state of energy manager for the BESS, employing a forecast of the required regulating energy for the next hour. The lower-layer MPC optimally allocates the power set-point between the turbine and the BESS. As an alternative approach, the chapter explores the practical viability of re-purposing aging Kaplan turbines into variable-speed propellers by employing full-size frequency converters. The motivation behind the latter approach is to improve the provision of FCR without operating the blade servomechanism. In this configuration, the control strategy aims to maximize the efficiency of the overall system by controlling guide vanes and the rotational speed of the propeller turbine only. Validation and the results of this framework will be presented and discussed in Chapters 6 and 7.

The chapter includes results from [P6, P7].

Research sub-questions:

- (f) *What are the optimal strategies for integrating RoR HPPs with BESSs to improve FCR provision and extend asset lifetimes?*
- (g) *What alternative approaches, besides BESS hybridization, could effectively enhance FCR provision of RoR HPPs?*

5.1 Introduction

BESS hybridization of RoR providing FCR has been gathering an increasing interest in the literature [22, 23, 24, 25, 109, 110]. In particular, [22] presents a discretized open-loop model for analyzing the combined operation of BESS and hydropower units in the FCR market, focusing on system responsiveness and wear and tear assessment. [109] includes an assessment of the economic benefits of reduced maintenance and deferred investment. However, both [22] and [109] are only simulation-based and suggest simple control techniques based on high-low pass filter or dead-band control. Experimental validation is provided in [24], but the control is also based on high-low pass filtering. [23] and [110] focus on the benefit of hybridization by providing an in-depth analysis of wear and tear reduction, but do not focus on the control strategy. Finally, [25] presents a model-based control algorithm to hybridize medium-head HPPs to reduce penstock fatigue. Despite the quality of the latter contribution, it does not focus on RoR HPPs, nor on the provision of FCR.

Overall, many of the existing contributions suggest simple control techniques based on dead-band control or fuzzy logic and are mostly simulation-based, underlying a need for model-aware control and experimental validation. To address these challenges, the first part of this chapter proposes an optimal control technique for hybrid RoR HPPs operating under a daily dispatch plan that provides FCR with a fixed droop characteristic. In particular, we present a double-layer MPC to drive the hybrid system. The upper layer MPC (slower and farsighted) ensures the continuous operation of the BESS, by acting as SOE manager, leveraging a forecast of the regulating energy necessary to provide the FCR service in the following hour. The lower layer (faster and short-sighted) is responsible for splitting the requested power set-point between the turbine and the BESS, ensuring the feasible operation of both systems. The developed framework is an attempt to answer to the research sub-question:

What are the optimal strategies for integrating RoR HPPs with BESSs to improve FCR provision and extend asset lifetimes?

The hybridization of HPPs with BESSs is not only being discussed in the literature but also applied in full-scale HPPs [24, 111]. In Europe, noteworthy examples of BESS hybridization include a 8 MW/10 MWh BESS in Austria [111], paired with a 8 MW turbine, and a 650 kW/350 kW BESS integrated with a 35 MW Kaplan turbine at the Vogelgrun (FR) power plant [24]. Despite the undeniable benefits of such hybridization, this solution comes at a notable initial CAPEX cost. Although the latter investment is relatively modest in size, the former requires a BESS with rated power equal to the one of the HPP, resulting in a considerably higher cost. This substantial investment is justified by the need to maintain the operational integrity of a power plant that would otherwise require extensive refurbishment. In similar situations, it is worth considering alternative solutions that require lower CAPEX investments, as anticipated by research sub-question (g):

5.2 Enhanced Frequency Containment Reserve Provision from Battery Hybridized Hydropower Plants

What alternative approaches, besides BESS hybridization, could effectively enhance FCR provision of RoR HPPs?

To answer the research sub-question, the second part of this chapter investigates the retrofit of existing Kaplan turbines with *Full-Size Frequency Converters* (FSFC), enabling *Variable-Speed* (VARspeed) control [112] while fixing the blade angle. This modification consists of re-purposing the Kaplan turbine as a VARspeed propeller. The utilization of FSFCs becomes particularly compelling in RoR HPPs equipped with Kaplan turbines, due to their typical rated powers in the tens of megawatts range. Unlike BESS hybridization, VARspeed operation requires only CAPEX investments associated with power electronics, with no requirement for energy storage. The concept of VARspeed operation for hydraulic turbines has been extensively examined in the literature, particularly focusing on Francis turbines and reversible pump turbines [40, 113, 114]. Moreover, numerous studies have provided compelling evidence for improved FCR provision through VARspeed technology [41, 115, 116]. However, despite the promising simulation results, the controllers need to be implemented and tested in a laboratory for further verification of performance, as they lack experimental validation. Moreover, [41, 115, 116] only discuss the VARspeed operation of Francis turbines. [112] treats the VARspeed operation of propellers and Kaplan turbines, but focuses only on efficiency improvements, neglecting transient operation and power dynamics. In this chapter, we present a control strategy for VARspeed propeller operation providing FCR, to be experimentally validated in a suited testing platform (described in Chapter 6). The chapter is divided as follows: in Section 5.2 a double-layer MPC to drive the BESS-hybrid HPP is discussed, while Section 5.3 proposes a model-based control for VARspeed propeller providing FCR. Finally, Section 5.4 discusses the main outcomes of the chapter.

5.2 Enhanced Frequency Containment Reserve Provision from Battery Hybridized Hydropower Plants

5.2.1 Problem Statement

The control addresses RoR HPPs operating under daily dispatch plans, scheduled hourly, and obligated to provide FCR service with a fixed droop¹ characteristic σ_f . The dispatch plan, input to the problem, is the product of an external optimization, and it is not the object of this study. The primary focus of this study is to propose an optimal set-point splitting policy that effectively achieves the following objectives:

- i) Ensuring dispatch tracking and high-quality FCR provision characterized by a rapid response time, in compliance with stringent FCR requirements [2, 117].

¹Numerous TSOs source their FCR in a shared market cleared each 4-hour [75]. However, HPP droop settings tend to remain fixed for extended periods (years or even decades) due to contractual agreements, making them constant inputs in our study.

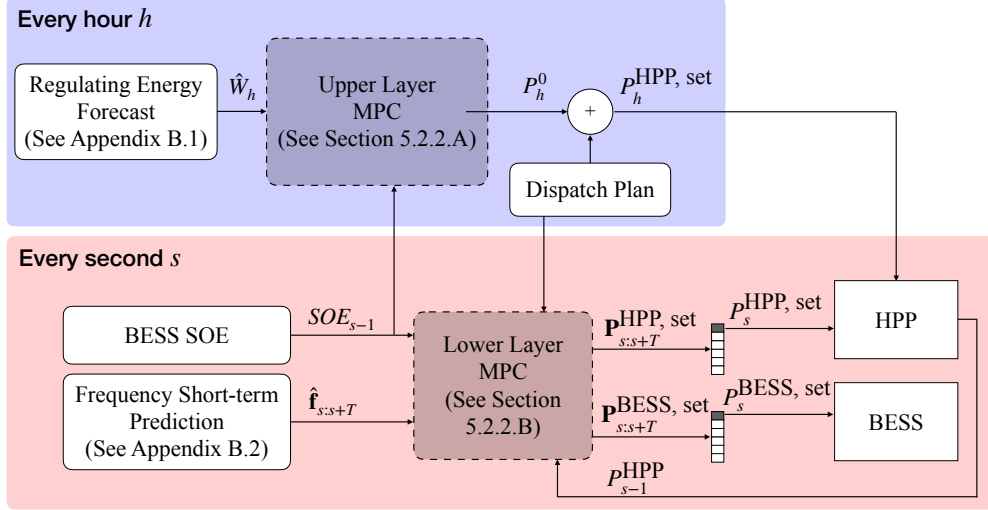


Figure 5.1: DLMPC structure: inputs and outputs of the UL (in blue) and LL (in red).

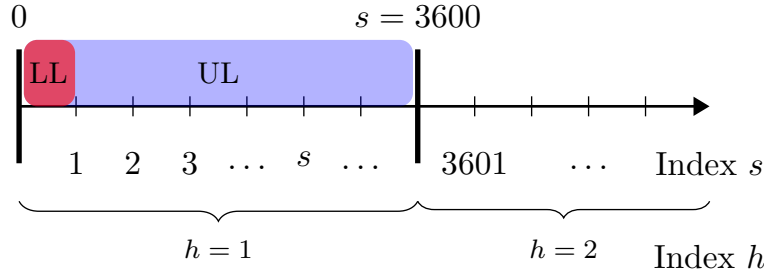


Figure 5.2: Timeline of the problem: actuation of the UL in blue, i.e., each hour h , and of the LL in red, i.e., each second s .

- ii) Minimizing the number of movements and the mileage of the hydropower servomechanisms.
- iii) Ensuring the continuous and efficient operation of the BESS by managing its SOE within physically feasible limits.
- iv) Validating the feasibility of the BESS power set-point to uphold operational constraints composed by the power converter capability curve.

To achieve these objectives, the study proposes the use of a *Double-Layer Model Predictive Control* (DLMPC), structured as visible in Fig. 5.1. The *Upper Layer* (UL) acts as a SOE manager for the BESS, employing a forecast of the required regulating energy² for each hour

²More information about the way this forecast is performed can be found in Appendix B.

h . The output of the UL is a constant power offset for the hour that directly modifies the dispatch plan of the HPP. The *Lower Layer* (LL) optimally allocates the power set point between the turbine and the BESS in real-time, that is, every second s (see the time indices used in Fig. 5.2). This control layer leverages short-term frequency prediction³, together with real-time measurement of the HPP power and the BESS SOE.

In Fig. 5.1, each quantity, e.g. P^{BESS} , is indicated with a certain time subscript: hour h or seconds s . In particular, if the quantity is a vector, including information from time s to $s + T$, it is indicated as:

$$\mathbf{P}_{s:s+T}^{\text{BESS}} = [P_s^{\text{BESS}}, P_{s+1}^{\text{BESS}}, P_{s+2}^{\text{BESS}}, \dots, P_{s+T-1}^{\text{BESS}}, P_{s+T}^{\text{BESS}}].$$

5.2.2 Control Framework

5.2.2.A Upper Layer MPC

Let us consider P^{HPP} as the power of the hydroelectric unit (active sign notation) and P^{BESS} as the power of BESS (passive sign notation). This MPC layer, executed at the beginning of every hour h , is responsible for computing the smallest constant hourly power offset P_h^0 that allows to keep the BESS SOE within its limits. The problem relies on the last measurement of the BESS SOE and on a forecast⁴ of the frequency integral over the next hour \hat{W}_h , together with its confidence intervals $\hat{W}_h^{\uparrow}, \hat{W}_h^{\downarrow}$. The forecast is modified to take into account the charging efficiency η_{ch} and the discharging efficiency η_{dch} of the BESS as:

$$W_h = \begin{cases} \hat{W}_h \cdot \eta_{\text{ch}}, & \text{if } \hat{W}_h < 0 \\ \hat{W}_h / \eta_{\text{dch}}, & \text{if } \hat{W}_h \geq 0 \end{cases} \quad (5.1)$$

The updated value W_h is an input for the upper layer MPC, where it is used together with the frequency droop σ_f to estimate the regulating energy for hour h for the FCR service:

$$E_h^{\text{FCR}} = \sigma_f \cdot W_h \quad (5.2)$$

The constant hourly offset P_h^0 is either positive (BESS is charging) or negative (BESS is discharging):

$$P_h^0 = \begin{cases} P_h^{0+}, & \text{if } P_h^0 \geq 0, \\ -P_h^{0-}, & \text{if } P_h^0 \leq 0 \end{cases} \quad (5.3)$$

³Appendix B examines the viability of this forecast by making references to relevant literature.

⁴Information on the forecasting method can be found in Appendix B.

Chapter 5. Control Strategies for Enhanced Frequency Containment Reserve Provision of Run-of-River Power Plants

where P_h^{0+} and P_h^{0-} are the charging and discharging BESS power in kW, respectively. The constant hourly offset P_h^0 is then computed according to the following OP:

$$P_h^0 = \underset{P_h^{0+} \& P_h^{0-} \in \mathbb{R}}{\operatorname{argmin}} (P_h^{0+} + P_h^{0-})^2 \quad (5.4a)$$

$$\text{s.t. } W_h = \begin{cases} \hat{W}_h \cdot \eta_{\text{ch}}, & \text{if } \hat{W}_h < 0 \\ \hat{W}_h / \eta_{\text{dch}}, & \text{if } \hat{W}_h \geq 0 \end{cases} \quad (5.4b)$$

$$E_h^{\text{FCR}} = \sigma_f \cdot W_h \quad (5.4c)$$

$$E_h^0 = \eta_{\text{ch}} \cdot P_h^{0+} - \frac{1}{\eta_{\text{dch}}} \cdot P_h^{0-} \quad (5.4d)$$

$$SOE_g = SOE_{h-1} + \left[E_g^0 + E_h^{\text{FCR}} \right] \frac{1}{E_{\text{nom}}^{\text{BESS}}} \quad (5.4e)$$

$$SOE_g^{\uparrow} = SOE_g + \left[\sigma_f \cdot \hat{W}_h^{\uparrow} \right] \frac{1}{E_{\text{nom}}^{\text{BESS}}} \quad (5.4f)$$

$$SOE_g^{\downarrow} = SOE_g - \left[\sigma_f \cdot \hat{W}_h^{\downarrow} \right] \frac{1}{E_{\text{nom}}^{\text{BESS}}} \quad (5.4g)$$

$$SOE_g^{\uparrow} \leq SOE_{\text{max}} \quad (5.4h)$$

$$SOE_g^{\downarrow} \geq SOE_{\text{min}} \quad (5.4i)$$

$$0 \leq P_h^{0+} \leq P_{\text{max}}^{\text{BESS}+} \quad (5.4j)$$

$$0 \leq P_h^{0-} \leq P_{\text{max}}^{\text{BESS}-} \quad (5.4k)$$

$$P_{\text{min}}^{\text{HPP}} \leq P_h^{\text{co}} + P_h^{0+} \leq P_{\text{max}}^{\text{HPP}} \quad (5.4l)$$

$$P_{\text{min}}^{\text{HPP}} \leq P_h^{\text{co}} - P_h^{0-} \leq P_{\text{max}}^{\text{HPP}} \quad (5.4m)$$

$$P_h^0 = P_h^{0+} - P_h^{0-} \quad (5.4n)$$

The energy variation E_h^0 due to the offset action during hour h is provided by Eq. (5.4d), as the power offset is applied for one hour. The latter is used, together with the forecast of W_h in Eq. (5.4e) to predict the SOE_h at the end of the hour h , taking into consideration the BESS capacity $E_{\text{nom}}^{\text{BESS}}$. Eqs. (5.4f)-(5.4i) compute the confidence interval of the SOE forecast and ensure the feasible operation in the considered intervals.

Separating the charging and discharging components of the power offset allows for taking into consideration charging and discharging efficiencies. Relaxation according to [118], visible in Eq. (5.4a) forces only one of the two decision variables to be different from zero so that Eq. (5.4n) is compatible with the definition in Eq. (5.3). Equations (5.4j)-(5.4k) ensure the final power of the battery to be within the operational limits. Finally, Eq. (5.4n) computes the final power output of the BESS, positive if charging. The offset is directly applied to modify the dispatch plan of the HPP, as visible in Fig. 5.1.

5.2.2.B Lower Layer MPC

The lower layer is a rolling-horizon MPC responsible for computing in real-time (i.e., each second) the set-point splitting policy between the HPP and the BESS, with the following objectives:

- a) Optimal tracking of the FCR provision.
- b) Minimization the number of movements and the total mileage of the hydropower servomechanisms;
- c) BESS operation within its physical limits.

For every time step:

$$s \in [s, s + T],$$

where T is the length of the MPC horizon, the expected power output P_s^{set} of the hybrid system is:

$$P_s^{\text{set}} = P_s^{\text{co}} + [f_{\text{nom}} - \hat{f}_s] \cdot \sigma_f \quad (5.5)$$

where the term \hat{f}_s indicates the expected value⁵ of the grid frequency at time s . As a consequence, the *Tracking Error* (TE) is the difference between the expected power output and the actual aggregated production of HPP + BESS, i.e. the power flow at the PCC:

$$\text{TE}_s = P_s^{\text{set}} - (P_s^{\text{HPP}} - P_s^{\text{BESS}}) \quad (5.6)$$

and, over the entire MPC window:

$$\mathbf{TE}_{s:s+T} = \|\mathbf{P}_{s:s+T}^{\text{set}} - (\mathbf{P}_{s:s+T}^{\text{HPP}} - \mathbf{P}_{s:s+T}^{\text{BESS}})\|_2 \quad (5.7)$$

The second objective, i.e. the reduction of the number of movements of the hydropower actuators, can be modeled as the minimization of the cardinality of the array containing the variation of the hydroelectric unit power output from the previous time instant:

$$\min \quad \text{card}(\Delta \mathbf{P}_{s:s+T}^{\text{HPP}}) \quad (5.8)$$

with $\Delta P_s^{\text{HPP}} = P_s^{\text{HPP}} - P_{s-1}^{\text{HPP}} \quad \forall s \in [s, s + T]$. As discussed in [119], the cardinality of a quantity can be relaxed with its ℓ_1 -norm. In other words, $\|\Delta \mathbf{P}_{s:s+T}^{\text{HPP}}\|_1$ is the convex envelope of the objective function of Eq. (5.8). The latter equation can therefore be relaxed, and assumes the following form:

$$\min \quad \omega_c \|\Delta \mathbf{P}_{s:s+T}^{\text{HPP}}\|_1 \quad (5.9)$$

where ω_c is a non-negative parameter tuned to achieve the desired sparsity. Eqs. (5.7) and (5.9) constitute the objective of the lower-layer MPC.

⁵Information about this short-term frequency forecast is contained in Appendix B.

Chapter 5. Control Strategies for Enhanced Frequency Containment Reserve Provision of Run-of-River Power Plants

The constraints of the OP ensure that the BESS and the HPP operate within their physical limits. In particular, the capability curve ξ of the BESS converter is considered as a simplified version of Eq. (4.16), where no reactive power flow is present:

$$P_s^{\text{BESS}} \leq \xi(\nu_s^{\text{DC}}, \nu_s^{\text{AC}}, \text{SOE}_s) \quad (5.10)$$

As shown in Chapter 4, the estimation of the BESS ν_s^{DC} is based on the battery TTC model, whose dynamic evolution can be expressed as a linear function of battery current by applying the transition matrices $\phi^\nu, \psi^\nu, \psi_1^\nu$ (see Eq. (4.17)). This modeling choice, based on [28], offers greater accuracy than the commonly used two-time constant model [106]. However, for BESS predictions with a 1-second horizon, simpler models can be utilized, as discussed in Chapter 7. The DC-current is computed as proposed in Eq. (4.18) and recalled in Eq. (5.12e). The active power at the DC bus P_s^{DC} is related to the active power set-point AC side of the converter $P_s^{\text{BESS, set}}$ according to (4.19), recalled in (5.12c). The magnitude of the direct sequence component ν_s^{AC} of the phase-to-phase voltage on the AC side of the converter, is assumed to be equal to the last available measurement, as indicated in (4.21) and as (5.12f) in OP. Finally, the BESS SOE evolution is computed in Eq. (5.12g), and ensured within its physical limits by Eq. (5.12h).

For the HPP, a first-order discrete-time dynamical system is used to model the response P_s^{HPP} to a set point $P_s^{\text{HPP, set}}$ considering a time constant τ_W :

$$P_s^{\text{HPP}} = \left(1 - \frac{\Delta s}{\tau_W}\right) \cdot P_{s-1}^{\text{HPP}} + \frac{\Delta s}{\tau_W} \cdot P_s^{\text{HPP, set}} \quad (5.11)$$

where Δs is the time interval between two consecutive discrete-time samples (i.e., one second). The HPP output power is limited within P_{\min}^{HPP} and P_{\max}^{HPP} by Eq. (5.12j) while Eq. (5.12k) ensures the power ramping rate to be lower than its maximum allowed value $\dot{P}_{\max}^{\text{HPP}}$, expressed in kW s^{-1} . As we assume the dispatch plan to include concession head control and given the short-term horizon of the MPC, no constraints on the concession head are introduced⁶. The LLMPC,

⁶In the case of need for modeling constraints on the concession head, similarly to what is done in [60], information about the hill-chart of the runner is needed, to translate power set-points into discharge values.

5.2 Enhanced Frequency Containment Reserve Provision from Battery Hybridized Hydropower Plants

running every second s , is the following OP:

$$\begin{aligned} [\mathbf{P}_{s:s+T}^{\text{HPP, set}}, \mathbf{P}_{s:s+T}^{\text{BESS, set}}] &= \\ &= \underset{\mathbf{P}^{\text{HPP}}, \mathbf{P}^{\text{BESS}} \in \mathbb{R}^T}{\text{argmin}} \quad \mathbf{TE}_{s:s+T} + \omega_c \cdot \|\Delta \mathbf{P}_{s:s+T}^{\text{HPP}}\|_1 \end{aligned} \quad (5.12a)$$

subject to:

$$P_s^{\text{BESS}} \leq \xi(v_s^{\text{DC}}, v_s^{\text{AC}}, \text{SOE}_s) \quad (5.12b)$$

$$P_s^{\text{DC}} = \begin{cases} P_s^{\text{BESS, set}} \cdot \eta_{\text{ch}}, & \forall P_s^{\text{BESS, set}} \geq 0 \\ P_s^{\text{BESS, set}} / \eta_{\text{dch}}, & \forall P_s^{\text{BESS, set}} < 0 \end{cases} \quad (5.12c)$$

$$v_s^{\text{DC}} = \phi_v x_{s-1} + \psi_v^v i_s^{\text{DC}} + \psi_1^v \mathbf{1} \quad (5.12d)$$

$$i_s^{\text{DC}} \approx \frac{P_s^{\text{DC}}}{v_s^{\text{DC}}} \quad (5.12e)$$

$$v_s^{\text{AC}} \approx v_{s-1}^{\text{AC}} \quad (5.12f)$$

$$\text{SOE}_s = \text{SOE}_{s-1} + i_s^{\text{DC}} v_s^{\text{DC}} \frac{1}{C_B} \quad (5.12g)$$

$$\text{SOE}_{\min} \leq \text{SOE}_s \leq \text{SOE}_{\max} \quad (5.12h)$$

$$P_s^{\text{HPP}} = \left(1 - \frac{\Delta s}{\tau_W}\right) \cdot P_{s-1}^{\text{HPP}} + \frac{\Delta s}{\tau_W} \cdot P_s^{\text{HPP, set}} \quad (5.12i)$$

$$P_{\min}^{\text{HPP}} \leq P_s^{\text{HPP}} \leq P_{\max}^{\text{HPP}} \quad (5.12j)$$

$$\begin{aligned} -\dot{P}_{\max}^{\text{HPP}} &\leq \Delta P_s^{\text{HPP}} \leq \dot{P}_{\max}^{\text{HPP}} \\ &\forall s \in [s, \dots, s+T] \end{aligned} \quad (5.12k)$$

A way to convexify constraints (5.12b) - (5.12f) has been presented in [29]. The optimization problem is solved at each time step s (with updated information) on a sliding horizon from the index s to $s+T$. At each s , the control trajectories for HPP and BESS for the whole residual horizon

$$[\mathbf{P}_{s:s+T}^{\text{HPP, set}}, \mathbf{P}_{s:s+T}^{\text{BESS, set}}]$$

are available. However, only the first components, denoted by:

$$[P_s^{\text{HPP, set}}, P_s^{\text{BESS, set}}]$$

are considered for actuation.

Hydropower Actuation: The set-point is fed to the Kaplan governor. As shown in Fig. 3.1, the governor includes the CAM block, indicating the relation between *Guide Vane Opening* (GVO) and *Runner Blade Angle* (RBA) that maximizes the efficiency for a given head value and a fixed rotational. Using surrogate models, such as the one presented in Eq. (3.8), one can directly calculate the efficiency of the Kaplan turbine for any combination of α , β , n_{ED} . The CAM is then obtained by running numerical optimization on this function, following the procedure of Algorithm 3 in Chapter 3. An example of the CAM curve for the reduced-scale Kaplan utilized

during the experimental tests, for a head value of 10 m, is visible in Fig. 5.3.

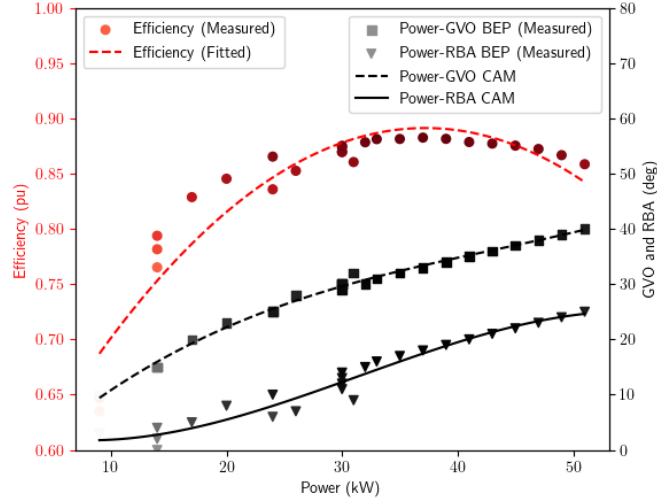


Figure 5.3: CAM Curves and expected efficiency for the Kaplan runner for a constant head $H = 10\text{ m}$ and a fixed speed of $n = 1500\text{ min}^{-1}$.

BESS Actuation: The experimental results discussed in Chapter 4 would advocate for the use of a BESS interfaced with a GFR converter, to enhance the quality of the FCR response. However, in the context of integrating BESSs with HPPs, the necessity for grid-forming capabilities can be reevaluated. The presence of the HPP's synchronous generator inherently provides grid-stabilizing features such as inertia and voltage regulation, which are fundamental attributes of grid-forming inverters. Consequently, the BESS, when coupled with the HPP, does not need to assume a grid-forming role. Indeed, the coupling of the BESS with the HPP is not aimed at enhancing the sub-second response of the system, but rather to reduce the number of mechanical movements of the HPP unit, thereby optimizing its operational longevity and efficiency. For this reason, the power set-point computed by Problem (5.12) is directly applied to the BESS operated in grid-following mode.

5.3 Experimental Investigation of Repurposed Kaplan Turbines as VARspeed Propellers for Maximizing FCR

5.3.1 Problem Statement

Similarly to Section 5.2.1, we consider a RoR HPP equipped with a Kaplan turbine that operates under a daily dispatch plan \hat{G} and is obliged to provide FCR with a fixed droop characteristic σ_f . As the unit approaches the end of its operational life, the HPP owner aims to mitigate the aging of the servomechanism while maintaining a continuous provision of FCR by fixing the blade servomechanism to a certain RBA $\beta = \beta_0$ and operating the unit as a VARspeed propeller. The primary objective of this study is to conduct a technical assessment comparing the latter solution to BESS hybridization, with a specific focus on the following objectives:

- i) Ensuring dispatch tracking and high-quality FCR provision with a rapid response time, in strict compliance with stringent FCR requirements [2, 117];
- ii) Reducing the number of movements and the mileage of the hydropower servomechanisms, with particular attention to the blade servomechanism;
- iii) Minimizing the overall efficiency loss of the system, caused by the presence of the power converter, and the limit on the blade's position.

5.3.2 Control Framework

As extensively treated in Section 3.3, the control mechanism for fixed-speed Kaplan turbines relies on the CAM block, which optimizes efficiency by linking the RBA β to the GVO α and the head. For Kaplan governors, the CAM block establishes the relationship between GVO and RBA for each head value.

In contrast, if the blades are fixed, i.e. in propeller operation, the efficiency drops dramatically for load values out of a narrow range in the neighborhood of rated power. VARspeed operation of a propeller turbine can substantially improve its performance, although keeping it below that of a Kaplan turbine. In VARspeed propellers, when the head remains fixed, the CAM block defines the optimal speed for each GVO [120, 112], assuming a constant RBA. To be able to compute both CAM blocks, a model of the turbine efficiency has to be provided. Following the same procedure as for the Kaplan CAM curve block, but using as control variable α and n , instead of α and β , the VARspeed CAM can be obtained:

$$\begin{aligned} [\alpha_\ell, n_\ell] &= \arg\max \quad \eta(\alpha_\ell, \beta_0, H, n_\ell) \\ \text{s.t.} \quad &\dot{V}(\alpha_\ell, \beta_0, H, n_\ell) = \dot{V}_\ell \\ &\alpha_\ell, \beta_\ell \in \Omega_{\alpha, \beta} \end{aligned} \tag{5.13}$$

Given the similarity between problem 5.13 and problem 3.6, this section does not discuss

how to obtain the final VARspeed CAM, as the entire process is presented in Section 3.3. An example of efficiency curves is visible in Fig. 5.4. The figure contains the measured points and a fit of the efficiency meta-model, while the VARspeed CAM is visible in black.

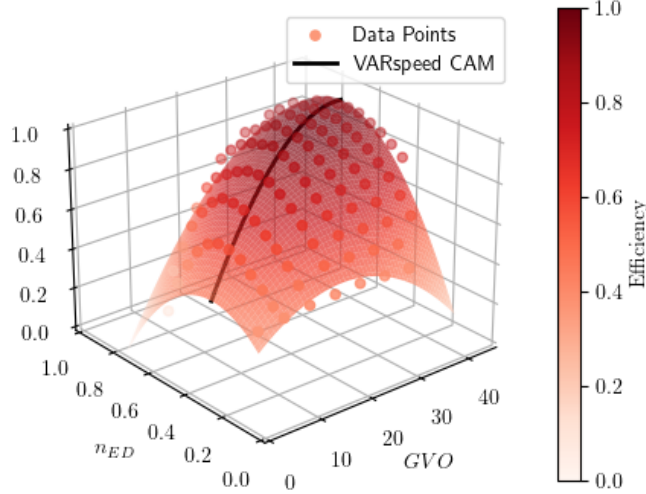


Figure 5.4: Efficiency hill-chart and speed CAM of the VARspeed propeller with $RBA = 18^\circ$.

5.4 Discussion

This chapter introduced two solutions to enhance FCR in RoR HPPs. The first solution involves hybridizing the Kaplan unit with a BESS, while the second solution employs an FSFC to enable the VARspeed operation of the Kaplan unit as a propeller. For each solution, an optimal control strategy is proposed to maximize the benefits of these technological integrations. While the control technique developed for each solution relies on a robust theoretical background, their practical effectiveness remains to be validated. The subsequent chapters will therefore focus on the experimental validation of these frameworks, comparing their performances and providing a comprehensive assessment of their applicability in real-world scenarios. Prior to this, the design and engineering of an appropriate test bench for dynamic testing, including the design of experiments, will be discussed in Chapter 6.

6 Design of Experiments for a BESS-Hybridized Hydro Turbine Test Rig

While research is focusing on optimal control strategies for BESS-hybridized HPPs, it becomes necessary to have experimental facilities able to test and validate upcoming solutions. Testing platforms are nowadays decoupling the hydraulic and the electric components, testing them separately. Therefore, they are not suitable for the validation of the control strategy under real grid conditions. The scope of this chapter is to present an experimental facility where different joint control techniques can be tested on reduced-scale models of hydraulic machines hybridized with a BESS. The presented test rig combines all the fundamental components, both on the hydraulic and the electrical side, within the same testing facility. The platform is an adaptation of one of the test rigs available at the "Plateforme Technologique Machines Hydrauliques", EPFL, Switzerland.

The Chapter includes results from [P8].

Research sub-questions:

- (h) How can the benefits of RoR HPPs and BESSs integration for FCR provision be effectively evaluated through experiments?*

6.1 Experimental Setup

6.1.1 Hydro-mechanical components

The experimental platform used for this study modernizes the existing testing platform in the *Plateforme Technologique Machines Hydrauliques* (PTMH), at EPFL. The upgraded platform is a closed-loop test rig (see Fig. 6.1) allowing the performance assessment of hydraulic machines with 0.2 % accuracy, complying with the IEC60193 standard for the testing of reduced-scale physical models [121]. Two centrifugal pumps allow for generating a maximum head of 100 m and a maximum discharge of $1.4 \text{ m}^3 \text{ s}^{-1}$. Hydraulic measurements are performed on the installed reduced-scale physical models, including the upstream inlet pipe, the spiral case, and the draft tube consisting of the cone, the elbow, and the diffuser. Electric actuators are used as servomechanisms to control guide vanes and, if needed by the reduced-scale model, blades. The models are connected with a 4-pole synchronous machine (i.e. with a nominal speed of 1500 min^{-1} at $f = 50 \text{ Hz}$), rated 100 kVA.

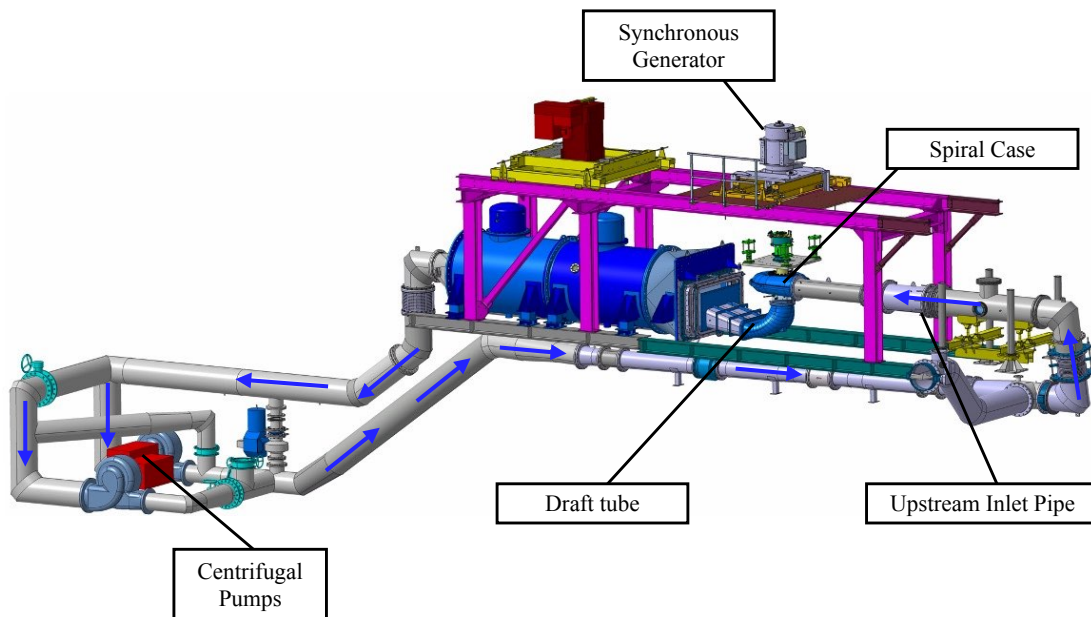


Figure 6.1: Hydro-mechanical side of the PTMH-PF3 platform for reduced scale physical turbine model tests. The electrical connections are shown in Fig. 6.2. The blue arrows show the direction of the water flow.

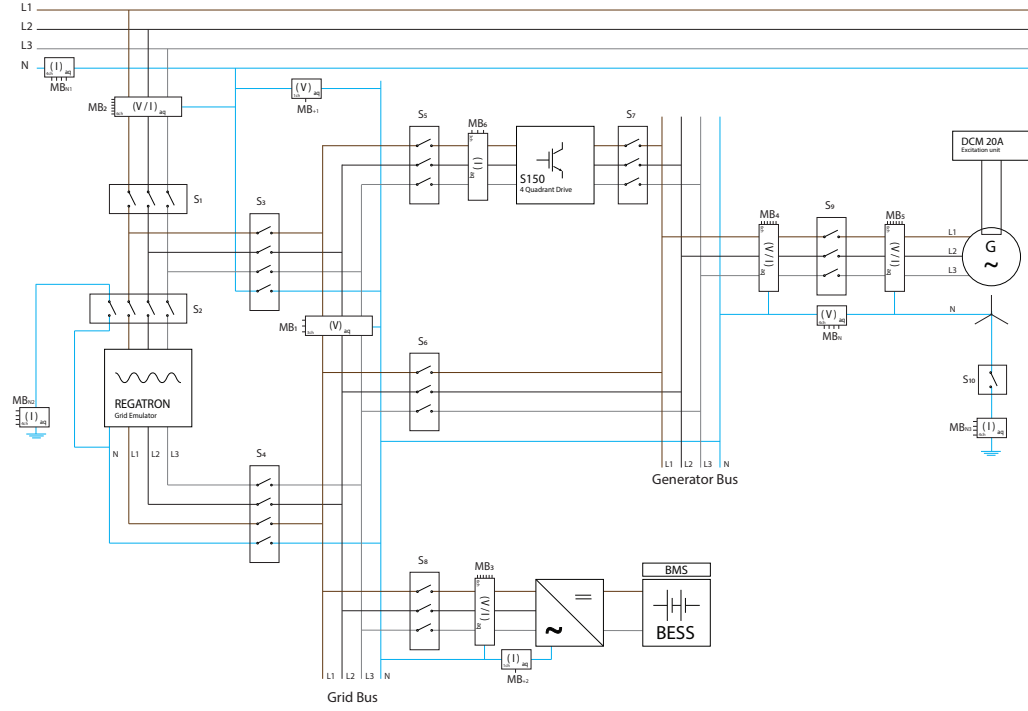


Figure 6.2: Test-rig 3-phase schematics, with switches and PMU measuring.

6.1.2 Electrical Components

As the turbine is connected to the grid through a synchronous machine, a synchro-check mechanism¹ is necessary to connect the machine to the "Generator Bus". The electrical measurement infrastructure employs a distributed sensing system based on PMUs relying on the *enhanced-Interpolated DFT* (e-IpDFT) algorithm developed in [122]. This system allows for real-time acquisition of accurate power flow data thanks to the high reporting rate of the PMUs (50 Hz). Moreover, the measurements have remarkable precision, with a standard deviation equivalent to 0.001 degrees (approximately 18 μ rad) and error in frequency estimation ≤ 0.4 mHz. The measuring points are indicated by the acronym "MB", i.e. measuring box, in Fig. 6.2. A distributed set of switches, enumerated from "S1" to "S9" in the figure, is controlled to modify the grid topology and test both BESS hybridization mode and VARspeed mode. In particular, the "Generator Bus" can be directly connected to the "Grid Bus", by closing S6, or can be connected via a full-size frequency converter, allowing for VARspeed test (S6 open, S5 and S7 closed). On the "Grid Bus", the grid frequency is imposed by a grid emulator (REGATRON) with a nominal power rating of 100 kVA. This component is a full 4 quadrant 3-phase AC power source able to reproduce different grid scenarios, with a high level of

¹As explored in the following subsection, this mechanism is implemented at the real-time level of a cRIO 9268. It involves calculating the positive sequence component of the voltage phasors on both sides of the switch. The amplitude and phase of these two direct sequences are then compared. If their frequency, phase, and amplitude align sufficiently within specific thresholds for a certain duration, the command to close the switch is issued.

Chapter 6. Design of Experiments for a BESS-Hybridized Hydro Turbine Test Rig

system dynamics (≤ 5 kHz modulation bandwidth). Reproducing different grid scenarios, especially frequency and voltage disturbances to test grid regulation services, is fundamental to evaluating the performance of different control techniques.

A BESS is connected in parallel with the synchronous generator as shown in Fig. 6.2. To study the optimal BESS sizing based on the developed control algorithms, due to the limitation of commercially available BESSs, the one of the test-rig (100 kW/92 kWh) is over-sized with respect to the power of the reduced-scale models. During the experimental campaign, the battery usable size (for both power and energy rating) can be software-modified depending on the needs, by shrinking the capability curve of the BESS and constraining the maximum and minimum state of charge to different values within the available range. Information about the installed BESS can be found in Table 6.1. The grid emulator can be bypassed by operating switches "S1, S2, S3, and S4", to directly connect the "Grid Bus" with the electrical grid of Lausanne, Switzerland (i.e. the synchronous area of continental Europe).

Battery		Converter	
Parameter	Value	Parameter	Value
N. of Modules	14	DC Voltage	450 ↔ 825 V
BESS Nominal Capacity	128 Ah	DC Current	480 A
BESS Energy	92.3 kWh	Rated Power	100 kVA
Nominal C-Rate	2 C	Max Power	110 kVA (30 min)
Rack Nominal Voltage	725.2 V	Rated AC Voltage	280 V (RMS)
Rack Voltage Range	588.0 ↔ 823.2 V	AC Voltage Range	224 ↔ 336 V
Operating T	23 ± 4 °C	Frequency Range	47.5 ↔ 51.5 Hz
N. of Cells per Modules	2 × 14 cells	Rated AC Current	206 A
Cell Energy	6.6 kWh	Max AC Current	235 A
Cell Nominal Voltage	51.8 V	THDI	≤ 3 %
Cell Voltage Range	42.0 ↔ 58.8 V	Max Efficiency	96.4 %

Table 6.1: Battery and Converter's Specifications.

Switch	Baseline	BESS Hybrid	VARspeed	BESS Hybrid - grid	VARspeed - grid
S1	ON	ON	ON	ON	ON
S2	ON	ON	ON	OFF	OFF
S3	OFF	OFF	OFF	ON	ON
S4	ON	ON	ON	OFF	OFF
S5	OFF	OFF	ON	OFF	ON
S6	OFF	ON	OFF	ON	OFF
S7	OFF	OFF	ON	OFF	ON
S8	OFF	ON	OFF	ON	OFF
S9	ON	ON	ON	ON	ON

Table 6.2: Switches Configuration for the Different Testing Setups.

Table 6.2 contains information about the switches' position for each testing configuration. In the table, the baseline scenario refers to the hydroelectric unit connected to the grid emulator via the synchronous generator. In the BESS scenario, a BESS is connected in parallel with the synchronous generator so that the power flow at the grid connection point is dispatched between the hydraulic machine and the BESS. Finally, in the VARspeed scenario, the FSFC indicated as "S150" in Fig. 6.2 is utilized. To perform VARspeed tests, the generator is specifically designed to withstand continuous operation around the nominal operating speed (from 500 min^{-1} to 1500 min^{-1}). The last two columns of Table 6.2 refer to the same "*BESS Hybrid*" and "*VARspeed*" configurations, but bypassing the grid emulator. In the next section, the different testing setups are discussed in detail.

6.1.3 Data-Flow and Software Infrastructure

Fig. 6.3 and Table 6.3 provide a simplified scheme and the details of the test rig's data flow, respectively. Every measuring box visible in Fig. 6.2 acquires analog voltage measurements

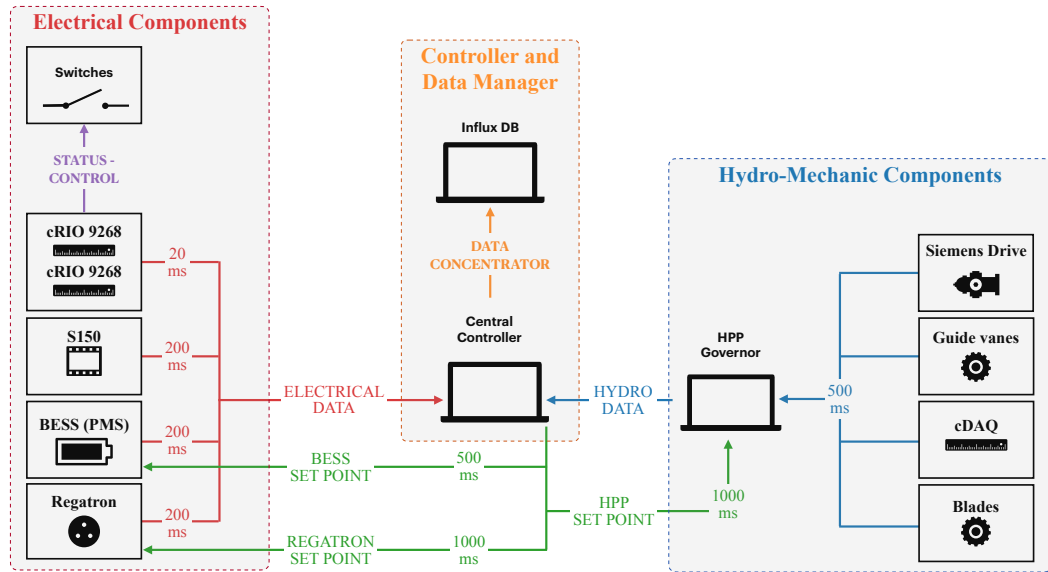


Figure 6.3: Data-Flow of the PTMH PF3 testing platform. The different data flows (indicated by arrows in the figure) are detailed in Table 6.3.

from LEM CV 3-1000 sensors ($\pm 0.2\%$ accuracy) and current measurements from LEM LF 205-S sensors ($\pm 0.5\%$ accuracy). The data acquisition and the e-IPDFT are implemented on the *Field Programmable Gate Array* (FPGA) of two NI Compact RIO 9068 real-time controllers. The synchrophasor extraction process is time synchronized by GPS and the synchrophasors are streamed every 20 ms to the centralized controller using the *User Datagram Protocol* (UDP). The two NI Compact RIOs 9068 are responsible for the following tasks:

- Analog data acquisition from LEM sensors (NI 9215, NI 9220).

Chapter 6. Design of Experiments for a BESS-Hybridized Hydro Turbine Test Rig

Description	Source	Target	Latency	Reference
Switches Status/Control	Switches	cRIO 9268	5 ms	Table 6.4
Electrical Data	cRIO 9268	Central Controller	200 ms	Table 6.4
Hydro Data	HPP Governor	Central Controller	500 ms	Table 6.6
BESS Set-points	Central Controller	BESS	500 ms	Table 6.5
Regatron Set-points	Central Controller	Regatron	1000 ms	Table 6.5
HPP Set-points	Central Controller	HPP Governor	1000 ms	Table 6.5
Data Concentrator	Central Controller	Influx-DB	-	-

Table 6.3: Data Flow Description for the PTMH PF3 Test Rig

- Synchrophasor estimation at the FPGA level.
- UDP data stream of synchrophasor data to the central controller.
- Analog data acquisition of feedback from Switches (NI 9235).
- Switches actuation (NI 9282), including the synchro-check mechanism for S9 running on the real-time controller.

Even though the cRIO is responsible for switch actuation, only the centralized controller can issue the command. This computer gathers operational data from the BESS and the Grid Emulator via the Modbus protocol, as well as from the FSFC (i.e., S150) and the synchronous machine's excitation unit (i.e., DCM 20A) through TCP/IP (see Table 6.4). In the table, the term auxiliaries refers to information related to the state of the unit, such as errors, warnings, or contactor states. Different measurements are supported based on the testing needs. Additionally, the central controller receives hydraulic information processed by the HPP governor. This ensures the safe operation of the hydro-mechanical system and aggregates measurements from the GVO and RBA servomotor, electrical drives for pumps and auxiliaries, and a cDAQ-9189-based acquisition system. Communication between the HPP governor and the central controller occurs via UDP, with the governor receiving set points every 1000 milliseconds. The central controller also sends set points to the BESS and the Grid emulator at intervals of 500 and 1000 milliseconds, respectively. An overview of all the set points from the central controller is provided by Table 6.5. Finally, the controller aggregates this data and streams it to a time series database for post-processing.

6.2 Different configurations

BESS		S150		Regatron		cRIO	
Name	Unit	Name	Unit	Name	Unit	Name	Unit
SOE	%	Speed	rpm	Voltage (ph)	V	Switches	
Active Power	kW	Exc. Current	A	Current (ph)	A	PMU Voltage	V
Reactive Power	kVAr	Temperature	°C	Auxiliaries		PMU Current	A
DC Voltage	V	Auxiliaries					
AC Voltage	V						
Temperature	°C						
Auxiliaries							

Table 6.4: Example of Electrical Measurements on the PTMH-PF3 Testing Platform During the Experiments.

Communication	Signals	Symbol	Measurement Units
BESS Set-points	BESS Active Power	P^{BESS}	kW
	BESS Reactive Power	Q^{BESS}	kVAr
Regatron Set-points	Emulated Grid Frequency	f^{PCC}	Hz
	Emulated Grid Voltage	v^{PCC}	V
HPP Set-point	HPP Active Power	P^{HPP}	kW
	HPP Reactive Power	Q^{HPP}	kVAr

Table 6.5: List of Set-points Dispatched by the Central Controller.

6.2 Different configurations

6.2.1 Baseline ("Only Hydro") Setup

In the baseline setup the Kaplan unit is connected to the synchronous machine and the "Generator Bus" is directly connected with the "Grid Bus". The FCR demand is entirely fulfilled by the hydro unit, as no BESS is connected in parallel. This baseline configuration is also used to conduct preliminary performance tests, suitable to measure the efficiency hill chart, the cavitation limits, and the critical pressure fluctuations in the hydraulic machine over the full operating range of the hydraulic machine. These tests, performed in steady-state conditions, are needed to collect the data necessary to build the reduced-scale unit meta-models (e.g. test to estimate the unit's hill chart, or to determine the CAM curve following the procedure discussed in Chapter 3).

6.2.2 BESS Setup

The BESS setup represents the hybridization scenario, where the BESS is connected in parallel with the synchronous generator as shown in Fig. 6.5. The objective of the tests executed

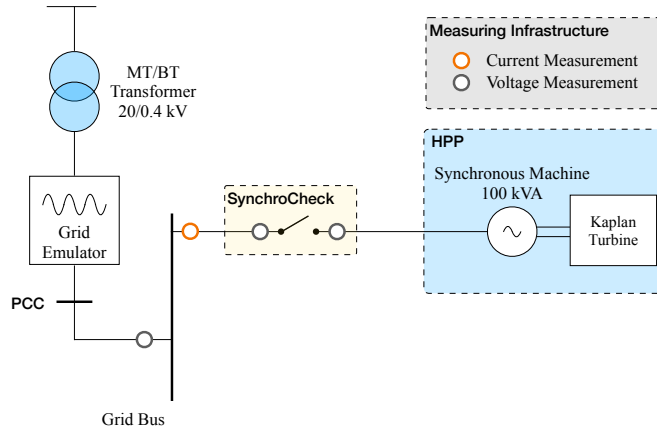


Figure 6.4: Schematics of the PTMH PF3 power grid used in the "Only Hydro" setup.

in this setup is to investigate the upgraded potential of a BESS integration in HPPs and the performances of the control strategy. These tests are essential to validate the best control framework which defines the optimal BESS sizing to increase the potential and benefits of the hybridization. For experiments where the power exceeds the nominal power of the grid emulator, or to test the hybrid unit directly connected to the grid, the grid emulator can be bypassed (acting on S1, S2, S3). This variation of the BESS setup is indicated as "*BESS Hybrid - grid*" in Table 6.2.

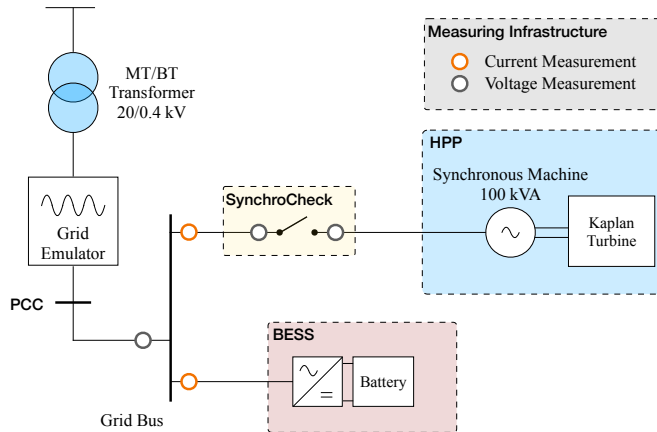


Figure 6.5: Schematics of the PTMH PF3 power grid used in the "BESS Hybrid" mode.

6.2.3 VARspeed Setup

The VARspeed Setup is used to operate the hydroelectric machine as a VARspeed unit and to test reduced-scale models with a nominal speed different from the one of the synchronous

generator (i.e. 1500 min^{-1} at $f_{\text{nom}} = 50 \text{ Hz}$). The BESS is disconnected², and the synchronous generator is connected to the FSFC as shown in Fig. 6.6. This setup allows for developing the optimal control framework for VARspeed hydroelectric units and as a benchmark to compare the performance of the hybrid setup with the state of the art. As for the BESS Setup, the grid emulator can be bypassed. This variation is indicated with the name "*VARspeed - grid*" in Table 6.2.

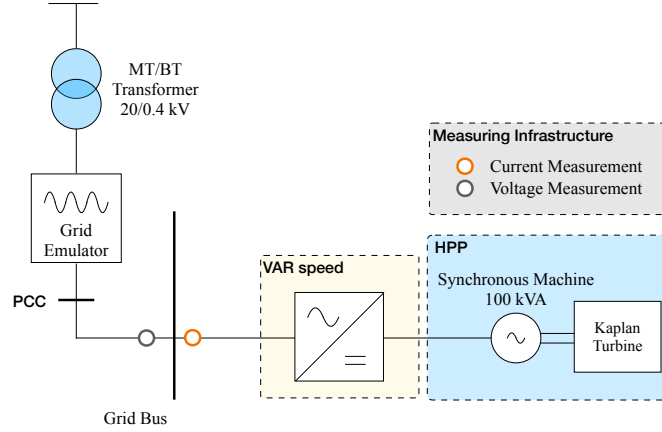


Figure 6.6: Schematics of the PTMH PF3 power grid used in the "*VARspeed*" setup.

6.3 Experimental Test

6.3.1 Reduced-Scale Model

The experimental tests for the validation of the controls proposed in Chapter 5 are conducted on a 1:20 reduced-scale physical model of the Kaplan turbine installed in the RoR HPP of Vogelgrun, France. The model has a specific speed $\nu = 1.53$ defined as follows:

$$\nu = \omega \cdot \frac{\dot{V}^{1/2}}{\pi^{1/2} \cdot (2 \cdot E_{\text{nom}})^{3/4}} \quad (6.1)$$

where \dot{V} is the hydraulic discharge, E_{nom} the machine specific energy and ω the angular speed in rad s^{-1} . The reduced-scale model is a 4-blade runner with an external diameter $D = 0.34 \text{ m}$. The list of measurements conducted on the hydro-mechanical model is detailed in Table 6.6.

Particular attention is paid to the measurement of the stresses on the connecting rod of one blade. The measurement is performed with a *HBM strain gauge* to evaluate the torque on the blade connecting rod and the related wear and tear. The strain gauge setup is visible in Fig. 6.7. As outlined in [123], strain gauge testing emerges as the only reliable approach to acquire static and dynamic stress information from the turbine runner. Over recent years, this

²By construction, the BESS can be connected even during VARspeed operation. However, the two configurations are normally considered as alternatives.

Name	Unit
Discharge	$\text{m}^3 \text{s}^{-1}$
Turbine Speed	min^{-1}
Head	m
Hydraulic Efficiency	%
Shaft Torque	N m
Guide Vanes Opening (GVO)	deg
Runner Blade Angle (RBA)	deg
Runner Blade Torque (RBT)	N m

Table 6.6: Hydro-Mechanical Measurements on the PTMH-PF3 Testing Platform.

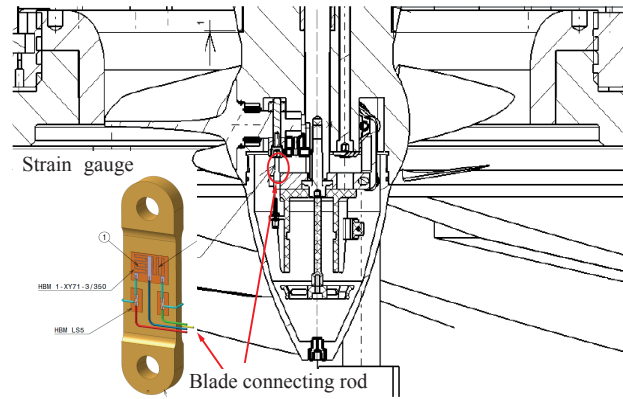


Figure 6.7: HBM strain gauge on the connecting rod of one blade of the Kaplan Turbine.

method has gained widespread acceptance as a standard practice for newly installed runners, as highlighted in [124].

6.3.2 BESS Sizing

The turbine, with a rated power of 50 kW, is hybridized with two different BESS sizing, to compare the reduced-scale experiments with the BESS-hybridized power plant of Vogelgrun [110]. As delineated in [110], the hydro-turbine governor at Vogelgrun HPP is characterized by a regulating power³ of 3.5 MW (10% of its nominal power), i.e. a droop of 17.5 MWhz^{-1} . Scaling this to the tested reduced-scale model yields a 25 kWhz^{-1} droop with 5 kW of regulating power at 200 mHz deviation. However, this regulating power isn't feasible due to battery size constraints and potential interference with power oscillation noise.

To address the latter problem, the facility's droop is increased by a factor of 5, leading to a

³In this thesis, we use the term "regulating power" to refer to the FCR power response to a frequency deviation of 200 mHz.

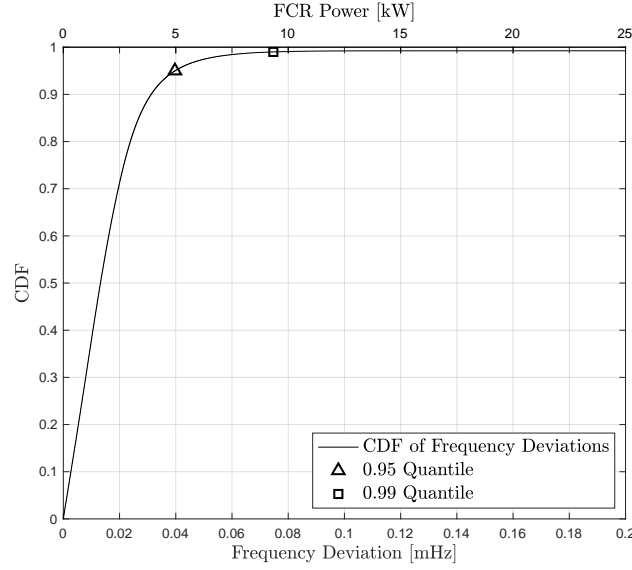


Figure 6.8: CDF of Frequency deviation in continental Europe, based on year-long time series collected between 2019 and 2020. The upper x-axis shows the FCR power associated with the frequency deviation, for a FCR droop of 125 kWhz^{-1} .

125 kWhz^{-1} final droop. In accordance with [110], the installed BESS at Vogelgrun constitutes 16.5% of the regulating energy, equivalent to 4.125 kW. For experimentation, we opted for two BESS sizes: 5 kW and 9 kW. The BESS power rating is the consequence of a statistical analysis of frequency time series in the continental Europe power system, aiming to cover 95% and 99% of frequency deviations. Figure 6.8 offers a visual representation of the CDF of frequency deviation in the ENTSO synchronous area, together with the power ratings derived by assuming a droop of 125 kWhz^{-1} . Regarding the BESS energy sizing, it is important to note that this assumption impacts the outcomes of the DLMPC. Specifically, a BESS with more energy capacity would necessitate fewer interventions from the DLMPC, whereas a BESS with lower energy capacity would require more frequent actions. Due to the complexity of the tests, we did not conduct experiments with varying energy ratings for each BESS power rating. Instead, we assume a power-to-energy ratio of 1, aligning with market availability as mentioned in [125]. Such an assumption is possible since the scope of this thesis is not to provide optimal sizing, but rather to propose and validate the control framework. Future studies will focus on evaluating the optimal BESS sizing for addressing challenges related to BESS hybridization in HPPs.

6.3.3 Grid Scenario

A series of 12-hour tests are performed, with frequency time series enforced at the PCC, i.e. at the "Grid Bus", by the grid emulator. The frequency data correspond to measurements taken on January 8th, 2021, when the ENTSO continental Europe synchronous area experienced a

Chapter 6. Design of Experiments for a BESS-Hybridized Hydro Turbine Test Rig

system split, and it is illustrated in Fig. 6.9. This particular time frame is chosen to ensure the

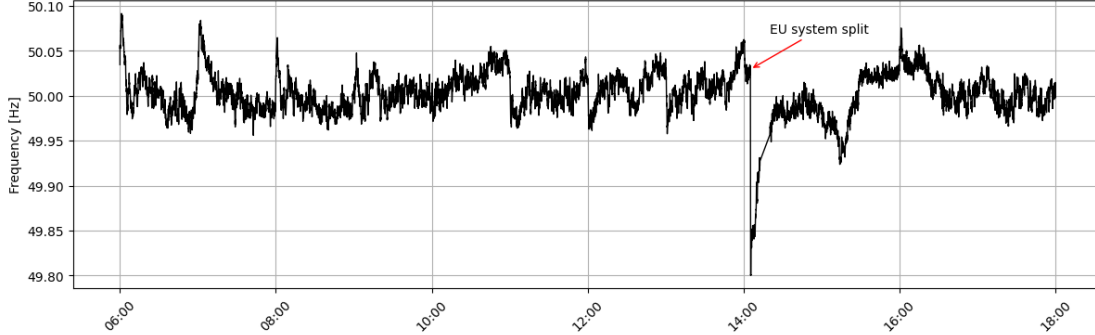


Figure 6.9: Frequency Time Series for the test. Measurement from SwissGrid during the system split on the 8th of January 2021. Data available from [126].

inclusion of typical daily frequency patterns, for the first 8 h of the test, and also to subject the system to more challenging scenarios in the remaining 4 h. More information on the system split event can be found in [126]. Under the described grid conditions, the following tests are conducted:

- a) Kaplan unit operating alone ('Only Hydro').
- b) Hybrid Kaplan unit with a 5 kW/5 kWh BESS (DBF + DLMPC).
- c) Hybrid Kaplan unit with a 9 kW/9 kWh BESS (DBF + DLMPC).
- d) VARspeed Propeller

All the tests are performed considering a flat dispatch plan of 27 kW, constant for the 12 hours, to ensure that the wear and tear analysis of the movements is only related to FCR support. Moreover, the head of the system is kept constant at 10 m. This operating point is selected for the sake of comparison with the findings in [110], which estimates the wear and tear on the BESS-hybrid HPP of Vogelgrun operating at approximately half its nominal power.

For the hybrid tests, DLMPC corresponds to the control described in Section 5.2.2, while DBF consists in the use of a *Dead-Band Filter* (DBF) block on the frequency signal. Each frequency deviation below the frequency threshold f_{\max} is fed to the BESS, while greater actions are taken by both HPP and BESS. A graphical representation of this simple benchmark control is shown in Fig. 6.10. Every hour, the SOE of the BESS is managed by running the ULMPC.

6.4 Key Performance Indicators (KPIs)

This section outlines the critical KPIs for the experimental validation. The KPIs are categorized into four main areas:

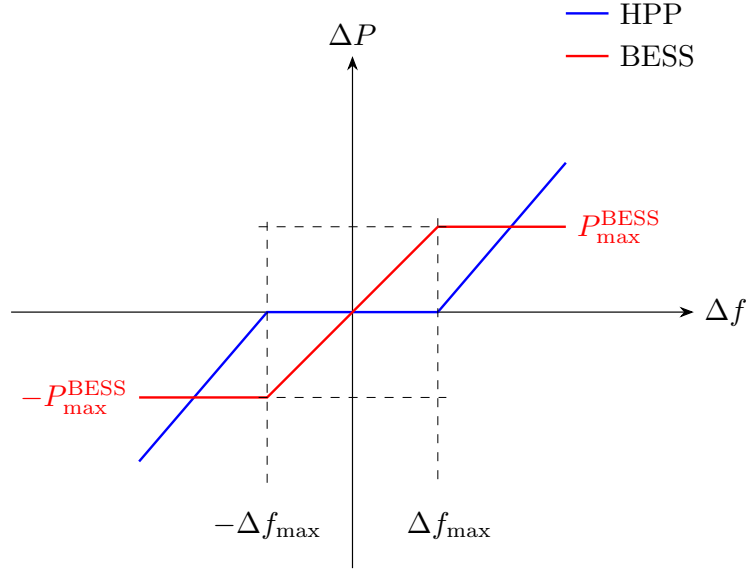


Figure 6.10: Dead-band controller used as a benchmark.

1. **FCR Provision Quality:** Evaluates the accuracy of FCR provision, focusing on active power flow at the PCC and tracking error metrics.
2. **Wear and Tear Reduction:** Assesses the impact on HPP's components, with specific KPIs to estimate the wear and tear on the governing servomechanisms.
3. **Hydraulic and Global Efficiency:** Focuses on the efficiency of the HPP, both in terms of hydraulic efficiency and overall energy conversion.
4. **Safe BESS Operation:** Concentrates on the BESS SOE, ensuring the framework enables continuous and safe operation of the BESS.

6.4.1 FCR Provision Quality

To assess the quality of the FCR provision, together with the dispatch tracking ability, the active power flow P^{PCC} measured at the PCC is considered. For every time step s the expected power output P_s^{set} of the HPP is:

$$P_s^{\text{set}} = P_s^{\text{disp}} + [50 - f_s] \cdot \sigma_f \quad (6.2)$$

where the term f_s indicates the grid frequency value at time s . As a consequence, the tracking error TE_s is the difference between the expected power output P_s^{set} and P_s^{PCC} :

$$\text{TE}_s = P_s^{\text{set}} - P_s^{\text{PCC}} \quad (6.3)$$

Chapter 6. Design of Experiments for a BESS-Hybridized Hydro Turbine Test Rig

To assess the effectiveness of the FCR provision, we consider the RMS of the tracking error array \mathbf{TE} , defined in Eq. (6.4), over the entire window from s_1 to s_2 :

$$RMS(\mathbf{TE}_{s_1:s_2}) = RMS\left(\mathbf{P}_{s_1:s_2}^{\text{set}} - \mathbf{P}_{s_1:s_2}^{\text{PCC}}\right) \quad (6.4)$$

where $\mathbf{TE}_{s_1:s_2}$ is an array containing the values $\text{TE}_s \forall s \in [s_1, s_2]$. The same nomenclature applies to $\mathbf{P}_{s_1:s_2}^{\text{set}}$ and $\mathbf{P}_{s_1:s_2}^{\text{PCC}}$.

The RMS of \mathbf{TE} , as defined in Eq. (6.4), is calculated based on the mean value of TE_s for each 30 s interval. This metric is used to assess the quality of FCR tracking. The use of 30 s averaging allows for the evaluation of the FCR response, specifically in terms of mean power, within a standard time frame for FCR provision. Indeed, many TSOs in Europe require full activation of the FCR response within the 30 s horizon [99, 127].

6.4.2 Wear and Tear Reduction

Wear reduction is assessed through three specific KPIs: servomotors mileage, servomotors NoM, and derivative of *Runner Blade Torque* (RBT). The reduction in both servomotors mileage and NoM serves as a significant indicator of the wear reduction achieved by hybridization [23]. For the definition of mileage and NoM, we refer to [13], as discussed in Chapter 3, and visible in Fig. 3.5. Finally, to estimate the forces affecting the blades and their servomechanisms, the torque on the blade connecting rod is evaluated. In particular, the CDF of the RBT derivative is analyzed.

6.4.3 Hydraulic and Global Efficiencies

Two key efficiency metrics are considered: global efficiency η^g and hydraulic efficiency η . Global efficiency, also known as overall efficiency, encompasses all losses within the energy conversion process, including mechanical, electrical, and hydraulic losses. For the experiments, the hydraulic power for each time k is calculated as a function of the measured discharge \dot{V}_s and net head H_s :

$$P_s^h = \rho \cdot g \cdot \dot{V}_s \cdot H_s \quad (6.5)$$

where ρ indicates the water density (i.e., 1000 kg m^{-3}) and g the gravitational acceleration (i.e., 9.81 m s^{-2}). With the knowledge of the electrical power, measured at the PCC, the global efficiency η_s^g is estimated as:

$$\eta_s^g = \frac{P_s^{\text{PCC}}}{P_s^h} \quad (6.6)$$

On the other hand, the hydraulic efficiency η specifically quantifies the efficiency of the water-to-mechanical energy conversion within the hydro machine. It is based primarily on the condition of the turbine runner and considers losses associated with hydraulic components. For the experiments, thanks to measurements of the torque T_s and speed n_s on the shaft, it is

possible to compute the mechanical power P_s^m and, therefore, the hydraulic efficiency η_s as follows:

$$P_s^m = T_s \cdot n_s \quad (6.7)$$

$$\eta_s = \frac{P_s^m}{P_s^h} \quad (6.8)$$

6.5 Discussion

In this section, the design of an experimental facility for reduced-scale model testing of hydraulic machines hybridized with a BESS is introduced. The capabilities of this upgraded platform and the type of tests that can be performed are also detailed. The presented test rig combines all the fundamental components of a hydroelectric unit, both the hydraulic and the electrical components, within the same testing facility. In such a facility, several testing conditions can be performed to investigate the behavior of hydroelectric units providing ancillary services to the power system under different control frameworks. Furthermore, it is possible to validate and quantify the benefits of the hybridization of a hydraulic unit with BESS, as well as the advantages of the VARspeed technology.

This platform serves as a valuable resource for OEMs or HPP operators to conduct control-in-the-loop testing of their BESS-hybrid HPP controls. Extended testing can be performed to determine the optimal BESS size. The presence of a grid emulator allows for testing the system with respect to various bulk power system dynamics, e.g. simulating typical dynamics of the synchronous area of Continental Europe, as well as the British power system or the European Nordic grid.

7 Experimental Validation of Enhanced FCR Provision from RoR HPPs including a BESS-hybridized configuration

This Chapter presents the experimental validation of the methodologies discussed in Chapter 5 to address wear and tear of RoR HPPs providing enhanced FCR. Reduced-scale experiments are performed on the one-of-a-kind testing platform presented in Chapter 6. For BESS-hybridized RoR HPPs, we validate the proposed MPC-based control considering a comparison with different control strategies and different BESS sizes. The results demonstrate the superior performance of the DLMPC controller, compared to simpler techniques like dead-band control or the standalone RoR scenario, leading to improved FCR provision, reduced servomechanism stress, and extended hydropower asset lifespan. Moreover, the experiments reveal that Kaplan turbines repurposed as VARspeed propellers exhibit similar dynamic response characteristics compared to the standalone Kaplan operation, with the added benefit of effectively eliminating blade movements. Furthermore, the ability to control the speed increases the hydraulic efficiency for certain operating points. In summary, investment in VARspeed technology emerges as a viable alternative to BESS-based hydropower hybridization.

The Chapter includes results from [P6, P7].

Research sub-questions:

- (f) *How can the benefits of RoR HPPs and BESSs integration for FCR provision be effectively evaluated through experiments?*

7.1 Overview

In this section, we present the experimental campaign to validate the framework for BESS-hybrid HPP presented in Section 5.2 and the control of VARspeed propeller presented in Section 5.3. As discussed in Section 6.3, a series of 12 h-long tests are performed under the same grid condition, for a total of 50 h of testing. The frequency time-series enforced at the PCC by the grid emulator is illustrated in Fig. 6.9. The experimental validation focuses on two different objectives:

- Considering BESS-Hybridization, what is the best control strategy to regulate the hybrid system?
- Considering VARspeed propeller operation, how does this compare to BESS-hybrid systems?

7.2 Optimal Control Strategy for BESS-Hybrid RoR HPPs

With respect to the KPIs proposed in Section 6.4, in this section we mainly focus on:

1. FCR Provision Quality
2. Wear and Tear Reduction
4. Safe BESS Operation

7.2.1 FCR Provision Quality

To assess the effectiveness of the FCR provision, we consider the RMS of the tracking error TE, as defined in Eq. (6.4), recalled here:

$$RMS(TE_{s_1:s_2}) = RMS\left(\mathbf{P}_{s_1:s_2}^{\text{set}} - \mathbf{P}_{s_1:s_2}^{\text{PCC}}\right) \quad (6.4)$$

The results in Table 7.1 provide a comprehensive analysis of the FCR tracking error, for various control configurations. These configurations include the baseline scenario, i.e. '*Only Hydro*', together with the BESS hybridization. The BESS hybrid configuration demonstrates a remarkable reduction when compared to the '*Only Hydro*'. This reduction is particularly evident, with all hybrid systems consistently achieving a reduction of at least 47% in tracking error compared to the non-hybrid '*Only Hydro*' system. Although the BESS size contributes to reducing the RMS of TE, the impact is not notably significant. Interestingly, DBF and DLMPC techniques can be considered equivalent in terms of set-point tracking quality. Interestingly, the performance of DBF and DLMPC techniques in terms of set-point tracking quality is comparable. Although DLMPC consistently outperforms DBF, the margin is not wide enough to definitively conclude superior FCR tracking by DLMPC.

7.2 Optimal Control Strategy for BESS-Hybrid RoR HPPs

Configuration	Error (30s)
DBF (5 kW/5 kWh BESS)	0.3872 (−47.18%)
DBF (9 kW/9 kWh BESS)	0.3544 (−51.65%)
DLMPC (5 kW/5 kWh BESS)	0.3696 (−49.58%)
DLMPC (9 kW/9 kWh BESS)	0.3468 (−52.69%)
Only Hydro	0.7331 (+ 0.00%)

Table 7.1: RMSE Values and Reduction (%) of the Tracking Error (TE) with respect to *Only Hydro*.

This can be attributed to the fact that in both cases, the BESS's FCR response is predominantly influenced by the control loop designated for FCR, rather than the set-point splitting policy itself. DLMPC's slight edge may come from its ability to prevent BESS saturation, allowing it to provide service for longer durations compared to scenarios where hydro is solely responsible. This subtle difference, though not drastically impactful, does underscore the benefits of employing DLMPC.

7.2.2 HPP Wear and Tear Reduction

The assessment of wear reduction benefits is undertaken through the consideration of three specific KPIs: servomotor mileage, NoM, and torque oscillation on the blades. The reduction in both guide vane and runner blade NoM and mileage are significant indicators of the wear reduction achieved through hybridization [23]. Table 7.2 provides a comprehensive overview of this wear reduction, underscoring the substantial advantages offered by the MPC technique. All the percentage values are computed relatively to the baseline configuration, represented by '*Only Hydro*'. The DLMPC control method demonstrates superior performance compared to the DBF control. The degree of improvement achieved through more sophisticated control techniques is particularly pronounced for smaller BESS sizes. In essence, when the BESS size is sufficiently large, the necessity for optimal control diminishes. For instance, in the 5 kW BESS experiments, the DBF control attains a substantial reduction of 90.7% in runner blade mileage and 91.6% in the number of movements. Similarly, with the same BESS size, the DLMPC algorithm demonstrates even greater reductions, achieving 94.0% and 97.1% reduction in RBA mileage and the number of movements, respectively. Comparable outcomes are observed when examining the corresponding reduction in GVO servomotors. These findings highlight the benefits of implementing hybridization with advanced control techniques such as DLMPC, particularly standing out for its wear reduction performance for smaller BESS sizes.

Finally, for an estimate of the forces that affect the blades and their servomechanisms, the torque oscillations occurring on the runner blades are evaluated. To capture torque data, strain gauges are employed on the runner blades. The torque values recorded from 14:00 to 15:00, immediately following the system split, are depicted in the first three subplots of Figure RBT (Fig. 7.1). These graphs offer insights into the performance across various configurations.

Chapter 7. Experimental Validation of Enhanced FCR Provision from RoR HPPs including a BESS-hybridized configuration

Configuration	Guide Vanes Opening (GVO)		Runner Blade Angle (RBA)	
	Mileage	NoM	Mileage	NoM
DBF (5 kW BESS)	4.18 (-91.5%)	662 (-92.9%)	3.06 (-90.7%)	753 (-91.6%)
DBF (9 kW BESS)	0.98 (-98.0%)	126 (-98.6%)	0.70 (-97.9%)	128 (-98.6%)
DLMPC (5 kW BESS)	3.33 (-93.2%)	292 (-96.8%)	1.98 (-94.0%)	258 (-97.1%)
DLMPC (9 kW BESS)	0.99 (-98.0%)	64 (-99.3%)	0.61 (-98.2%)	52 (-99.4%)
Only Hydro	49.03 (+0.00%)	9261 (+0.00%)	32.93 (+0.00%)	8970 (+0.00%)

Table 7.2: Reduction in Mileage and Movements (%) of the GVO and RBA Servomechanisms.

The uppermost subplot focuses on the scenario where the Kaplan turbine is the sole FCR provider. Here, the torque on the turbine blades exhibits continuous oscillations, which can be attributed to servomotor movements and consequent fluctuating flow/discharge conditions.

In the second subplot, we compare the behavior of the DBF-controlled 5 kW BESS hybrid system and the DLMPC-controlled 5 kW BESS hybrid system. Initially, both systems demonstrate parallel behavior up until 14:10. At this point, a significant frequency deviation occurs, leading to the saturation of BESS action in the DBF system. Consequently, from 14:10 to 14:22, the HPP is primarily responsible for regulation, as indicated by the noticeable torque oscillations during this interval. In contrast, the DLMPC system preemptively adapts the HPP power output to de-saturate the BESS, thereby maintaining its ability to provide rapid regulation. This adaptability underscores the fundamental difference between the simplistic DBF control strategy and the more sophisticated DLMPC approach. A similar trend is observable in the third subplot, which examines systems with larger BESS capacities. However, it is important to note that the benefits of a more advanced control strategy are less pronounced with larger BESS sizes. Overall, the time-domain subplots (the first three from the top) in Fig. 7.1 demonstrate that incorporating any BESS-hybrid system, regardless of its size, substantially reduces torque oscillations on the turbine blades compared to the 'Only Hydro' configuration.

To obtain a comprehensive analysis of torque oscillation reduction over the experiment duration, the CDF of the blade torque derivative is further examined in the last subplot of Fig. 7.1. In line with the trends observed in other wear reduction KPIs and with what is visible in the time-domain subplots, the sole hydro case demonstrated inferior performance, characterized by elevated levels of torque oscillations on the blades. In the case of the 5 kW BESS, it is noticeable that the CDF of the blade torque derivative is significantly narrower under the DLMPC control strategy compared to DBF. This narrower distribution implies that there are fewer occurrences of high torque oscillations, indicating improved performance in mitigating such oscillations with DLMPC. The presence of a larger BESS size demonstrates a positive impact on the torque oscillation reduction. The 'Only Hydro' scenario emerges as the least effective, marked by higher torque oscillations, thus underperforming in comparison to other configurations.

7.2 Optimal Control Strategy for BESS-Hybrid RoR HPPs

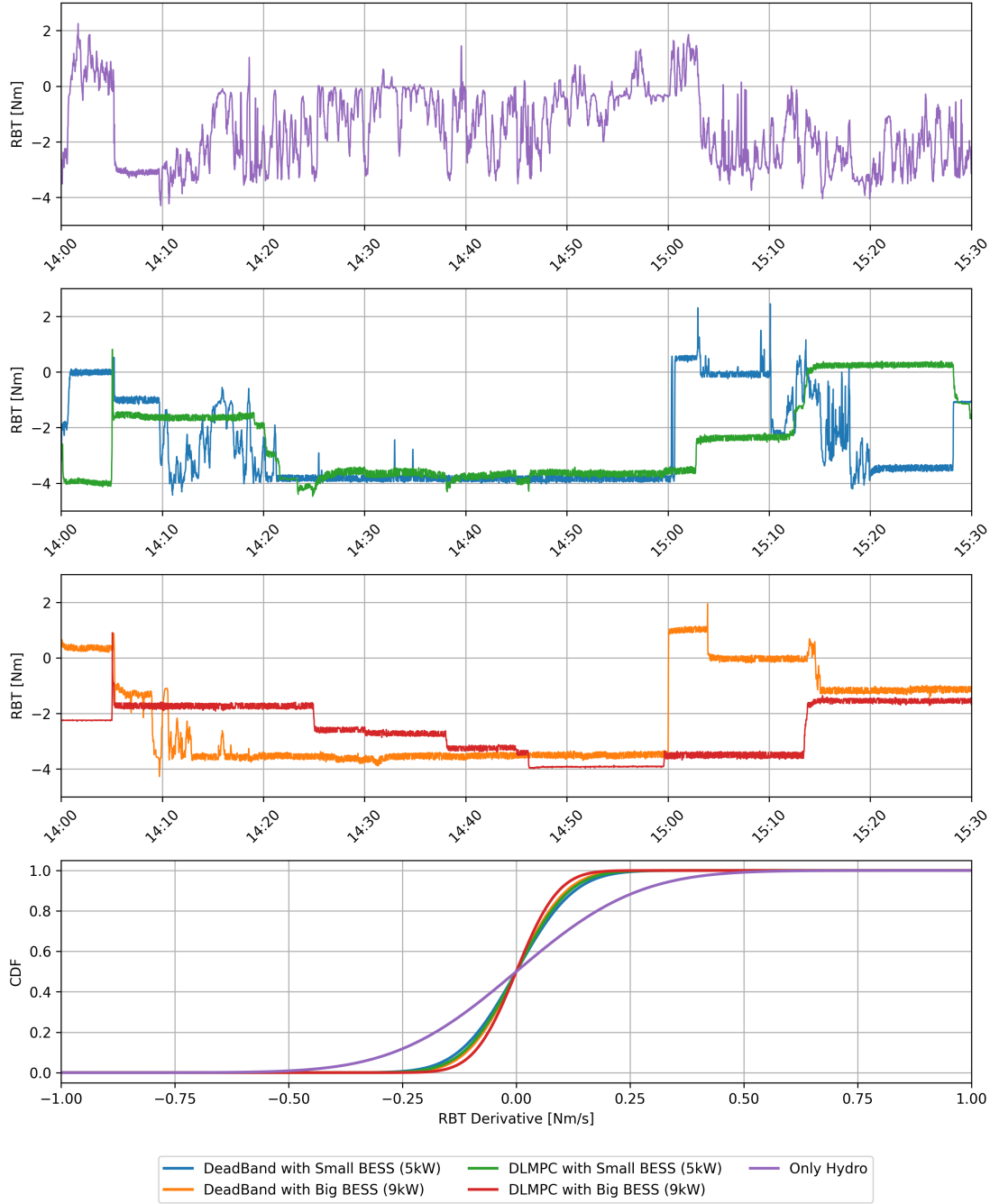


Figure 7.1: Comparative analysis of blade torque oscillation across all test scenarios.

7.2.3 Safe BESS Operation

The BESS SOE evolution over the 12 hours, for each experiment, is illustrated in Fig. 7.2. It is worth noting that, the two DBF experiments operate effectively until the grid split event occurs, around 14h00. Indeed, the regulating energy prediction from Eq. (3.22), is designed to

Chapter 7. Experimental Validation of Enhanced FCR Provision from RoR HPPs including a BESS-hybridized configuration

function correctly in approximately 95% of cases (see Table B.1) under normal grid conditions. However, in the event of a grid disruption, the power grid dynamics drastically change, and the new grid configuration differs from the one on which the SARIMA model was originally trained (see Appendix B). Consequently, both DBF control strategies are unable to control the SOE within its limits during the latter half of the experiment. In contrast, the DLMPC strategy continuously monitors the BESS SOE through the LLMPC. This frequent monitoring guarantees that the BESS operates within its predefined operational limits, even if the FCR energy prediction E^{FCR} deviates from the expected values. This feature substantially bolsters the system's reliability, allowing it to adapt to unforeseen grid dynamics.

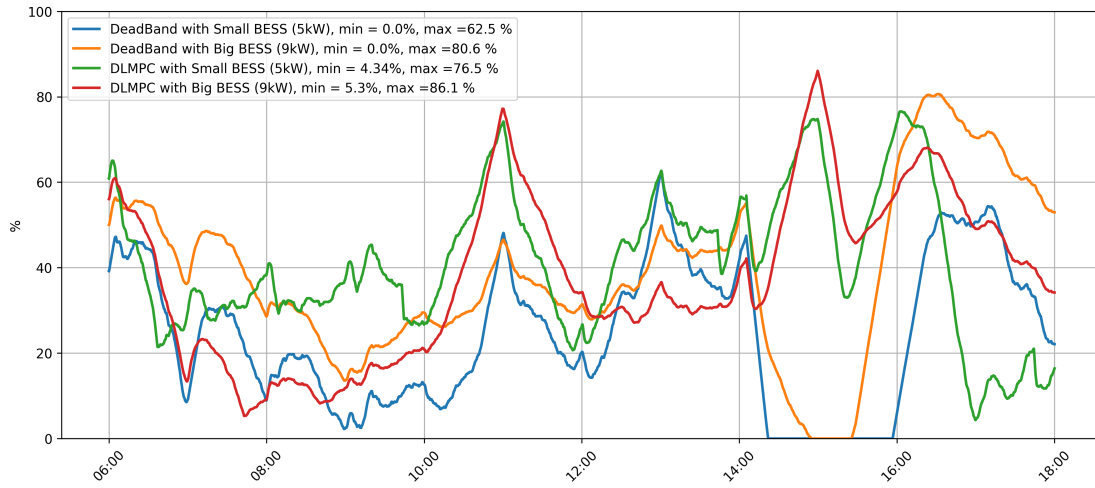


Figure 7.2: BESS SOE evolution during the different experiments.

7.2.4 Summary

This analysis aims to highlight the advantages of BESS hybridization in HPP providing FCR and to conduct a comparative assessment of distinct control techniques across various KPIs. This study covers three primary aspects: the quality of the FCR provision, the mitigation of wear and tear on the hydroelectric governing system, and the safe operation of the BESS. By integrating BESS with RoR HPPs using a double-layer MPC approach, we validate a novel strategy to enhance FCR capabilities and simultaneously reduce wear and tear. The experimental results showcased the superiority of the double-layer MPC strategy over simpler techniques such as dead-band control. The hybridized system showcased enhanced FCR provision quality and a notable reduction in servomechanism stress. The analysis of wear reduction revealed a substantial decrease in both GVO and RBA mileage, ranging from 93.2% with a 5 kW BESS to as much as 98% for a 9 kW BESS. Similar reductions were observed in the case of movements. Moreover, reduced torque oscillations on the blades further emphasize the benefits of the proposed hybridization approach.

7.3 Experimental Investigation of Repurposed Kaplan Turbines as Variable-Speed Propellers for Maximizing FCR

In this section, we compare the VARspeed operation of the Kaplan used as a propeller with the BESS-hybridized operation, operated with DLMPC control, as it is the one that performs better for each BESS size. With respect to the KPIs proposed in Section 6.4, we mainly focus on:

1. FCR Provision Quality.
2. Servomechanisms Wear and Tear Reduction.
3. Hydraulic and Global Efficiencies.

7.3.1 FCR Provision Quality

Similarly to Table 7.1, Table 7.3 provides a comprehensive analysis of the FCR tracking error for various control configurations. These configurations include 'Only Hydro', the two DLMPC-driven BESS hybridization scenarios, and the VARspeed scenario. As previously proved, the BESS hybrid configuration demonstrates a remarkable reduction when compared to the 'Only Hydro'. Interestingly, the VAR-speed propeller operation shows slightly worse performance than BESS-hybridization but still manages to reduce tracking error by 15% compared to the non-hybrid 'Only Hydro' system.

Configuration	Error (30s)
DLMPC (5 kW/5 kWh BESS)	0.3696 (−49.58%)
DLMPC (9 kW/9 kWh BESS)	0.3468 (−52.69%)
Only Hydro	0.7331 (+ 0.00%)
VARspeed	0.6284 (−14.18%)

Table 7.3: RMSE Values and Reduction (%) of the Tracking Error (TE) with respect to *Only Hydro*.

7.3.2 HPP Wear and Tear Reduction

Table 7.4 compares the wear reduction achieved through the BESS hybridization or VARspeed operation against the one in Kaplan standalone operation. Similarly to the previous section, all percentage values are relative to the 'Only Hydro' baseline configuration. The BESS hybridized Kaplan operation reduces both GVO and RBA mileage and NoM with respect to the baseline configuration. For example, with a 5 kW BESS, the hybrid setup achieves a substantial 94.0% mileage reduction for both GVO and RBA compared to the "Only Hydro" configuration. An even greater reduction is visible for the number of movements (-97%). Notably, the VARspeed propeller case exhibits a unique characteristic in which the turbine blades remain stationary,

Chapter 7. Experimental Validation of Enhanced FCR Provision from RoR HPPs including a BESS-hybridized configuration

resulting in zero blade movement and mileage for the servomotors (-100%). Simultaneously, it is essential to acknowledge that VARspeed control significantly increases GVO movements (+45%) and mileage (+122%). In this respect, the increased load on GVO mechanisms might seem concerning. However, it is crucial to recognize that GVO servomechanisms are inherently more resilient to wear compared to RBAs [128]. For this reason, despite the extra wear, VARspeed remains a viable alternative to BESS-hybridization.

Configuration	Guide Vanes Opening (GVO)		Runner Blade Angle (RBA)	
	Mileage	NoM	Mileage	NoM
DLMPC (5 kW BESS)	3.33 (-93.2%)	292 (-96.8%)	1.98 (-94.0%)	258 (-97.1%)
DLMPC (9 kW BESS)	0.99 (-98.0%)	64 (-99.3%)	0.61 (-98.2%)	52 (-99.4%)
Only Hydro	49.03 (+0.0%)	9261 (+0.0%)	32.93 (+0.0%)	8970 (+0.0%)
VARspeed	109.09 (+122.5%)	13484 (+45.6%)	0.0 (-100.0%)	0.0 (-100.0%)

Table 7.4: Reduction in Mileage and Movements (%) of the GVO and RBA servomechanisms.

Finally, for an estimate of the forces that affect the blades and their servomechanisms, the derivative of the torque occurring on the runner blades' servomechanism is evaluated. Similarly to Fig. 7.1, Fig. 7.3 shows the blade torque measurement for the first 6 h of the experiment in the upper subplots and the CDF of the RBT derivative on the lower one. In line with the trends observed in other wear reduction KPIs, the 'Only Hydro' case demonstrates inferior performance, characterized by elevated levels of torque derivative on the blades. The CDF of the RBT derivative is most constricted in the VARspeed case, surpassing both BESS hybrid setups in reducing torque variations. Specifically, Fig. 7.3 highlights the significant advantage of lacking the RBA servomechanism. Indeed, for the VARspeed scenario, the torque on the blade pin maintains a near-constant level (as visible from the first subplot), signifying minimal torque fluctuations throughout the operation.

7.3.3 Hydraulic and Global Efficiencies

Fig. 7.4 illustrates the hydraulic efficiency of the fixed-speed Kaplan turbine and the VARspeed propeller (fixed blades) across the range of operating conditions tested. The graph demonstrates that the VARspeed propeller exhibits slightly higher hydraulic efficiency on average (+ 1.5%), despite being less efficient in part-load conditions. This is caused by the choice to fix the Kaplan RBA to 18°, close to the power of the best efficiency point, as visible from Fig. 5.3. Overall, the increase in hydraulic efficiency by the VARspeed control strongly depends on the operating point. Hence, we cannot definitively claim that the VARspeed operation of a retrofitted Kaplan turbine as a propeller is superior in efficiency to its original Kaplan operation. However, we can at least consider them to be viable alternatives. The hydraulic efficiency of the fixed-speed Kaplan, shown in Fig. 7.4 in green, is in line with the expected efficiency values of Fig. 5.3. It is worth noticing that these efficiencies can be considered repre-

7.3 Experimental Investigation of Repurposed Kaplan Turbines as Variable-Speed Propellers for Maximizing FCR

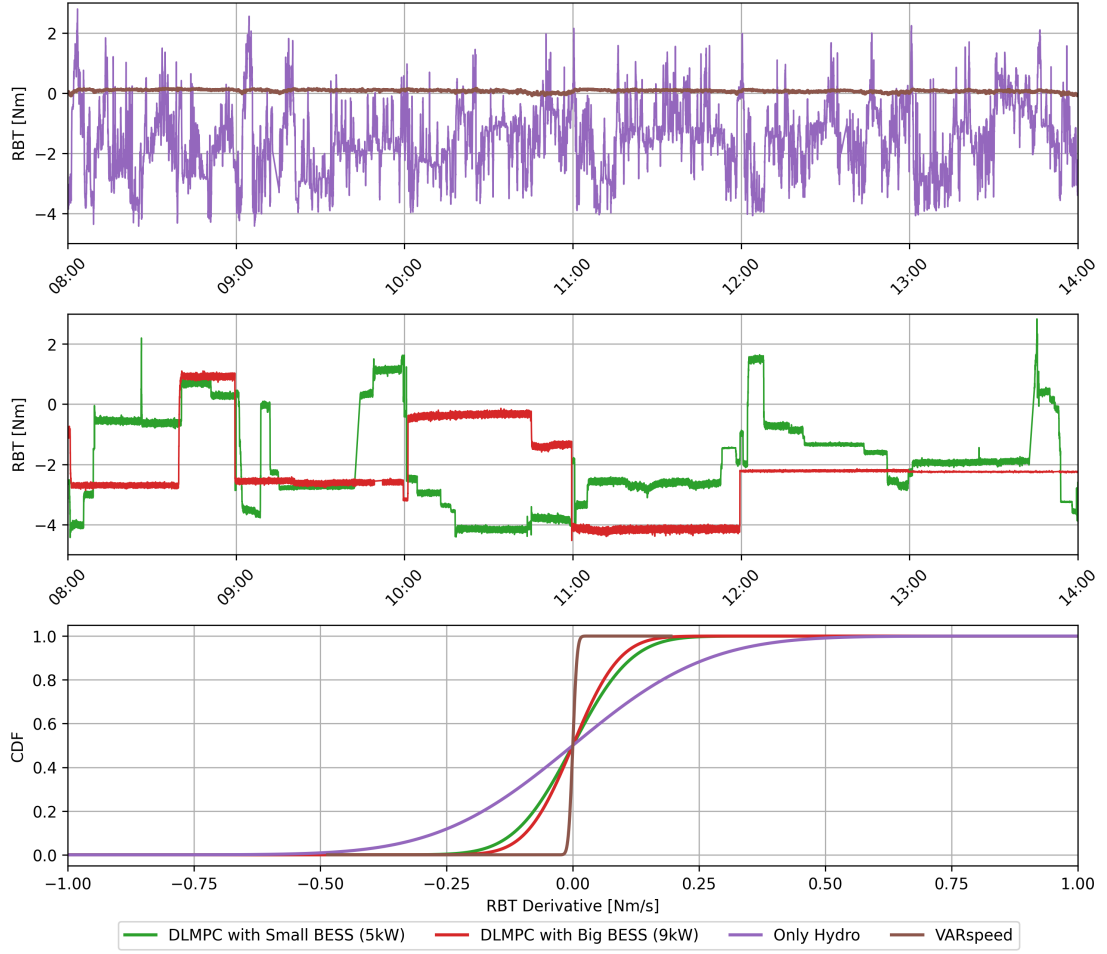


Figure 7.3: Comparative analysis of blade torque oscillation across all test scenarios.

sentative of the prototype machine in hydraulic similarity to the reduced-scale model tested. In Fig. 7.5, the global efficiency for the baseline case and the VARspeed propeller are displayed. The global efficiency includes the efficiency of the generator for the fixed-speed case and the combined efficiency of the generator + FSFC for the VARspeed case. The graph shows that, when accounting for the losses incurred by the power converter, the global efficiency of VARspeed propeller turbines tends to be lower compared to the fixed-speed Kaplan. However, the efficiency of the synchronous machine and the converter do not scale to the prototype, making it hard to conduct a precise quantitative analysis.

7.3.4 Summary

In conclusion, Table 7.5 summarizes the performance of each configuration. In particular, the "+" or "-" symbols indicate whether a configuration performs better or worse, respectively, than the baseline "Only Hydro" scenario. When both configurations outperform the baseline,

Chapter 7. Experimental Validation of Enhanced FCR Provision from RoR HPPs including a BESS-hybridized configuration

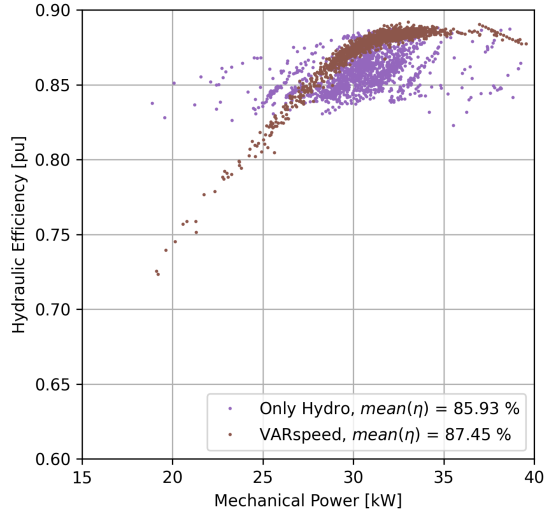


Figure 7.4: Hydraulic Efficiency η .

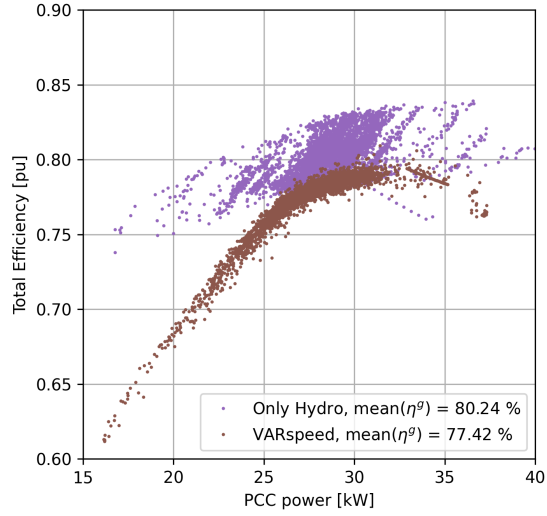


Figure 7.5: Global Efficiency η^g .

we use "++" to highlight the superior performer. In the "FCR" column, the symbol "+" signifies more accurate tracking of the FCR power, indicating a smaller error. Regarding wear and tear, the "+" value denotes a greater reduction in wear, resulting in less mileage, reduced movements, and lower values of the RBT derivative. In the latter columns, the symbol "+ -" is used to indicate similar performance to the baseline configuration.

Configuration	FCR RMS(TE)	Wear and Tear			Efficiency	
		GVO	RBA	RBT	η	η^g
BESS Hybrid HPP	++	+	+	+	+ -	+ -
VARspeed	+	-	++	++	+ ¹	- ²

Table 7.5: KPIs Comparison with the 'Only Hydro' Scenario.

¹ As discussed in Section 7.3.3, this result strongly depends on the operating points of the hydraulic turbine. It is not possible to claim an overall increase of η when converting a Kaplan turbine into a VARspeed propeller.

² It is not possible to scale η^g to the prototype. However, it is clear that the presence of the FSFC results in a decrease of the overall efficiency.

7.4 Discussion

In this chapter, we have explored solutions for operational challenges in RoR HPPs related to FCR provision. The strategies analyzed include the integration of BESS with RoR HPPs using a double-layer MPC approach, and the implementation of VARspeed control for the Kaplan turbine used as a propeller.

BESS Integration with RoR HPPs: The proposed control framework consists of an upper layer MPC responsible for SOE management of the BESS and a lower layer MPC for optimal splitting policy of power set points between the turbine and the BESS. Rigorous reduced-scale experiments conducted in an innovative testing platform validated the effectiveness of the proposed MPC-based control strategy across diverse grid scenarios and BESS sizing. The experimental results showcased the superiority of the double-layer MPC strategy over simpler techniques such as dead-band control. The hybridized system showcased enhanced FCR provision quality and a notable reduction in servomechanism stress. The analysis of wear reduction revealed a substantial decrease in both GVO and RBA mileage, ranging from 93.2% with a 5 kW BESS to as much as 98% for a 9 kW BESS. Similar reductions were observed in the case of movements. Moreover, reduced torque oscillations on the blades further emphasize the benefits of the proposed hybridization approach. These results provide valuable information for HPP owners and operators, highlighting the benefits of incorporating a BESS asset into their power plants. By adopting optimal control strategies, they can not only enhance the return on their investment but also maximize the advantages of the hybridization system.

VARspeed Propeller Operation: The VARspeed propeller strategy stands out as a solid alternative to BESS hybridization. Its primary strength is in being able to operate the system without any RBA servomechanism movement, effectively minimizing stress on the link pin. This approach, however, leads to increased activity in the GVO mechanisms. It is important to note that wear and tear concerns are typically more pronounced with the RBA than the GVO. In terms of FCR tracking, the VARspeed operation performs better than the baseline Kaplan operation, but it does not quite reach the FCR tracking quality of the BESS hybrid configuration.

Considering the sensitivity of the Kaplan turbine's blade mechanism, a conclusive preference between the two setups is not evident. The choice depends largely on the specific conditions of the HPP. When the Kaplan turbine is nearing the end of its operational life and the blade servomotors are no longer functional, VARspeed control offers an attractive solution that does not require any blade movement. In contrast, when the Kaplan turbine is aging but still operational, the BESS hybrid configuration stands out, extending the turbine's life while ensuring efficient power generation. The experimental comparison underscores the need for power plant owners to adopt a case-dependent approach, aligning their capital expenditure (CAPEX) strategies with the specific conditions and life cycle of their equipment.

8 Conclusion

This Ph.D. thesis has proposed, discussed, and validated optimal control techniques for the enhanced provision of ancillary services by HPPs, specifically focusing on FCR and aFRR. Keeping in mind the main research question: *"How can we optimize the integration and control of hydropower plants with new technologies to boost their role in ancillary service provision and ensure asset longevity?"*, we summarize the findings by answering to each research sub-question introduced in Chapter 1.

(a) *How can we maximize aFRR provision of PSPs while reducing the number of start-ups and stops of its units?*

Chapter 2 presented a methodology for optimizing the power dispatch and reserve allocation in hydropower plants, leveraging the HSC operating mode. The proposed approach solves a series of convex optimization problems efficiently, rather than relying on a single MIP problem. Validated by simulating the operation of PSP of Grand'Maison (12 units), the method efficiently solves complex a short-term dispatch problem (e.g aFRR and dispatch allocation for the next 15-30 minutes) in a sub-minute horizon, making it a viable algorithm for PSP operation. Furthermore, the presented methodology offers a tool for hydropower plant operators to optimize power dispatch and reserve allocation, reducing the number of start-up and stops (-5.5% over one year of operation for the case study).

(b) *How does FCR provision affect RoR HPPs equipped with Kaplan turbines?*

The provision of FCR is responsible for an increase in wear and fatigue and a decrease in the machine's performance, especially in terms of efficiency. Chapter 3 presents a method to track the decrease in performance of Kaplan turbines over time. The proposed tool allows for performing a fast online check of the CAM relationship, without altering the HPP production. The system operating with the updated CAM relation proves a substantial performance improvement with respect to a turbine control system where the machine aging is not taken into consideration. The method is validated via numerical simulations, and its performance is

Chapter 8. Conclusion

thoroughly assessed. The results from the case study show that thanks to the updated CAM, the unit can achieve an efficiency increase of 2.6% over one year of operation.

(c) Which control strategy can improve FCR provision of RoR HPPs, while slowing down the aging of its units?

In Chapter 3, a droop-based control framework to enhance FCR provision with a RoR HPP is developed. The framework relies on the forecast of the energy required for FCR provision over a time horizon of one hour, thanks to a suitably identified AR model, presented in Appendix B. It has been shown that, by considering the information provided by such forecasts, the HPP control can provide more regulating power while ensuring the system's reliability in terms of discharge control. The discharge is controlled by computing an offset discharge once per hour which, in turn, reduces the number of movements of the regulating components of the hydroelectric unit. This constitutes an improvement for the standard control system that imposes continuous movements of guide vanes and blades to respect the discharge set-point. However, despite advancements in aging monitoring and movement reduction in RoR HPPs, a large portion of servomechanism activity is still originated by FCR provision.

(d) What are the main limitations of BESSs when providing FCR?

Chapter 4 studied the BESSs' ability to supply FCR support, especially if interfaced with GFR converters, while concurrently providing other grid services. Nevertheless, a notable operative constraint is given by the BESS power and energy budgets, which limit the extent of FCR provision. The relation between FCR provision and BESS energy is expressed in mathematical terms by the day ahead formulation of the framework. This stage proposes a dispatch plan by accounting for the uncertainty in the forecast of PV production and load demand. The problem calculates the necessary portion of the BESS's energy budget required to manage these uncertainties and ensure the dispatch plan is followed. Typically, this calculated portion is a fraction of the BESS's total capacity. If there is remaining capacity in the BESS after covering the forecast uncertainties, we utilize it to provide FCR services. The droop setting is carefully chosen to fully utilize, but not exceed, the BESS's remaining capacity.

(e) How can we maximize the ancillary service provision of BESS assets?

A comprehensive framework for the simultaneous provision of multiple services (i.e., feeder dispatchability, frequency, and voltage regulation) to the grid utilizing a GFR-converter-interfaced BESS is proposed in Chapter 4. Thanks to the forecast of the energy required for FCR provision, the framework maximizes the amount of FCR that can reliably be provided by the BESS. Moreover, the BESS modeling proposed in Chapter 4 is fundamental for what is presented by Chapter 5, where an optimal control for BESS-hybrid HPP is developed.

(f) What are the optimal strategies for RoR HPPs hybridized with BESS to improve FCR provision and extend the HPP asset lifetime?

An optimal control strategy for RoR HPPs hybridized with BESSs, relying on a double-layer MPC, is developed in Chapter 5. The upper layer MPC acts as a state-of-energy manager for the BESS, employing a forecast of the required regulating energy for the next hour. The lower-layer MPC optimally allocates the power set-point between the turbine and the BESS. In Chapter 7, experimental results prove the superiority of the double-layer MPC strategy over simpler techniques such as dead-band control. The hybridized system showcased enhanced FCR provision quality and a notable reduction in servomechanism stress. The analysis of wear reduction revealed a substantial decrease in both GVO and RBA mileage. This decrease ranges from 93.2% with a BESS-rated power equal to 20% of the HPP regulating power, up to 98% when the BESS power constitutes 36% of the HPP regulating power. Similar reductions were observed in the case of movements. Moreover, reduced torque oscillations on the blades further emphasize the benefits of the proposed hybridization approach.

(g) What alternative approaches, besides BESS hybridization, could effectively enhance FCR provision of RoR HPPs?

In Chapter 7, the VARspeed propeller strategy is experimentally investigated as a possible alternative to BESS hybridization. The test results prove the VARspeed strategy to provide good FCR tracking quality while operating without any RBA servomechanism movement, effectively minimizing stress on the blade link pin. However, an increased activity in the GVO mechanisms is detected (+45.6% movements). Considering the sensitivity of the Kaplan turbine's blade mechanism, a conclusive preference between BESS hybridization and VARspeed operation is not evident. The choice depends largely on the specific operating conditions of the HPP. When the Kaplan turbine is nearing the end of its operational life and the blade servomotors are no longer functional, VARspeed control offers an attractive solution that does not require any blade movement. In contrast, when the Kaplan turbine is aging but still operational, BESS hybridization is preferable. The experimental comparison underscores the need for power plant owners to adopt a case-dependent approach, aligning their CAPEX strategies with the specific conditions and life cycle of their equipment.

(h) How can the benefits of RoR HPPs and BESSs integration for FCR provision be effectively evaluated through experiments?

Chapter 6 presented the design of an experimental facility for reduced scale model testing of hydraulic machines hybridized with a BESS. This platform serves as a valuable resource for OEMs or HPP operators to conduct control-in-the-loop testing of their BESS-hybrid HPP controls. Extended testing can be performed to determine the optimal BESS size. The presence of a grid emulator allows for testing the system with respect to various bulk power system

Chapter 8. Conclusion

dynamics, e.g. simulating typical dynamics of the synchronous area of Continental Europe, as well as the British power system or the European Nordic grid.

A Convexification of Problem (3.6)

A.1 Methodology

In this appendix, the CAM computation problem presented in (3.6) and recalled here below is formulated as a convex optimization problem, to target the global optimal solution and to ensure time-efficient computation.

$$\begin{aligned} [\alpha_\ell, \beta_\ell] &= \operatorname{argmax} \quad \eta(\alpha_\ell, \beta_\ell, H, n_{\text{nom}}) \\ \text{s.t.} \quad &\dot{V}(\alpha_\ell, \beta_\ell, H, n_{\text{nom}}) = \dot{V}_\ell \\ &\alpha_\ell, \beta_\ell \in \Omega_{\alpha, \beta} \end{aligned} \quad (3.6)$$

First of all, it is necessary to prove the function η^* to be convex (or concave). In general, efficiency models of hydraulic turbines have a hill-like shape, usually called *hill-chart*. This characteristic supports the hypothesis of concavity, even though it does not prove it mathematically. For this reason, a way to assess the concavity/convexity of the efficiency meta-model is proposed in Appendix A. In this regard, the *Second-Order Condition* for concavity [119] is considered. This allows for proving the concavity of a function by analyzing its Hessian. By construction, η^* is twice differentiable. Moreover, the guide vane opening angle α and the blade opening angle β are limited within respectively $[\alpha_{\min}, \alpha_{\max}]$ and $[\beta_{\min}, \beta_{\max}]$. By normalizing α and β , it is trivial to prove that:

$$\text{dom } \eta^* = \text{dom } \dot{V}^* = \Omega_{\alpha, \beta} = [0; 1] \quad (A.1)$$

is convex. Therefore, it is possible to determine whether η^* is a concave function, for a single value of n_{ED} , i.e., for a certain head, by proving that:

$$\nabla^2 \eta^*(\alpha, \beta, n_{\text{ED}}) \leq 0 \quad \forall \alpha, \beta \in \Omega_{\alpha, \beta} \quad (A.2)$$

Appendix A. Convexification of Problem (3.6)

for each given value of n_{ED} (i.e. for each given value of H , since n is fixed to the synchronous rotational speed). It is possible to reformulate (A.2) as follows:

$$\zeta_\eta = \zeta_\eta(\alpha, \beta) = \max_{i=1}^2 \lambda_i(\nabla^2 \eta^*(\alpha, \beta, n_{\text{ED}})) \leq 0 \quad (\text{A.3})$$

where, for each of the Hessian matrices, $\lambda_{1,2}(\alpha, \beta)$ are the two eigenvalues of the matrix, and ζ is its spectral abscissa. For a single value of head H , and for each value of discharge \dot{V}_ℓ , the optimization Problem (3.6) can be reformulated in:

$$\begin{aligned} \min_{\alpha_\ell, \beta_\ell} \quad & \omega_\eta \cdot \left[1 - \eta^*(\alpha_\ell, \beta_\ell, n_{\text{ED}}) \right] + \\ & \omega_{\dot{V}} \cdot \left[\dot{V}_\ell - \dot{V}^*(\alpha_\ell, \beta_\ell, n_{\text{ED}}) \right]^2 \\ \text{s.t.} \quad & \alpha_\ell, \beta_\ell \in \Omega_{\alpha, \beta} \\ & \alpha_{\ell-1} \leq \alpha_\ell \\ & \beta_{\ell-1} \leq \beta_\ell \end{aligned} \quad (\text{A.4})$$

where the last two constraints ensure the CAM to be a monotonically increasing function with respect to α and β . The two weights $\omega_\eta, \omega_{\dot{V}}$ are chosen to, first, comply with the discharge set-point and, secondly, maximize the efficiency. Problem (A.4) is a convex optimization problem if Eq. (A.3) is satisfied, and if the discharge surrogate model \dot{V}^* is linear. This is generally not the case, since \dot{V}^* is built as indicated in Section 3.3.2, as a sum of piece-wise polynomials of different orders. Nevertheless, the last two constraints of Problem (A.4) are forcing the solution $[\alpha_\ell, \beta_\ell]$ to be around $\alpha_{\ell-1}, \beta_{\ell-1}$, especially when $\dot{V}_{\ell-1}$ is close to \dot{V}_ℓ . In particular, if L is large enough, \dot{V}_ℓ can be seen as a relatively small deviation from $\dot{V}_{\ell-1}$. In full-scale HPPs, the discharge is controlled with a precision of $\pm 1\%$ of the nominal discharge. For this reason, L has to be chosen such that $\dot{V}_\ell - \dot{V}_{\ell-1}$ is at least smaller than this value, i.e. $L \geq 100$. This allows for a linearization of \dot{V}^* around $(\alpha_{\ell-1}, \beta_{\ell-1})$, indicated with the term $\overline{\dot{V}}^*|_{\ell-1}$. The linearized form can be substituted in Problem (A.4), obtaining:

$$\begin{aligned} \min_{\alpha_\ell, \beta_\ell} \quad & \omega_\eta \cdot \left[1 - \eta^*(\alpha_\ell, \beta_\ell, n_{\text{ED}}) \right] + \\ & \omega_{\dot{V}} \cdot \left[\dot{V}_\ell - \overline{\dot{V}}^*(\alpha_\ell, \beta_\ell, n_{\text{ED}})|_{\ell-1} \right]^2 \\ \text{s.t.} \quad & \alpha_\ell, \beta_\ell \in \Omega_{\alpha, \beta} \\ & \alpha_{\ell-1} \leq \alpha_\ell \\ & \beta_{\ell-1} \leq \beta_\ell \end{aligned} \quad (\text{A.5})$$

If inequality (A.3) is satisfied, then Problem (A.5) is a convex optimization problem.

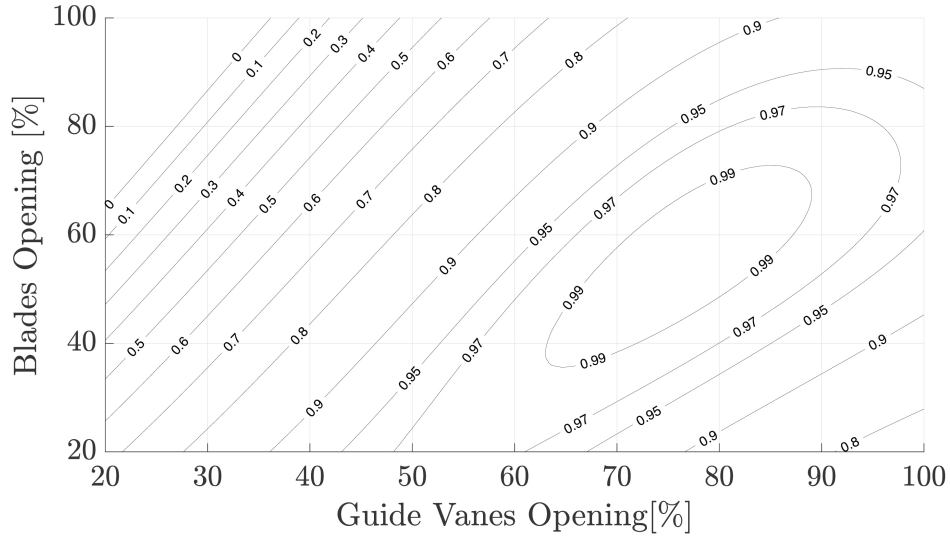


Figure A.1: Surrogate model of the efficiency η^* , as a function of the guide vanes opening and the blade opening. The values for η , α , and β are normalized with respect to their maximum value.

A.2 Results

A graphical representation of the modeled function η^* , supporting the hypothesis of concavity, is shown in Fig. A.1. To obtain a mathematical proof of the concavity of η^* , (A.3) is considered. Fig. A.2 shows in blue the portion of $\Omega_{\alpha,\beta}$ where ζ_η is ≤ 0 , for a head value of $H = 12$ m, and, therefore, where η^* can be considered concave. Moreover, it is possible to observe the constant discharge iso-lines. For every discharge value (i.e. for every line) the optimization algorithm is responsible for choosing the best combination of α and β , which maximizes efficiency. The hypothesis of concavity does not hold on the border between the blue and the red regions. It can also be proven that the red region alone is concave, hence the optimal solution is reached for constant discharge lines falling entirely in this area. Nevertheless, for the discharge iso-lines crossing the border, the optimization problem has to select a local minimum. A similar result is obtained for other head values. Therefore, the application of Algorithm 3 returns the global minimum (i.e. the maximum efficiency) for the larger portion of $\Omega_{\alpha,\beta}$, where the concavity condition holds. Since the non-convex area represents a small portion of the domain, this does not drastically affect the result.

Appendix A. Convexification of Problem (3.6)

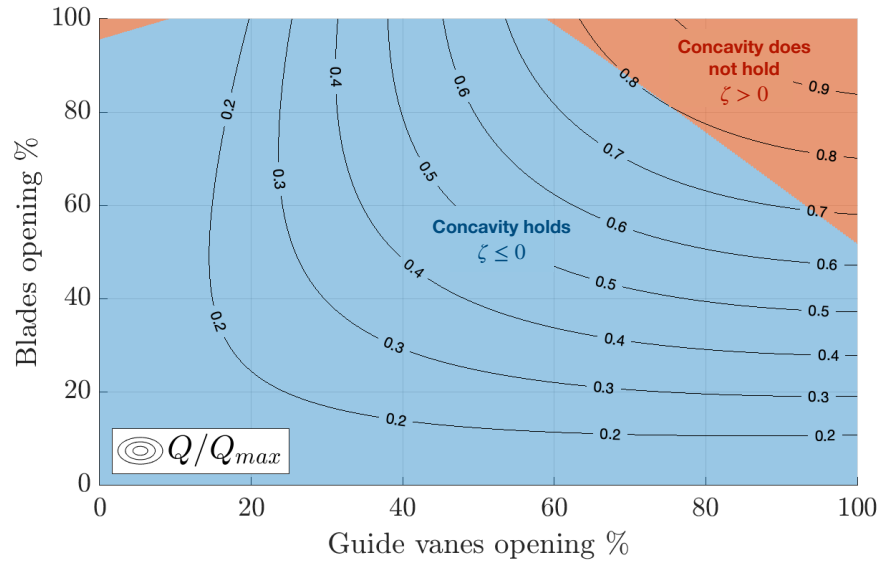


Figure A.2: Space of the solutions for Eq. (A.3) for $H = 12\text{m}$. The contour lines represent different discharge levels, normalized with respect to their maximum value.

B Forecasting the Grid's Frequency

B.1 Regulating Energy Forecasting

This appendix discusses estimating the integral of the forecast of the FCR regulating energy. For the sake of clarity, we recall Eq. (3.22) here below:

$$E_h^{\text{FCR}} = \sigma_f \int_h \Delta f dt = \sigma_f W_h \quad (3.22)$$

The quantity E^{FCR} is supposed to be zero over a sufficiently long period, if the aFRR is well planned in the synchronous area (e.g. the Synchronous area of Continental Europe). However, this is not verified for a shorter time window (e.g., 1 h). The ability to predict this quantity was initially introduced in [77] and subsequently adopted by various researchers, including [P2]. [77] proves that *Auto-Regressive* (AR) models can be exploited to forecast W_h . In particular, the study shows that AR models of order 8 (i.e. AR(8)) are well suited for the scope. Figure B.1 shows the expected domain for the forecast \hat{W}_h from [77, 78], computed on the EPFL data-set.

In this contribution, we propose an enhanced model for frequency forecasting and compare its performance with the model from [77] in terms of standard deviation. where $T = 1$ hour. The motivation for updating the models stems from a more comprehensive statistical analysis carried out by the authors using a one-year-long set of frequency time series (from March 2019 to April 2020). This analysis demonstrates a discernible daily seasonality effect, as evident from Fig. B.2, which was not considered in the model of [77]. For this reason, a new *Seasonal Auto-Regressive Integrated Moving Average* (SARIMA) model is introduced. We present the model and its performance over a testing set of data (from September 2020 to December 2020) in Table B.1, by comparing it to the forecasting model used in [77]. In this table, v^F indicates the time intervals at which the residuals exceed the corresponding 95% or 99% confidence intervals. It is defined as follows:

$$v^F = \frac{\text{Time with } |r_i| \geq \hat{W}^{\dagger\dagger}}{\text{Total observation time}}, \quad (B.1)$$

Appendix B. Forecasting the Grid's Frequency

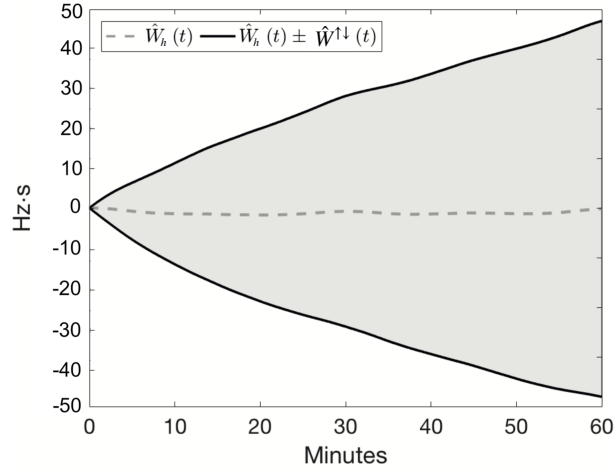


Figure B.1: In light gray, the CI of the expected evolution of $W_h(t)$ in 1-hour time intervals, EPFL data-set, (CI = 5-95%).

Models	σ	ρ	v^F	MSE
ARIMA(8, 0, 0)(0, 0, 0)	25	95%	7.2%	562
	25	99%	1.5%	562
SARIMA(6, 0, 0)(0, 1, 1) ₂₄	22	95%	7.2%	485
	22	99%	2.1%	485
Dataset: PMU-5, EPFL, September 2020 - December 2020 [108]				

Table B.1: Comparison Between the Forecasting Models.

Lastly, a residual analysis of the SARIMA model is conducted, to demonstrate that the proposed model cannot be further improved by increasing the order of the model. The residuals exhibit a zero-mean normal distribution. Furthermore, a Durbin-Watson test confirms the absence of correlation among the residuals. The test statistic is computed as:

$$s = \frac{\sum_{i=2}^N (r_i - r_{i-1})^2}{\sum_{i=1}^N (r_i)^2} = 2.0051.$$

Given its enhanced performance, the forecaster selected to produce the regulating energy prediction is SARIMA(6, 0, 0)(0, 1, 1)₂₄.

B.2 Short-Term Frequency Forecasting

Frequency prediction is a crucial component of the lower-layer MPC. Specifically, the experimental validation that employs the lower layer MPC necessitates second-interval predictions for a 30-second horizon. The inherent stochastic behavior of grid frequency in bulk power systems poses a significant challenge in achieving accurate predictions. Only a limited number of studies have explored the feasibility of such predictions. One exception can be found in [129], which introduces the real-time prediction of grid voltage and frequency using artificial neural networks. This method primarily focuses on short-term frequency prediction (0.183 ms and 1 sec), demonstrating satisfactory *Root Mean Squared Error* (RMSE) values for both one-step and three-step ahead predictions. However, the RMSE achieved through this approach is on par with the RMSE obtained from a simple AR(0) regression model. This regression model essentially assumes continuity, implying that the subsequent frequency measurement remains consistent with the preceding one. In detail, [129] claims an RMSE= 0.0039 Hz of their one-sec ahead forecaster tested for during one day of May 2019. AR(0) regression model for secondly-sampled frequency time-series for the same month (data from: [130]) results in an RMSE = 0.0024. However, given that the data set utilized in [129] is not publicly accessible, offering more comprehensive insights presents a challenge. Consequently, the frequency predictor for the lower-layer MPC does not hinge on genuine forecasting but rather assumes that the forthcoming 30 seconds of frequency will mirror the preceding values.

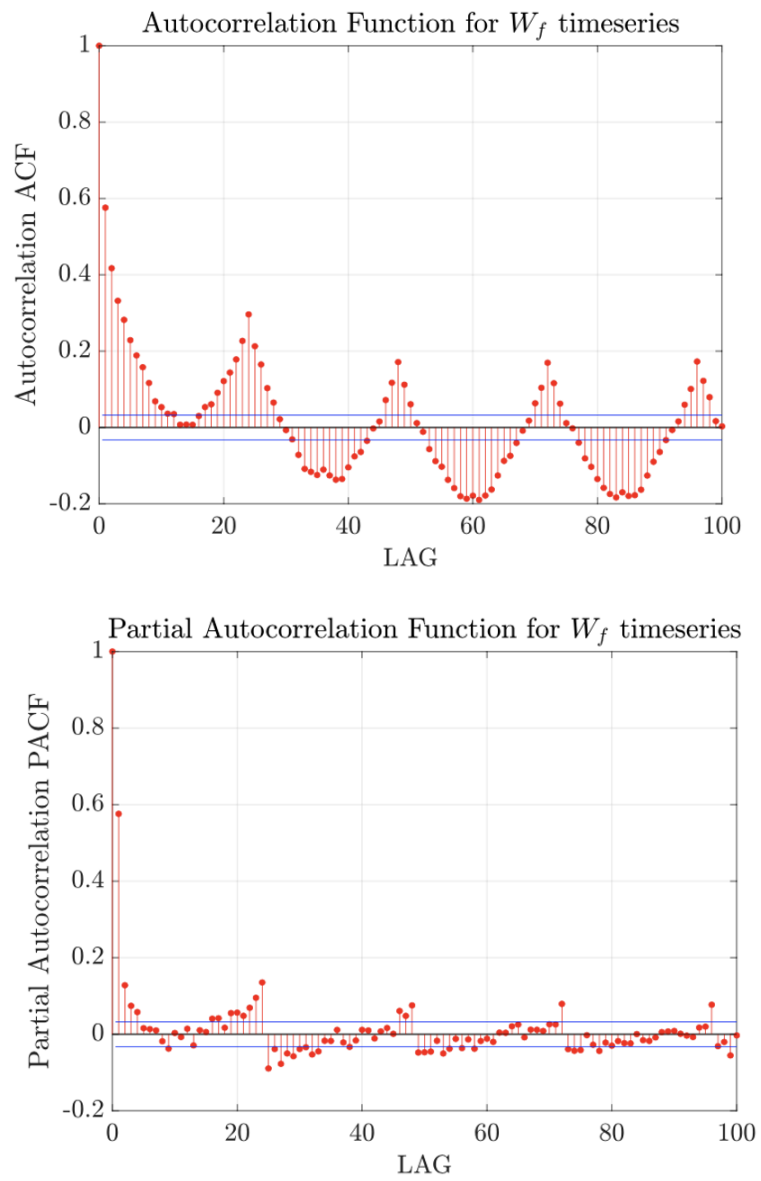


Figure B.2: W_f Auto-Correlation Function (ACF) above and Partial Auto-Correlation Function (PACF) below.

C Forecasting Load

Once the optimization problem Eqs. (4.4a) to (4.4e) is defined, the challenge stands in the forecast of the prosumption and the frequency deviation, in particular their confidence intervals, denoting the maximum and minimum expected realizations, namely S_a^\uparrow , S_a^\downarrow for the prosumption. As correctly appointed by [28], the local prosumption is characterized by high volatility due to the reduced spatial smoothing effect of PV generation and the prominence of isolated stochastic events, such as induction motors intrushes due to the insertion of pumps or elevators. For these reasons, the existing forecasting methodologies, developed by considering high levels of aggregation [131], are not suitable for predicting low-populated aggregates of prosumers. For the proposed application, the problem of identifying S_a^\uparrow and S_a^\downarrow is divided into two sub-problems:

- (i) load consumption forecast and
- (ii) PV production forecast.

For the first one, a simple non-parametric forecasting strategy relying on the statistical properties of the time series is proposed. The PV production forecast is performed by taking advantage of solar radiation and meteorological data services providing a day-ahead prediction of the *Global Horizontal Irradiance* (GHI) together with its uncertainty. The GHI forecast, together with the information related to the PV installation (i.e. total capacity, location, tilt, azimuth) allows computing the *Global Normal Irradiance* (GNI) and obtaining an estimation of the total PV production, and the related uncertainties. The best and worst PV production scenarios are computed by transposing the GHI forecast data and applying a physical model of PV generation accounting for the air temperature [132]. For a given day-ahead forecast, the vector containing the best and worst production scenario for the PV, with a time resolution of 5 minutes are named \mathbf{PV}^\uparrow and \mathbf{PV}^\downarrow , respectively.

As previously mentioned, while the PV production forecast leverages GHI data, the load forecast only relies on the statistical properties of recorded time series. In particular, a set of historical observations \mathcal{G} at the PCC point is considered. The historical load consumption \mathcal{C}

Appendix C. Forecasting Load

is computed for every time step n corresponding to a 5 minutes window and every day d , as:

$$\begin{aligned}\mathcal{C}_{n,d} &= \mathcal{G}_{n,d} - \mathcal{P}_{n,d} - \mathcal{PV}_{n,d} \\ \forall n \in [1, N] \quad \forall d \in [1, D]\end{aligned}\tag{C.1}$$

where \mathcal{P}_a is the historical measure of the BESS power at time n and \mathcal{PV}_a is the estimated PV production at the same time relying on the onsite measures of GHI, and D is the total number of recorded days. The process described by Eq. (C.1), also known as disaggregation, allows for the decoupling of the PV production and the load consumption \mathcal{C} , composed of 288 samples for each recorded day. The different consumption scenarios are generated by applying the following heuristic:

- The data-set \mathcal{C} is divided into sub-sets $\Omega_{A,B,C,D1,D2}$ by selecting consumption data corresponding respectively to: (A) first working day of the week, i.e. Mondays or days after holidays; (B) last working day of the week, i.e. Friday or days before holidays; (C) holidays, i.e. Saturday (subcategory D1), Sundays and festivities (subcategory D2).
- For each sub-set, the mean and covariance are inferred. where the function `mean` returns an array of 288 points, each of which represents a mean value for a particular 5-minute window of the day and the function `cov` returns a 288x288 matrix corresponding to the covariance matrix of the observation.
- Both mean and covariance are computed by considering an exponential forgetting factor to prioritize the latest measurement to the older one, as defined in [133].
- A given number S of possible scenarios is generated by considering the same multivariate normal distribution, with mean equal to the estimated mean and covariance equal to the estimated covariance.
- $\mathbf{P}^{\text{LOAD}\downarrow}$ and $\mathbf{P}^{\text{LOAD}\uparrow}$ are defined as the load scenarios characterized by the lowest and highest load profile, respectively.

Finally, the presumption minimum end maximum expected realization are computed by combining $\mathbf{P}^{\text{LOAD}\downarrow}$ and $\mathbf{P}^{\text{LOAD}\uparrow}$ with \mathbf{PV}^\uparrow and \mathbf{PV}^\downarrow as follows:

$$S_a^\uparrow = P_a^{\text{LOAD}\uparrow} - PV_a^\downarrow\tag{C.2}$$

$$S_a^\downarrow = P_a^{\text{LOAD}\downarrow} - PV_a^\uparrow\tag{C.3}$$

$$\forall n \in [1, N]$$

Concerning the prediction of W_f , while [27] only relies on the statistical properties of the time series, this paper uses an auto-regressive model, as supported by [77] which indicates the possibility to predict W_f to reduce the variance of the forecast in respect to the historical variance of the time series.

Bibliography

- [1] EUROPEAN COMMISSION. *The European Green Deal*. Nov. 2019. URL: https://eur-lex.europa.eu/resource.html?uri=cellar:b828d165-1c22-11ea-8c1f-01aa75ed71a1.0002.02/DOC_1&format=PDF.
- [2] ENTSOE. *All CE TSOs' proposal for additional properties of FCR in accordance with Article 154(2) of the Commission Regulation (EU) 2017/1485 of 2 August 2017 establishing a guideline on electricity transmission system operation*. 2019. URL: [https://eepublicdownloads.entsoe.eu/clean-documents/nc-tasks/EBGL/SOGL_A118_A154\(2\)_190322_Additional%20Properties%20of%20FCR_All%20TSO%27s%20CE-final%20submission_Explanatory%20Note.pdf](https://eepublicdownloads.entsoe.eu/clean-documents/nc-tasks/EBGL/SOGL_A118_A154(2)_190322_Additional%20Properties%20of%20FCR_All%20TSO%27s%20CE-final%20submission_Explanatory%20Note.pdf).
- [3] ENTSOE. "Statistical Factsheet 2022". en. In: *Oil shale* 1.31 (2022). URL: https://eepublicdownloads.blob.core.windows.net/public-cdn-container/clean-documents/Publications/Statistics/Factsheet/entsoe_sfs2022_web.pdf.
- [4] A.C. Padoan, C. Nicolet, B. Kawkabani, J.-J. Simond, A. Schwery, and F. Avellan. "Stability study of a mixed islanded power network". In: *2010 IEEE/PES Transmission and Distribution Conference and Exposition: Latin America (T&D-LA)*. Sao Paulo, Brazil: IEEE, Nov. 2010, pp. 218–225. ISBN: 978-1-4577-0488-8. DOI: 10.1109/TDC-LA.2010.5762885. URL: <http://ieeexplore.ieee.org/document/5762885/> (visited on 04/28/2021).
- [5] Luis Ignacio Levieux, Fernando A. Inthamoussou, and Hernán De Battista. "Power dispatch assessment of a wind farm and a hydropower plant: A case study in Argentina". en. In: *Energy Conversion and Management* 180 (Jan. 2019), pp. 391–400. ISSN: 01968904. DOI: 10.1016/j.enconman.2018.10.101. URL: <https://linkinghub.elsevier.com/retrieve/pii/S0196890418312299> (visited on 05/03/2021).
- [6] Juntao Zhang, Chuntian Cheng, Shen Yu, Huijun Wu, and Mengping Gao. "Sharing hydropower flexibility in interconnected power systems: A case study for the China Southern power grid". en. In: *Applied Energy* 288 (Apr. 2021), p. 116645. ISSN: 03062619. DOI: 10.1016/j.apenergy.2021.116645. URL: <https://linkinghub.elsevier.com/retrieve/pii/S0306261921001781> (visited on 06/06/2021).
- [7] Hugo Villegas Pico and James McCalley. "Modeling and analysis of speed controls in hydro-turbines for frequency performance". In: *2011 North American Power Symposium*. Boston, MA, USA: IEEE, Aug. 2011, pp. 1–7. ISBN: 978-1-4577-0417-8. DOI:

Bibliography

- 10.1109/NAPS.2011.6024847. URL: <http://ieeexplore.ieee.org/document/6024847/> (visited on 04/28/2021).
- [8] Zhigao Zhao, Jiandong Yang, Weijia Yang, Jinhong Hu, and Man Chen. “A coordinated optimization framework for flexible operation of pumped storage hydropower system: Nonlinear modeling, strategy optimization and decision making”. en. In: *Energy Conversion and Management* 194 (Aug. 2019), pp. 75–93. ISSN: 01968904. DOI: 10.1016/j.enconman.2019.04.068. URL: <https://linkinghub.elsevier.com/retrieve/pii/S0196890419305023> (visited on 05/03/2021).
- [9] Weijia Yang, Per Norrlund, Linn Saarinen, Adam Witt, Brennan Smith, Jiandong Yang, and Urban Lundin. “Burden on hydropower units for short-term balancing of renewable power systems”. en. In: *Nature Communications* 9.1 (Dec. 2018), p. 2633. ISSN: 2041-1723. DOI: 10.1038/s41467-018-05060-4. URL: <http://www.nature.com/articles/s41467-018-05060-4> (visited on 11/10/2020).
- [10] Bastian Hase and Christian Seidel. “Balancing services by run-of-river-hydropower at low reservoir amplitudes: Potentials, revenues and emission impacts”. en. In: *Applied Energy* 294 (July 2021), p. 116988. ISSN: 03062619. DOI: 10.1016/j.apenergy.2021.116988. URL: <https://linkinghub.elsevier.com/retrieve/pii/S0306261921004578> (visited on 06/06/2021).
- [11] Bastian Hase and Christian Seidel. “Using Short-Time Storage Potentials of Run-of-River Hydropower for Frequency Control.” in: *Using Short-Time Storage Potentials of Run-of-River Hydropower for Frequency Control*: Bonn, Germany, 2021. DOI: 10.2991/ahe.k.210202.026. URL: <https://www.atlantis-press.com/article/125952236> (visited on 11/22/2023).
- [12] W Yang, P Norrlund, and J Yang. “Analysis on regulation strategies for extending service life of hydropower turbines”. en. In: *IOP Conference Series: Earth and Environmental Science* 49 (Nov. 2016), p. 052013. ISSN: 1755-1307, 1755-1315. DOI: 10.1088/1755-1315/49/5/052013. URL: <https://iopscience.iop.org/article/10.1088/1755-1315/49/5/052013> (visited on 11/10/2020).
- [13] Weijia Yang, Per Norrlund, Linn Saarinen, Jiandong Yang, Wencheng Guo, and Wei Zeng. “Wear and tear on hydro power turbines – Influence from primary frequency control”. en. In: *Renewable Energy* 87 (Mar. 2016), pp. 88–95. ISSN: 09601481. DOI: 10.1016/j.renene.2015.10.009. URL: <https://linkinghub.elsevier.com/retrieve/pii/S0960148115303621> (visited on 11/10/2020).
- [14] Bruce Dunn, Haresh Kamath, and Jean-Marie Tarascon. “Electrical Energy Storage for the Grid: A Battery of Choices”. en. In: *Science* 334.6058 (Nov. 2011), pp. 928–935. ISSN: 0036-8075, 1095-9203. DOI: 10.1126/science.1212741. URL: <https://www.science.org/doi/10.1126/science.1212741> (visited on 03/11/2022).

-
- [15] P. Mercier, R. Cherkaoui, and A. Oudalov. "Optimizing a Battery Energy Storage System for Frequency Control Application in an Isolated Power System". In: *IEEE Transactions on Power Systems* 24.3 (Aug. 2009), pp. 1469–1477. ISSN: 0885-8950, 1558-0679. DOI: 10.1109/TPWRS.2009.2022997. (Visited on 06/21/2021).
- [16] Bo Lian, Adam Sims, Dongmin Yu, Cheng Wang, and Roderick W. Dunn. "Optimizing LiFePO₄ Battery Energy Storage Systems for Frequency Response in the UK System". In: *IEEE Transactions on Sustainable Energy* 8.1 (Jan. 2017), pp. 385–394. ISSN: 1949-3029, 1949-3037. DOI: 10.1109/TSTE.2016.2600274. URL: <http://ieeexplore.ieee.org/document/7543520/> (visited on 09/11/2023).
- [17] Kai Doenges, Ignacio Egido, Lukas Sigrist, Enrique Lobato Miguelez, and Luis Rouco. "Improving AGC Performance in Power Systems With Regulation Response Accuracy Margins Using Battery Energy Storage System (BESS)". In: *IEEE Transactions on Power Systems* 35.4 (July 2020), pp. 2816–2825. ISSN: 0885-8950, 1558-0679. DOI: 10.1109/TPWRS.2019.2960450. URL: <https://ieeexplore.ieee.org/document/8935195/> (visited on 09/11/2023).
- [18] Antonio Giannitrapani, Simone Paoletti, Antonio Vicino, and Donato Zarrilli. "Optimal Allocation of Energy Storage Systems for Voltage Control in LV Distribution Networks". In: *IEEE Transactions on Smart Grid* 8.6 (Nov. 2017), pp. 2859–2870. ISSN: 1949-3053, 1949-3061. DOI: 10.1109/TSG.2016.2602480. URL: <http://ieeexplore.ieee.org/document/7552579/> (visited on 09/11/2023).
- [19] Tianqiao Zhao, Alessandra Parisio, and Jovica V. Milanović. "Distributed control of battery energy storage systems in distribution networks for voltage regulation at transmission–distribution network interconnection points". en. In: *Control Engineering Practice* 119 (Feb. 2022), p. 104988. ISSN: 09670661. DOI: 10.1016/j.conengprac.2021.104988. URL: <https://linkinghub.elsevier.com/retrieve/pii/S0967066121002616> (visited on 09/11/2023).
- [20] Rahul Gupta, Fabrizio Sossan, and Mario Paolone. "Grid-Aware Distributed Model Predictive Control of Heterogeneous Resources in a Distribution Network: Theory and Experimental Validation". en. In: *IEEE Transactions on Energy Conversion* 36.2 (June 2021), pp. 1392–1402. ISSN: 0885-8969, 1558-0059. DOI: 10.1109/TEC.2020.3015271. URL: <https://ieeexplore.ieee.org/document/9163265/> (visited on 09/27/2021).
- [21] Yihui Zuo, Mario Paolone, and Fabrizio Sossan. "Effect of voltage source converters with electrochemical storage systems on dynamics of reduced-inertia bulk power grids". en. In: *Electric Power Systems Research* 189 (Dec. 2020), p. 106766. ISSN: 03787796. DOI: 10.1016/j.epsr.2020.106766. URL: <https://linkinghub.elsevier.com/retrieve/pii/S0378779620305691> (visited on 06/09/2021).
- [22] Tomi Makinen, Aki Leinonen, and Markus Ovaskainen. "Modelling and benefits of combined operation of hydropower unit and battery energy storage system on grid primary frequency control". en. In: *2020 IEEE International Conference on Environment and Electrical Engineering and 2020 IEEE Industrial and Commercial Power Systems*

Bibliography

- Europe (EEEIC / I&CPS Europe)*. Madrid, Spain: IEEE, June 2020, pp. 1–6. ISBN: 978-1-72817-455-6. DOI: 10.1109/EEEIC/ICPSEurope49358.2020.9160666. URL: <https://ieeexplore.ieee.org/document/9160666/> (visited on 07/28/2023).
- [23] David Valentín, Alexandre Presas, Mònica Egusquiza, Jean-Louis Drommi, and Carme Valero. “Benefits of battery hybridization in hydraulic turbines. Wear and tear evaluation in a Kaplan prototype”. en. In: *Renewable Energy* 199 (Nov. 2022), pp. 35–43. ISSN: 09601481. DOI: 10.1016/j.renene.2022.08.117. URL: <https://linkinghub.elsevier.com/retrieve/pii/S0960148122012927> (visited on 07/28/2023).
- [24] Serdar Kadam, Wolfgang Hofbauer, Stefan Lais, Magdalena Neuhauser, Erich Wurm, Luisa Fernandes Lameiro, Yves-Marie Bourien, Grégory Païs, Jean-Louis Drommi, Christophe Nicolet, Christian Landry, Matthieu Dreyer, Carme Valero, Alexandre Presas, and David Valentin. “Hybridization of a RoR HPP with a BESS—The XFLEX HYDRO Vogelgrun Demonstrator”. en. In: *Energies* 16.13 (June 2023), p. 5074. ISSN: 1996-1073. DOI: 10.3390/en16135074. URL: <https://www.mdpi.com/1996-1073/16/13/5074> (visited on 07/28/2023).
- [25] Stefano Cassano and Fabrizio Sossan. “Model predictive control for a medium-head hydropower plant hybridized with battery energy storage to reduce penstock fatigue”. en. In: *Electric Power Systems Research* 213 (Dec. 2022), p. 108545. ISSN: 03787796. DOI: 10.1016/j.epsr.2022.108545. URL: <https://linkinghub.elsevier.com/retrieve/pii/S0378779622006484> (visited on 07/28/2023).
- [26] EUROPEAN COMMISSION. *Hydropower Extending Power System Flexibility*. July 2019. URL: <https://cordis.europa.eu/project/id/857832>.
- [27] Emil Namor and Rachid Cherkaoui. “Control of Battery Storage Systems for the Simultaneous Provision of Multiple Services”. en. In: *IEEE TRANSACTIONS ON SMART GRID* 10.3 (2019), p. 10.
- [28] Fabrizio Sossan, Emil Namor, Rachid Cherkaoui, and Mario Paolone. “Achieving the Dispatchability of Distribution Feeders Through Prosumers Data Driven Forecasting and Model Predictive Control of Electrochemical Storage”. In: *IEEE Transactions on Sustainable Energy* (Oct. 2016). ISSN: 1949-3029, 1949-3037. DOI: 10.1109/TSTE.2016.2600103. (Visited on 03/30/2021).
- [29] Antonio Zecchino, Zhao Yuan, Fabrizio Sossan, Rachid Cherkaoui, and Mario Paolone. “Optimal provision of concurrent primary frequency and local voltage control from a BESS considering variable capability curves: Modelling and experimental assessment”. en. In: *Electric Power Systems Research* 190 (Jan. 2021), p. 106643. ISSN: 03787796. DOI: 10.1016/j.epsr.2020.106643. (Visited on 06/22/2021).
- [30] Christoph Hodel. *Overview of ancillary services*. en. Dec. 2019. URL: <https://www.swissgrid.ch/dam/swissgrid/customers/topics/ancillary-services/as-documents/AS-concept-V1-1-en.pdf>.

-
- [31] EUROPEAN COMMISSION EUROPEAN COMMISSION. *REPowerEU Plan, COMMUNICATION FROM THE COMMISSION TO THE EUROPEAN PARLIAMENT, THE EUROPEAN COUNCIL, THE COUNCIL, THE EUROPEAN ECONOMIC AND SOCIAL COMMITTEE AND THE COMMITTEE OF THE REGIONS*. Tech. rep. EU-52022DC0230. EUROPEAN COMMISSION, May 2022. URL: <https://eur-lex.europa.eu/legal-content/EN/TXT/?uri=COM%3A2022%3A230%3AFIN>.
 - [32] Emanuele Quaranta, George Aggidis, Robert M. Boes, Claudio Comoglio, Carlo De Michele, Epari Ritesh Patro, Evgeniia Georgievskaja, Atle Harby, Ioannis Kougias, Sebastian Muntean, Juan Pérez-Díaz, Pedro Romero-Gomez, Marco Rosa-Clot, Anton J. Schleiss, Elena Vagnoni, Markus Wirth, and Alberto Pistocchi. “Assessing the energy potential of modernizing the European hydropower fleet”. en. In: *Energy Conversion and Management* 246 (Oct. 2021), p. 114655. ISSN: 01968904. DOI: 10.1016/j.enconman.2021.114655. URL: <https://linkinghub.elsevier.com/retrieve/pii/S0196890421008311> (visited on 01/12/2023).
 - [33] C Landry, C Nicolet, C Badina, H Pichon, and J-L Drommi. “Contribution for the roadmap of hydraulic short circuit implementation: Case of Grand-Maison pumped storage power plant”. In: *IOP Conference Series: Earth and Environmental Science* 1079.1 (Sept. 2022), p. 012107. ISSN: 1755-1307, 1755-1315. DOI: 10.1088/1755-1315/1079/1/012107. URL: <https://iopscience.iop.org/article/10.1088/1755-1315/1079/1/012107> (visited on 05/19/2023).
 - [34] J Decaix, D Biner, J-L. Drommi, F Avellan, and C Münch-alligné. “CFD simulations of a Y-junction for the implementation of hydraulic short-circuit operating mode”. In: *IOP Conference Series: Earth and Environmental Science* 774.1 (June 2021), p. 012013. ISSN: 1755-1307, 1755-1315. DOI: 10.1088/1755-1315/774/1/012013. URL: <https://iopscience.iop.org/article/10.1088/1755-1315/774/1/012013> (visited on 05/19/2023).
 - [35] Thomas Gaal and Manfred Sallaberger. “Pumped Storage Machines – Hydraulic Short-circuit Operation”. en. In: *Advances in Energy Storage*. Ed. by Andreas Hauer. 1st ed. Wiley, Apr. 2022, pp. 289–301. DOI: 10.1002/9781119239390.ch16. URL: <https://onlinelibrary.wiley.com/doi/10.1002/9781119239390.ch16> (visited on 01/12/2023).
 - [36] Juan I. Pérez-Díaz, José I. Sarasúa, and José R. Wilhelmi. “Contribution of a hydraulic short-circuit pumped-storage power plant to the load–frequency regulation of an isolated power system”. en. In: *International Journal of Electrical Power & Energy Systems* 62 (Nov. 2014), pp. 199–211. ISSN: 01420615. DOI: 10.1016/j.ijepes.2014.04.042. URL: <https://linkinghub.elsevier.com/retrieve/pii/S0142061514002373> (visited on 01/12/2023).
 - [37] C Nicolet, Y Vaillant, B Kawkabani, P Allenbach, and F Avellan. “Pumped storage units to stabilize mixed islanded power network: a transient analysis”. en. In: *Proceedings of HYDRO* (2008).

Bibliography

- [38] C Nicolet, A Béguin, J-D Dayer, and G Micoulet. “Hydraulic transient challenges for the upgrade of FMHL+ pumped storage power plant from 240MW to 420MW”. In: *IOP Conference Series: Earth and Environmental Science* 240 (Mar. 2019), p. 052026. ISSN: 1755-1315. DOI: 10.1088/1755-1315/240/5/052026. URL: <https://iopscience.iop.org/article/10.1088/1755-1315/240/5/052026> (visited on 01/12/2023).
- [39] Manuel Chazarra, Juan Ignacio Perez-Diaz, and Javier Garcia-Gonzalez. “Optimal Energy and Reserve Scheduling of Pumped-Storage Power Plants Considering Hydraulic Short-Circuit Operation”. In: *IEEE Transactions on Power Systems* 32.1 (Jan. 2017), pp. 344–353. ISSN: 0885-8950, 1558-0679. DOI: 10.1109/TPWRS.2016.2545740. URL: <http://ieeexplore.ieee.org/document/7439818/> (visited on 01/12/2023).
- [40] Manuel Chazarra, Juan Ignacio Perez-Diaz, and Javier Garcia-Gonzalez. “Optimal Joint Energy and Secondary Regulation Reserve Hourly Scheduling of Variable Speed Pumped Storage Hydropower Plants”. In: *IEEE Transactions on Power Systems* 33.1 (Jan. 2018), pp. 103–115. ISSN: 0885-8950, 1558-0679. DOI: 10.1109/TPWRS.2017.2699920. URL: <http://ieeexplore.ieee.org/document/7914792/> (visited on 01/12/2023).
- [41] M Dreyer, C Nicolet, S Alligné, M Seydoux, A Jung, and D Cordeiro. “Pushing the envelope of ancillary services with variable speed technology”. In: *IOP Conference Series: Earth and Environmental Science* 1079.1 (Sept. 2022), p. 012110. ISSN: 1755-1307, 1755-1315. DOI: 10.1088/1755-1315/1079/1/012110. URL: <https://iopscience.iop.org/article/10.1088/1755-1315/1079/1/012110> (visited on 01/12/2023).
- [42] Sebastian Braun and Rainer Hoffmann. “Intraday Optimization of Pumped Hydro Power Plants in the German Electricity Market”. en. In: *Energy Procedia* 87 (Jan. 2016), pp. 45–52. ISSN: 18766102. DOI: 10.1016/j.egypro.2015.12.356. URL: <https://linkinghub.elsevier.com/retrieve/pii/S1876610215030453> (visited on 05/16/2023).
- [43] Fereidoon P. Sioshansi. “Competition in Liberalized European Electricity Markets”. en. In: *The Electricity Journal* 14.2 (Mar. 2001), pp. 73–83. ISSN: 10406190. DOI: 10.1016/S1040-6190(01)00178-6. URL: <https://linkinghub.elsevier.com/retrieve/pii/S1040619001001786> (visited on 12/16/2022).
- [44] Rodica Loisel and Corentin Simon. “Market strategies for large-scale energy storage: Vertical integration versus stand-alone player”. en. In: *Energy Policy* 151 (Apr. 2021), p. 112169. ISSN: 03014215. DOI: 10.1016/j.enpol.2021.112169. URL: <https://linkinghub.elsevier.com/retrieve/pii/S0301421521000380> (visited on 12/16/2022).
- [45] G. Weisrock. “Hydroelectric Power Station Control Systems”. en. In: *IFAC Proceedings Volumes* 19.16 (Dec. 1986), pp. 7–14. ISSN: 14746670. DOI: 10.1016/S1474-6670(17)59354-4. URL: <https://linkinghub.elsevier.com/retrieve/pii/S1474667017593544> (visited on 12/16/2022).
- [46] Ali Thaeer Hammid, Omar I. Awad, Mohd Herwan Sulaiman, Saraswathy Shamini Gunasekaran, Salama A. Mostafa, Nallapaneni Manoj Kumar, Bashar Ahmad Khalaf, Yasir Amer Al-Jawhar, and Raed Abdulkareem Abdulhasan. “A Review of Optimization Algorithms in Solving Hydro Generation Scheduling Problems”. en. In: *Energies* 13.11

- (June 2020), p. 2787. ISSN: 1996-1073. DOI: 10.3390/en13112787. URL: <https://www.mdpi.com/1996-1073/13/11/2787> (visited on 05/16/2023).
- [47] J Decaix, J-L Drommi, F Avellan, and C Münch-Alligné. “CFD simulations of hydraulic short-circuits in junctions, application to the Grand’Maison power plant”. In: *IOP Conference Series: Earth and Environmental Science* 1079.1 (Sept. 2022), p. 012106. ISSN: 1755-1307, 1755-1315. DOI: 10.1088/1755-1315/1079/1/012106. URL: <https://iopscience.iop.org/article/10.1088/1755-1315/1079/1/012106> (visited on 05/19/2023).
- [48] C Nicolet. “A New tool for the simulation of dynamic behaviour of hydroelectric power plants”. In: *IAHR: A New tool for the simulation of dynamic behaviour of hydroelectric power plants*. Trondheim, Norway, 2001, p. 12. URL: https://www.powervision-eng.ch/Profile/Publications/pdf/IAHR_WG1_2001.pdf.
- [49] Jerome H. Friedman. “Multivariate Adaptive Regression Splines”. In: *The Annals of Statistics* 19.1 (Mar. 1991). ISSN: 0090-5364. DOI: 10.1214/aos/1176347963. URL: <https://projecteuclid.org/journals/annals-of-statistics/volume-19/issue-1/Multivariate-Adaptive-Regression-Splines/10.1214/aos/1176347963.full> (visited on 04/28/2021).
- [50] E.C. Finardi and E.L. Da Silva. “Unit commitment of single hydroelectric plant”. en. In: *Electric Power Systems Research* 75.2-3 (Aug. 2005), pp. 116–123. ISSN: 03787796. DOI: 10.1016/j.epsr.2005.01.008. URL: <https://linkinghub.elsevier.com/retrieve/pii/S0378779605000970> (visited on 08/30/2023).
- [51] E Javier Diaz, Javier Contreras, José Ignacio Munoz, and David Pozo. “Optimal Scheduling of a Price-Taker Cascaded Reservoir System in a Pool-Based Electricity Market”. In: *IEEE Transactions on Power Systems* 26.2 (May 2011), pp. 604–615. ISSN: 0885-8950, 1558-0679. DOI: 10.1109/TPWRS.2010.2063042. URL: <http://ieeexplore.ieee.org/document/5565530/> (visited on 08/30/2023).
- [52] Erik Tengs, Pål-Tore Storli, and Martin Holst. “Optimization procedure for variable speed turbine design”. en. In: *Engineering Applications of Computational Fluid Mechanics* 12.1 (Jan. 2018), pp. 652–661. ISSN: 1994-2060, 1997-003X. DOI: 10.1080/19942060.2018.1507950. URL: <https://www.tandfonline.com/doi/full/10.1080/19942060.2018.1507950> (visited on 08/30/2023).
- [53] Erik Tengs, Pål-Tore Storli, and Martin Aasved Holst. “Numerical Generation of Hill-Diagrams; Validation on the Francis99 Model Turbine”. en. In: *International Journal of Fluid Machinery and Systems* 11.3 (Sept. 2018), pp. 294–303. ISSN: 1882-9554. DOI: 10.5293/IJFMS.2018.11.3.294. URL: <http://www.dbpia.co.kr/Journal/ArticleDetail/NODE07537957> (visited on 08/30/2023).
- [54] European Network of Transmission System Operators for Electricity. *ENTSO-E Statistical Factsheet*. Tech. rep. ENTSO-E, 2019.

Bibliography

- [55] Platero, Sánchez, Nicolet, and Allenbach. “Hydropower Plants Frequency Regulation Depending on Upper Reservoir Water Level”. en. In: *Energies* 12.9 (Apr. 2019), p. 1637. ISSN: 1996-1073. DOI: 10.3390/en12091637. URL: <https://www.mdpi.com/1996-1073/12/9/1637> (visited on 04/28/2021).
- [56] Ming Zhang, David Valentín, Carme Valero, Mònica Egusquiza, and Eduard Egusquiza. “Failure investigation of a Kaplan turbine blade”. en. In: *Engineering Failure Analysis* 97 (Mar. 2019), pp. 690–700. ISSN: 13506307. DOI: 10.1016/j.engfailanal.2019.01.056. URL: <https://linkinghub.elsevier.com/retrieve/pii/S1350630718309191> (visited on 11/16/2020).
- [57] J L Gordon. “Hydraulic turbine efficiency”. en. In: *Canadian Journal of Civil Engineering* 28.2 (Apr. 2001), pp. 238–253. ISSN: 0315-1468, 1208-6029. DOI: 10.1139/l00-102. URL: <http://www.nrcresearchpress.com/doi/10.1139/l00-102> (visited on 10/11/2023).
- [58] Khalid Tourkey Atta, Andreas Johansson, Michel J. Cervantes, and Thomas Gustafsson. “Phasor extremum seeking and its application in Kaplan turbine control”. en. In: *2014 IEEE Conference on Control Applications (CCA)*. Juan Les Antibes, France: IEEE, Oct. 2014, pp. 298–303. ISBN: 978-1-4799-7409-2. DOI: 10.1109/CCA.2014.6981362. URL: <http://ieeexplore.ieee.org/document/6981362/> (visited on 06/15/2021).
- [59] Huixuan Shi, Zhaohui Li, and Yaxiong Bi. “An On-line Cavitation Monitoring System for Large Kaplan Turbines”. en. In: *2007 IEEE Power Engineering Society General Meeting*. ISSN: 1932-5517. Tampa, FL, USA: IEEE, June 2007, pp. 1–6. DOI: 10.1109/PES.2007.385723. URL: <http://ieeexplore.ieee.org/document/4275489/> (visited on 11/10/2020).
- [60] A Borghetti, M Di Silvestro, G Naldi, M Paolone, and M Alberti. “Maximum Efficiency Point Tracking for Adjustable-Speed Small Hydro Power Plant”. en. In: *2008 Power Systems Computation Conference (PSCC)*. IEEE, 2008, p. 7.
- [61] G. Lazzaro, S. Basso, M. Schirmer, and G. Botter. “Water management strategies for run-of-river power plants: Profitability and hydrologic impact between the intake and the outflow: Hydroeconomic Performances of Water Management Strategies”. en. In: *Water Resources Research* 49.12 (Dec. 2013), pp. 8285–8298. ISSN: 00431397. DOI: 10.1002/2013WR014210. URL: <http://doi.wiley.com/10.1002/2013WR014210> (visited on 04/28/2021).
- [62] G. Robert and F. Michaud. “A Simple Multi-objective Control for Cascaded Hydro Power Plants”. en. In: *IFAC Proceedings Volumes* 44.1 (Jan. 2011), pp. 4960–4963. ISSN: 14746670. DOI: 10.3182/20110828-6-IT-1002.00654. URL: <https://linkinghub.elsevier.com/retrieve/pii/S1474667016443922> (visited on 04/28/2021).
- [63] Jiangnan Xi, Harold R. Chamorro, Jonas Persson, Andreas Westberg, Daniel Wall, and Mehrdad Ghandhari. “On the influence of the backlash governor settings on the frequency response in power systems”. In: *2016 IEEE PES Asia-Pacific Power and Energy Engineering Conference (APPEEC)*. Xi'an, China: IEEE, Oct. 2016, pp. 732–737. ISBN: 978-1-5090-5418-3. DOI: 10.1109/APPEEC.2016.7779650. URL: <http://ieeexplore.ieee.org/document/7779650/> (visited on 08/25/2021).

- [64] G.P. Liu and S. Daley. "Optimal-tuning nonlinear PID control of hydraulic systems". en. In: *Control Engineering Practice* 8.9 (Sept. 2000), pp. 1045–1053. ISSN: 09670661. DOI: 10.1016/S0967-0661(00)00042-3. URL: <https://linkinghub.elsevier.com/retrieve/pii/S0967066100000423> (visited on 05/03/2021).
- [65] Ertuğrul Çam. "Application of fuzzy logic for load frequency control of hydroelectrical power plants". en. In: *Energy Conversion and Management* 48.4 (Apr. 2007), pp. 1281–1288. ISSN: 01968904. DOI: 10.1016/j.enconman.2006.09.026. URL: <https://linkinghub.elsevier.com/retrieve/pii/S0196890406003062> (visited on 05/03/2021).
- [66] Chunlian Jin, Ning Lu, Shuai Lu, Yuri Makarov, and Roger A. Dougal. "Coordinated control algorithm for hybrid energy storage systems". In: *2011 IEEE Power and Energy Society General Meeting*. San Diego, CA: IEEE, July 2011, pp. 1–7. DOI: 10.1109/PES.2011.6039893. URL: <https://ieeexplore.ieee.org/document/6039893/> (visited on 05/03/2021).
- [67] Weijia Yang, Per Norrlund, Linn Saarinen, Jiandong Yang, Wei Zeng, and Urban Lundin. "Wear Reduction for Hydropower Turbines Considering Frequency Quality of Power Systems: A Study on Controller Filters". In: *IEEE Transactions on Power Systems* 32.2 (Mar. 2017), pp. 1191–1201. ISSN: 0885-8950, 1558-0679. DOI: 10.1109/TPWRS.2016.2590504. URL: <https://ieeexplore.ieee.org/document/7514942/> (visited on 04/28/2021).
- [68] Prabha Kundur. "Power System Stability". en. In: *Power System Stability and Control*. Ed. by Leonard Grigsby. Vol. 20073061. Series Title: Electrical Engineering Handbook. CRC Press, May 2007. DOI: 10.1201/9781420009248.sec2. URL: <http://www.crcnetbase.com/doi/abs/10.1201/9781420009248.sec2> (visited on 08/21/2023).
- [69] D. Kosterev. "Hydro Turbine-Governor Model Validation in Pacific Northwest". en. In: *IEEE Transactions on Power Systems* 19.2 (May 2004), pp. 1144–1149. ISSN: 0885-8950. DOI: 10.1109/TPWRS.2003.821464. URL: <http://ieeexplore.ieee.org/document/1295026/> (visited on 04/28/2021).
- [70] K. Amiri, B. Mulu, M.J. Cervantes, and M. Raisee. "Effects of load variation on a Kaplan turbine runner". en. In: *International Journal of Fluid Machinery and Systems* 9.2 (June 2016), pp. 182–193. ISSN: 1882-9554. DOI: 10.5293/IJFMS.2016.9.2.182. URL: <http://koreascience.or.kr/journal/view.jsp?kj=OCGKEU&py=2016&vnc=v9n2&sp=182> (visited on 09/11/2023).
- [71] Eduard Doujak. *Effects of Increased Solar and Wind Energy on Hydro Plant Operation*. 2014. URL: <https://www.renewableenergyworld.com/baseload/hydropower/effects-of-increased-solar-and-wind-energy-on-hydro-plant-operation/#gref>.
- [72] M. Brezovec, I. Kuzle, and T. Tomisa. "Nonlinear Digital Simulation Model of Hydroelectric Power Unit With Kaplan Turbine". en. In: *IEEE Transactions on Energy Conversion* 21.1 (Mar. 2006), pp. 235–241. ISSN: 0885-8969. DOI: 10.1109/TEC.2005.847963. URL: <http://ieeexplore.ieee.org/document/1597342/> (visited on 04/28/2021).

Bibliography

- [73] Christian Vessaz, Loïc Andolfatto, François Avellan, and Christophe Tournier. “Toward design optimization of a Pelton turbine runner”. en. In: *Structural and Multidisciplinary Optimization* 55.1 (Jan. 2017), pp. 37–51. ISSN: 1615-147X, 1615-1488. DOI: 10.1007/s00158-016-1465-7. URL: <http://link.springer.com/10.1007/s00158-016-1465-7> (visited on 04/28/2021).
- [74] E. Vagnoni, L. Andolfatto, R. Guillaume, P. Leroy, and F. Avellan. “Interaction of a rotating two-phase flow with the pressure and torque stability of a reversible pump-turbine operating in condenser mode”. en. In: *International Journal of Multiphase Flow* 111 (Feb. 2019), pp. 112–121. ISSN: 03019322. DOI: 10.1016/j.ijmultiphaseflow.2018.11.013. URL: <https://linkinghub.elsevier.com/retrieve/pii/S0301932218302763> (visited on 04/28/2021).
- [75] ENTSOE. *TSOs’ proposal for the establishment of common and harmonised rules and processes for the exchange and procurement of Balancing Capacity for Frequency Containment Reserves (FCR) in accordance with Article 33 of Commission Regulation (EU) 2017/2195 establishing a guideline on electricity balancing*. 2018. URL: https://eepublicdownloads.blob.core.windows.net/public-cdn-container/clean-documents/Network%20codes%20documents/NC%20EB/FCR_Proposal-Article_33_1%20EBGL_20181018_FV.PDF.
- [76] Ihämäki Laura. *Terms and conditions for providers of Frequency Containment Reserves (FCR)*. en. Tech. rep. Fingrid, 2019, p. 19. URL: https://www.fingrid.fi/globalassets/dokumentit/en/electricity-market/reserves/fcr-liite1---ehdot-janedellytykset_en.pdf.
- [77] Giacomo Piero Schiapparelli, Stefano Massucco, Emil Namor, Fabrizio Sossan, Rachid Cherkaoui, and Mario Paolone. “Quantification of Primary Frequency Control Provision from Battery Energy Storage Systems Connected to Active Distribution Networks”. In: *2018 Power Systems Computation Conference (PSCC)*. Dublin: IEEE, June 2018, pp. 1–7. ISBN: 978-1-910963-10-4. DOI: 10.23919/PSCC.2018.8442554. URL: <https://ieeexplore.ieee.org/document/8442554/> (visited on 04/28/2021).
- [78] Emil Namor. “Advanced models and algorithms to provide multiple grid services with battery storage systems”. en. Publisher: Lausanne, EPFL. PhD thesis. EPFL, 2018. URL: <http://infoscience.epfl.ch/record/256959> (visited on 08/12/2021).
- [79] Henrique Augusto Menarin, Heliara A. Costa, Guilherme Luiz Minetto Fredo, Rodrigo Pereira Gosmann, Erlon Cristian Finardi, and Leonardo Augusto Weiss. “Dynamic Modeling of Kaplan Turbines Including Flow Rate and Efficiency Static Characteristics”. In: *IEEE Transactions on Power Systems* 34.4 (July 2019), pp. 3026–3034. ISSN: 0885-8950, 1558-0679. DOI: 10.1109/TPWRS.2019.2899815. URL: <https://ieeexplore.ieee.org/document/8642905/> (visited on 04/28/2021).
- [80] Jie Zhao, Li Wang, Dichen Liu, Jun Wang, Yu Zhao, Tian Liu, and Haoyu Wang. “Dynamic Model of Kaplan Turbine Regulating System Suitable for Power System Analysis”. en. In: *Mathematical Problems in Engineering* 2015 (2015), pp. 1–12. ISSN: 1024-123X,

- 1563-5147. DOI: 10.1155/2015/294523. URL: <http://www.hindawi.com/journals/mpe/2015/294523/> (visited on 11/06/2020).
- [81] P. Schniter and L. Wozniak. "Efficiency based optimal control of Kaplan hydrogenerators". In: *IEEE Transactions on Energy Conversion* 10.2 (June 1995), pp. 348–353. ISSN: 08858969. DOI: 10.1109/60.391902. URL: <http://ieeexplore.ieee.org/document/391902/> (visited on 05/07/2021).
- [82] L. Saarinen, P. Norrlund, W. Yang, and U. Lundin. "Allocation of Frequency Control Reserves and Its Impact on Wear and Tear on a Hydropower Fleet". In: *IEEE Transactions on Power Systems* 33.1 (Jan. 2018). IEEE Transactions on Power Systems, pp. 430–439. ISSN: 1558-0679. DOI: 10.1109/TPWRS.2017.2702280.
- [83] Wesley J Cole and Allister Frazier. *Cost Projections for Utility-Scale Battery Storage*. en. Tech. rep. NREL/TP-6A20-73222, 1529218. National Renewable Energy Laboratory, June 2019, NREL/TP-6A20-73222, 1529218. DOI: 10.2172/1529218. URL: <http://www.osti.gov/servlets/purl/1529218/> (visited on 03/11/2022).
- [84] Guishi Wang, Georgios Konstantinou, Christopher D. Townsend, Josep Pou, Sergio Vazquez, Georgios D. Demetriades, and Vassilios Georgios Agelidis. "A Review of Power Electronics for Grid Connection of Utility-Scale Battery Energy Storage Systems". In: *IEEE Transactions on Sustainable Energy* 7.4 (Oct. 2016), pp. 1778–1790. ISSN: 1949-3029, 1949-3037. DOI: 10.1109/TSTE.2016.2586941. (Visited on 06/21/2021).
- [85] AEMO. *Initial operation of the Hornsdale Power Reserve Battery Energy Storage System*. 2018. URL: https://www.aemo.com.au/-/media/Files/Media_Centre/2018/Initial-operation-of-the-Hornsdale-Power-Reserve.pdf.
- [86] Olivier Mégel, Johanna L. Mathieu, and Göran Andersson. "Scheduling distributed energy storage units to provide multiple services under forecast error". en. In: *International Journal of Electrical Power & Energy Systems* 72 (Nov. 2015), pp. 48–57. ISSN: 01420615. DOI: 10.1016/j.ijepes.2015.02.010. URL: <https://linkinghub.elsevier.com/retrieve/pii/S0142061515000939> (visited on 09/11/2023).
- [87] Ali Reza Reisi, Mohammad Hassan Moradi, and Shahriar Jamasb. "Classification and comparison of maximum power point tracking techniques for photovoltaic system: A review". en. In: *Renewable and Sustainable Energy Reviews* 19 (Mar. 2013), pp. 433–443. ISSN: 13640321. DOI: 10.1016/j.rser.2012.11.052. URL: <https://linkinghub.elsevier.com/retrieve/pii/S1364032112006661> (visited on 09/11/2023).
- [88] Jamal A. Baroudi, Venkata Dinavahi, and Andrew M. Knight. "A review of power converter topologies for wind generators". en. In: *Renewable Energy* 32.14 (Nov. 2007), pp. 2369–2385. ISSN: 09601481. DOI: 10.1016/j.renene.2006.12.002. URL: <https://linkinghub.elsevier.com/retrieve/pii/S0960148106003430> (visited on 06/22/2021).
- [89] Jef Beerten, Oriol Gomis-Bellmunt, Xavier Guillaud, Johan Rimez, Arjen van der Meer, and Dirk Van Hertem. "Modeling and control of HVDC grids: A key challenge for the future power system". In: *2014 Power Systems Computation Conference*. Wrocław,

Bibliography

- Poland: IEEE, Aug. 2014, pp. 1–21. ISBN: 978-83-935801-3-2. DOI: 10.1109/PSCC.2014.7038505. URL: <http://ieeexplore.ieee.org/document/7038505/> (visited on 06/22/2021).
- [90] Yashen Lin, Joseph Eto, Brian Johnson, Jack Flicker, Robert Lasseter, Hugo Villegas Pico, Gab-Su Seo, Brian Pierre, and Abraham Ellis. *Research Roadmap on Grid-Forming Inverters*. Tech. rep. NREL/TP-5D00-73476, 1721727, MainId:6978. National Renewable Energy Laboratory, Nov. 2020, NREL/TP-5D00-73476, 1721727, MainId:6978. DOI: 10.2172/1721727. URL: <https://www.osti.gov/servlets/purl/1721727/> (visited on 09/11/2023).
- [91] Julia Matevosyan, Babak Badrzadeh, Thibault Prevost, Eckard Quitmann, Deepak Ramasubramanian, Helge Urdal, Sebastian Achilles, Jason MacDowell, Shun Hsien Huang, Vijay Vital, Jon O’Sullivan, and Ryan Quint. “Grid-Forming Inverters: Are They the Key for High Renewable Penetration?” In: *IEEE Power and Energy Magazine* 17.6 (Nov. 2019), pp. 89–98. ISSN: 1540-7977, 1558-4216. DOI: 10.1109/MPE.2019.2933072. URL: <https://ieeexplore.ieee.org/document/8879610/> (visited on 09/11/2023).
- [92] Yihui Zuo, Zhao Yuan, Fabrizio Sossan, Antonio Zecchino, Rachid Cherkaoui, and Mario Paolone. “Performance assessment of grid-forming and grid-following converter-interfaced battery energy storage systems on frequency regulation in low-inertia power grids”. en. In: *Sustainable Energy, Grids and Networks* (Sept. 2021). ISSN: 23524677. DOI: 10.1016/j.segan.2021.100496. (Visited on 06/08/2021).
- [93] Jia Liu, Yushi Miura, and Toshifumi Ise. “Comparison of Dynamic Characteristics Between Virtual Synchronous Generator and Droop Control in Inverter-Based Distributed Generators”. In: *IEEE Transactions on Power Electronics* 31.5 (May 2016), pp. 3600–3611. ISSN: 0885-8993, 1941-0107. DOI: 10.1109/TPEL.2015.2465852. URL: <http://ieeexplore.ieee.org/document/7182342/> (visited on 06/22/2021).
- [94] Taoufik Qoria, Ebrahim Rokrok, Antoine Bruyere, Bruno Francois, and Xavier Guillaud. “A PLL-Free Grid-Forming Control With Decoupled Functionalities for High-Power Transmission System Applications”. In: *IEEE Access* 8 (2020), pp. 197363–197378. ISSN: 2169-3536. DOI: 10.1109/ACCESS.2020.3034149. URL: <https://ieeexplore.ieee.org/document/9240975/> (visited on 06/22/2021).
- [95] Roberto Rosso, Soenke Engelken, and Marco Liserre. “Robust Stability Analysis of Synchronverters Operating in Parallel”. In: *IEEE Transactions on Power Electronics* 34.11 (Nov. 2019), pp. 11309–11319. ISSN: 0885-8993, 1941-0107. DOI: 10.1109/TPEL.2019.2896707. URL: <https://ieeexplore.ieee.org/document/8630646/> (visited on 06/22/2021).
- [96] Mario Paolone, Trevor Gaunt, Xavier Guillaud, Marco Liserre, Sakis Meliopoulos, Antonello Monti, Thierry Van Cutsem, Vijay Vittal, and Costas Vournas. “Fundamentals of power systems modelling in the presence of converter-interfaced generation”. en. In: *Electric Power Systems Research* 189 (Dec. 2020), p. 106811. ISSN: 03787796. DOI: 10.1016/j.epsr.2020.106811. URL: <https://linkinghub.elsevier.com/retrieve/pii/S037877962030482X> (visited on 06/21/2021).

- [97] Joan Rocabert, Alvaro Luna, Frede Blaabjerg, and Pedro Rodríguez. “Control of Power Converters in AC Microgrids”. In: *IEEE Transactions on Power Electronics* 27.11 (Nov. 2012), pp. 4734–4749. ISSN: 0885-8993, 1941-0107. DOI: 10.1109/TPEL.2012.2199334. URL: <http://ieeexplore.ieee.org/document/6200347/> (visited on 06/21/2021).
- [98] Shuai Lu, Pavel V. Etingov, Da Meng, Xinxin Guo, Chunlian Jin, and Nader A. Samaan. *NV Energy Large-Scale Photovoltaic Integration Study: Intra-Hour Dispatch and AGC Simulation*. en. Tech. rep. PNNL-22069, 1060649. US Department of Energy, Jan. 2013, PNNL-22069, 1060649. DOI: 10.2172/1060649. URL: <http://www.osti.gov/servlets/purl/1060649/> (visited on 09/11/2023).
- [99] Swissgrid Ltd. *Balancing Roadmap Switzerland*. en. Apr. 2018. URL: <https://www.swissgrid.ch/dam/swissgrid/about-us/newsroom/publications/balancing-roadmap-ch-en.pdf>.
- [100] Walter Sattinger. *Test zur Sekundärregelfähigkeit*. de. May 2020. URL: <https://www.swissgrid.ch/dam/swissgrid/customers/topics/ancillary-services/prequalification/3/F20200529-test-for-primary-control-capability-de.pdf>.
- [101] Stavroula Margelou. *Präqualifikationsunterlagen Primärregelung*. de. May 2020. URL: <https://www.swissgrid.ch/dam/swissgrid/customers/topics/ancillary-services/prequalification/3/F20200529-prequalification-documents-primary-control-de.pdf>.
- [102] Tobias Ott. *Requirements for schedule data*. en. June 2020. URL: https://www.swissgrid.ch/dam/swissgrid/customers/topics/ancillary-services/prequalification/1/D200630-requirements-schedule-and-electronic-data-V8R0_en.pdf.
- [103] Abhimanyu Kaushal and Dirk Van Hertem. “An overview of Ancillary Services and HVDC systems in European Context”. en. In: *Energies* 12.18 (Sept. 2019), p. 3481. ISSN: 1996-1073. DOI: 10.3390/en12183481. URL: <https://www.mdpi.com/1996-1073/12/18/3481> (visited on 08/12/2021).
- [104] EUROPEAN COMMISSION. “COMMISSION REGULATION (EU) 2016/ 631 - of 14 April 2016 - establishing a network code on requirements for grid connection of generators”. en. In: *Official Journal of the European Union* (Apr. 2016), p. 68. URL: <https://eur-lex.europa.eu/legal-content/EN/TXT/?uri=CELEX%3A32016R0631>.
- [105] Enrica Scolari, Lorenzo Reyes-Chamorro, Fabrizio Sossan, and Mario Paolone. “A Comprehensive Assessment of the Short-Term Uncertainty of Grid-Connected PV Systems”. In: *IEEE Transactions on Sustainable Energy* 9.3 (July 2018), pp. 1458–1467. ISSN: 1949-3029, 1949-3037. DOI: 10.1109/TSTE.2018.2789937. URL: <https://ieeexplore.ieee.org/document/8247241/> (visited on 09/11/2023).
- [106] Maryam Bahramipanah, Dimitri Torregrossa, Rachid Cherkaoui, and Mario Paolone. “Enhanced electrical model of Lithium-based batteries accounting the charge redistribution effect”. In: *2014 Power Systems Computation Conference*. Wrocław, Poland: IEEE, Aug. 2014, pp. 1–8. ISBN: 978-83-935801-3-2. DOI: 10.1109/PSCC.2014.7038481. URL: <http://ieeexplore.ieee.org/document/7038481/> (visited on 04/12/2022).

Bibliography

- [107] Marco Pignati, Miroslav Popovic, Sergio Barreto, Rachid Cherkaoui, German Dario Flores, Jean-Yves Le Boudec, Maaz Mohiuddin, Mario Paolone, Paolo Romano, Styliani Sarri, Teklemariam Tesfay, Dan-Cristian Tomozei, and Lorenzo Zanni. “Real-time state estimation of the EPFL-campus medium-voltage grid by using PMUs”. In: *2015 IEEE Power & Energy Society Innovative Smart Grid Technologies Conference (ISGT)*. Washington, DC, USA: IEEE, Feb. 2015, pp. 1–5. ISBN: 978-1-4799-1785-3. DOI: 10.1109/ISGT.2015.7131877. URL: <http://ieeexplore.ieee.org/document/7131877/> (visited on 04/28/2021).
- [108] Lorenzo Zanni, Asja Derviškić, Marco Pignati, Chenxi Xu, Paolo Romano, Rachid Cherkaoui, Ali Abur, and Mario Paolone. “PMU-based linear state estimation of Lausanne subtransmission network: Experimental validation”. en. In: *Electric Power Systems Research* 189 (Dec. 2020), p. 106649. ISSN: 03787796. DOI: 10.1016/j.epsr.2020.106649. URL: <https://linkinghub.elsevier.com/retrieve/pii/S0378779620304521> (visited on 08/11/2023).
- [109] Bilal Ahmad Bhatti, Sarmad Hanif, Jan Alam, Bhaskar Mitra, Roshan Kini, and Di Wu. “Using energy storage systems to extend the life of hydropower plants”. en. In: *Applied Energy* 337 (May 2023), p. 120894. ISSN: 03062619. DOI: 10.1016/j.apenergy.2023.120894. URL: <https://linkinghub.elsevier.com/retrieve/pii/S0306261923002581> (visited on 03/29/2023).
- [110] David Valentín, Alexandre Presas, Mònica Egusquiza, and Carme Valero. “Hybridization in Kaplan turbines. Wear and tear assessment”. en. In: *IOP Conference Series: Earth and Environmental Science* 1079.1 (Sept. 2022), p. 012108. ISSN: 1755-1307, 1755-1315. DOI: 10.1088/1755-1315/1079/1/012108. URL: <https://iopscience.iop.org/article/10.1088/1755-1315/1079/1/012108> (visited on 06/22/2023).
- [111] Nidec-Industrial. *8 MW/ 10 MWH BESS coupled to hydro for primary control, Power for Verbund, Austria*. 2020. URL: <https://www.nidec-industrial.com/document/bess-coupled-to-hydro-for-primary-control-power-case-study/>.
- [112] J. Fraile-Ardanuy, J.R. Wilhelmi, J.J. Fraile-Mora, and J.I. Perez. “Variable-Speed Hydro Generation: Operational Aspects and Control”. en. In: *IEEE Transactions on Energy Conversion* 21.2 (June 2006), pp. 569–574. ISSN: 0885-8969. DOI: 10.1109/TEC.2005.858084. URL: <http://ieeexplore.ieee.org/document/1634606/> (visited on 06/30/2023).
- [113] Thomas Mercier, Julien Jomaux, Emmanuel De Jaeger, and Mathieu Olivier. “Provision of primary frequency control with variable-speed pumped-storage hydropower”. In: *2017 IEEE Manchester PowerTech*. Manchester, United Kingdom: IEEE, June 2017, pp. 1–6. ISBN: 978-1-5090-4237-1. DOI: 10.1109/PTC.2017.7980920. URL: <http://ieeexplore.ieee.org/document/7980920/> (visited on 08/26/2021).
- [114] Weijia Yang and Jiandong Yang. “Advantage of variable-speed pumped storage plants for mitigating wind power variations: Integrated modelling and performance assessment”. en. In: *Applied Energy* 237 (Mar. 2019), pp. 720–732. ISSN: 03062619. DOI:

- 10.1016/j.apenergy.2018.12.090. URL: <https://linkinghub.elsevier.com/retrieve/pii/S0306261918319019> (visited on 05/03/2021).
- [115] Tor Inge Reigstad and Kjetil Uhlen. “Optimized Control of Variable Speed Hydropower for Provision of Fast Frequency Reserves”. en. In: *Electric Power Systems Research* 189 (Dec. 2020), p. 106668. ISSN: 03787796. DOI: 10.1016/j.epsr.2020.106668. URL: <https://linkinghub.elsevier.com/retrieve/pii/S0378779620304715> (visited on 07/14/2021).
- [116] Tor Inge Reigstad and Kjetil Uhlen. “Nonlinear model predictive control of variable speed hydropower for provision of fast frequency reserves”. en. In: *Electric Power Systems Research* 194 (May 2021), p. 107067. ISSN: 03787796. DOI: 10.1016/j.epsr.2021.107067. URL: <https://linkinghub.elsevier.com/retrieve/pii/S0378779621000481> (visited on 09/28/2023).
- [117] Swissgrid Ltd. *Conditions for prequalification (primary, secondary and tertiary control, in German) - Präqualifikationsbedingungen*. de. 2009. URL: <https://www.swissgrid.ch/dam/swissgrid/customers/topics/ancillary-services/prequalification/2/Anhang-01-Praequalifikationsbedingungen-de.pdf>.
- [118] Pierre Haessig. “Convex Storage Loss Modeling for Optimal Energy Management”. In: *2021 IEEE Madrid PowerTech*. Madrid, Spain: IEEE, June 2021, pp. 1–6. ISBN: 978-1-66543-597-0. DOI: 10.1109/PowerTech46648.2021.9494786. URL: <https://ieeexplore.ieee.org/document/9494786/> (visited on 08/22/2023).
- [119] Stephen P. Boyd and Lieven Vandenbergh. *Convex optimization*. en. Cambridge, UK ; New York: Cambridge University Press, 2004. ISBN: 978-0-521-83378-3.
- [120] Dariusz Borkowski and Marek Majdak. “Small Hydropower Plants with Variable Speed Operation—An Optimal Operation Curve Determination”. en. In: *Energies* 13.23 (Nov. 2020), p. 6230. ISSN: 1996-1073. DOI: 10.3390/en13236230. URL: <https://www.mdpi.com/1996-1073/13/23/6230> (visited on 09/15/2023).
- [121] IEC and others Standard. “Hydraulic turbines, storage pumps and pump-turbines—model acceptance tests”. In: *International Electrotechnical Commission*, (1999). URL: <https://webstore.iec.ch/publication/60951>.
- [122] Paolo Romano and Mario Paolone. “Enhanced Interpolated-DFT for Synchrophasor Estimation in FPGAs: Theory, Implementation, and Validation of a PMU Prototype”. In: *IEEE Transactions on Instrumentation and Measurement* 63.12 (Dec. 2014), pp. 2824–2836. ISSN: 0018-9456, 1557-9662. DOI: 10.1109/TIM.2014.2321463. URL: <http://ieeexplore.ieee.org/document/6818415/> (visited on 09/12/2023).
- [123] Alexandre Presas, David Valentin, Weiqiang Zhao, Mònica Egusquiza, Carme Valero, and Eduard Egusquiza. “On the use of neural networks for dynamic stress prediction in Francis turbines by means of stationary sensors”. en. In: *Renewable Energy* 170 (June 2021), pp. 652–660. ISSN: 09601481. DOI: 10.1016/j.renene.2021.02.013. URL: <https://linkinghub.elsevier.com/retrieve/pii/S0960148121001804> (visited on 09/07/2023).

Bibliography

- [124] Alexandre Presas, Yongyao Luo, Zhengwei Wang, and Bao Guo. “Fatigue life estimation of Francis turbines based on experimental strain measurements: Review of the actual data and future trends”. en. In: *Renewable and Sustainable Energy Reviews* 102 (Mar. 2019), pp. 96–110. ISSN: 13640321. DOI: 10.1016/j.rser.2018.12.001. URL: <https://linkinghub.elsevier.com/retrieve/pii/S1364032118307974> (visited on 09/07/2023).
- [125] Holger Hesse, Michael Schimpe, Daniel Kucevic, and Andreas Jossen. “Lithium-Ion Battery Storage for the Grid—A Review of Stationary Battery Storage System Design Tailored for Applications in Modern Power Grids”. en. In: *Energies* 10.12 (Dec. 2017), p. 2107. ISSN: 1996-1073. DOI: 10.3390/en10122107. URL: <https://www.mdpi.com/1996-1073/10/12/2107> (visited on 08/21/2023).
- [126] ENTSOE ICS Investigation Expert Panel. *Continental Europe Synchronous Area Separation on 08 January 2021 - Final Report*. Tech. rep. ENTSO-E, July 2021. URL: https://eepublicdownloads.azureedge.net/clean-documents/SOC%20documents/SOC%20Reports/entso-e_CESysSep_Final_Report_210715.pdf.
- [127] *Regelleistung Website*. URL: <https://www.regelleistung.net>.
- [128] Waleed Khalid Mohammed Ridha, Kazem Reza Kashyzadeh, and Siamak Ghorbani. “Common Failures in Hydraulic Kaplan Turbine Blades and Practical Solutions”. en. In: *Materials* 16.9 (Apr. 2023), p. 3303. ISSN: 1996-1944. DOI: 10.3390/ma16093303. URL: <https://www.mdpi.com/1996-1944/16/9/3303> (visited on 12/05/2023).
- [129] N. Chettibi, A. Massi Pavan, A. Mellit, A.J. Forsyth, and R. Todd. “Real-time prediction of grid voltage and frequency using artificial neural networks: An experimental validation”. en. In: *Sustainable Energy, Grids and Networks* 27 (Sept. 2021), p. 100502. ISSN: 23524677. DOI: 10.1016/j.segan.2021.100502. URL: <https://linkinghub.elsevier.com/retrieve/pii/S2352467721000734> (visited on 08/18/2023).
- [130] NGESO. *Historic Frequency Data*. 2019. URL: <https://data.nationalgrideso.com/system/system-frequency-data?from=40#resources>.
- [131] B.-J. Chen, M.-W. Chang, and C.-J. Lin. “Load Forecasting Using Support Vector Machines: A Study on EUNITE Competition 2001”. en. In: *IEEE Transactions on Power Systems* 19.4 (Nov. 2004), pp. 1821–1830. ISSN: 0885-8950. DOI: 10.1109/TPWRS.2004.835679. URL: <http://ieeexplore.ieee.org/document/1350819/> (visited on 09/27/2021).
- [132] Fabrizio Sossan, Enrica Scolari, Rahul Gupta, and Mario Paolone. “Solar irradiance estimations for modeling the variability of photovoltaic generation and assessing violations of grid constraints: A comparison between satellite and pyranometers measurements with load flow simulations”. en. In: *Journal of Renewable and Sustainable Energy* 11.5 (Sept. 2019), p. 056103. ISSN: 1941-7012. DOI: 10.1063/1.5109076. URL: <http://aip.scitation.org/doi/10.1063/1.5109076> (visited on 09/27/2021).
- [133] F. Pozzi, T. Di Matteo, and T. Aste. “Exponential smoothing weighted correlations”. en. In: *The European Physical Journal B* 85.6 (June 2012), p. 175. ISSN: 1434-6028, 1434-6036. DOI: 10.1140/epjb/e2012-20697-x. URL: <http://link.springer.com/10.1140/epjb/e2012-20697-x> (visited on 09/27/2021).

Author's Publications

- [P1] Francesco Gerini, Elena Vagnoni, Rachid Cherkaoui, and Mario Paolone. “Optimal Short-Term Dispatch of Pumped-Storage Hydropower Plants Including Hydraulic Short Circuit”. In: *Submitted to IEEE Transactions on Sustainable Energy* (2023). (Visited on 09/28/2023).
- [P2] Francesco Gerini, Elena Vagnoni, Rachid Cherkaoui, and Mario Paolone. “Improving frequency containment reserve provision in run-of-river hydropower plants”. en. In: *Sustainable Energy, Grids and Networks* 28 (Dec. 2021), p. 100538. ISSN: 23524677. DOI: 10.1016/j.segan.2021.100538. URL: <https://linkinghub.elsevier.com/retrieve/pii/S2352467721001090> (visited on 10/03/2022).
- [P3] Francesco Gerini, Elena Vagnoni, Rachid Cherkaoui, and Mario Paolone. “Optimal CAM Computation of Kaplan Turbines Accounting for Wear and Tear Originated by Frequency Control”. In: *2021 IEEE Madrid PowerTech*. Madrid, Spain: IEEE, June 2021, pp. 1–6. ISBN: 978-1-66543-597-0. DOI: 10.1109/PowerTech46648.2021.9495080. URL: <https://ieeexplore.ieee.org/document/9495080/> (visited on 08/12/2021).
- [P4] Francesco Gerini, Yihui Zuo, Rahul Gupta, Antonio Zecchino, Zhao Yuan, Elena Vagnoni, Rachid Cherkaoui, and Mario Paolone. “Optimal grid-forming control of battery energy storage systems providing multiple services: Modeling and experimental validation”. en. In: *Electric Power Systems Research* 212 (Nov. 2022), p. 108567. ISSN: 03787796. DOI: 10.1016/j.epsr.2022.108567. URL: <https://linkinghub.elsevier.com/retrieve/pii/S0378779622006496> (visited on 10/03/2022).
- [P5] Antonio Zecchino, Francesco Gerini, Yihui Zuo, Rachid Cherkaoui, Mario Paolone, and Elena Vagnoni. “Local Effects of Grid-Forming Converters Providing Frequency Regulation to Bulk Power Grids”. en. In: *2021 IEEE PES Innovative Smart Grid Technology – Asia*. Brisbane, Australia: IEEE, Dec. 2021, p. 5.
- [P6] Francesco Gerini, Elena Vagnoni, Martin Seydoux, Rachid Cherkaoui, and Mario Paolone. “Enhanced Frequency Containment Reserve Provision from Battery Hybridized Hydropower Plants: Theory and Experimental Validation”. In: *PSCC2024, Power Systems Computation Conference, Paris, France* (2023). Publisher: arXiv Version Number: 1. DOI: 10.48550/ARXIV.2309.15660. URL: <https://arxiv.org/abs/2309.15660> (visited on 09/28/2023).

Author's Publications

- [P7] Francesco Gerini, Elena Vagnoni, Rachid Cherkaoui, and Mario Paolone. “Experimental Investigation of Repurposed Kaplan Turbines as Variable-Speed Propellers for Maximizing Frequency Containment Reserve”. In: *PSCC2024, Power Systems Computation Conference, Paris, France* (2023). (Visited on 09/28/2023).
- [P8] Francesco Gerini, Elena Vagnoni, Martin Seydoux, Rachid Cherkaoui, and Mario Paolone. “Experimental facility for reduced scale model testing of hydraulic machines hybridized with a battery energy storage system”. In: *IOP Conference Series: Earth and Environmental Science* 774.1 (June 2021), p. 012119. ISSN: 1755-1307, 1755-1315. DOI: 10.1088/1755-1315/774/1/012119. URL: <https://iopscience.iop.org/article/10.1088/1755-1315/774/1/012119> (visited on 07/28/2023).

Francesco Gerini

ELL 117, Station 11, EPFL, Lausanne, Switzerland 1015

francesco.gerini@epfl.ch, +41 77 967 32 92

[Google Scholar](#) ◇ [ResearchGate](#) ◇ [LinkedIn](#) ◇ [Orcid](#)

EDUCATION

Ph.D. in Electrical Engineering

09/2019 - 01/2024

Distributed Electrical Systems Laboratory (DESL),

École Polytechnique Fédérale de Lausanne (EPFL), Switzerland

Thesis title: *"Advanced Control Strategies to Exploit the Hydropower Potential Enhancing Ancillary Services Provision to the Power System"*

Thesis directors: *Dr. Rachid Cherkaoui (EPFL), Prof. Mario Paolone (EPFL)*

M.Sc. in Electrical Engineering

09/2016 - 03/2019

Alma Mater Studiorum,

Università di Bologna (UNIBO), Bologna, Italy

Thesis title: *"Locating lightning strikes and flashovers along overhead power transmission lines using electromagnetic time reversal based similarity characteristics."*

Thesis directors: *Prof. Carlo Alberto Nucci (UNIBO)*

Final Grade: 110/110 with honors

B.Tech in Energy Engineering

09/2013 - 10/2016

Alma Mater Studiorum,

Università di Bologna (UNIBO), Bologna, Italy

Thesis title: *"Analysis of voltage profiles and power flows in different types of distribution networks using OpenDSS software"*

Thesis directors: *"Prof. Alberto Borghetti (UNIBO), Prof. Carlo Alberto Nucci (UNIBO)"*

Final Grade: 110/110

EXPERIENCE

Doctoral Researcher, DESL, EPFL, Switzerland

09/2019 - present

- Participated in the development of a Smart Power Plant Supervisor (SPPS), for optimal control of hydropower plants assets.
- Validation of the SPPS on different power plants including: Grand'Maison and Vogelgrun, France, operated by EDF and Frades, Portugal, operated by EDP.
- Contributed to hybridizing a reduce scale turbine unit with a battery to improve dynamic frequency response and reduce governor actions.
- Joint Control of the BESS hybridized hydropower plant
- Development of a control framework for GFR converter-interfaced BESS for multiple services provision including feeder dispatchability, FCR, and voltage regulation in the face of uncertainties from demand, distributed generation, and grid frequency.
- Experimental validation of the above control schemes on real-life medium-voltage distribution networks (in the EPFL Campus, Lausanne, Switzerland).

PUBLICATIONS

Journal Articles:

1. **Francesco Gerini**, Elena Vagnoni, Rachid Cherkaoui, Mario Paolone. *"Improving frequency containment reserve provision in run-of-river hydropower plants."* Sustainable Energy, Grids and Networks 28 (2021): 100538. [Publisher Link](#).
2. **Francesco Gerini**, Yihui Zuo, R Gupta, A Zecchino, Z Yuan, Elena Vagnoni, Rachid Cherkaoui, Mario Paolone. *"Optimal grid-forming control of battery energy storage systems providing multiple services: Modeling and experimental validation."* Electric Power Systems Research 212 (2022): 108567. [Publisher Link](#).
3. **Francesco Gerini**, Elena Vagnoni, Martin Seydoux, Rachid Cherkaoui, Mario Paolone. *"Enhanced Frequency Containment Reserve Provision from Battery Hybridized Hydropower Plants: Theory and Experimental Validation."* PSCC2024, Power Systems Computation Conference, Paris, France (2023). arXiv preprint arXiv:2309.15660 (2023). [Publisher Link](#).
4. **Francesco Gerini**, Elena Vagnoni, Rachid Cherkaoui, and Mario Paolone. *"Experimental Investigation of Repurposed Kaplan Turbines as Variable-Speed Propellers for Maximizing Frequency Containment Reserve."* PSCC2024, Power Systems Computation Conference, Paris, France (2023).
5. **Francesco Gerini**, Elena Vagnoni, Rachid Cherkaoui, and Mario Paolone. *"Optimal Short-Term Dispatch of Pumped-Storage Hydropower Plants Including Hydraulic Short Circuit."* Submitted to IEEE Transactions on Power System (2023).

Conference Papers:

1. **Francesco Gerini**, Elena Vagnoni, Rachid Cherkaoui, Mario Paolone. *"Optimal CAM Computation of Kaplan Turbines Accounting for Wear and Tear Originated by Frequency Control."* 2021 IEEE Madrid PowerTech . [Publisher Link](#).
2. **Francesco Gerini**, Elena Vagnoni, Martin Seydoux, Rachid Cherkaoui, Mario Paolone. *"Experimental facility for reduced scale model testing of hydraulic machines hybridized with a battery energy storage system."* IOP Conference Series: Earth and Environmental Science 774.1 (2021): 012119. [Publisher Link](#).
3. Antonio Zecchino, **Francesco Gerini**, Yihui Zuo, Rachid Cherkaoui, Mario Paolone, Elena Vagnoni. *"Local effects of grid-forming converters providing frequency regulation to bulk power grids."* 2021 IEEE PES Innovative Smart Grid Technologies-Asia (ISGT Asia) (2021): 1-5. [Publisher Link](#).
4. Elena Vagnoni, **Francesco Gerini**, Rachid Cherkaoui, Mario Paolone. *"Digitalization in hydropower generation: development and numerical validation of a model-based Smart Power Plant Supervisor."* IOP Conference Series: Earth and Environmental Science 774.1 (2021): 012107. [Publisher Link](#).
5. Zhaoyang Wang, **Francesco Gerini**, Mario Paolone, Carlo A. Nucci and Farhad Rachidi. *"Using Electromagnetic Time Reversal Similarity Metric to Locate Lightning-Originated Flashovers on Overhead Transmission Lines."* 2019 International Symposium on Lightning Protection (XV SIPDA) (2019): 1-6. [Publisher Link](#).

PRESENTATIONS

Conferences:

1. XV SIPDA 2019, Sao Paolo, Brasil: *Using Electromagnetic Time Reversal Similarity Metric to Locate Lightning-Originated Flashovers on Overhead Transmission Line.*
2. IEEE Madrid PowerTech 2021: *"Optimal CAM Computation of Kaplan Turbines Accounting for Wear and Tear Originated by Frequency Control."*
3. 30th IAHR Symposium on Hydraulic Machinery and Systems 2021: *"Experimental facility for reduced scale model testing of hydraulic machines hybridized with a battery energy storage system."*
4. IEEE PES ISGT Asia 2021: *"Local effects of grid-forming converters providing frequency regulation to bulk power grids."*

Invited:

5. ISGT Europe 2021, Espoo, Finland, Panel 2: *"Battery Energy Storage Systems to support the power system : demonstrations and perspectives from the H2020 OSMOSE project"*.
6. World Hydropower Congress (WHC) 2023, Powering Sustainable Growth, Bali, Indonesia: *"Enhanced Frequency Containment Reserve Provision from Battery Hybridized Hydropower Plants"*.

INVOLVEMENT IN RESEARCH PROJECTS

[XFLEX HYDRO](#), H2020 funded project 2019 - 2023

- Modeling and optimal control of hydropower plants
- Collaboration with the hydropower plant of Vogelgrun, France, operated by EDF
- Collaboration with the hydropower plant of Grand'Maison, France, operated by EDF
- Collaboration with the hydropower plant of Frades, Portugal, operated by EDP

[OSMOSE](#), H2020 funded project 2022

- Optimal control of grid-forming converter interfaced battery energy storage systems
- Validation of real-time control algorithm on a real-life medium voltage distribution network EPFL campus, Switzerland hosting 560kWh/720kW battery storage capacity

[HydroLEAP](#), Swiss Federal Office of Energy (SFOE) funded project 2022-present

- Development of a experimental platform for dynamic testing of hydropower response to grid dynamics

[S4S - Helios NeuroCAM](#), EPFL funded project 2023-present

- Validation of a OPF-based real-time control algorithm on a real-life medium voltage distribution network in the EPFL campus, Switzerland hosting 560kWh/720kW battery storage capacity, 100 kWp photovoltaic, 250 kW base demand.
- Development of the software for operation of the BESS for real-time control.

TEACHING ACTIVITIES

Teaching Assistant, course on "*Energy Conversion*", EPFL 2019 - 2023
B.Tech in Electrical and Electronics Engineering

Teaching Assistant, course on "*Principles of Power Systems*", EPFL 2019 - 2023
M.Sc. in Energy Science and Technology
Nominated for the "*School of Engineering Teaching Assistant Award*" for the year 2023.

Teaching Assistant, course on "*Power distribution networks*", EPFL 2019 - 2023
B.Tech in Electrical and Electronics Engineering

Teaching Assistant, course on "*Smart grids technologies*", EPFL 2022
M.Sc. in Electrical and Electronics Engineering

SUPERVISED STUDENT PROJECTS

1. *Testing Optimal Control Strategies for Run-of-River Hydropower Plant in MATLAB/Simulink*, BA Semester project, Fall 2021.
2. *Experimental Validation of a Real-time Control Software for Battery Energy Storage Systems*, BA Semester project, Sinan Ulcay, Spring 2022.
3. *State of Health estimation for a large-scale Battery Energy Storage System*, M.Sc. semester project, Ludovic Pujol, Spring 2022.
4. *Model Predictive Control (MPC) for a Low-head Hydropower Plant Hybridized with Battery Energy Storage*, M.Sc. Semester project, Robin Leibundgut, Spring 2023.
5. *Testing Optimal Short-Term Dispatching for Pumped-Storage Hydropower Plants Including Hydraulic Short Circuit Operation*, M.Sc. semester project, Sinan Ulcay, Spring 2023.
6. *Reinforcement Learning Solutions for Frequency Containment Reserve Provision from Battery Hybridized Hydropower Plants*, M.Sc. semester project, Justin Manson, Fall 2023.

SKILLS

- Operation and planning of hydropower plant assets
- Model predictive control, measurement-based/data-driven control.
- Convex optimization, convexification methods (linearization, relaxation etc.).
- Robust and stochastic-based optimization for control and scheduling of power distribution networks.
- Hands-on experience in operating grid-scale battery storage
- Intra-day and day-ahead forecasting of stochastic resources such as PV generation and demand.
- Hands-on experience in operating reduce-scale models of hydraulic turbines for performance assessment under dynamic grid condition

Programming Languages and Frameworks:

Matlab, Python, LabVIEW, EMTP-RV

Languages:

Italian (Native), English (Fluent), French (Conversational)

REFEREES

Dr. Rachid Cherkaoui, Power System Group,
EPFL, Switzerland

✉ rachid.cherkaoui@epfl.ch

☎ +41 21 693 20 58

Ph.D. Thesis Supervisor

Prof. Mario Paolone, Distributed Electrical System Laboratory,
EPFL, Switzerland

✉ mario.paolone@epfl.ch

☎ +41 21 693 26 62

Ph.D. Thesis co-Supervisor